Title
Investigations of the Oxygen Electrode

Author
Klaus, Shannon

Publication Date
2015

Peer reviewed|Thesis/dissertation

Investigations of the Oxygen Electrode

by

Shannon Leigh Klaus

A dissertation submitted in partial satisfaction of the
requirements for the degree of
Doctor of Philosophy

In

Chemical Engineering

in the

Graduate Division

of the

University of California, Berkeley

Committee in charge:

Professor Alexis T. Bell, Chair
Professor Bryan McCloskey
Professor Tanja Ćuk

Summer 2015

Investigations of the Oxygen Electrode

Abstract

Investigations of the Oxygen Electrode

by

Shannon Leigh Klaus

Doctor of Philosophy in Chemical Engineering

University of California, Berkeley

Professor Alexis T. Bell, Chair

A third of anthropomorphic greenhouse gas emissions originate from the energy and transportation sectors. Since these emissions contribute to increased pollution and climate change, the development of new energy sources with decreased environmental impact is critical. The use of hydrogen as a fuel is an attractive way to increase energy security and reduce carbon emissions, and hence there is considerable interest in the efficient production and use of hydrogen. The production of hydrogen without the generation of CO_2 can be done by the electrolysis of water, and the hydrogen thus generated can be used to provide electrical power via its consumption in a fuel cell. However, both processes suffer from the inefficiency of the electrodes used for the oxygen evolution reaction (OER), or water oxidation reaction, and the oxygen reduction reaction (ORR). This project has focused on developing a deeper understanding of the factors limiting the catalytic performance of both the oxygen reduction (Part I) and oxygen evolution reactions (Part II).

In Part I, in-situ surface-enhanced Raman spectroscopy was used to investigate the oxidation state of Pt and the nature of adsorbed species involved in the ORR. For scans commencing at 1.25 V vs. RHE and above, bulk α-PtO_2 is observed. Amorphous surface oxide/hydroxide is formed at lower potentials, which reduces as the cathodic sweep proceeds and features characteristic of adsorbed water are detected. Additionally, in oxygen-saturated electrolyte, several Raman peaks are observed at potentials below 0.87 V, which can be assigned to adsorbed molecular oxygen species. The presence of these features cannot be attributed exclusively to ORR reaction intermediates but is consistent with recent theoretical studies suggesting that below 0.9 V vs RHE, the reduction of oxygen is limited by the formation of OOH on the surface of metallic Pt.

Part II explores catalysts (and specifically the role of Fe) for the oxygen evolution reaction. The effect of ppb-level Fe electrolyte impurities on the structure and OER activity of NiOOH electrocatalysts was explored. Films aged in Fe-free electrolyte are predominantly disordered β-$Ni(OH)_2$/β-NiOOH if maintained below 0.7 V vs Hg/HgO in 1 M KOH and will "overcharge" to form a mixture of γ- and β-NiOOH above this potential. Both NiOOH phases are found to be very poor OER catalysts. In contrast, $Ni(OH)_2$ aged in unpurified KOH electrolyte exhibits enhanced OER activity and structural changes consistent with a NiFe-layered double hydroxide phase, providing direct evidence that a Ni–Fe layered double (oxy)hydroxide (LDH) phase is critical for high OER activity. The effect of Fe^{3+} electrolyte impurities over Au was also investigated. This work demonstrates that increased OER activity at low overpotentials is not due to the formation

of a transient, “superactive” Au(III) surfaquo species as previously reported, but instead arises from reversibly-adsorbed Fe impurities. Finally, integration of $Ni_{1-x}Fe_xOOH$ catalysts with light-absorbing semiconductors is necessary for photoelectrochemical fuel generation. Since the application of cathodic potentials required for typical electrochemical catalyst deposition restricts the use of certain photoanode materials, sputter deposition of catalysts was also investigated. We find that for sputter-deposited or electrodeposited $Ni_{1-x}Fe_xOOH$ catalyst films, Fe^{3+} cations substitute for Ni^{3+} cations in the framework of NiOOH. This substitution can occur for up to 20% Fe content, and further addition of Fe results in the formation of a separate FeOOH phase, corresponding to a decrease in OER activity above this Fe composition. $Ni_{1-x}Fe_xOOH$ films prepared by both methods exhibit comparable OER activity, enabling application of $Ni_{1-x}Fe_xOOH$ catalysts to a wider library of photoanodes for light-driven water-splitting applications.

To current and future graduate students

Table of Contents

List of Figures

List of Tables

List of abbreviations and symbols

η	overpotential
AFM	atomic force microscopy
CV	cyclic voltammogram
DFT	density functional theory
EELS	electron energy loss spectroscopy
EIS	electrochemical impedance spectroscopy
E_o	thermodynamic equilibrium potential
E_{meas}	measured potential vs. Hg/HgO
E_{rev}	reversible potential
ICP-MS	inductively coupled plasma mass spectrometry
ICP-OES	inductively coupled plasma optical emission spectrometry
j	geometric current density
LDH	layered double hydroxide
LSV	linear sweep voltammogram
OER	oxygen evolution reaction
ORR	oxygen reduction reaction
PEIS	potentiostatic electrochemical impedance spectroscopy
pzc	point of zero charge
Q	charge
QCM	quartz crystal microbalance
R_u	uncompensated series resistance
RDE	rotating disc electrode
RHE	reference hydrogen electrode
rpm/RPM	rotations per minute
RRDE	rotating ring-disc electrode
SEIRAS	Surface enhanced infrared absorption spectroscopy
SERS	surface-enhanced Raman spectroscopy
TOF	turnover frequency
XAS	X-ray absorption spectroscopy
XPS	X-ray photoelectron spectroscopy

Acknowledgements

First, I'd like to thank my family. Rents, above all, you always encouraged me to pursue my own interests. Thanks for not being Tiger Mom and Dad—I wouldn't be where I am today without your love and support. Chelsea, I'm really glad to have had you in my life the past 28 years. I know that no matter what happens, you will always be there, which is more than I can say for most people. Erica, you have grown a lot during my years in Berkeley, and I look forward to seeing where your own adventures take you.

Thank you to those especially supportive during my leave. Marty and Care, your kindness and generosity are unparalleled, and I wouldn't have made it without your continued guidance through the storm. Thanks for being so great! I also really appreciated the visits from Maureen and Alan, Kierston and Forrest, Mary, and Sudip. Thanks as well to those who checked in virtually--Barclay, Todd, Christina Shaama, and Zheng.

Many thanks to everyone at JCAP. In particular, Lena, Mary, and Yun: you were all fantastic Team OER members, and thanks to Ezra, Meenesh, Peter, Youngkook, Mark H., and Lucas as well. Erin, you are a wonderful work wife, and I wish you much success on your own journey! Jason and David, thanks for XPS crisis management, and thanks as well to David and Le for your help with the recent sputtering plights. I also appreciate Alan and Ian's trouble-shooting help, and Kellie, Theresa, Sherry, and Kristin were also immensely helpful. Additionally, I greatly appreciate the efforts of the amazing LBL shuttle drivers.

The Bell lab members from my years on campus were also awesome, including Amber, Anastasia, Andrew, Anton, Anthony, Bean, Chidam, David, Ferenc, Fuat, Greg, Georges, Jason W., Jennifer, Joe G., Joe Z., Kostas, Kris, Mike, Pingping, Sasi, Sebastian, Sean, Shaama, Shylesh, T.J., Vlad, Will, and Zheng. I probably just forgot someone, but all of you were wonderful coworkers. A sincere thank you to those running the lab behind the scenes. Fuat completed most of the lab responsibilities when I first joined the group, and Amber and Bean spent many hours maintaining lab safety. In recent years, Rachel has been most instrumental to keeping our lab alive and well, and Joe was always there to successfully resolve my many computer woes. The lab would have been inoperable without these members' contributions.

I would also like to thank the amazing staff in the College of Chemistry. Rocio, you were an amazing GSAO, and I appreciate your help even when you were no longer within our department. Kristin, you have always gone above and beyond to help in times of need and are, in general, a rock star. Esayas, you were awesome for the lab course, and Eric G., thanks for making all of our electrochemical cells (and attempting the crumbling Mn electrodes…).

Prof. Bell, I have grown more as a person and researcher as a member of your group than I could have imagined. Thanks to my dissertation committee members, Prof. Maboudian for being a great qualifying exam chair, Prof. Chu for telling me I didn't fail my prelim, Prof. Prausnitz for being a well-rounded engineer, and Mark Lucia being one of the best campus resources available. A special thank you to Prof. Newman and members of the Newman lab: Maureen, Alan, Tony, Nate, and Penny. It was great to be an honorary ECS member. Thanks to Nis and Ali for your commiseration, Sudip for your encouragement and humor, Eric D. for your advice and support, Mrs. Chatlos for being the best math teacher, and my non-engineering friends for being so interesting. Thanks as well to the support of the Soroptimist Founder Region, Society of Women Engineers, and the Berkeley Section Club.

And finally, a special shout-out to the entering class of 2008. I remember an older grad student pointing to our sheet of first-year photos and stating (very matter-of-factly, I might add) that at least one of us would not complete our PhD. Despite the odds, we've prevailed!

Chapter 1

Introduction

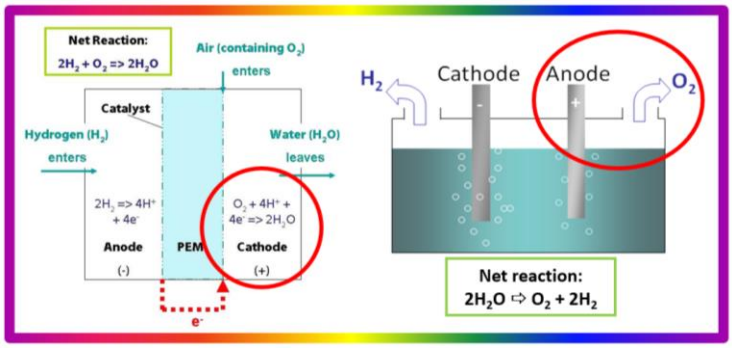

The use of hydrogen fuel cells is a potential option for increasing energy security and reducing carbon emissions. Hydrogen fuel cell technology even passes through Berkeley by the hour inside "Hydrogen Zero Emission" buses. While these vehicles inspire hope for a greener future, the current hydrogen buses cost twice the amount of a diesel bus to operate, and the hydrogen fuel elsewhere generates 2-3 times the carbon dioxide emitted by a diesel bus.[1,2] Since fuel cells use electrochemical energy and not combustion heat energy, theoretical efficiencies greater than 90% can be attained. In practice, though, automotive fuel cell efficiencies are closer to 40-50%, mainly due to kinetic losses of the oxygen reduction reaction (ORR), which proceeds in acid as

$$O_2 + 4H^+ + 4e^- \rightarrow 2H_2O \qquad (1.1)$$

To improve the efficiency of this reaction, platinum-based catalysts are typically used. However, even for platinum, the most active elemental material for the oxygen electrode, the efficiency loss is ten times that of the hydrogen electrode.[3,4] Given the high expense and inefficiency of Pt for the ORR, there has been motivation to seek alternative cathode electrocatalysts based upon earth-abundant materials.

One of the difficulties in improving the efficiency of catalyst materials is that the active catalyst phases are often poorly defined or understood. It is therefore challenging to directly relate observed reaction activities to catalyst structure and/or composition. To address this difficult, a primary effort of my dissertation has been to investigate surface structure and phases of oxygen reduction (and evolution) catalysts under reaction conditions and relate phase transformations to the occurring electrochemical processes.

To help guide the search of earth-abundant oxygen reduction catalysts, it is desirable to understand the factors limiting the catalyst activity of Pt, such as the oxidation state and surface structure of the catalyst under working conditions. Theoretical analyses of the ORR have been carried out under the assumption that oxygen reduction occurs on the surface of metallic Pt and does not take into account the influence that oxide or adsorbed water layers might have on the kinetics.[5] Since experimental studies have shown that the rate of oxygen reduction is affected by stable Pt oxide species present at low overpotentials,[6,7] knowledge of the state of oxidation state of Pt is essential for developing an understanding of the factors influencing the kinetics of the ORR. Additionally, several distinct Pt (hydr)oxides can form, depending on the applied potential,

which makes it difficult to define the distribution of species present on the working electrocatalyst.[8]

To address these challenges, we carried out in-situ Raman characterization of Pt electrodes under ORR conditions in order to determine the nature of oxide structure and other adsorbed surface species present during this reaction. Part I (Chapter 2) details these results, which provides insights into the composition of platinum oxides formed, the conditions under which this oxide is reduced, and potentials at which water is adsorbed on the Pt electrode during the ORR. By understanding the structure and adsorbed surface species under relevant reaction conditions for platinum, the most active catalyst material, we can further guide the search for other, efficient ORR catalysts derived from earth-abudant elements.

An additional requirement to enable wide-spread use of hydrogen fuel cells is that hydrogen must also be generated economically from renewable resources, which is the focus of Part II of this dissertation. One possibility is the electrochemical generation of hydrogen from water. Though hydrogen production is the goal, the efficiency bottleneck of water-splitting actually occurs at the opposite electrode, due to the oxygen evolution reaction (OER, the inverse of ORR), which proceeds in acid as:

$$2H_2O \rightarrow 4H^+ + O_2 + 4e^- \quad (1.2)$$

and in base as:

$$4OH^- \rightarrow 2H_2O + O_2 + 4e^- \quad (1.3)$$

The viability of such a system hinges upon efficiency: a highly active oxygen electrode catalyst is critical. Iridium is the most active elemental catalysts for oxygen evolution but is far too rare and expensive for realistic use. Instead, efficient oxygen evolution must be obtained through the use of earth-abundant materials. The remainder of the chapters (Chapters 3-5) focuses on investigations of oxygen evolution catalyst materials.

Chapters 3 and 4 examine the effect of Fe^{3+} alkaline electrolyte impurities on the oxygen evolution activity over NiOOH and Au_2O_3 materials. Ni-(oxy)hydroxide-based materials are promising earth-abundant catalysts for electrochemical water oxidation in basic media, and recent findings demonstrate that incorporation of trace Fe impurities from commonly used KOH electrolytes significantly improves the OER activity over these materials. Since previous studies detailing structural differences between the α-$Ni(OH)_2$/γ-NiOOH and β-$Ni(OH)_2$/β-NiOOH phases were likely all completed in unpurified electrolytes, it is unclear whether these structural changes are unique to the aging phase transformation of NiOOH or arise due to inadvertent Fe incorporation. In Chapter 3, we examine the effects of Fe incorporation on the structure and OER activity of Ni-(oxy)hydroxide. These findings are the first to demonstrate the in situ changes in the catalyst structure resulting from the incorporation of Fe electrolyte impurities within Ni-(oxy)hydroxide and provide direct evidence that formation of a Ni-Fe layered double (oxy)hydroxide (LDH) phase is responsible for the high OER activity observed after aging $Ni(OH)_2$ in unpurified alkaline electrolytes. Chapter 4 outlines a similar effect of Fe^{3+} impurities over Au electrodes. Previous studies attribute an increase in OER current over Au at low overpotentials to the presence of "superactive" Au(III) surfaquo species.[9] However, we demonstrate that this observed OER activity increase is actually due to Fe^{3+} impurities chemically bound over the Au_2O_3 surface. Density functional theory was used to compare theoretical oxygen

evolution overpotentials over Au_2O_3 and Fe-Au_2O_3 and confirms that Fe-Au_2O_3 provides more optimal binding energetics of OER reaction intermediates vs Au_2O_3 alone, and as a result, reduces the required overpotential for oxygen evolution.

Finally, Chapter 5 focuses on the deposition of $Ni_{1-x}Fe_xOOH$ catalysts for application to photoabsorber materials. Within the Joint Center for Artificial Photosynthesis, the overall goal is to convert solar energy into viable transportation fuels, including hydrogen. Integration of $Ni_{1-x}Fe_xOOH$ catalysts with light-absorbing semiconductors is therefore required for photoelectrochemical fuel generation. However, the application of cathodic potentials required for electrodeposition may not be amenable for integration with many semiconductor photoanode materials.[10,11] To circumvent this limitation, sputter deposition of catalysts can be used for facile catalyst layering without an applied potential. We compare the structure and OER activity of sputter-deposited and electrodeposited $Ni_{1-x}Fe_xOOH$ thin films and find that both film preparation methods produce catalysts with similar electrochemical behavior and OER activity across all compositions, with a maximum OER activity observed at ~20% Fe content (above which a separate, FeOOH-type phase is observed to form). These findings enable greater versatility in the application of $Ni_{1-x}Fe_xOOH$ catalyst layers over photoanodes for light-driven water-splitting applications.

References

1. "National Fuel Cell Bus Program: Accelerated Testing Evaluation Report #2 AC Transit" http://www.nrel.gov/hydrogen/pdfs/48106-2.pdf
2. Patzek et al. "The Overall Energy Balance of the Hydrogen Bus in Berkeley, CA." http://gaia.pge.utexas.edu/papers/HydrogenBus20040525.pdf
3. Gewirth, A. A.; Thorum, M. S., Inorganic Chemistry **2010,** 49 (8), 3557-3566.
4. Gasteiger, H. A.; Panels, J. E.; Yan, S. G. Journal of Power Sources **2004**, 127, 162–171.
5. Nørskov, J. K.; Rossmeisl, J.; Logadottir, A.; Lindqvist, L.; Kitchin, J. R.; Bligaard, T.; Jónsson, H., Origin of the Overpotential for Oxygen Reduction at a Fuel-Cell Cathode. The Journal of Physical Chemistry B 2004, 108, 17886-17892.
6. Hansen, H. A.; Rossmeisl, J.; Norskov, J. K., Physical Chemistry Chemical Physics **2008,** 10 (25), 3722-3730.
7. Damjanovic, A.; Dey, A.; Bockris, J. O. M., Electrochimica Acta **1966,** 11 (7), 791-814.
8. Burke, L.D.; Buckley, D.T., Journal of Electroanalytical Chemistry **1996** 405, 101-109.
9. Doyle, R.; Lyons, M. G., J Solid State Electrochem **2014**, 18, 3271-3286.
10. Seabold, J. A.; Choi, K. S., Journal of the American Chemical Society **2012**, 134, 2186-2192.
11. Park, Y.; McDonald, K. J.; Choi, K. S., Chemical Society Reviews **2013**, 42, 2321-2337.

Part I

The Oxygen Reduction Reaction

Chapter 2

Surface-Enhanced Raman Studies of Oxide Reduction and the Electrochemical Reduction of Oxygen on Platinum

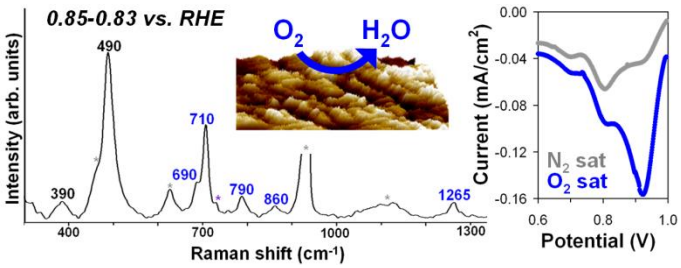

Abstract

Confocal surface-enhanced Raman spectroscopy (SERS) was used to identify adsorbed species present on electrochemically roughened Pt during the reduction of platinum oxide and the reduction of oxygen in 0.5 M $HClO_4$. Raman spectra were acquired during 1 mV s^{-1} cathodic linear sweep voltammograms (LSVs). A broad Raman band corresponding to amorphous oxide is initially present in nitrogen saturated electrolyte, which reduces in intensity as the cathodic sweep proceeds. Upon deuteration of the electrolyte, the oxide band redshifts in frequency, confirming the presence of Pt-OH species. Greater irreversibility of oxide reduction occurs in LSVs initiated at higher potentials; for scans commencing at 1.25 V vs RHE or above, bulk α-PtO_2 is observed. Subsequent to oxide reduction, vibrations are observed for water adsorbed on the surface of Pt in both O_2 and N_2-saturated electrolyte. For LSVs completed in oxygen-saturated electrolyte, several Raman peaks are observed at potentials below 0.87 V that can be assigned to adsorbed O, O_2, and OOH. The presence of these bands is consistent with recent theoretical studies suggesting that at these potentials, the reduction of oxygen is limited by the formation of OOH on the surface of metallic Pt.

2.1. Introduction

Hydrogen-based fuel cells offer a potentially attractive source of electrical power for automotive transportation.[1-3] Because fuel cells are not heat engines, their efficiency is not constrained by Carnot's law, and theoretical efficiencies in excess of 90% can be attained.[4] In practice, though, automotive fuel cell efficiencies are closer to 40-50%, due principally to the slow kinetics of the oxygen reduction reaction (ORR) at the cathode. Even for Pt, the most active elemental catalyst for the ORR, an overpotential of 500-600 mV at 80 °C is required to achieve current densities of about 1.5 A cm^{-2}.[2,5] By contrast, the overpotential at the anode, where H_2 is activated to produce protons and electrons, is only 50 mV. Given the high expense and inefficiency of Pt for the ORR, there is strong motivation to seek alternative cathode electrocatalysts based upon earth-abundant elements. To help guide this search, it is desirable to understand the factors limiting the catalyst activity of Pt, such as the oxidation state of the catalyst under working conditions and the elementary reactions which limit the rate of the ORR.

It has been proposed that oxygen reduction on Pt in acidic electrolyte proceeds via either a direct, four-electron reduction process:

$$O_2 + 4H^+ + 4e^- \rightarrow 2H_2O \quad (2.1)$$

or via a series process involving two sequential two-electron reductions in which hydrogen peroxide is produced as an intermediate:

$$O_2 + 2H^+ + 2e^- \rightarrow H_2O_2 \quad (2.2)$$

$$H_2O_2 + 2H^+ + 2e^- \rightarrow 2H_2O \quad (2.3)$$

The consensus of previous studies is that the direct, four-electron reduction is dominant on Pt electrodes in acidic electrolyte;[2,6,9] however, evidence for the formation of hydrogen peroxide has also been reported.[10,12]

Previous experimental studies of the ORR over Pt show that a plot of the logarithm of the current versus the applied potential (a Tafel plot) exhibits two slopes: 60 mV dec^{-1} for potentials between 1.23 V and ~ 0.8 V (vs RHE) and 120 mV dec^{-1} below ~ 0.8 V. This observation suggests that a change in the ORR mechanism occurs between low and high overpotentials due to a change of adsorbed species present on the electrode,[7,13,18] or alternatively, a change in the number of accessible oxygen reduction active sites between low and high overpotentials.[19] Evidence for a change in the composition of adspecies present at potentials where oxygen reduction occurs over Pt(111) has come from ex-situ X-ray photoelectron spectroscopy (XPS)[20] and in-situ electrochemical impedance spectroscopy (EIS) studies,[21] and is also supported by theoretical calculations.[22] The EIS parameters determined for N_2-saturated and O_2-saturated $HClO_4$ are similar, suggesting that the adsorbate structures present on Pt(111) in the presence and absence of O_2 are comparable. For potentials between 1.2 and 0.8 V, the surface of Pt(111) in N_2-sparged acid electrolyte is dominated by adsorbed O atoms and H_2O, with the surface coverage of O atoms declining with decreasing potential.[20] Below 0.8 V, the Pt(111) surface is covered primarily by OH species as well as H_2O, and the surface concentration of OH species decreases as the voltage is reduced to 0.6 V vs RHE. In contrast to Pt(111), nearly equivalent concentrations of O and OH are observed ex-situ for polycrystalline Pt in N_2-saturated HF formed at potentials between 1.1 V and 0.8 V. As the voltage is decreased, the surface coverage of OH and O are reported to decrease monotonically and the surface coverage of adsorbed H_2O increases, with H_2O becoming the primary surface species observed ex-situ for potentials below 0.8 V vs RHE.[20]

The mechanism by which the ORR proceeds on Pt has been the subject of considerable discussion for the past 50 years. Two broad classes of mechanism have been identified, referred to as the dissociative and associative pathways. The dissociative pathway assumes that O_2 adsorbs dissociatively to form O atoms, which then undergo a two-step reduction via OH species to produce H_2O. By contrast, the associative pathway considers that O_2 reduction is initiated by reduction of molecularly adsorbed O_2 to form an OOH species. The OOH species then dissociates to form O and OH, which are subsequently reduced to H_2O. While most theoretical calculations of oxygen reduction on Pt(111) indicate that the energetics of O_2 reduction are less demanding those for O_2 dissociation, some authors suggest that both pathways may be operative at overpotentials where the ORR occurs.[23] It is also worth noting that theoretical calculations show that while OOH species could be reduced to hydrogen peroxide, this process is energetically unfavorable relative to the dissociation of OOH to produce O and OH.[22,25]

Theoretical analyses of the ORR have been carried out under the assumption that oxygen reduction occurs on the surface of metallic Pt and, hence, does not take into account the influence that an oxide layer might have on the kinetics. Since experimental studies have shown that the rate of oxygen reduction is affected by stable Pt oxide species present at low overpotentials, knowledge

of the state of oxidation state of Pt is essential for developing an understanding of the factors influencing the kinetics of the ORR.[26,27] Further complicating matters is the observation that several distinct Pt oxides can form, depending on the applied potential, making it difficult to define the distribution of species present on the working electrocatalyst.[28]

The perspective emerging from an examination of the experimental and theoretical literature is that the progress of the ORR can be influenced by the extent of Pt surface oxidation and the composition of the principal adsorbed species (i.e., O, OH, or H_2O). For these reasons, it would be desirable to carry out *in-situ* characterization of Pt electrodes in order to determine the state of oxidation over the range of potentials in which oxygen reduction occurs and to determine the nature of the adsorbed species present during oxygen reduction.

In-situ spectroscopic studies of electrochemical processes are difficult to carry out due to the presence of electrolyte, and as a result, only a limited number of studies investigating oxide formation/reduction over Pt have been reported. Weaver and co-workers have characterized the oxide formed electrochemically on a thin Pt film electrodeposited on a roughed Au electrode in 0.1 M $HClO_4$.[29,30] They found that an amorphous oxide, characterized by a band ca. 570 cm^{-1}, forms under anodic conditions. A redshift in the frequency of this feature occurred upon deuteration of the electrolyte, indicating the presence of Pt-OH species. Raman spectroscopy has been also used to characterize electrochemical processes occurring over a polished Pt electrode in acid. Maeda et al. report the appearance of a weak feature at 500 cm^{-1}, which the authors ascribed to Pt-O based upon the observed frequency and faradic charge measured during potential scanning.[31]

Surface enhanced infrared absorption spectroscopy (SEIRAS) and surface enhanced Raman spectroscopy (SERS) have also been used to characterize the surface species present over Au during the electrochemical reduction of O_2.[32,34] A SERS band at 1150 cm^{-1} was observed over a roughened Au electrode in alkaline electrolyte by Gewirth and coworkers, which the authors assigned to the ν(O-O) mode of superoxide, O_2^-.[34] During the ORR in acid electrolyte, a vibration observed at 1162 cm^{-1} was assigned to HO_2; however, this feature was only detectable in the presence of Bi.[32] Shao and Adzic have detected a SEIRAS vibration at 1268 cm^{-1} over Au in base, which the authors ascribed to the antisymmetric bending mode of adsorbed HO_2^-.[33] By contrast, only two in-situ IR investigations have observed reaction intermediates during oxygen reduction over Pt. Shao et al. have reported a SEIRAS band at 1005-1016 cm^{-1} on a Pt electrode in alkaline electrolyte during oxygen reduction, which they ascribe to a superoxide intermediate.[10] More recently Kunimatsu et al. have observed a band at 1400 cm^{-1}, assigned to an absorbed O_2 intermediate, during oxygen reduction at a Pt-Nafion interface.[35] Unfortunately, due to the strong IR absorption of water, neither study acquired spectra below 800 cm^{-1}, where vibrations of surface oxide and hydroxide species occur.[29,30]

In this work, in-situ SERS was used to elucidate the electrochemical reduction of platinum oxide and the reduction of oxygen over Pt in acid electrolyte. To capture the dynamics of these processes, Raman spectra were acquired during slow cathodic potential scans in N_2 and O_2 saturated 0.5 M $HClO_4$. The results of this study provide insights into the composition of platinum oxide formed, the conditions under which this oxide is reduced, and the nature of surface species formed on surface of a reduced Pt electrode during the electrochemical reduction of O_2.

2.2. Experimental

A schematic of the SERS-electrochemistry setup is shown in Figure 2.1. Experiments were conducted within a Teflon electrochemical cell, containing a Pt wire counter electrode and an Hg/Hg_2SO_4 reference electrode (Hach REF601). Unless indicated, all potentials are referenced to the reversible hydrogen electrode (RHE) (+0.68 V vs Hg/Hg_2SO_4 in 0.5 M $HClO_4$). Supporting electrolyte was comprised of 0.5 M perchloric acid prepared from 70% perchloric acid (ACS reagent, Sigma-Aldrich) and ultrapure water (18.2 MΩ cm, EMD Millipore). Deuterated studies were completed using 68% $DClO_4$ (68 wt. % in D_2O, 99 atom % D, Aldrich) in D_2O (99 atom % D, Aldrich).

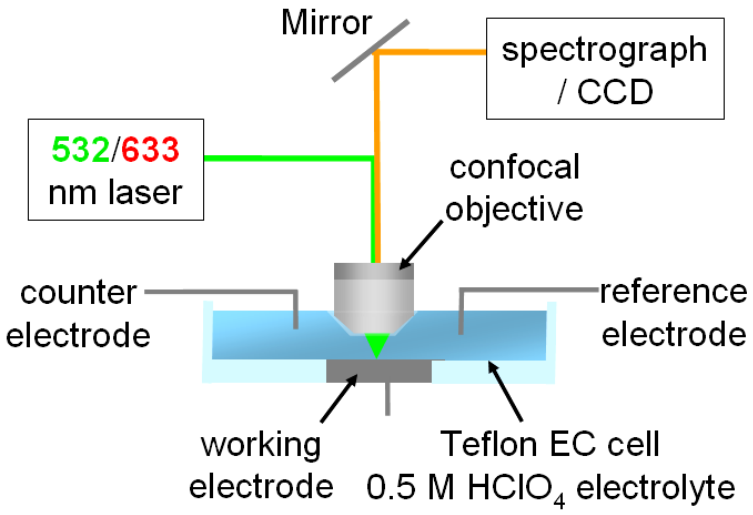

Figure 2.1. Schematic of the electrochemical Raman setup.

A potentiostat/galvanostat (Gamry Reference 600) controlled the potential of the working electrode. A polycrystalline platinum electrode, consisting of a 4 mm-diameter disk encased in Teflon, was polished with successive 1, 0.3 and 0.05 μm alumina slurries to obtain a mirror-like finish, with sonication in high purity for at least ten minutes between each polishing step. Polished electrodes were then electrochemically roughened to create the nm-scale features required for generation of SERS activity. The procedure chosen for this work is similar to that developed by Xu et al.[36] To ensure a stable surface, 500 mV s^{-1} cyclic potential scans between -0.65 and 0.75 V vs Hg/Hg_2SO_4 were applied in 0.5 M $HClO_4$ for 15 min, after which the electrode surface was roughened by employing 500 Hz square-wave oxidation-reduction potential steps of 1.75 and -0.65 V vs Hg/Hg_2SO_4 in 0.5 M $HClO_4$ for 30,000 cycles. Surface roughening was confirmed via an increase in the Pt surface area observable in cyclic voltammograms, as well as through atomic force microscopy.

Raman spectra were obtained using an epi-illumination confocal Raman microscope (LabRam HR, Horiba Jobin Yvon). A Nd:YAG laser supplied the 532 nm Raman excitation line, with approximately 15 mW at the electrode surface. Back-scattered light was filtered by a 532 nm edge filter and then directed into a spectrograph/charge-coupled device detector (Andor). To maintain the laser optical path, a high numerical aperture water-immersible objective (numerical aperture = 1.23, LOMO) was used.[37] The objective was wrapped in 0.001 in thick, transparent perfluoroalkoxy film (McMaster-Carr) to protect from corrosion in strong acid, with 15 μL of water placed between the front lens and film to preserve the refractive index. Spectra were

collected over 15 s intervals, initiated at the indicated potential, during 1 mV s^{-1} potential scans. Baseline subtraction was taken and high frequency noise removed from the Raman spectra via a smoothing filter within the Raman processing software (Labspec v. 5.45.09). Electrolyte solutions were freshly prepared and saturated with high purity nitrogen or oxygen gas prior to each experiment. All measurements were completed at room temperature.

2.3. Results and Discussion

2.3.1 Electrode characterization and electrochemical performance

A characteristic atomic force microscope image of the electrode surface post-roughening is presented in Figure 2.2. Surface features on the nm-scale are observed; these are necessary for generating a SERS-active surface. The total hydrogen desorption charge and an estimated 210μC cm^{-2} monolayer hydrogen charge density[38] were used to determine the roughened Pt surface area of 8.45 cm^2, a value 68 × larger than the geometric surface area of the electrode. Pt electrodes of moderate surface roughness, i.e. surface areas 30-100 × larger than the geometric surface area, have been demonstrated to generate maximum Raman signal intensity yet maintain the cyclic voltammogram features typical of polished Pt electrodes.[39]

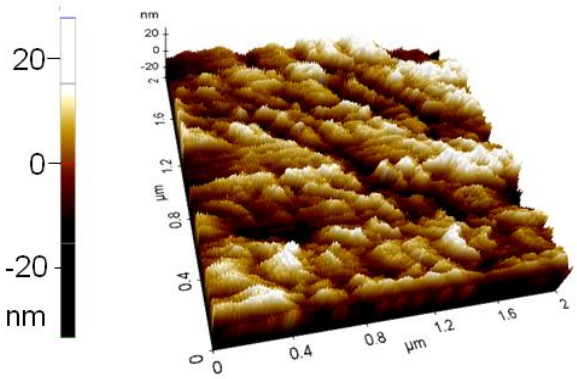

Figure 2.2. AFM image of the Pt electrode surface post-electrochemical roughening.

Characteristic cyclic voltammograms of roughened Pt electrodes in nitrogen saturated 0.5 M $HClO_4$ (black) and $DClO_4$ (gray) at a scan rate of 100 mV s^{-1} are presented in Figure 2.3. Minimal difference exists between the voltammograms in protonated and deuterated electrolyte, consistent with previous findings.[40] Within the voltammogram, reversible underpotential hydrogen adsorption and desorption occurs between 0 and 0.3 V. Platinum oxidation commences ca. 0.75 V, while the cathodic sweep reveals the corresponding oxide reduction peak coupled with oxygen reduction at 1.0-0.6 V. All features are in accordance with those previously reported for polycrystalline Pt electrodes in acid electrolyte.[31,39]

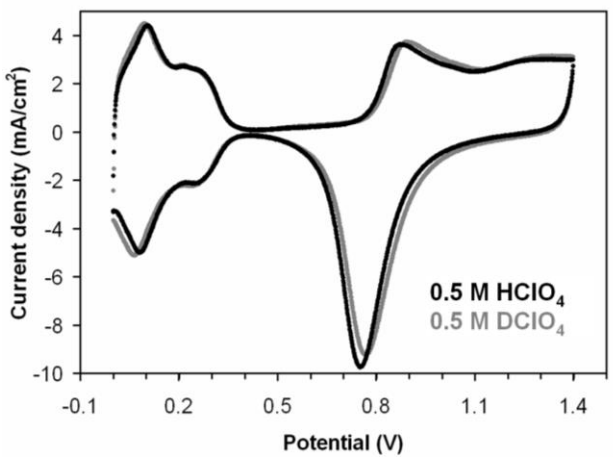

Figure 2.3. Cyclic voltammogram (100 mV s^{-1}) obtained for electrochemically roughened Pt in N_2-saturated 0.5 M $HClO_4$ (black) and 0.5 M $DClO_4$ (gray), reported vs reversible hydrogen electrode (RHE).

3.2. Oxide reduction

Figure 2.44 shows linear sweep voltammograms completed at 1 mV s^{-1} over the electrochemically roughened Pt electrode in nitrogen-saturated 0.5 M $HClO_4$ (black) and $DClO_4$ (gray). Similar reduction currents are observed in both electrolytes, with at least two distinguishable current peaks. The potential of peak current for both electrolytes is greater than that observed in Figure 2.3, as expected for a slower scan rate of this irreversible process. It is noted that variation in the position of the immersible objective relative to the working electrode noticeably affected the resulting current; this effect was minimized by maintaining the same position of the cell and electrodes relative to the objective lens for comparable runs.

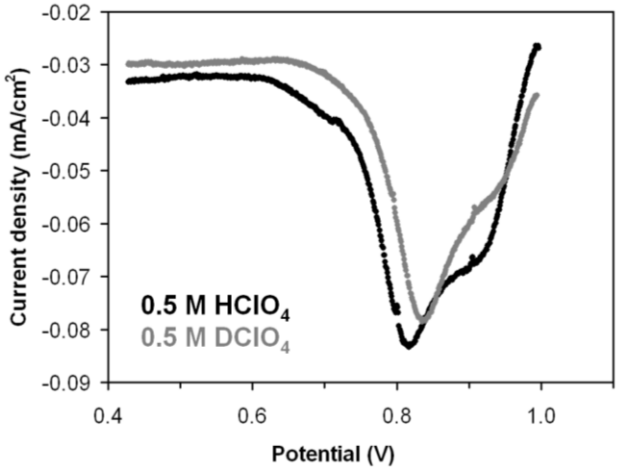

Figure 2.4. Linear sweep voltammograms (1 mV s^{-1}) obtained for electrochemically roughened Pt in N_2-saturated 0.5 M $HClO_4$ (black) and 0.5 M $DClO_4$ (gray).

Raman spectra acquired during the cathodic potential scan in protonated electrolyte are displayed in Figure 2.5a. Each spectrum was initiated at the potential indicated from 1.0 to 0.43 V. Bands at 462 and 628 cm^{-1}, observed independent of potential, are characteristic of the

perchlorate anions.[41] A small feature at ~ 733 cm^{-1}, also present in most spectra, originates from the ν(C-F) vibrations of the PFA film.[42]

In addition to the Raman features of the electrolyte and PFA film, which are observed independent of potential, a broad band located initially at 550 cm^{-1} is seen in the scan commencing at 1.0 V in 0.5 M $HClO_4$. The 550 cm^{-1} feature gradually diminishes in intensity and redshifts with the cathodic scan until it is no longer observed at 0.87 V. Previous observations of a broad Raman feature ca. 570 cm^{-1} for Pt thin films over Au observed at similar potentials in perchloric acid have been ascribed to amorphous platinum oxide containing Pt-OH bonds.[29,30] Ex-situ XPS studies have also reported nearly identical surface coverages by oxide and hydroxide species formed on polycrystalline Pt in acid from 0.8 to 1.1 V.[20] As seen in Fig. 2.5b, the band at 550 cm^{-1}exhibits a ~10 cm^{-1} red-shift in deuterated electrolyte, confirming the presence of hydroxide species. It is also noted that the band is less intense in deuterated electrolyte, consistent with the decreased current density in $DClO_4$.

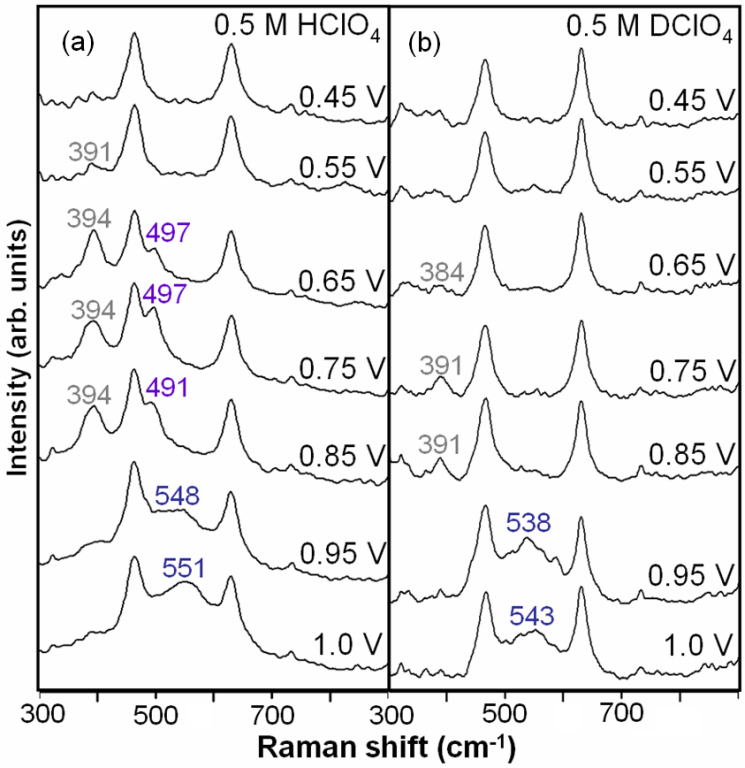

Figure 2.5. Selected sequential Raman spectra recorded over electrochemically roughened Pt in N_2-saturated (a) 0.5 M $HClO_4$ and (b) 0.5 M $DClO_4$ electrolyte concurrent with 1 mV s^{-1} potential scans from 1.0 to 0.43 V (see Fig. 2.4).

With continuation of the cathodic scan, Raman bands appear at 390 and 491-497 cm^{-1} for potentials lower than 0.85 V and remain observable to 0.55 V. In deuterated electrolyte, the 390 cm^{-1} feature exhibits a redshift of 3-5 cm^{-1}, while the 490 cm^{-1} band is no longer observed (see Supporting Information), most likely due to a redshift causing the band to overlap the perchlorate Raman feature at 462 cm^{-1}. The ν(M-O) of water is observed from 310 to 490 cm^{-1} and reported to redshift 6-16 cm^{-1} upon deuteration, while $\rho_w(H_2O)$, observed from 460 to 645 cm^{-1}, redshifts 70

to 150 cm^{-1} for D_2O.[43] Based upon these findings, the 390 cm^{-1} and 490 cm^{-1} bands are ascribed to the ν(Pt-O) and $\rho_w(H_2O)$ of adsorbed water, respectively.

At potentials where the specific adsorption of perchlorate anions occurs, adsorbed water significantly reorients at the electrode-electrolyte interface to an oxygen-down configuration.[44] The potential range for specific adsorption of perchlorate anions has been reported as 0.4-0.8 V,[45] which coincides with the 0.5 to 0.8 V region in the voltammogram where the ν(Pt-O) and $\rho_w(H_2O)$ vibrations are observed. As the applied potential approaches the pzc, reported for platinum stepped surfaces in perchloric acid ca. 0.3 V vs RHE,[46] water reorients to form an ice-like structure on the surface, with increased amounts of hydrogen bonding, coinciding with the disappearance of the 390 cm^{-1} feature.[44] The weaker observance and earlier disappearance of the 390 cm^{-1} vibration in deuterated electrolyte is expected based upon stronger hydrogen bonding in D_2O inducing an earlier transition to the ice-like structure.[47]

Other potential assignments of the 390 and 490 cm^{-1} bands can be eliminated. It is known that trace amounts of chloride anions present in perchloric acid can exhibit strong specific adsorption on Pt.[48,49] The possibility of chloride contamination was investigated. Upon addition of HCl to the electrolyte, a new Raman band was observed ca. 325 cm^{-1}, significantly below the frequency of bands currently in discussion. The position of this band is consistent with that attributed to chloride contamination present in perchloric acid ca. 335 cm^{-1}.[29,30] The assignment of the features at 390 and 490 cm^{-1} to different oxide species formed during the cathodic scan can also be excluded. The redshift of the oxide feature upon deuteration indicates that the species being reduced contains substantial Pt-OH, which would be reduced to form water. Previous studies have also reported that upon reduction, the surface oxide species remains the same, with only the surface coverage of the oxide species changing at various potentials.[50]

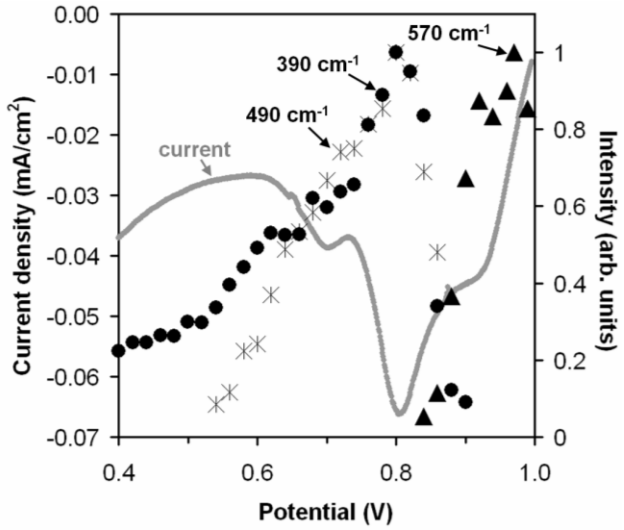

Figure 2.6. Normalized intensity of 550 cm^{-1} (triangles), 490 cm^{-1} (stars) and 390 cm^{-1} (circles) Raman bands vs linear sweep voltammogram (gray) for electrochemically roughened Pt in N_2-saturated 0.5 M $HClO_4$.

The relation between the observed cathodic current and relative Raman peak intensities are better visualized in Figure 2.6, which compares normalized band areas of the 390, 490 and 550 cm^{-1} Raman features with the linear sweep voltammogram. The decrease in the normalized

intensity of the band for amorphous oxide (550 cm^{-1}) corresponds closely with the first current wave of the cathodic potential scan. As the Raman feature attributed to oxide/hydroxide decays, the second current peak and maximum current density is reached. Below 0.81 V, the 390 and 490 cm^{-1} Raman band intensities decay as current contributions due to oxide reduction decrease. We note that the potentials at which surface oxide/hydroxide and adsorbed water species exist qualitatively agrees with the ex-situ x-ray photoelectron spectroscopy studies over a polycrystalline Pt electrode in acid.[20]

To investigate the possibility of bulk oxide formation, expected to occur at potentials exceeding 1.2 V, linear potential scans beginning at 1.25 V were completed in 0.5 M $HClO_4$ and $DClO_4$. As seen for scans commencing at this potential (Fig. 2.7), the resulting current is initially positive as oxide formation occurs on the electrode. The subsequent peak current is larger and exhibits greater irreversibility than that of the potential scan originated at 1.0 V. Again, less current is produced upon deuteration of the electrolyte, and the peak current occurs at higher potentials, indicating the oxide in deuterated electrolyte is less stable than in its protonated form. This trend coincides with previous electrochemical investigations, [40] which found that while heavy water is a stronger oxidant than regular water at increased potentials, oxide layers formed in deuterated acid are less stable than those formed in protonated acid. This difference of oxidation in deuterated and protonated acid electrolyte for Pt can be attributed to the altered steric factor of the water molecule upon deuteration.[40] A small feature at 325 cm^{-1} throughout scans in $DClO_4$ indicates that chloride contamination is present:[29,30] coadsorption of chloride species could inhibit oxide formation in deuterated electrolyte, also contributing to the reduced coverage of oxide within this solution.

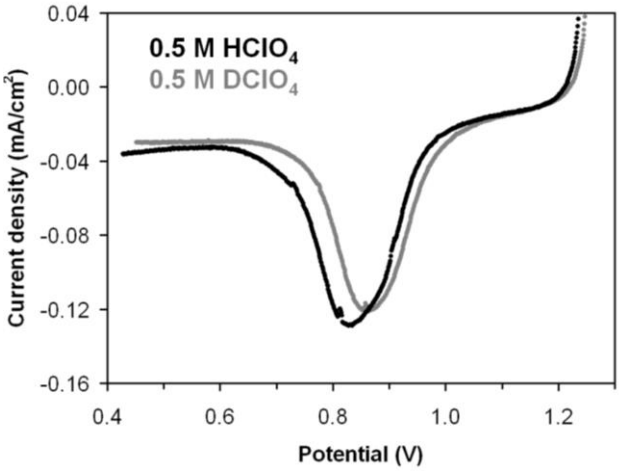

Figure 2.7. Linear sweep voltammogram (1 mV s^{-1}) obtained for electrochemically roughened Pt in N_2-saturated 0.5 M $HClO_4$ (black) and 0.5 M $DClO_4$ (gray).

Selected Raman acquisitions during the 1 mV s^{-1} cathodic scans from 1.25 V in 0.5 M $HClO_4$ and $DClO_4$ are presented in Figs. 2.8a and 2.8b, respectively. With the cathodic scan commencing at potentials where greater oxidation is expected, an increase in the amorphous oxide band intensity and frequency is observed in the Raman spectra. Continuation of the cathodic sweep reveals the emergence of two new peaks at 515 and 555 cm^{-1} ca. 0.85 V. These features rapidly attenuate as the voltage decreases below 0.85 V in $HClO_4$. These peaks have not been reported previously during electrochemical oxidation or reduction of Pt and are ascribed to a bulk platinum

oxide phase, α-PtO_2.[51] Similar bands are not observed in the scan from 1.25 V in deuterated electrolyte, which may result from the inherently decreased oxide formation within $DClO_4$ solution.

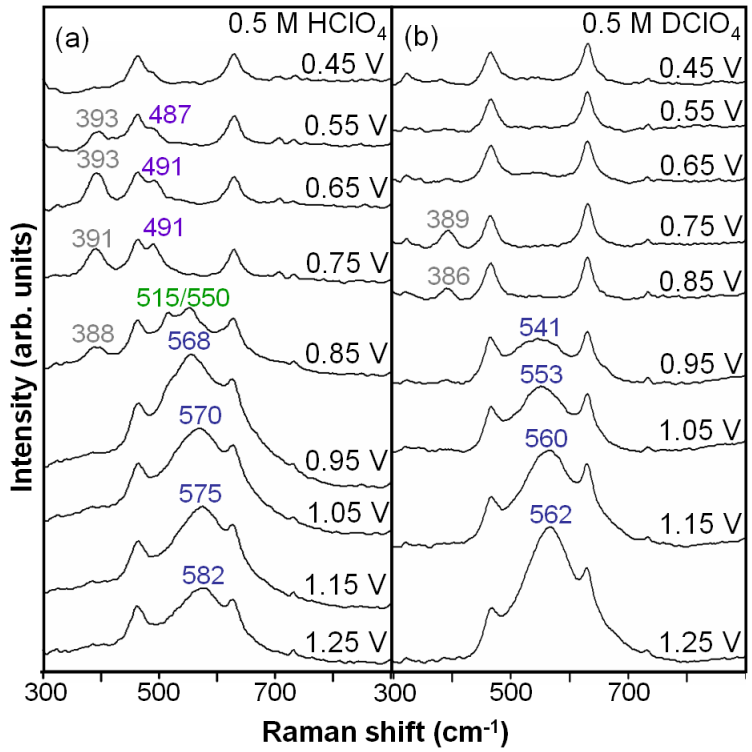

Figure 2.8. Selected sequential Raman spectra recorded for electrochemically roughened Pt in N_2-saturated (a) 0.5 M $HClO_4$ and (b) 0.5 M $DClO_4$ electrolyte concurrent with 1 mV s^{-1} linear potential scan from 1.25 to 0.43 V (shown in Fig. 2.7).

Existence of α-PtO_2 under the conditions used in the present study is supported by prior work. XPS investigations have shown that galvanostatic oxidation of Pt in both perchloric acid and sulfuric acid produced hydrated PtO_2.[52] Furthermore, the bands at 515 and 555 cm^{-1} are only observed after application of an anodic potential greater than 1.25 V vs RHE, coinciding with previous experimental findings of Pt bulk-oxide formation at potentials exceeding 1 to 1.2 V[50] and theoretical calculations of α-PtO_2 evidencing thermodynamic stability at potentials exceeding 1.2 V.[53]

To determine whether α-PtO_2 could be observed in deuterated electrolyte as well, 1 mV s^{-1} cathodic scans were completed from 1.35 V in both 0.5 M $HClO_4$ and $DClO_4$, presented in Figure 2.9. Here again, further decrease in reversibility of oxide reduction and greater peak current density was observed. Figures 2.10a and 2.10b show Raman spectra acquired during the potential sweep in 0.5 M $HClO_4$ and 0.5 M $DClO_4$, respectively. For both protonated and deuterated electrolyte, the Raman features associated with the presence of bulk platinum oxide formation (ca. 515 and 555 cm^{-1}) were observed after potential scans initiated at 1.35 V. The absence of a shift in the position of these bands upon deuteration of the solvent provides further evidence these features derive from bulk α-PtO_2. Weak Raman features due to α-PtO_2 were also detected while holding the potential at 1.35 V. The lower Raman intensities in this case results from overlap of

the 515 and 555 cm^{-1} bands with the broad feature at 590 cm^{-1} for amorphous platinum oxide, as well as a loss in the SERS effect due to the presence of a thicker oxide covering the Pt electrode.

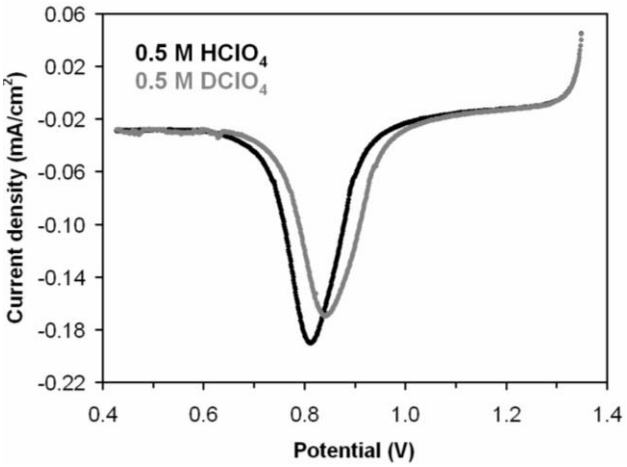

Figure 2.9. Linear sweep voltammogram (1 mV s^{-1}) obtained for electrochemically roughened Pt in N_2-saturated 0.5 M $HClO_4$ (black) and 0.5 M $DClO_4$ (gray).

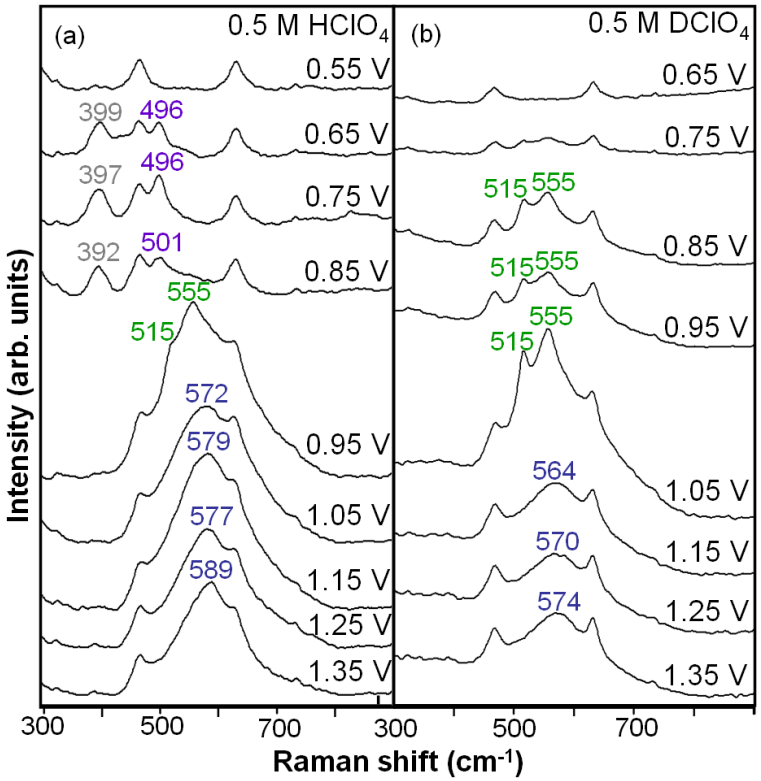

Figure 2.10. Selected sequential Raman spectra recorded over electrochemically roughened Pt in N_2-saturated (a) 0.5 M $HClO_4$ and (b) 0.5 M $DClO_4$ concurrent with 1 mV s^{-1} potential scan from 1.35 to 0.43 V (Fig. 2.9).

The results presented in Figures 2.5, 2.8, and 2.10 demonstrate that at high anodic potentials, the Pt electrode is covered with an oxide layer containing Pt-OH species. As the applied potential is reduced from 0.95 V to 0.85 V, the oxide is rapidly reduced, as evidenced by the rapid increase in the negative current and the loss in intensity for the PtO_x/Pt-OH feature at 550 cm^{-1} (seen in Fig. 2.6). When the reduction of the oxide layer is carried out in deuterated electrolyte, the disappearance of the PtO_x/Pt-OD feature at 540 cm^{-1} occurs at a higher voltage, 0.89 V, suggesting that reduction of the oxide layer by D^+ is somewhat faster than by H^+. This pattern is clearly seen in both the voltammogram and the Raman spectra shown in Figs. 2.7 and 2.8, respectively.

2.3.3. Oxygen reduction

Experiments were conducted using 0.5 M $HClO_4$ pre-saturated with oxygen in order to identify surface species formed during the ORR. Figure 2.11 shows 1 mV s^{-1} cathodic potential sweeps within the oxygen reduction potential range carried out in oxygen saturated and nitrogen saturated 0.5 M $HClO_4$. Current generated during the potential scan from 1.0 to 0.05 V in N_2 saturated electrolyte is attributed to oxide reduction coupled with double-layer charging. The significantly larger current produced in the same potential range using oxygen-saturated electrolyte is attributed to the ORR coupled with greater oxide reduction,[54] as discussed below.

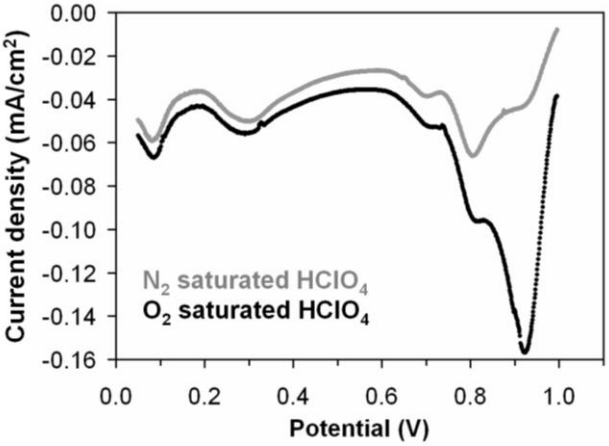

Figure 2.11. LSV (1 mV s^{-1}) obtained for electrochemically roughened Pt in N_2- (gray) and O_2-saturated (black) 0.5 M $HClO_4$.

Raman spectra recorded during the cathodic sweeps are presented in Figure 2.12. In addition to the aforementioned bands at 462 and 628 cm^{-1}, the bands at 936 and 1128 cm^{-1} are also attributed to perchlorate anions.[41] The amorphous oxide band appears more intense upon oxygen saturation of the electrolyte and exhibits a higher initial frequency (570 cm^{-1}) than that observed in N_2 saturated electrolyte (550 cm^{-1}). Although the relative intensity of the oxide band is stronger, the band attenuates more rapidly in O_2 saturated electrolyte and is no longer observable by 0.91 V, whereas in N_2 saturated 0.5 M $HClO_4$ this band disappears at 0.87 V.

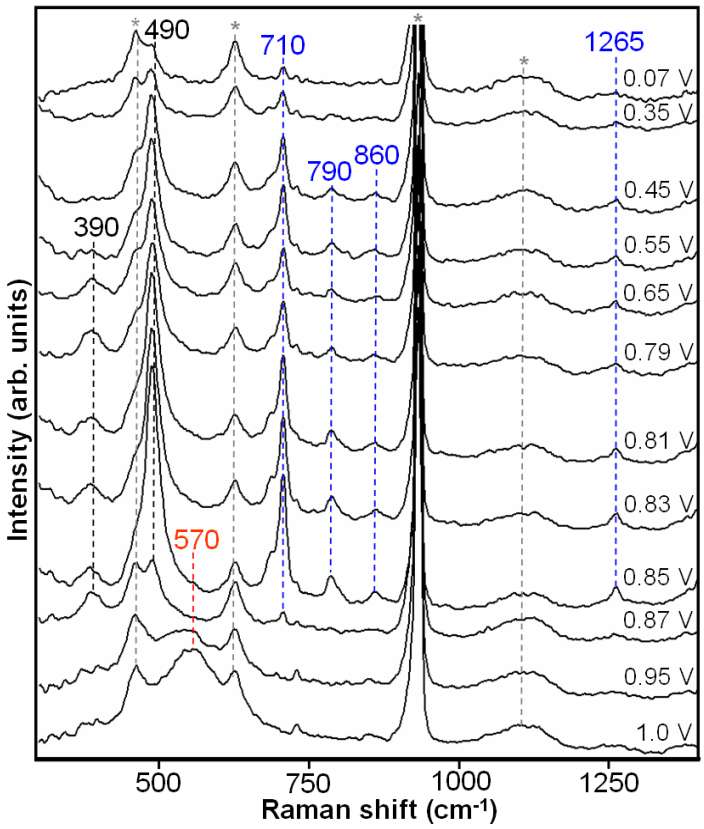

Figure 2.12. Selected sequential Raman spectra over electrochemically roughened Pt concurrent with 1 mV s^{-1} potential scan from 1.0 to 0.05 V in O_2-saturated 0.5 M $HClO_4$ (Fig. 2.11).

After decay of the feature at 570 cm^{-1}, bands again appear at 390 and 490 cm^{-1} in oxygen saturated electrolyte. The intensity of the band at 390 cm^{-1} is comparable to that observed in the N_2 saturated electrolyte (see Figure 2.5), but this feature attenuates more rapidly in the oxygen-saturated electrolyte and is no longer detected by 0.55 V. The band at 490 cm^{-1} is much more intense in the presence of oxygen and remains observable down to 0.02 V.

In addition to the features at 390 and 490 cm^{-1}, present after reduction of the amorphous Pt oxide, new Raman features appear at 710, 790, 860, and 1265 cm^{-1} when the voltage is reduced to 0.87 V in O_2 saturated $HClO_4$. These features increase in intensity at 0.85 V and then gradually attenuate as the potential is decreased to 0 V, coinciding with the potential window for the ORR. Potential scans within the ORR potential window were also completed in oxygen saturated 0.5 M $DClO_4$; the signals from oxygen-related Raman features were significantly less intense in this electrolyte. Figure 2.13 compares spectra recorded for protonated and deuterated O_2 saturated electrolyte beginning at 0.37 V, the potential at which Raman features derived from oxygen-containing species are strongest in deuterated electrolyte. A band at 325 cm^{-1} is observed below 0.95 V throughout scans acquired in $DClO_4$ and is attributed to chloride contamination. Adsorption of chloride anions has been shown to significantly decrease the current associated with oxygen reduction,[55] providing a possible explanation for the decreased intensity and the observance of Raman features at lower potentials for O_2-saturated $DClO_4$. The peaks at 490 and 710 cm^{-1} exhibit less intensity but no shift in frequency in $DClO_4$, while bands at 790, 860, and 1265 cm^{-1} are not observed upon deuteration of the electrolyte. Additional peaks present in the

deuterated electrolyte originate from the D_2O solvent: ν(Pt-O) of D_2O at 378 cm^{-1} and $\delta(D_2O)$ at 1205 cm^{-1}.

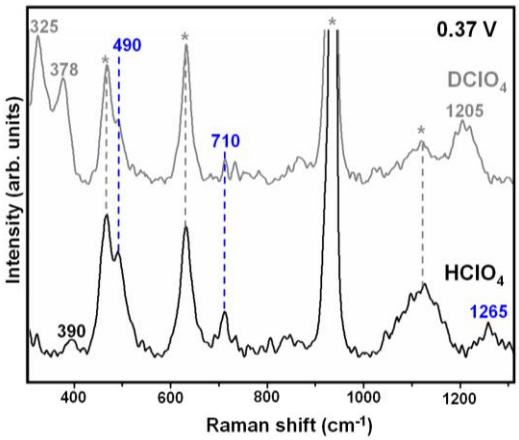

Figure 2.13. Raman spectra recorded over electrochemically roughened Pt in O_2 saturated 0.5 M $HClO_4$ (black) and 0.5 M $DClO_4$ (gray) during cathodic potential scanning (1 mV s^{-1}) from 1.0 to 0.05 V.

Assignments of the bands observed in oxygen-saturated electrolyte are reported in Table 2.1. The minimal change in the intensity of the 390 cm^{-1} feature after oxygen saturation of the electrolyte supports the assignment of this vibration to the Pt-O stretch of adsorbed water.[43] Disappearance of this feature at higher potentials during the cathodic sweep carried out in O_2-saturated than in N_2-saturated electrolyte is likely due to the occupation of Pt surface sites by adsorbed oxygen species, which may inhibit the adsorption of water. The band at 490 cm^{-1} is much stronger in O_2-staturated electrolyte, suggesting that this peak is likely due to a separate, oxygen-containing species. We assign this feature to a Pt-O stretch on the basis of the report of Pt-O observed in the EELS spectrum of O_2 adsorbed on Pt(111), as well as our own density functional theory calculations, which predict the ν(Pt-O) of Pt-O or Pt-OOH at similar frequencies (see Table 2.2 and Supporting Information).[56]

The Raman features at 690 and 710 cm^{-1} are in the frequency range reported for peroxo species present on the surface of Pt. EELS spectra of a Pt(111) surface containing O_2 adsorbed at 90 K exhibit a band at 700 cm^{-1} that is attributed to the ν(O-O) stretching vibration of a two-fold coordinated peroxo-type (O_2^{2-}) adspecies[57] or to a peroxo-type species adsorbed at Pt defect sites.[58] Infrared investigations have also observed a peroxo-type adspecies on Pt(111) at 680 cm^{-1},[59] while a band at 690 cm^{-1} has been attributed to peroxo-like molecular oxygen species in an EELS study of oxygen adsorbed on a Pt(111) surface. [60] This assignment is consistent with theoretical calculations, which predict peroxo vibrations at 690 or 710 cm^{-1}, depending upon the adsorption site.[61] The possibility that the band at 710 cm^{-1} is assignable to Pt_3O_4, which exhibits a band at 709 cm^{-1},[51] can be ruled out, since this feature appears after the reduction of surface oxide and maintains a strong intensity through the entire ORR potential regime. Our own calculations show that the ν(O-O) of a Pt-OOH species is also expected ~700 cm^{-1}, and minimal shift of this frequency should occur upon deuteration of the electrolyte (Table 2.2).

Vibrations at 790 cm^{-1} have also been reported for various oxygen-containing Pt species. A band at 789 cm^{-1} has been observed in the Raman spectrum of a Pt(II) μ-hydroxo-μ-peroxo-

complex and ascribed to ν(O-O),[62] while a band at the same frequency was also assigned to ν(O-O) in the resonance Raman spectrum of a Fe(III)-OOH complex.[63]

Table 2.1: Vibrational frequencies reported for metal-bonded oxygen and water species

Observed frequency in protonated and (deuterated) electrolyte (cm^{-1})	Reported frequency (cm^{-1})	Reported band assignment	Reported species	Ref.
393 (388)	395	ν(M-O)	$[Mn(H_2O)_6]SiF_6$	43
490 (490)	490	ν(Pt-O)	O_{ads}	56,58
490 (N/A)	460	$\rho_w(H_2O)$	$[Mg(H_2O)_6]SO_4 \cdot H_2O$	43
550-590 (540-570)	500-600	ν(Pt-O)	$O_{x\ ads} + OH_{\ ads}$	29
690 (N/A)	690	ν(O-O)	$O_2^{2-}{}_{\ ads,\ bridging}$	57
710 (710)	703	ν(O-O)	$O_2^{2-}{}_{\ ads}$	59,60
	700	ν(O-O)	$O_2^{2-}{}_{\ ads,\ defect}$	58
	711	ν(Pt-O)	Pt_3O_4	51
790 (N/A)	789	ν(O-O)	Pt-OO-Pt complex	62
	790	ν(O-O)	$[Fe(N4Py)(OOH)]^{2+}$	63
860 (N/A)	840-860	ν_3(O-O)	$H_2O_{2\ ads}$	6
	875	ν(O-O)	$O_2^{2-}{}_{ads}$	57,58
	850	ν(O-O)	$O_2^{-}{}_{ads}$	59,60
1265 (N/A)	1268	$\nu_6(HO_2)$	$HO_2^{-}{}_{ads}$	33

Table 2.2: Comparison of experimental and calculated Raman frequencies

	ν_{symm}(Pt-O) (cm^{-1})	ν(O-O) (cm^{-1})	$\nu_6(HO_2)$ (cm^{-1})
Experiment	490	700	1265
Calculated Pt_4-OOH	489	694	1228
Calculated Pt_4-OOD	475	693	916

Several studies of O_2 adsorbed on a Pt(111) surface have found a vibrational mode near 860 cm^{-1}, which have been assigned to a peroxo or superoxo species. EELS studies of O_2 over Pt(111) report a feature near 870 cm^{-1} that is ascribed to a peroxo species adsorbed to a single Pt site, [57,58] while a more recent EELS investigation assigns this band to a superoxo species.[60] Infrared spectra of O_2 adsorbed on a Pt(111) surface also exhibit a peak at 850 cm^{-1}, ascribed to a bridge-bonded superoxo species based upon agreement with calculated frequencies for this adspecies.[60,61] The ν(O-O) vibration of adsorbed H_2O_2 has been observed at 840-860 cm^{-1} in SERS spectra of a Pt/Au electrode exposed to H_2O_2 in 0.1 M H_2SO_4.[64] Based on this evidence, we assign the weak band at 860 cm^{-1} to the ν(O-O) of a peroxo or superoxo adspecies.

The position of the feature at 1265 cm^{-1} is very similar to that observed at 1268 cm^{-1} during the electrochemical reduction of oxygen over a thin Au film. This feature has been assigned to the

antisymmetric (ν_6) bending vibration of adsorbed HO_2^-.[33] While the vibrational spectrum for Pt-OOH has not been reported, x-ray photoelectron spectroscopy has detected an adsorbed OOH species after oxygen dosing a hydrogenated Pt(111) surface. Additionally, the experimentally observed 1265 cm^{-1} frequency aligns closely with the calculated frequency of the antisymmetric bending mode of Pt-OOH (Table 2.2).[65] The bending vibration for HO_2 is expected to redshift approximately 300 cm^{-1} upon deuteration (also observed in the calculated frequency, shown in Table 2.2);[66,67] however, no distinguishable band was observed near 965 cm^{-1} for Raman spectra acquired in deuterated electrolyte. We believe this could be due to overlap of the weak Pt-OOD feature with the large perchlorate vibration at 930 cm^{-1}.

Figure 2.14 presents the difference in the voltammograms measured in O_2- and N_2-saturated $HClO_4$ (see Figure 2.11). Subtraction of the N_2 saturated electrolyte current from the current observed in O_2 saturated electrolyte is taken in order to emphasize the portion of the current density that is associated with the ORR. It should be noted, though, that the difference in current densities occurring between 1.0 V and 0.87 V contains a contribution from the reduction of the Pt oxide film present on the electrode immersed on O_2-saturated $HClO_4$. The reason that this contribution is not removed from the difference in current densities is that the amount of Pt oxide formed at 1.0 V on the electrode immersed O_2-saturated electrolyte is larger than that formed on the electrode immersed in N_2-saturated electrolyte (see Figure 2.11). The current difference between the two electrolytes reaches its lowest value at a voltage of ~ 0.92 V, slightly above the potential at which oxide is completely removed from the Pt surface.

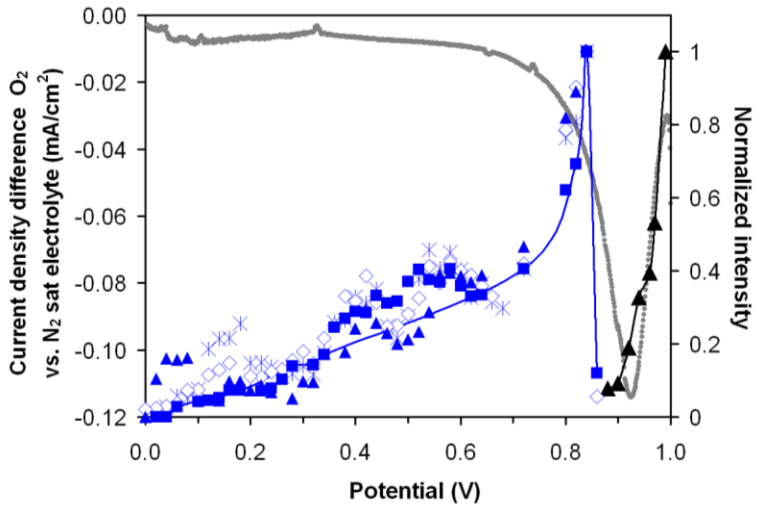

Figure 2.14. Normalized intensity of 570 cm^{-1} (black triangles), 490 cm^{-1} (blue stars), 690/710 cm^{-1} (white diamonds), 790 cm^{-1} (blue squares), and 1264 cm^{-1} (blue triangles) Raman bands vs current density difference between O_2 and N_2 saturated 0.5 M $HClO_4$ (gray) during a 1 mV s^{-1} linear sweep voltammogram for electrochemically roughened Pt in O_2-saturated 0.5 M $HClO_4$. Black and blue curves are included to guide the eye.

The variation in the intensities of the normalized Raman band with applied potential acquired for the O_2-satruated electrolyte are also shown in Figure 2.14. Between 1.0 V to 0.9 V, the only observable feature is that for PtO_x/Pt-OH characterized by the band at 570 cm^{-1}. Once this band disappears, features characteristic of OOH and/or O_2 (710 cm^{-1} and 790 cm^{-1}), OOH (1265 cm^{-1}), di-σ O_2 or O_2^{2-} (860 cm^{-1}), and O or OOH (490 cm^{-1}) are observed for voltages below 0.87

V. All of these features are observed only in the spectra taken using O_2-saturated electrolyte. The intensities of these bands reach a maximum at 0.85 V and then decay as a consequence of the increasingly diffusion-limited transport of O_2 from the bulk electrolyte. It is also noted that the relative intensities of all intermediates change to the same extent with decreasing voltage. Significant deviations from the curve drawn through the data occur, however, due to the need to occasionally refocus on the electrode during the course of the experiment.

Although the ORR occurs through the entire potential window where oxygen-related vibrations are observed, the Raman features remain significantly more intense through the diffusion-limited potential regime than would be expected. This surprising observation can be rationalized, though, in several ways. Wu et al. have reported that the application of a negative potential can increase and blueshift the SERS plasmon resonance band and facilitate polarization of the conduction band electrons, both effects which can increase electromagnetic SERS enhancement.[68] Additionally, chemical enhancement of Raman spectra is known to vary significantly with applied potential.[69,70] Chemical enhancement can occur either through new electronic states created when a metal-adsorbate surface complex is formed or via photon-driven charge transfer, in which the energy of the Raman laser coincides with the energy difference between the Fermi energy of the metal and the HOMO or LUMO of the surface molecule.[71,72] Furthermore, transition metal surfaces exhibit much stronger adsorption than do coinage metals, and the high bond strength can also shift the frequency of the surface plasmon resonance and alter the local electric field of the transition metal surface.[73]

The data presented in Figure 2.4 suggests that for voltages greater than 0.87 V, O_2 reduction is limited by a thin layer of Pt oxide and hydroxide covering the Pt electrode, in agreement with previous observations.[13,14] At lower potentials, O_2 reduction occurs under progressively diffusion-limited conditions on a reduced, oxide-free surface. The Raman spectra now show clear evidence for several intermediates hypothesized to be present during the ORR on an oxide-Pt electrode (we note, however, that we cannot definitively assign these surface species as ORR intermediates). Of particular note is the presence of bands for O_2 and/or O_2^{2-} and for OOH. The presence of a feature for OOH could provide support for the occurrence of O_2 reduction via the associative mechanism. The concurrent appearance of a strong peak which could be due to atomically adsorbed O suggests that this species is produced by the dissociation of OOH, but its formation via direct dissociation of adsorbed O_2 cannot be ruled out. Therefore, in situ Raman spectroscopy does not allow one to draw a definitive conclusion as to whether the associative or the dissociative pathway is dominant. Nevertheless, it is useful to consider the results of the present study in the context of the mechanism for the ORR proposed on the basis of theoretical analyses.[22-25] Since such analyses pertain solely to metallic Pt, we restrict our comparisons to voltages below 0.87 V.

The sequence of elementary steps proposed in theoretical studies of oxygen reduction on a Pt(111) surface is as follows:

$$O_2 \rightarrow O_{2\,ads} \quad (2.5)$$

$$O_{2\,ads} + H^+ + e^- \rightarrow OOH_{ads} \quad (2.6)$$

$$OOH_{ads} + H^+ + e^- \rightarrow O_{ads} + H_2O_{ads} \quad (2.7)$$

$$O_{ads} + H^+ + e^- \rightarrow OH_{ads} \quad (2.8)$$

$$OH_{ads} + H^+ + e^- \rightarrow H_2O_{ads} \quad (2.9)$$

$$H_2O_{ads} \rightarrow H_2O \quad (2.10)$$

If O_2 dissociation occurs, then one must include Reaction 2.11 in addition to Reactions 2.7 and 2.8:

$$O_{2\,ads} \rightarrow 2O_{ads} \quad (2.11)$$

While several theoretical studies conclude that that the barrier for Reaction 2.11 is higher than that for Reaction 2.6 at voltages below 0.9 V,[22,24,25,74] work by Goddard and coworkers[75] suggests that Reaction 2.11 occurs without activation on Pt(111) once the effects of the solvent (i.e., the electrolyte) are included. This work also suggests that Reaction 2.12 should be considered as an alternative to Reactions 2.7 or 2.8:

$$O_{2\,ads} + H_2O_{ads} \rightarrow 2OH_{ads} \qquad (2.12)$$

As noted in the introduction, the observation of a change in the Tafel slope near a potential of 0.8 V vs RHE suggests that the nature of the rate-limiting step in the pathway for the reduction of oxygen is different above and below this potential. A theoretical analysis of this issue has been carried out by Janik et al.,[76] with particular attention given to the first step in the reduction sequence, Reaction 2.6, and the dependence of the activation energy for OOH_{ads} formation as a function of the applied potential. Their work shows that as the proton diffuses through the electrode double layer, the adsorbed O_2 "instigates" the transfer of an electron to produce an H atom near the oxygen. The reaction of this H atom with adsorbed O_2 results in the formation of OOH_{ads}. The apparent activation barrier for the overall process is 0.81 eV at the equilibrium potential of 1.23 V but decreases nearly linearly with decreasing potential, reaching a value of 0.31 eV at 0.8 V. Subsequent work by Neurock et al[25] and by Yeh and Janik[77] have shown that at 0.8 V, the activation barriers for Reactions 2.7-2.9 are lower than that for Reaction 2.6, suggesting that below 0.8 V, Reaction 2.6 is the rate-limiting step for the ORR. At significantly higher potentials, OH adsorption is predicted to limit the rate of oxygen reduction. Therefore, these studies suggest that at potentials below 0.8 V, the dominant surface species should be $O_{2\,ads}$, and that at potentials above 0.8 V, the dominant species should be O_{ads} and OH_{ads}. The results of the present study are qualitatively consistent with these projections.

Previous studies have shown that the rate of the ORR is first order in the concentrations of dissolved O_2 and H^+ in acid electrolyte.[78] These kinetics can be rationalized by assuming that Reaction 2.5 is quasi-equilibrated and Reaction 2.6 is rate-limiting. Since the concentration of protons in the electrolyte occupying the volume between the objective and the Pt electrode is minimally depleted of H^+ cation during the course of an experiment (see Supporting Information), the effective rate coefficient, k_{eff}, is given by $K_5k_6\,exp\left(\frac{-\beta F}{RT}\eta\right)$ exp(-βFη/RT), where K_5 is the equilibrium constant for O_2 adsorption from the electrolyte, k_6 is the rate coefficient for Reaction 2.6, $[H^+]$ is the concentration of protons, β is the cathodic transfer coefficient, F is Faraday's constant, R is the universal gas constant, and η is the applied overpotential (see Supporting Information). In the presence of diffusional mass transfer, the apparent rate coefficient, k_{app}, will become smaller than k_{eff}, as shown by Eq. 2.13:

$$k_{app} = \frac{k_{eff}k_{MT}}{(k_{eff} + k_{MT})}, \qquad (2.13)$$

where k_{MT} is the mass transfer coefficient. As k_{eff} increases with a reduction in the applied potential, the value of k_{app} decreases from a maximum of k_{eff} to a minimum of k_{MT}. Since the rate of the ORR is given by $k_{eff}[O_{2\,ads}]$, where $[O_{2\,ads}]$ is the concentration of adsorbed O_2, it can be shown (see Supporting Information) that $[O_{2\,ads}]$ is related to the concentration of O_2 in the bulk of the electrolyte, $[O_{2\,b}]$ by

$$[O_{2\,ads}] = \frac{k_{MT}K_5}{(k_{eff} + k_{MT})[O_{2\,b}]} \qquad (2.14)$$

It is evident from Eq. 2.14 that as the value of k_{eff} increases with increasing overpotential, the concentration of adsorbed O_2 will decrease, due to the increasing effects of diffusional mass

transfer. The decrease in the surface concentration of adsorbed O_2 (evidenced possibly by the Raman features at 690 and/or 710 cm^{-1}) with decreasing applied potential seen in Figure 2.14 can, therefore, be ascribed to the increasingly higher value of k_6 and hence k_{eff}.

Finally, as noted earlier, Figure 2.14 shows that the concentrations of all adsorbed oxygen-containing species (which may or may not be oxygen reduction intermediates) decrease by the same degree as that of adsorbed O_2. This is exactly what would be expected if Reaction 2.6 were the rate-limiting step, since the surface concentrations of all other adsorbed species will be linearly related to $[O_{2\ ads}]$. Thus, for example, the surface concentration of hydroperoxo species, $[OOH_{ads}]$, will be given by $[OOH_{ads}] = (k_6/k_7)[O_{2\ ads}]$, and the surface concentration of adsorbed atomic oxygen, $[O_{ads}]$, will be given by $[O_{ads}] = (k_6/k_8)[O_{2\ ads}]$.

2.4. Conclusions

Surface-enhanced, confocal Raman spectroscopy was used to characterize the species present on an electrochemically roughened Pt electrode during the reduction of platinum oxide and the oxygen reduction reaction carried out in 0.1 M $HClO_4$. High surface sensitivity was achieved using an objective protected by a thin Teflon film immersed in the acid electrolyte, with SERS acquisitions completed concurrent to slow cathodic potential scans. The platinum oxide composition is found to depend upon the initial scan potential: an amorphous oxide containing Pt-OH species is observed for LSVs commenced at 1V and above, with α-PtO_2 additionally observed for scans initiated above 1.2 V. In N_2-saturated electrolyte, both platinum oxide forms are fully reduced as the applied potential is cathodically swept to 0.85 V. For cathodic scans initiated at all potentials, specifically adsorbed water is observed subsequent to oxide removal. Raman features possibly associated with oxygen reduction were observed below 0.85 V in O_2-saturated electrolyte. Specifically, vibrational modes consistent with superoxo, hydroperoxo, and atomic oxygen were observed. With decreasing applied potential, the intensities of these bands decreased due to the increasing effects of mass transfer of O_2 dissolved in the electrolyte to the Pt electrode surface. The presence of these surface species could indicate that the ORR proceeds (at least in part) via an associative pathway through an OOH surface intermediate.

ACKNOWLEDGEMENTS

We thank Joseph S. Gomes for his DFT calculation contributions.

References

1. Markovic, N. M.; Ross, P. N. *CATTECH* **2000**, *4*, 110.
2. Gewirth, A. A.; Thorum, M. S., *Inorganic Chemistry* **2010,** *49* (8), 3557-3566.
3. Vielstich, W.; Lamm, A.; Gasteiger, H. *Handbook of Fuel Cells: Fundamentals, Technology, Applications*; John Wiley and Sons: Chichester,U.K., 2003.
4. Lutz, A. E.; Larson, R. S.; Keller, J. O. *International Journal of Hydrogen Energy* **2002**,27, 1103–1111.
5. Gasteiger, H. A.; Panels, J. E.; Yan, S. G. *Journal of Power Sources* **2004**, 127, 162–171.
6. Chatenet, M.; Genies-Bultel, L.; Aurousseau, M.; Durand, R.; Andolfatto, F., *Journal of Applied Electrochemistry* **2002,** *32* (10), 1131-1140.
7. Markovic, N. M.; Adzic, R.R.; Cahan, B.D.; Yeager, E.B. *Journal of Electroanalytical Chemistry* **1994**, *377*, 249.
8. Markovic, N. M.; Ross, P. N., *Surface Science Reports* **2002,** *45* (4-6), 121-229.
9. Adzic, R. R.; Wang, J. X., *Solid State Ionics* **2002,** *150* (1-2), 105-114.
10. Shao, M. H.; Liu, P.; Adzic, R. R., *Journal of the American Chemical Society* **2006,** *128* (23), 7408-7409.
11. R. Adzic, Electrocatalysis, ed. J. Lipkowski and P. N. Ross, Wiley-VCH, New York, 1998, ch. 5, p. 197.
12. Bonakdarpour, A.; Dahn, T. R.; Atanasoski, R. T.; Debe, M. K.; Dahn, J. R. *Electrochemical and. Solid- State Letters.* **2008**, 11, B208–B211.
13. Damjanovic, A., *Journal of The Electrochemical Society* **1991,** *138* (8), 2315-2320.
14. Damjanovic, A.; Brusic, V., *Electrochimica Acta* **1967,** *12* (6), 615-628.
15. Tarasevich, M. R. *Elektrokhimjya* **1973** *9*, 59.
16. Uribe, F. A.; Springer, T. E.; Gottesfeld, S., *Journal of the Electrochemical Society* **1992,** *139* (3), 765-773.
17. Vukmirovic, M. B.; Zhang, J.; Sasaki, K.; Nilekar, A. U.; Uribe, F.; Mavrikakis, M.; Adzic, R. R., *Electrochimica Acta* **2007,** *52* (6), 2257-2263.
18. Wang, J. X.; Zhang, J.; Adzic, R. R., *The Journal of Physical Chemistry A* **2007,** *111* (49), 12702-12710.
19. Holewinski, A.; Linic, S. *Journal of the Electrochemical Society* **2012**, 159 (11), H864-H870.
20. Wakisaka, M.; Suzuki, H.; Mitsui, S.; Uchida, H.; Watanabe, M., *Langmuir* **2009,** *25* (4), 1897-1900.
21. Bondarenko, A. S.; Stephens, I. E. L.; Hansen, H. A.; Pérez-Alonso, F. J.; Tripkovic, V.; Johansson, T. P.; Rossmeisl, J.; Nørskov, J. K.; Chorkendorff, I., *Langmuir* **2011,** *27* (5), 2058-2066.
22. Tripkovic, V.; Skúlason, E.; Siahrostami, S.; Nørskov, J. K.; Rossmeisl, J., *Electrochimica Acta* **2010,** *55* (27), 7975-7981.
23. Nørskov, J. K.; Rossmeisl, J.; Logadottir, A.; Lindqvist, L.; Kitchin, J. R.; Bligaard, T.; Jonsson, H., *Journal of Physical Chemistry B* **2004,** *108* (46), 17886-17892.
24. Rossmeisl, J.; Karlberg, G. S.; Jaramillo, T.; Norskov, J. K., *Faraday Discussions* 2008, *140*, 337-346.
25. Neurock, M; Mei, D; Prascher, B. Theoretical Insights into the Mechanisms and Kinetics in the Electrocatalytic Reduction of Oxygen. Presented at the 22nd North American Meeting of the North American Catalysis Society, Detroit, MI, June 6, 2011.

26. Hansen, H. A.; Rossmeisl, J.; Norskov, J. K., *Physical Chemistry Chemical Physics* **2008,** *10* (25), 3722-3730.
27. Damjanovic, A.; Dey, A.; Bockris, J. O. M., *Electrochimica Acta* **1966,** *11* (7), 791-814.
28. Burke, L.D.; Buckley, D.T., *Journal of Electroanalytical Chemistry* **1996** 405, 101-109.
29. Zou, S. Z.; Chan, H. Y. H.; Williams, C. T.; Weaver, M. J., *Langmuir* **2000,** *16* (2), 754-763.
30. Zhang, Y.; Gao, X. P.; Weaver, M. J., *Journal of Physical Chemistry* **1993,** *97* (33), 8656-8663.
31. Maeda, T.; Sasaki, C.; Horie, C.; Osawa, M. *Journal of Electron Spectroscopy* **1993**, *64/65*, 381-389.
32. Li, X.; Gewirth, A. A., *Journal of the American Chemical Society* **2005,** *127* (14), 5252-5260.
33. Shao, M. H.; Adzic, R. R., *The Journal of Physical Chemistry B* **2005,** *109* (35), 16563-16566.
34. Kim, J.; Gewirth, A. A., *The Journal of Physical Chemistry B* **2006,** *110* (6), 2565-2571.
35. Kunimatsu, K.; Yoda, T.; Tryk, D. A.; Uchida, H.; Wantabe, M., *Physical Chemistry Chemical Physics* **2010,** *12*, 621-629.
36. Xu, X.; Wu, D. Y.; Ren, B.; Xian, H.; Tian, Z. Q., *Chemical Physics Letters* **1999,** *311* (3-4), 193-201.
37. Tian, Z. Q.; Ren, B., *Annual Review of Physical Chemistry* **2004,** *55*, 197-229.
38. Ren, B.; Xu, X.; Li, X. Q.; Cai, W. B.; Tian, Z. Q., *Surface Science* **1999,** *428*, 157-161.
39. Cai, W. B.; Ren, B.; Li, X. Q.; She, C. X.; Liu, F. M.; Cai, X. W.; Tian, Z. Q., *Surface Science* **1998,** *406* (1-3), 9-22.
40. Jaksic, M. M.; Johansen, B.; Tunold, R., *International Journal of Hydrogen Energy* **1993,** *18* (10), 817-837.
41. Ratcliffe, C. I.; Irish, D. E., *Canadian Journal of Chemistry-Revue Canadienne De Chimie* **1984,** *62* (6), 1134-1144.
42. Legeay, G.; Coudreuse, A.; Legeais, J.-M.; Werner, L.; Bulou, A.; Buzar, J.-Y.; Emery, J.; Silly, G., *European Polymer Journal* **1998,** *34* (10), 1457-1465.
43. Nakagawa, I.; Shimanouchi, T., *Spectrochimica Acta* **1964,** *20* (3), 429-439.
44. Ataka, K.; Yotsuyanagi, T.; Osawa, M., *Journal of Physical Chemistry* **1996,** *100* (25), 10664-10672.
45. Santos, M. C.; Miwa, D. W.; Machado, S. A. S., *Electrochemistry Communications* **2000,** *2* (10), 692-696.
46. Gómez, R.; Climent, V.; Feliu, J.M.; Weaver, M. J. *Journal of Physical Chemistry B* **2000,** *104*, 597-605.
47. Soper, A. K.; Benmore, C. J., *Physical Review Letters* **2008**, *101* (6), 065502.
48. Tripkovic, D. V.; Strmcnik, D.; van der Vliet, D.; Stamenkovic, V.; Markovic, N. M., *Faraday Discussions* **2008,** *140*, 25-40.
49. Conway, B. E., *Progress in Surface Science* **1984,** *16* (1), 1-137.
50. Conway, B. E., *Progress in Surface Science* **1995,** *49* (4), 331-452.
51. Graham, G. W.; Weber, W. H.; McBride, J. R.; Peters, C. R., *Journal of Raman Spectroscopy* **1991,** *22* (1), 1-9.
52. Hammond, J. S.; Winograd, N., *Journal of Electroanalytical Chemistry* **1977,** *78* (1), 55-69.
53. Jacob, T., *Journal of Electroanalytical Chemistry* **2007,** 607 (1-2), 158-166.

54. Jin, W.; Du, H.; Zheng, S. L.; Xu, H. B.; Zhang, Y., *J. of Physical Chemistry B* **2010,** *114* (19), 6542-6548.
55. Schmidt, T. J.; Paulus, U. A.; Gasteiger, H. A.; Behm, R. J., *Journal of Electroanalytical Chemistry* **2001,** *508* (1-2), 41-47.
56. Fisher, G.B.; Sexton, B.A. *Physical Review Letters* **1980**, *44*, 683-686.
57. Steininger, H.; Lehwald, S.; Ibach, H., *Surface Science* **1982,** *123* (1), 1-17.
58. Gland, J. L.; Sexton, B. A.; Fisher, G. B., *Surface Science* **1980,** *95* (2-3), 587-602.
59. Gustafsson, K.; Andersson, S., *Journal of Chemical Physics* **2004,** *120* (16), 7750-7754.
60. Nolan, P. D.; Lutz, B. R.; Tanaka, P. L.; Davis, J. E.; Mullins, C. B., *Journal of Chemical Physics* **1999,** *111* (8), 3696-3704.
61. Eichler, A.; Hafner, J., *Pysical Review Letters* **1997**, *79*, 4481.
62. Hughes, G. R.; Mingos, D. M. P., *Transition Metal Chemistry* **1978,** *3* (6), 381-382.
63. Ho, R. Y. N.; Roelfes, G.; Feringa, B. L.; Que, L., *Journal of the American Chemical Society* **1999,** *121* (1).
64. Li, X.; Heryadi, D.; Gewirth, A. A., *Langmuir* **2005,** *21* (20), 9251-9259.
65. MacNaughton, J. B.; Naslund, L. A.; Anniyev, T.; Ogasawara, H.; Nilsson, A., *Physical Chemistry Chemical Physics* **2010,** *12* (21), 5712-5716.
66. Pettersson, M.; Tuominen, S.; Rasanen, M. *Journal of Physical Chemistry A* **1997**, *101*, 1166.
67. Engdahl, A.; Nelander, B.; Karlstrom, G. *Journal of Physical Chemistry A* **2001**, *105*, 8393.
68. Wu, D. Y.; Li, J. F.; Ren, B.; Tian, Z. Q. *Chemical Society Reviews* **2008**, *37*, 1025–1041.
69. Osawa, M.; Matsuda, N.; Yoshii, K.; Uchida, I. *Journal of Physical Chemistry* **1994**, *98*, 12702-12707.
70. Brolo, A. G.; Irish, D. E.; Smith, B. D.; *Journal of Molecular Structure* **1997**, *405*, 29-44.
71. Avila, F.; Ruano, C.; Lopez-Tocon, I.; Arenas, J. F.; Soto, J.; Otero, J. C. *Chem. Commun*. **2011**, *47*, 4213–4215.
72. Zhao, L. L.; Jensen, L.; Schatz, G. C. *Journal of the American Chemical Society* **2006**, *128*, 2911-2919
73. Ren, B.; Liu, G. K.; Lian, X. B.; Yang, Z. L.; Tian, Z. Q., *Analytical and Bioanalytical Chemistry* **2007,** *388* (1), 29-45.
74. Hyman, M. P.; Medlin, J. W. *Journal of Physical Chemistry B* **2006**, *110*, 15338–15344.
75. Sha, Y.; Yu, T. H.; Liu, Y.; Merinov, B. V.; Goddard, W. A. *Journal of Physical Chemistry Letters* **2010**, 1, 856– 861.
76. Janik, M. J.; Taylor, C. D.; Neurock, M., *Journal of the Electrochemical Society* **2009,** *156* (1), B126-B135:
77. Yeh, K.-Y.; Janik, M. J. *Journal of Computational Chemistry* **2011** *32* (16), 3399-3408.
78. Hsueh, K-L.; Gonzalez, E.R., and Srinivasa, S. *Electrochimica Acta* 1983 *28* (5), 691-697.

2.5. Supporting Information

S.2.1. Redshift of 395 cm^{-1} band in deuterated electrolyte

To better show the redshift of this weak band, we include Raman spectra in the potential region where the 395 cm^{-1} vibration appears as Figure S2.1.

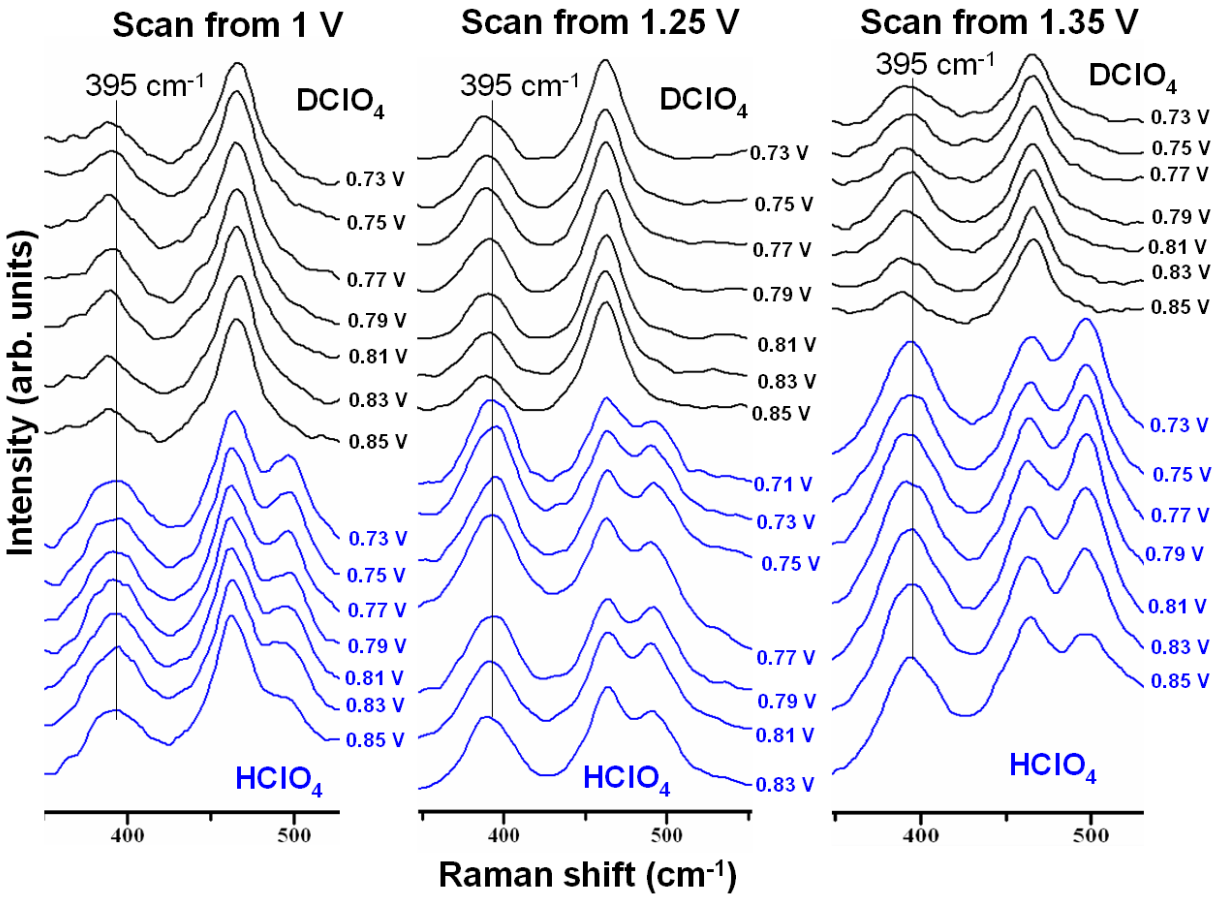

Figure S2.1. Sequential Raman spectra recorded over electrochemically roughened Pt in nitrogen saturated 0.5 M $HClO_4$ (blue) and 0.5 M $DClO_4$ (black) electrolytes concurrent with 1 mV/s cathodic potential scans from 1.0, 1.25 and 1.35 V vs. RHE.

S.2.2. Estimated H^+ and O_2 consumed vs. calculated amount present in electrolyte.

Integration of the current density difference vs. potential between O_2 and N_2 saturated electrolyte yields an area of 0.1995 V-mA/cm^2.

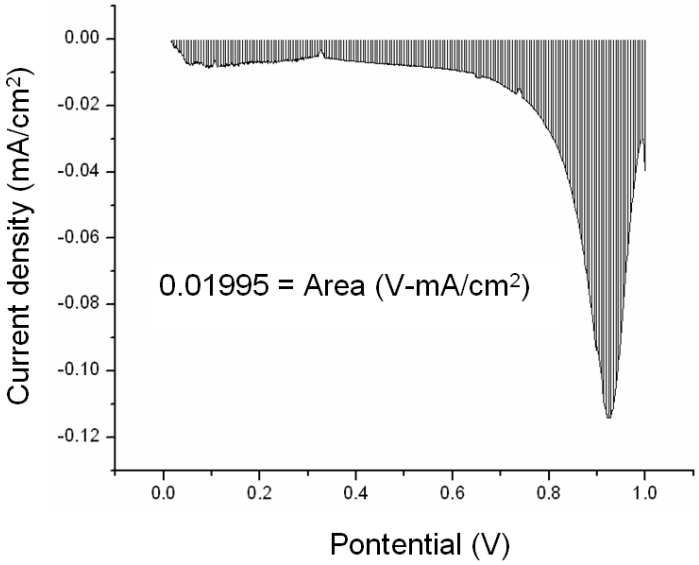

Given the area of the electrode is 0.12566 cm^2, 1000 mA = 1 A, and 1 V = 1000s scan time (at a s scan rate):

$$0.01995\frac{V-mA}{cm^2} = 2.5078\cdot10^{-3}V-mA = 2.5078\cdot10^{-6}V-A = 2.5078\cdot10^{-3}A-s = 2.5078\cdot10^{-3}C$$

With 96485.34 coulombs per Faraday, 1 Faraday = 1 mol electrons, and 4e$^-$ consumed per molecule of O_2 reduced to H_2O:

$2.5078\cdot10^{-3}C = 2.60\cdot10^{-8}F = 1.56\cdot10^{16}electrons = 6.5\cdot10^{-9}$ mol O_2 consumed

The amount of O_2 dissolved in the immediate vicinity of the electrode is $4.02\cdot10^{-8}$ mol (4 mm diameter x 2 mm height = 0.0251 cm^3 and using a O_2 solubility of $1.6\cdot10^{-6}$ mol/cm^3 in 1 M $HClO_4$ at 25°C.[1])

By dividing the calculated moles of oxygen reduced by the theoretical amount present near the electrode surface:

$$\%\ O_2\ consumed = \frac{6.50\cdot10^{-8}\ mol}{4.02\cdot10^{-4}\ mol}\cdot 100\% = 16.2\%$$

Similarly for H^+, assuming 4 H^+ react for every 1 O_2 to for 2 H_2O:

$6.5\cdot10^{-9}molO_2\cdot 4 = 2.60\cdot10^{-8}$ mol H_2 consumed

Assuming full dissociation of the strong acid, 0.5 M $HClO_4$ = 0.005 mol/cm^3 H^+ and multiplying by the volume of electrolyte near the electrode:

0.005 mol/cm^3 H^+·0.0251 cm^3 = $1.26\cdot10^{-4}$ mol H^+ near electrode

$$\%\ H^+\ consumed = \frac{2.6\cdot10^{-8}mol}{1.26\cdot10^{-4}mol}\cdot 100\% = 0.02\%$$

S.2.3. Vibrational Frequency Calculations of Pt-O and Pt-OOH

To aid confirmation of Raman assignments, density functional theory calculations were completed to determine the vibrational frequencies of O and OOH adsorbed to a Pt_4 or Pt_{25} cluster. All simulations employ the spin-polarized PBE functional paired with the LANL2DZ basis set. The initial Pt_{25} structure is that presented by Trout and coworkers.[2] During geometry optimizations, energies were converged to 10^{-6} Ha and the maximum norm of the Cartestian gradient was converged to 10^{-3} Ha $bohr^{-1}$. Frequency calculations were performed to ensure that optimized geometries corresponded to local minima on the potential energy surface possessing zero negative eigenvalues. The optimized geometries of adsorbed O and OOH are presented in Figure S2.3.

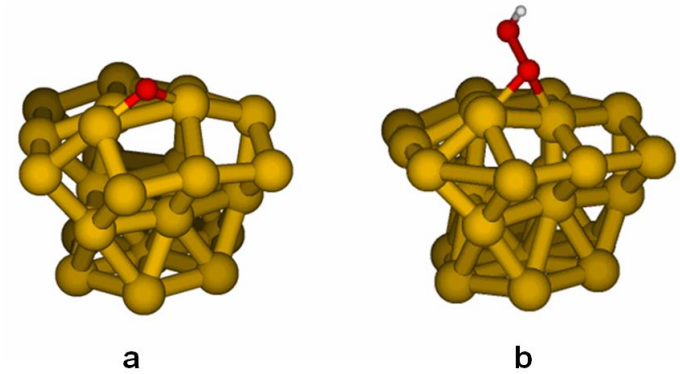

Figure S2.3. Optimized geometries of a) $Pt_{25}O$ and b) $Pt_{25}OOH$.

Calculated vibrational frequencies of adsorbed O and OOH on the Pt_{25} cluster are presented in Table S2.3a, and frequencies of adsorbed H_2O on the Pt_4 cluster are presented in Table S2.3b. Though the calculated frequencies are redshifted compared to experiment, the relative ordering of vibrational modes is consistent with the Raman assignments.

Table S2.3a: Calculated vibrational frequencies of Pt_{25}-O and Pt_{25}-OOH

	Calculated Pt-O (cm^{-1})	Calculated Pt-OOH (cm^{-1})	Experiment (cm^{-1})	ν_{expt}/ν_{Ocalc}	$\nu_{expt}/\nu_{OOH,calc}$
ν_{symm}(Pt-O)	421	387	490	1.16	1.27
ν(O-O)	N/A	570	700	N/A	1.22
$\nu_6(HO_2)$	N/A	1111	1265	N/A	1.14

Table S2.3b: Calculated vibrational frequencies of Pt_4-OH_2

	ν (Pt-OH_2) (cm^{-1})	$\rho_w(H_2O)$ (cm^{-1})
Experiment	390	490
Calculated Pt_4-OH_2	313	472

S.2.4. Oxygen reduction reaction rate expressions

The proposed elementary step sequence for oxygen reduction is as follows:

$O_{2,b} + * \rightarrow O_{2,ads}$ (S2.5)
$O_{2,ads} + H^+ + e^- \rightarrow OOH_{ads}$ (S2.6)
$OOH_{ads} + H^+ + e^- \rightarrow O_{ads} + H_2O$ (S2.7)
$O_{ads} + H^+ + e^- \rightarrow OH_{ads}$ (S2.8)
$OH_{ads} + H^+ + e^- \rightarrow OH_{2,ads}$ (S2.9)
$OH_{2,ads} \rightarrow H_2O + *$ (S2.10)

Reaction S2.6 has previously been reported as the kinetic rate-limiting step.[3, 4] Under kinetic-limiting conditions, oxygen adsorption on the Pt surface becomes equilibrated:

$$K_5[O_{2\,b}] = [O_{2\,ads}] \quad \text{(S2.11)}$$

where K_5 is the equilibrium rate constant of reaction 5, $[O_{2\,b}]$ is the bulk O_2 concentration and $[O_{2\,ads}]$ is the adsorbed O_2 concentration. The rate of reaction for Reaction S2.6, assumed to occur irreversibly, can be expressed as

$$r_6 = r_{ORR} = k_6[H^+][O_{2\,ads}]exp\left(\frac{-\beta F}{RT}\eta\right) = K_5 k_6[H^+][O_{2\,b}]exp\left(\frac{-\beta F}{RT}\eta\right) \quad \text{(S2.12)}$$

where k_6 is the rate constant for Reaction S2.6, $[H^+]$ is the concentration of protons, β is the cathodic transfer coefficient, F is Faraday's constant, R is the universal gas constant, and η is the applied overpotential. The rate limiting step for oxygen reduction, r_6, can be reduced to

$$r_6 = K_5 k_6 exp\left(\frac{-\beta F}{RT}\eta\right)[H^+][O_{2\,b}] = k_{eff}[H^+][O_{2\,b}] \quad \text{(S2.13)}$$

Under conditions of diffusional mass transfer of O_2 (observed in our system at potentials <0.87 V), the apparent rate coefficient can become smaller than the effective rate coefficient due to the concentration of O_2 in the electrolyte adjacent to the electrode becoming less than the concentration in the bulk electrolyte. Under such circumstances, the apparent rate coefficient, k_{app}, will be given by:

$$k_{app} = \frac{k_{eff}k_{MT}}{(k_{eff}+k_{MT})} \quad \text{(S2.14)}$$

where k_{MT} is the mass-transfer rate constant. As k_{eff} increases with a reduction in the applied potential, the value of k_{app} decreases from a maximum of k_{eff} to a minimum of k_{MT}. Applying relation (S2.14) to put $[O_{2\,ads}]$ in terms of $[O_{2\,b}]$:

$$[O_{2\,ads}] = \frac{k_{MT}K_5}{(k_{eff}+k_{MT})}[O_{2\,b}] \quad \text{(S2.15)}$$

Since k_{eff} is exponentially dependent on the overpotential, the adsorbed surface O_2 concentration will decrease and diffusional mass transfer will begin to dominate with increasing overpotential, explaining the decay in both the current density and the Raman intensity of surface intermediates.

By relating the rate of Reaction S2.7 to Reaction S2.6:

$$r_6 = r_7 = k_6[H^+][O_{2\,ads}]exp\left(\frac{-\beta F}{RT}\eta\right) = k_7[H^+][OOH_{ads}]exp\left(\frac{-\beta F}{RT}\eta\right) \quad \text{(S2.16)}$$

Then arranging to express $[OOH_{ads}]$ in terms of $[O_{2\,ads}]$:

$$[OOH_{ads}] = \frac{k_6}{k_7}[O_{2\,ads}] \quad \text{(S2.17)}$$

Similarly, for Reaction 8 to express $[O_{ads}]$ in terms of $[O_{2\,ads}]$:

$$[O_{ads}] = \frac{k_6}{k_8}[O_{2\,ads}] \quad \text{(S2.18)}$$

All intermediates are first-order with respect to adsorbed molecular oxygen concentration, supporting the observation that all oxygen intermediates in the Raman spectra change proportionally to the concentration of adsorbed molecular oxygen (shown in Fig. S.14).

References

S1. Hsueh, K-L.; Gonzalez, E.R., and Srinivasa, S. *Electrochimica Acta* **1983**, *28* (5), 691-697.

S2. Lin, X.; Ramer, N. J.; Rappe, A. M.; Hass, K. C.; Schneider, W. F.; Trout, B. L., *Journal of Physical Chemistry B* **2001,** *105* (32) 7739-7747.

S3. Yeh, K.-Y.; Janik, M. J. *Journal of Computational Chemistry* 2011 *32* (16), 3400-3408.

S4. Neurock, M; Mei, D; Prascher, B. Theoretical Insights into the Mechanisms and Kinetics in the Electrocatalytic Reduction of Oxygen. Presented at the 22nd North American Meeting of the North American Catalysis Society, Detroit, MI, June 6, 2011.

Part II

The Oxygen Evolution Reaction

Chapter 3

Effects of Fe Electrolyte Impurities on $Ni(OH)_2$/NiOOH Structure and Oxygen Evolution Activity

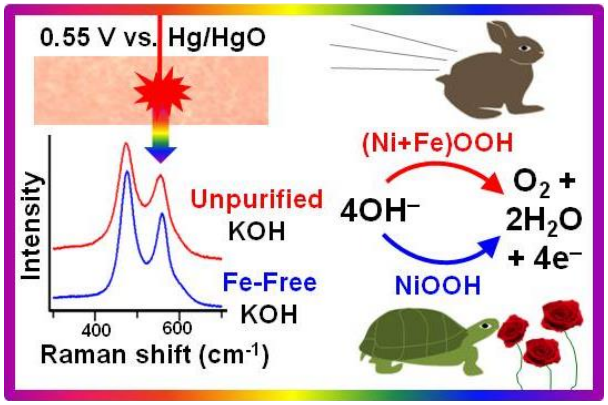

Abstract

Ni-(oxy)hydroxide-based materials are promising earth-abundant catalysts for electrochemical water oxidation in basic media. Recent findings demonstrate that incorporation of trace Fe impurities from commonly used KOH electrolytes significantly improves oxygen evolution reaction (OER) activity over NiOOH electrocatalysts. Because nearly all previous studies detailing structural differences between α-$Ni(OH)_2$/γ-NiOOH and β-$Ni(OH)_2$/β-NiOOH were completed in unpurified electrolytes, it is unclear whether these structural changes are unique to the aging phase transition in the Ni-(oxy)hydroxide matrix or if they arise fully or in part from inadvertent Fe incorporation. Here, we report an investigation of the effects of Fe incorporation on structure–activity relationships in Ni-(oxy)hydroxide. Electrochemical, in situ Raman, X-ray photoelectron spectroscopy, and electrochemical quartz crystal microbalance measurements were employed to investigate $Ni(OH)_2$ thin films aged in Fe-free and unpurified (reagent-grade) 1 M KOH (<1 ppm Fe). We find that Ni films aged in unpurified electrolyte can incorporate ≥20% Fe after 5 weeks of aging, and the maximum catalyst activity is comparable to that reported for optimized $Ni_{1-x}Fe_xOOH$ catalysts. Conversely, Fe-free $Ni(OH)_2$ films exhibit a substantially lower activity and higher Tafel slope for the OER. Films aged in Fe-free electrolyte are predominantly disordered β-$Ni(OH)_2$/β-NiOOH if maintained below 0.7 V vs Hg/HgO in 1 M KOH and will "overcharge" to form a mixture of γ- and β-NiOOH above this potential. Fe-containing $Ni(OH)_2$ films evidence a lesser extent of β-$Ni(OH)_2$ formation and instead exhibit NiOOH structural changes in accordance with the formation of a NiFe-layered double hydroxide phase. Furthermore, turnover frequency calculations indicate that Fe is the active site within this phase, and above ~11% Fe content, a separate, Fe-rich phase forms. These findings are the first to demonstrate the in situ changes in the catalyst structure resulting from the incorporation of Fe electrolyte impurities within Ni-(oxy)hydroxide, providing direct evidence that a Ni–Fe layered double (oxy)hydroxide (LDH) phase is critical for high OER activity.

3.1. Introduction

Electrochemical water-splitting to form molecular oxygen (O_2) and hydrogen (H_2) offers a promising means for the storage of energy generated from intermittent energy sources, such as wind and solar.[1,2] A major challenge to accomplish this conversion efficiently, however, is the slow kinetics of the oxygen evolution reaction (OER, $4OH^- \rightarrow 2H_2O + O_2 + 4e^-$ in base and $2H_2O \rightarrow 4H^+ + O_2 + 4e^-$ in acid) at the anode, which results in a large reaction overpotential.[1-3] To improve the overall energy efficiency of such systems, a highly active and cost-effective electrocatalyst for the OER is critical.

In alkaline electrolyte, nickel-based materials are particularly promising OER catalysts due to their high stability and earth-abundance.[4,5] The OER-active phase of nickel catalysts has been shown to be Ni^{3+} or a mixture of Ni^{3+} and Ni^{4+} present as a NiOOH-type structure.[6-9] At potentials well below the onset of the OER, the catalyst is present as $Ni(OH)_2$, and prior to the onset of oxygen evolution, this phase is oxidized to NiOOH via the reaction $Ni(OH)_2 + OH^- \rightarrow NiOOH + H_2O + e^-$.[5,8] Numerous studies have reported that the activity of NiOOH can be increased in two ways: 1) by addition of Fe to NiOOH[10-21] and 2) by transformation of the OER active phase γ-NiOOH to β-NiOOH via aging, shown in the Bode scheme in Fig. 3.1.[5,22-28]

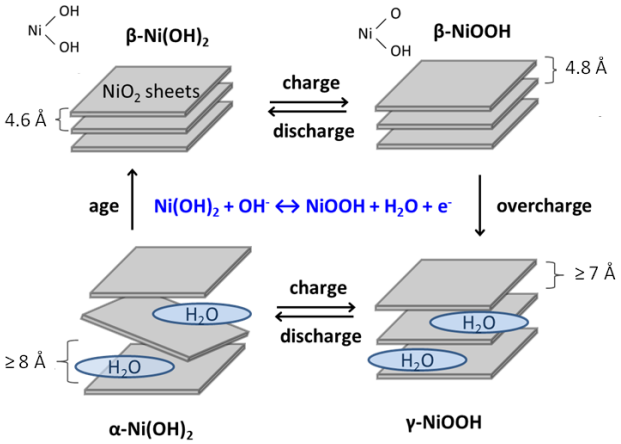

Figure 3.1. Bode Scheme[28] for the $Ni(OH)_2$/NiOOH redox transformation.

Given that addition of Fe is a primary means to improve the activity of NiOOH catalysts, previous work from our group has focused on elucidation of the effects of Fe within the $Ni(OH)_2$/NiOOH structures. X-ray absorption spectroscopy (XAS) investigations show that while no change occurs in the Ni–O bond length with Fe addition, the Fe–O bond length exhibits a significant contraction upon electrochemical oxidation to $Ni_{1-x}Fe_xOOH$.[29] Corresponding density-functional theory calculations show that this Fe–O bond contraction optimizes the binding energies of OER reaction intermediates over these sites, which is the proposed mechanism of improved OER activity over $Ni_{1-x}Fe_xOOH$ materials.

Trotochaud et al.[30] recently revealed that the increase in OER activity observed with aging in KOH is not due to the transition of γ-NiOOH to β-NiOOH, as had been concluded in previous studies. They show that Fe-free NiOOH is a poor catalyst for the OER, exhibiting an overpotential in excess of 500 mV at 10 mA cm^{-2}. Instead, increased activity with aging arises from Fe impurities present in KOH electrolyte, which readily incorporate into the NiOOH films. This work also showed that 25% *co-deposited* Fe produces a Ni-Fe layered double hydroxide, which inhibits the

aging phase transformation of α-$Ni(OH)_2$ to β-$Ni(OH)_2$. However, the effects of *Fe-impurity* incorporation on structural changes were not addressed.

Since nearly all previous efforts aimed at investigating structural differences between α-$Ni(OH)_2$/γ-NiOOH and β-$Ni(OH)_2$/β-NiOOH were likely carried out using Fe-contaminated KOH, it is not clear to what degree these structural changes are due to unintentional Fe incorporation and how structural changes affect activity in the absence of Fe.[24,25] In this study, we attempt to separate the effects of Fe-incorporation and aging on NiOOH structure by employing electrochemistry, spectroscopy, and microgravimetry techniques to investigate $Ni(OH)_2$/NiOOH films aged in both Fe-free and unpurified KOH electrolyte. These findings distinguish the true effects of aging vs. Fe-incorporation on thin film Ni-(oxy)hydroxide OER catalyst structure and activity, specifically that 1) in Fe-free electrolyte, the traditional description of structural changes developed by Bode holds, despite previous aging/overcharging studies completed in the presence of Fe contaminants, 2) Fe incorporates into the Ni-(oxy)hydroxide lattice and forms a distinct structure consistent with an NiFe-layered double (oxy)hydroxide (LDH) structure, and 3) it is the Fe-sites within this mixed Ni-Fe LDH phase which are critical for the improved OER activity observed in unpurified KOH.

3.2. Experimental

3.2.1 Electrocatalyst deposition and aging.

Experiments were conducted in both purified (Fe-free) and unpurified reagent-grade (containing Fe impurities) 1M KOH electrolyte. Fe-free 1 M KOH was prepared from 45% Baker Analyzed Electronic Grade KOH solution (VWR JT3144-3) and purified according to the method outlined by Trotochaud et al. (see Supporting Information S3.1).[30] Unpurified 1 M KOH solutions were prepared using ACS reagent-grade KOH pellets (≥85%, ≤0.001% Fe, Sigma-Aldrich 221473). Additionally, all experiments were performed in a PFA beaker to avoid possible contamination due to glass-etching.[10]

$Ni(OH)_2$ films were deposited electrochemically onto 5 mm diameter Au electrodes. Prior to each deposition, an Au electrode was polished mechanically with 1 μm and 0.05 μm diameter alumina, with sonication in H_2O (18 MΩ cm resistance, Milli Q Millipore) for 10 min between each polishing step. The Au electrode was then cycled electrochemically from -1.0 to 0.7 V vs. a Hg/HgO reference electrode filled with 1 M KOH (CH Instruments) at 10 mV s^{-1} in Fe-free 1 M KOH until the cyclic voltammogram was fully stabilized (typically ~50 cycles). This procedure ensured that Ni deposition occurred on a fully stabilized electrode surface. Alternatively, for Raman experiments, the Au electrode was roughened electrochemically in 0.1 M KCl (Sigma-Aldrich P3911) through application of a previously reported waveform (see Supporting Information S3.2).[31] $Ni(OH)_2$ was electrodeposited from a nitrogen-sparged high purity 0.01 M $Ni(NO_3)_2$ solution (from 99.999% nickel nitrate hexahydrate, Sigma Aldrich 203874) using a cathodic geometric-surface-area current density of 1 mA cm^{-2}. The deposition time was 75 s over quartz crystal microbalance (QCM) and rotating disc electrodes (RDEs) to obtain films with ~30 nm thickness based on a QCM mass-change deposition profile (Supporting Information S3.3). Films deposited for Raman experiments are estimated to be ~12-15 nm thick due to the roughness of the underlying Au substrate.

A coiled Pt wire served as the counter electrode for all experiments, with a separate Pt wire used for Ni deposition. Both Pt wire counter electrodes were periodically cleaned by overnight soaking in 5 M nitric acid or 1 M sulfuric acid.

Aging of $Ni(OH)_2$ films was carried out by immersing the $Ni(OH)_2$/Au electrode in 1.125 mL of Fe-free or unpurified 1 M KOH at room temperature and in the absence of applied electrochemical potential. For each day of electrochemical measurements, fresh KOH electrolyte solution was used. To investigate the progressive aging process, the OER performance was measured each day on the same $Ni(OH)_2$/Au electrode for a period of six days.

3.2.2 Electrochemical measurements

All rotating disk electrode (RDE) experiments were performed on 5 mm Au electrodes (Pine Research Instrumentation). A coiled Pt wire served as the counter electrode, and all potentials are recorded vs. a Hg/HgO reference electrode. The potential of the Hg/HgO reference was routinely checked against another Hg/HgO reference electrode to ensure electrode stability and differed by 2.5 mV or less. Current-voltage curves for $Ni(OH)_2$ films were acquired with RDEs immersed in 45-50 mL of freshly prepared Fe-free or unpurified 1 M KOH solution using a rotation rate of 1600 rpm and a sweep rate of 10 mV s^{-1}. The typical potential range for OER measurement vs. Hg/HgO was 0.00 to 0.65 V (for regular KOH) and 0.00 to 0.92 V (for Fe-free KOH), and the 12^{th} voltammogram cycle is reported. All electrochemical potentials reported here were corrected for uncompensated series resistance (R_u), which was determined by potentiostatic electrochemical impedance spectroscopy (PEIS). Generally, R_u was ~ 4-6 Ω in 1 M KOH solution. Unless otherwise mentioned, all potentials cited in this work are referenced to the Hg/HgO electrode. The overpotential η was calculated using the equation $\eta = E_{meas}$ (internally corrected for 95% R_u) − E_{rev}, where E_{meas} is the potential measured vs. Hg/HgO and E_{rev} is the reversible potential of the OER vs. Hg/HgO (0.306 V at pH 14 or 0.365 V at pH 13). All reported current densities were calculated based on geometric surface area.

3.2.3 Characterization

The Ni and Fe content of films aged in regular KOH were measured by inductively coupled plasma optical emission spectrometry (ICP-OES, Optima 7000 DV, Perkin-Elmer). Films were dissolved overnight in 5 M nitric acid (Sigma-Aldrich 84385) and sonicated for 1 min prior to dilution. Final solutions contained 5 wt % nitric acid, and concentrations were calculated using an internal yttrium standard (Sigma-Aldrich 01357) and 0 to 500 ppb Ni and Fe calibration standards (Sigma-Aldrich 28944 and 43149, respectively).

X-ray photoelectron spectroscopy (XPS) studies were carried out using a Kratos Axis Ultra spectrometer with a Mg Kα non-monochromated flood source (10 mA, 15 kV, spectra acquired with a 20 eV pass energy, 50 meV step energy, and a dwell time of 200 ms) to avoid the Ni Auger features in the Fe 2p region present with the Al source. The base chamber pressure was 10^{-9} Torr, and no charge neutralization was applied. CasaXPS (Casa Software, Ltd.) was used for sample analysis. Baseline and non-monochromated satellite subtractions were applied (see examples in Supporting Information S3.4.1), and all binding energies were adjusted to the adventitious carbon C 1s signal at 284.8 eV to compensate for charging effects.

Electrochemical quartz crystal microbalance (QCM) measurements were carried out with a Stanford Research Systems QCM 200. The Au/Ti quartz crystal was stabilized in 1 M KOH prior to electrodeposition, and the deposition current was adjusted for the larger area of this electrode (approximately 1.38 cm^2). Film mass changes were estimated from changes in the resonance frequency using the Sauerbrey equation, $\Delta f = -C_f \Delta m$, where Δf is the observed frequency change (Hz), C_f is the sensitivity factor of the quartz crystal, and Δm is the change in mass per unit area (μg cm^{-2}).[32] The quartz crystal sensitivity factor, 54.5 ± 0.5 Hz μg^{-1} cm^2, was calibrated by Faradaic deposition of Ag metal from a 0.05 M silver nitrate solution and is an average of three measurements. (Further information regarding QCM calibration in Supporting Information S3.3.)

An epoxy-free version of our previously described Teflon cell[24,25,33] was built in-house and used for the combined electrochemical and in situ Raman spectroscopy studies. A $Ni(OH)_2$ film deposited over a 5 mm electrochemically roughened Au disc sheathed in Teflon served as the working electrode. All Raman experiments were completed in 0.1 M KOH due to considerable background signal in 1 M KOH. In situ Raman spectra of the electrodes were recorded using a confocal Raman microscope (LabRam HR, Horiba Jobin Yvon). A high numerical aperture water-immersion objective (70 x magnification, N.A. = 1.23, LOMO) was used to achieve a high collection efficiency. Prior to each experiment, the objective was wrapped in 0.001" PFA film (McMaster Carr) to avoid corrosion, and a droplet of water was placed between the objective and film to preserve the refractive index.[24,25,33]

Raman spectra were acquired with 1−2 mW of power (measured at the sample surface) delivered by a laser operating at 633 nm, with a laser spot size of ~1 μm. Each Raman spectrum was recorded with a resolution of 1 cm^{-1} by averaging three scans, each of 3 s duration. For these experiments, the electrode potential was scanned at a rate of 1 mV s^{-1}. The spectral position was checked against a Si wafer prior to each sample scan and recalibrated if >1 cm^{-1} variation of the 520.7 cm^{-1} silicon phonon mode was observed. To more clearly show the Raman peaks within this region, high wavenumber (3000-3800 cm^{-1}) spectra were background subtracted within the Raman instrument software (Labspec).

3.3. Results

3.3.1 Electrochemical characterization of aged $Ni(OH)_2$ films by cyclic voltammetry

Extended electrode immersion in alkaline electrolyte converts the as-deposited α-$Ni(OH)_2$ phase to the more compact β-$Ni(OH)_2$ structure in a process referred to as aging.[4,5,25,27,28,34] To track electrochemical changes with electrode aging, cyclic voltammograms (CVs) were obtained for $Ni(OH)_2$ films freshly prepared and after each day of aging in 1 M Fe-free (Fig. 3.2a) and unpurified (Fig. 3.2b) KOH. Fig. 3.2a shows that the OER current decreases when $Ni(OH)_2$ is aged in Fe-free electrolyte, whereas a dramatic increase in the OER current occurs for $Ni(OH)_2$/NiOOH cycled in unpurified electrolyte, even on day 0 after just 12 voltammogram cycles.

With initial cycling, a significant oxidation wave is observed at 0.43 V vs. Hg/HgO for samples in both purified and unpurified electrolyte. This feature is attributed to the oxidation of Ni in the film.[5,8] The position of the oxidation wave maximum shifts to 0.47 V after six days of aging in Fe-free KOH and to 0.50 V after six days of aging in unpurified KOH.

The voltammograms recorded in Fe-free electrolyte during days 1-3 clearly display two peaks within the Ni(II)/Ni(III) oxidation region. Two smaller oxidation features are also observed after the primary oxidation wave, which are similar to those reported by Trotochaud et al.[30] The first feature, centered at 0.6 V, diminishes with aging, while the second feature emerges on day 1 at ~0.7 V and intensifies with aging in the absence of impurities. Note that when Fe impurities are present, these two smaller oxidation waves at higher potentials would be obscured by significant oxygen evolution current.

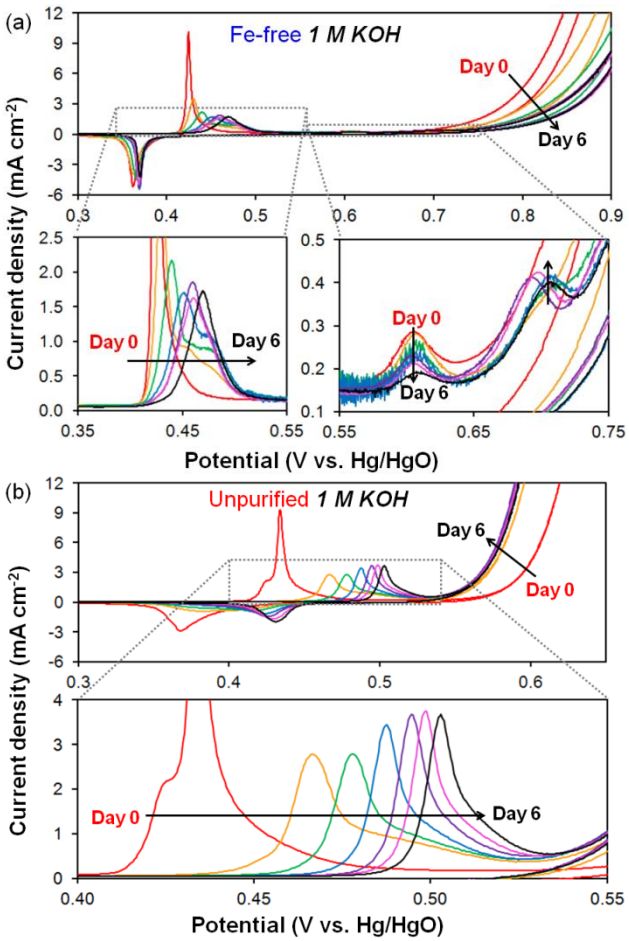

Figure 3.2. Cyclic voltammograms obtained for $Ni(OH)_2$ films deposited on polished Au-RDEs. Voltammograms were collected at 10 mV s^{-1} and 1600 rpm in a (a) Fe-free and (b) unpurified 1 M KOH after each day of aging in either Fe-free or unpurified 1 M KOH, respectively. The oxygen evolution equilibrium potential is 0.306 V vs. Hg/HgO in 1 M KOH.

3.3.2 Fe impurity uptake and effects on OER activity

The composition of $Ni(OH)_2$ films aged in 1 M KOH was determined using surface (XPS) and bulk (ICP-OES) techniques (Figure 3.3). No evidence for the accumulation of Fe was observed for Ni films aged in Fe-free electrolyte from XPS (Supporting Information S3.4). 1 M KOH solutions made from ACS reagent-grade KOH pellets (≤ 0.001% Fe) are estimated to contain ≤ 0.66 ppm Fe. Using this unpurified electrolyte, the Ni film (~30 nm thick) is comprised of ~5% Fe after just 12 voltammogram cycles. The Fe content increases to 23-26% of total metal in the film after extended aging (38 days). The peak potentials of the $Ni(OH)_2$/NiOOH redox waves continue to shift toward more oxidizing potentials with each subsequent day of aging (Supporting Information S3.5), evidence that Fe still continues to incorporate even after more than one month of aging.

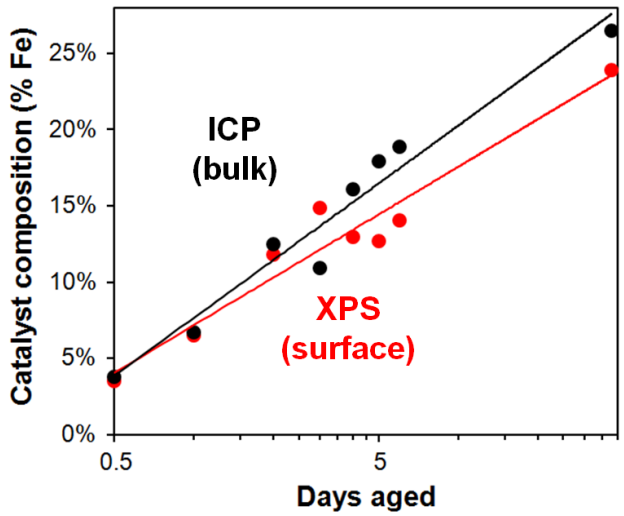

Figure 3.3. Iron content of $Ni(OH)_2$ films deposited on polished Au-RDEs measured from X-ray photoelectron spectroscopy (XPS) and inductively coupled plasma optical emission spectroscopy (ICP-OES) vs. days aged in unpurified 1 M KOH. Lines show a logarithmic best-fit ($y = aln(x) + b$) to each data set. Values of a and b for each data set can be found in the Supporting Information file.

The Fe content of the film appears to increase logarithmically with respect to aging time, and Fe contents determined from both XPS and ICP-OES are similar. Elemental analysis also shows that, in general, total film mass is comparable between samples, indicating the films are not dissolving in the aging solution. This is consistent with known values for $Ni(OH)_2$ solubility (see explanation and table in SI S3.6).[35]

Ni films aged in unpurified 1 M KOH exhibit a much lower overpotential at 10 mA cm^{-2} than films aged in Fe-free electrolyte (Figure 3.4). Activities were comparable between 0.1 and 1 M KOH (Supporting Information S3.7). The overpotential for Fe-free films at 10 mA cm^{-2} is 529 mV and increases with aging, stabilizing at ~605 mV after three days. The overpotential for films aged in unpurified electrolyte is minimized at 280 mV after five days, then slightly increases by ~7 mV with subsequent aging. This overpotential is comparable to those obtained with intentional Fe-incorporation.[10,24]

The OER Tafel slope for Fe-free films (Fig. 3.4, Tafel plots in Supporting Information S3.8), was 106 mV dec^{-1} on day 0 and increased to 134 mV dec^{-1} by day 6; both of these values are significantly higher than the Tafel slopes previously reported for both freshly-prepared and aged Ni electrocatalysts where Fe impurities were presumably present.[9,23,36,37] In contrast, $Ni(OH)_2$ films cycled and aged in unpurified 1 M KOH exhibited an initial Tafel slope of 45-55 mV dec^{-1}, which decreased to ~40 mV dec^{-1} within 12 voltammogram cycles. The Tafel slope remained stable at 38-40 mV dec^{-1} through six days of aging; this value is consistent with previous Tafel slopes recorded over Ni-Fe (oxy)hydroxide electrocatalysts.[12,16,17,24]

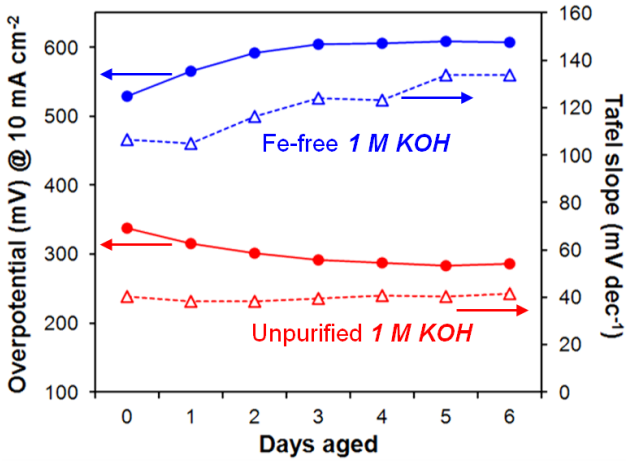

Figure 3.4. The effect of aging on the overpotential at 10 mA cm^{-2} geometric current density (filled circles) and Tafel slope (open triangles) for $Ni(OH)_2$ films deposited on polished Au-RDEs aged in Fe-free (blue) vs. unpurified (red) 1 M KOH.

All current densities presented are calculated based on geometric electrode surface areas. A plot of current density (j at η = 300 mV) and overpotential (η at j = 10 mA cm^{-2}) as a function of surface composition is shown in Fig. 3.5. Maximum OER activity, with j = 25-28.7 mA cm^{-2} and η = 280 mV is reached with 12-17% Fe incorporation. Compared to the activities for Fe-free NiOOH, these changes represent a 200-fold increase in current density and a nearly 250 mV decrease in overpotential. With further incorporation of Fe, no additional activity enhancement is observed.

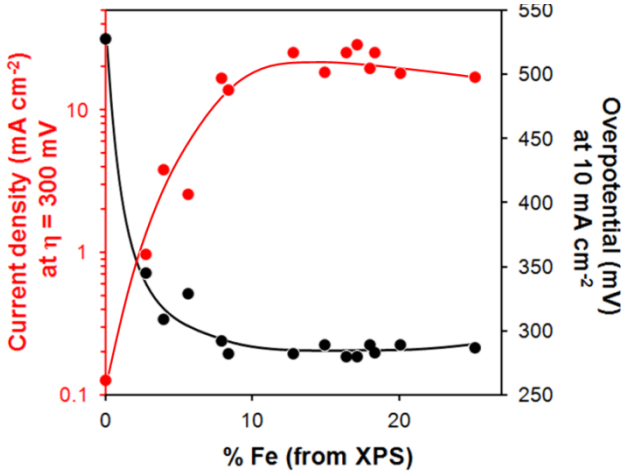

Figure 3.5. Oxygen evolution activity of electrodeposited NiOOH films deposited on Au RDEs at 300 mV overpotential and 10 mA cm^{-2} geometric current density in 1 M KOH as a function of Fe content. Curves are included to guide the eye.

3.3.3 In-situ Raman spectroscopy of aged $Ni(OH)_2$ thin films

The effects of aging on the composition and structure of $Ni(OH)_2$ films were followed by in situ Raman spectroscopy. Spectra of $Ni(OH)_2$/NiOOH films, obtained before and after six days of aging in Fe-free and unpurified 1 M KOH, were acquired in 0.1 M KOH during 1 mV s^{-1} oxidation sweeps and are presented in Fig. 3.6.

For the films aged in Fe-free KOH, Raman peaks are observed on day 0 (Fig. 3.6a) at 453 and 495 cm^{-1} for potentials between 0.0 and 0.4 V. These features then rapidly attenuate with increasing potential. Starting at 0.4 V, peaks emerge at 477 and 560 cm^{-1}; these features intensify as the potential is increased to 0.6 V (i.e. through the oxidation wave observed in CVs). After six days of aging in Fe-free KOH, only a weak feature at 495 cm^{-1} is observed at 0 V, and the 480/560cm^{-1} peaks first appear at 0.35 V.

When films are aged in unpurified KOH (Fig. 3.6b), the Raman bands observed initially on day 0 at 453 and 495 cm^{-1} diminish with increasing applied potential, while the 477 and 558 cm^{-1} Raman peaks are observed for potentials above 0.4 V. On day 6, the band at 495 cm^{-1} is also present at 0 V but is obscured by the Raman signals at 476 and 555 cm^{-1} for potentials of 0.2 V and above.

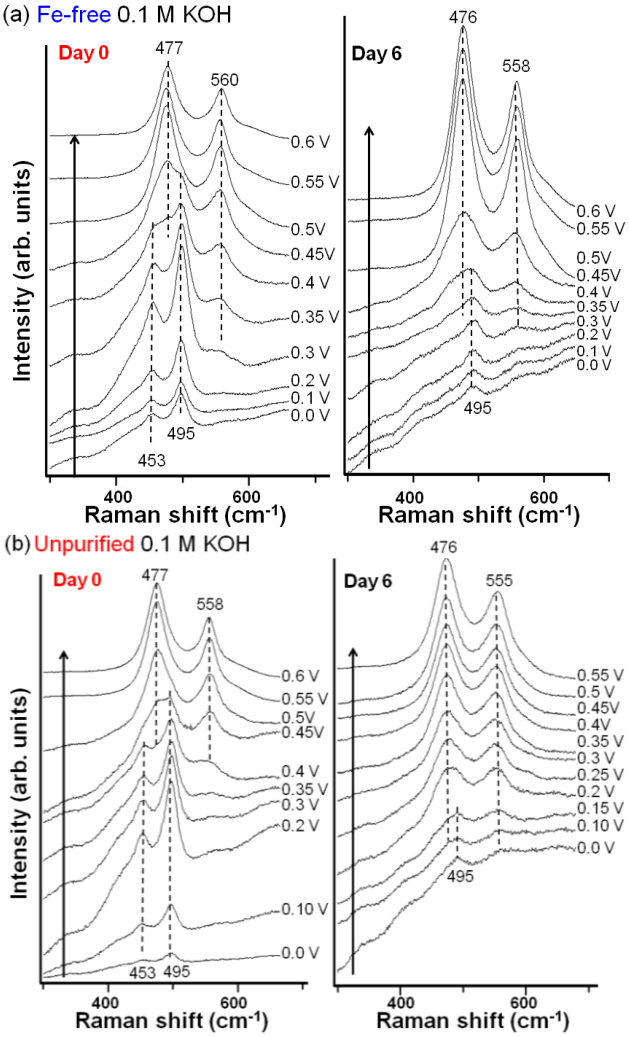

Figure 3.6. In situ Raman spectra collected over $Ni(OH)_2$/NiOOH films deposited on roughened Au in (a) Fe-free and (b) unpurified 0.1 M KOH on Day 0 and Day 6. Potentials are reported vs. Hg/HgO. The oxygen evolution equilibrium potential is 0.365 V vs. Hg/HgO in 0.1 M KOH.

Raman spectra were also acquired at high wavenumbers (3000-3800 cm^{-1}) to observe the ν(O-H) modes of the $Ni(OH)_2$ phases (Figure 3.7).[8] In Fe-free electrolyte at 0.2 V, a 3665 cm^{-1} Raman band predominates at day 0, whereas a feature at 3581 cm^{-1} appears after a day of aging. With continued aging, the band at 3665 cm^{-1} decreases in intensity, while that at 3581 cm^{-1} becomes stronger. In unpurified electrolyte, the bands at 3581 cm^{-1} and 3665 cm^{-1} are both present on day 0, and the intensity of both peaks decrease with aging. By day 6, there is minimal evidence for the band at 3665 cm^{-1} and only a small 3581 cm^{-1} feature is observed. (Additional Raman spectra are available in Supporting Information S3.9.)

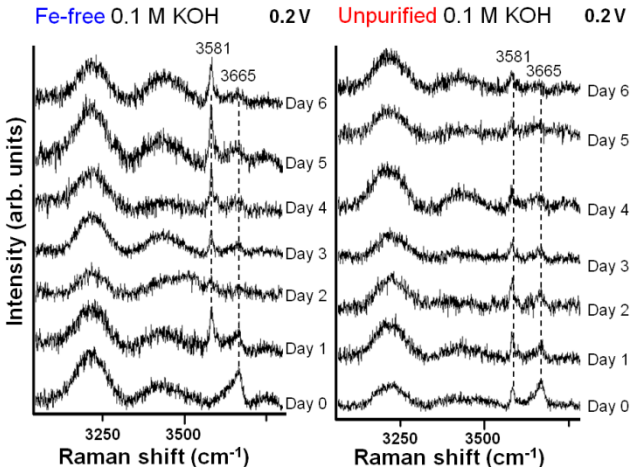

Figure 3.7. In situ Raman spectra collected over $Ni(OH)_2$ films deposited on roughened Au and recorded at 0.2 V vs. Hg/HgO in Fe-free and unpurified 0.1 M KOH. The oxygen evolution equilibrium potential is 0.365 V vs. Hg/HgO in 0.1 M KOH.

3.3.4 Electrochemical quartz crystal microgravimetry

Electrochemical quartz crystal microbalance experiments were completed to track the conversion of α-$Ni(OH)_2$ to β-$Ni(OH)_2$ with aging in Fe-free and unpurified KOH. Electrochemical microgravimetry has previously been used to differentiate the α/γ and β/β phase couples: an increase in film mass occurs during the oxidation of α-$Ni(OH)_2$ to γ-NiOOH due to intercalation of water and ions, whereas film mass decreases or remains constant during the oxidation of β-$Ni(OH)_2$ to β-NiOOH.[27,38] For $Ni(OH)_2$ films initially cycled in both Fe-free and unpurified 0.1 M KOH, there is a 10 Hz decrease in frequency (SI S3.10), corresponding to a ~160 ng cm^{-2} increase in mass during $Ni(OH)_2$ oxidation to NiOOH (Fig. 3.8). By contrast, samples aged six days in either purified or unpurified KOH exhibit a decrease in mass upon oxidation. However, after 6 days of aging, the ~110 ng cm^{-2} mass density decrease observed during film oxidation for the Fe-free films is much greater than the ~50 ng cm^{-2} decrease for films aged in unpurified KOH.

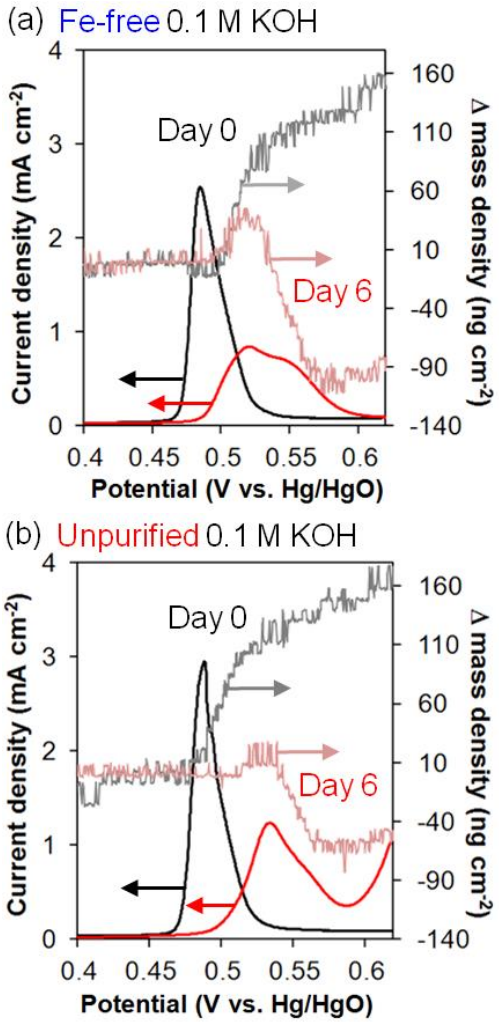

Figure 3.8. QCM mass density change with concurrent 10 mV s^{-1} potential scans for $Ni(OH)_2$ films deposited on Au/Ti quartz crystals in (a) Fe-free and (b) unpurified 0.1 M KOH before and after six days of aging in 1 M KOH. The oxygen evolution equilibrium potential is 0.365 V vs. Hg/HgO in 0.1 M KOH.

3.3.5 Electrochemical overcharging of the $Ni(OH)_2$/NiOOH structure

It was previously reported that β-NiOOH can transform to γ-NiOOH via "overcharging" at potentials exceeding 0.7 V;[27,28] this conversion was investigated by maintaining films below this threshold during six days of aging and then applying a potential scan to 0.85 V. The results of this overcharging cycle for a roughened Au electrode are shown in Fig. 3.9 (corresponding cycles over a QCM are presented in SI 11). As expected, the main oxidation feature of the overcharge cycle (red) aligns with that of the last stabilization cycle to 0.7 V (black). However, as the potential is increased to 0.85 V, a large oxidation feature is observed at 0.79 V. Subsequent CV cycles (purple) show a cathodic shift of the primary Ni oxidation wave (from 0.53 to 0.50 V) and the presence of a shoulder at ~0.52 V. An additional oxidation feature emerges at ~0.66 V, and the 0.79 V oxidation peak present in the first overcharge cycle is diminished and shifted cathodically to ~0.76 V.

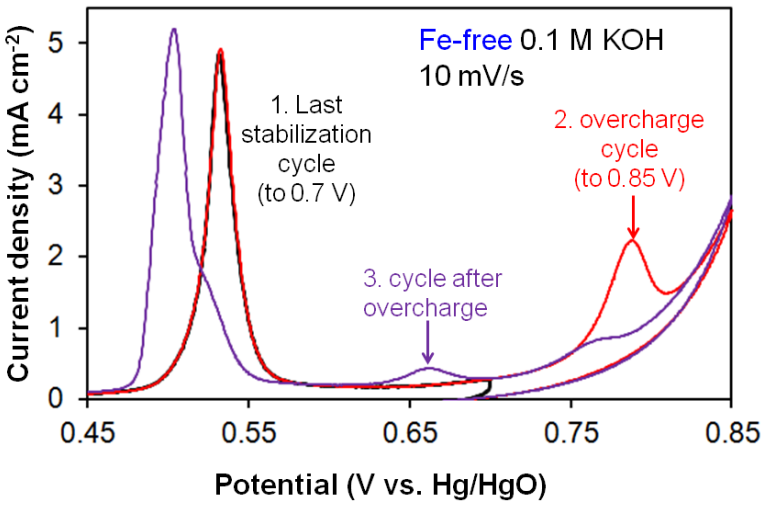

Figure 3.9. Cyclic voltammogram of an aged $Ni(OH)_2$ film in 0.1 M Fe-free KOH (after six days of aging in 1 M Fe-free KOH) with a 10 mV s^{-1} scan rate. The electrodes were stabilized to 0.7 V before a 10 mV s^{-1} overcharge scan to 0.85 V. The oxygen evolution equilibrium potential is 0.365 V vs. Hg/HgO in 0.1 M KOH.

Corresponding QCM measurements, shown in Fig. 3.10, were completed to track mass changes before and after the 0.85 V overcharging scans in both Fe-free and unpurified KOH. For the Ni film aged in Fe-free electrolyte, a decrease in mass is observed with the primary oxidation wave from 0.54-0.58 V. After overcharge, the primary oxidation wave more closely resembles that of the day 0 electrode (Fig. 3.8), and essentially no mass change is observed during the primary oxidation wave.

For the $Ni(OH)_2$ film aged in unpurified KOH electrolyte, minimal difference is observed between the CVs before and after an overcharge cycle to 0.85 V. After overcharge, the QCM mass density decreases slightly compared to the prior oxidation cycle, possibly due to oxygen bubble-formation on the quartz crystal surface.

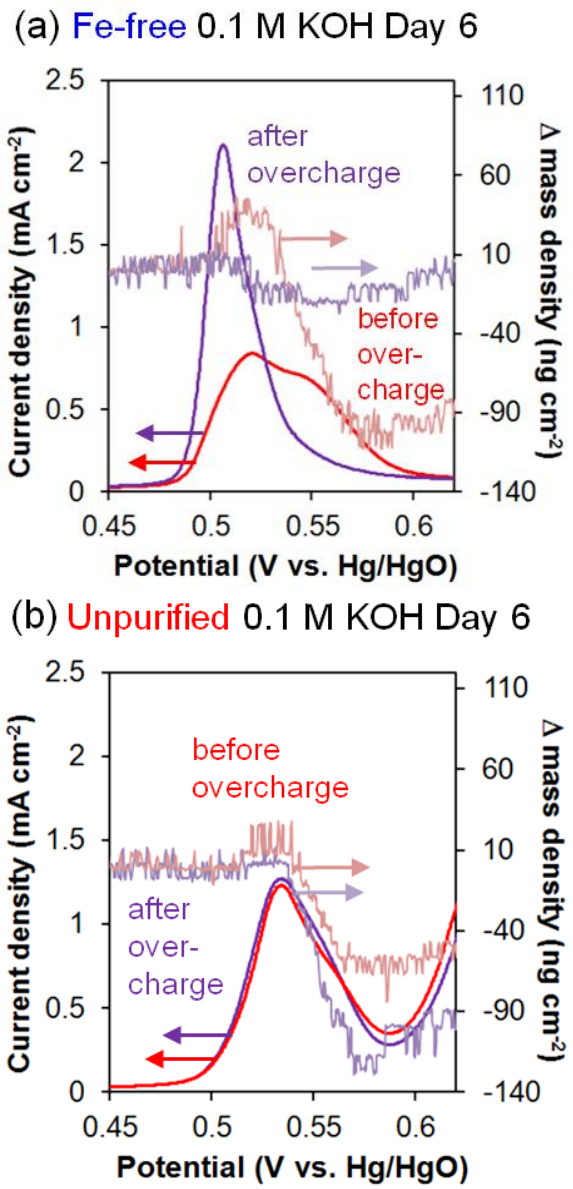

Figure 3.10. QCM mass density change with concurrent 10 mV s^{-1} potential scans for $Ni(OH)_2$ films deposited on Au/Ti quartz crystals in (a) Fe-free and (b) unpurified 0.1 M KOH (both after six days of aging in 1 M KOH). Cycles are shown before and after the 10 mV s^{-1} overcharge scan to 0.85 V. The oxygen evolution equilibrium potential is 0.365 V vs. Hg/HgO in 0.1 M KOH.

3.4. Discussion

3.4.1 $Ni(OH)_2$/NiOOH structural changes with aging and overcharging in Fe-free KOH

While the transformation of α-$Ni(OH)_2$ to β-$Ni(OH)_2$ with aging has been reported previously, all earlier observations were carried out in KOH contaminated with Fe and, therefore, the results were unintentionally convoluted with the effects of Fe accumulation in the sample.[25,28] The Raman feature observed in this work at 453 cm^{-1} is consistent with that of lattice vibrations of β-$Ni(OH)_2$ (445-449 cm^{-1})[6,8,39,40] or α-$Ni(OH)_2$ (460-465 cm^{-1}),[8,39] and thus could indicate the presence of either phase. The feature seen at 490 cm^{-1}, also observed at low potentials, has

previously been assigned to a Ni-O vibration present in defective or disordered $Ni(OH)_2$.[8,24,41,42] Commercially available, crystalline β-$Ni(OH)_2$ is isostructural to brucite, whereas α-$Ni(OH)_2$ is described as planes of β-$Ni(OH)_2$ intercalated with water.[39,43,44] However, additional structural variations can occur due to hydration and structural defects.[43,44]

The γ-NiOOH and β-NiOOH phases are also structurally similar, with the larger sheet spacing between the γ-NiOOH layers being the primary difference between these phases. The Raman features at 476-477 cm^{-1} and 555-560 cm^{-1}, present at higher potentials, are ascribed to Ni-O vibrations of NiOOH; both the γ- and β-NiOOH phases are reported to exhibit Raman features at these wavenumbers.[6,8,25,39]

Raman spectra of α-$Ni(OH)_2$ are expected to be similar to those of β-$Ni(OH)_2$, since there is only an increase in c-axis of the unit cell (due to a larger inter-sheet spacing) and no major change in crystal symmetry.[39] Within mixed phase samples, the overlap of Raman features at low wavenumbers creates further difficulty in distinguishing these phases.[44] Since the low-frequency modes of α- and β-$Ni(OH)_2$ are difficult to differentiate, features observed in the O-H stretching region (3000-3800 cm^{-1}) provide an additional basis for discrimination between α- and β-$Ni(OH)_2$. The characteristic O-H stretch for β-$Ni(OH)_2$ is expected at 3581 cm^{-1},[8,24,44] while that for α-$Ni(OH)_2$ is reported at ~3660 cm^{-1}.[8,44] The broad features observed at 3000-3600 cm^{-1} are characteristic of water.8

The results presented above demonstrate that $Ni(OH)_2$ does indeed undergo structural transformation upon aging in Fe-free KOH. As-deposited $Ni(OH)_2$ is present as α-$Ni(OH)_2$, as evidenced by the Raman stretching mode ν(O-H), observed at 3665 cm^{-1} at 0.2 V. Further evidence for the presence of α-$Ni(OH)_2$ prior to aging is given by the change in sample mass, measured by QCM, before and after oxidation (Fig. 3.10a). For the day 0 sample, the α-$Ni(OH)_2$ to γ-NiOOH conversion results in a 152 ng cm^{-2} increase in mass due to ion intercalation upon oxidation.

After a day or more of aging, the presence of the 3581 cm^{-1} Raman peak is characteristic of a β-$Ni(OH)_2$ phase. We note that the 3581 cm^{-1} feature is much weaker than that recorded for crystalline β-$Ni(OH)_2$,[8,24] indicating structural disorder within this phase. The transformation of α-$Ni(OH)_2$ to β-$Ni(OH)_2$ is also observed in QCM measurements: after six days of aging, a 125 ng cm^{-2} mass *decrease* with oxidation occurs, a mass loss generally attributed to proton extraction from β-$Ni(OH)_2$ to form β-NiOOH.[27,38,45] Previous investigations have also confirmed the QCM mass change (mass increase for α/γ vs. mass decrease for β/β with oxidation) tracks with the structural transformation of α-$Ni(OH)_2$ to β-$Ni(OH)_2$, observed via X-ray diffraction.[45]

The aging phase transformation in Fe-free KOH is also accompanied by several changes in the voltammograms presented in Fig. 3.2a. Since minimal change occurs in the NiOOH $\rightarrow$ $Ni(OH)_2$ reduction peak position, consistent with previous reports,[46] we focus our discussion on the oxidation features. With increasing days of aging, the 0.43 V oxidation wave shifts anodically and decreases in intensity; this wave is attributed to the oxidation of α-$Ni(OH)_2$ to γ-NiOOH. After aging, an additional oxidation wave appears at ~0.47 V, which is primarily attributed to the oxidation of β-$Ni(OH)_2$ to β-NiOOH. This shift is similar to that reported previously for aging of $Ni(OH)_2$ films in Fe-free KOH and is in line with the Bode model, which reports that $\alpha\rightarrow\gamma$ conversion should occur at a lower potential than $\beta\rightarrow\beta$ conversion.[5,28,30] However, these phases are structurally disordered and intermediate phases between α/γ and β/β could exist, which could produce additional main oxidation wave contributions, such as that observed for day 1 in Fe-free electrolyte. We note that in Fig. 3.2a, potentials in excess of the "overcharging" potential (~0.75 V) are scanned, producing a mixture of the α/γ and β/β phases even after six days of aging.

However, only one primary oxidation wave is apparent after six days of aging due to α-$Ni(OH)_2$ oxidation to γ-NiOOH overlapping with β-$Ni(OH)_2$ oxidation to β-NiOOH (further discussion in SI 11). It appears that the formation of β/β impedes the oxidation of α/γ, resulting in the anodic shift of α-$Ni(OH)_2$ to γ-NiOOH oxidation and the merging of these two previously distinct oxidation waves.

For samples maintained below 0.7 V during six days of aging in 1 M Fe-free KOH, "overcharging" of NiOOH to 0.85 V produces clear changes in the voltammograms: the main oxidation wave shifts to lower potentials, and two additional oxidation features become apparent over the roughened Au Raman electrode, which has a 2-2.5 times thinner film of $Ni(OH)_2$ compared to the QCM samples (Fig. 3.9 vs. Fig. 3.10 and SI Fig. S3.11.1). The 30 mV cathodic shift of the main oxidation wave after overcharging in Fig. 3.9 contrasts with the 30-60 mV anodic shift of the main oxidation waves observed after aging in Fig. 3.8a, suggesting that overcharging reverses the effects of aging (i.e. overcharging converts β/β back to α/γ). The smaller 0.60/0.66 V oxidation feature observed in 0.1 M KOH/1 M KOH is present on day 0 (Fig. 3.2a) as well as after overcharging (Fig. 3.9); this smaller wave accompanies the main, as-deposited oxidation wave. We thus propose that this oxidation feature is related to the γ-NiOOH phase, perhaps as the formation of some higher oxidation state Ni^{IV}. Meanwhile, the 0.7/0.76 V oxidation peak is strongest on the initial overcharge cycle and corresponds with a QCM mass increase (Supporting Information S3.12); we therefore attribute it to the overcharge conversion of β-NiOOH to γ-NiOOH. This oxidation current could be due to an increase of the average Ni oxidation state; the average oxidation state of Ni in γ-NiOOH is reported to be 3.3-3.7, whereas the average oxidation state of Ni within β-NiOOH is estimated to be 2.7-3.0.[5,7,34,47]

Since the frequency of a vibrational mode is proportional to bond strength, a decrease in the average nickel oxidation state after aging γ-NiOOH to β-NiOOH is expected to decrease the band frequency.6 This is consistent with a slight shift in the NiOOH features after aging to lower wavenumbers (477 to 476 cm^{-1} and 560 to 558 cm^{-1}). However, Raman peak intensities are expected to be more sensitive than the peak frequencies; relative peak intensities can vary based on local structural disorder, hydrogen and vacancy content, and nickel oxidation state.8 Previous investigations have found that the 480 cm^{-1}/560 cm^{-1} Raman peak height ratio is significantly lower for β-NiOOH than for γ-NiOOH.8,25

We investigated the Raman peak ratio as a function of applied potential before and after six days of aging in the absence (and presence, to be discussed in the following section) of Fe electrolyte impurities (Supporting Information S3.9.4); the results are summarized in Table 3.1. In Fe-free KOH, this ratio is initially ~1.4 after the onset of NiOOH formation at 0.47 V and stabilizes to 1.55 after the $Ni(OH)_2$ oxidation wave (above 0.52 V). Films aged for six days in Fe-free electrolyte follow the same trend with an overall lower ratio, 1.25 increasing to 1.42 with further oxidation (above 0.54 V). The lower peak ratio after aging is evidence for conversion of the film from α/γ to β/β with aging.

Table 3.1: NiOOH 480 cm^{-1}/560 cm^{-1} Raman peak height ratio at 0.6 V in 0.1 M KOH

	Day 0	Day 6 (after aging)	Day 6 (after overcharging)
Fe-free KOH	1.55	1.42	1.48
Unpurified KOH	1.55	1.28	**

** Due to extensive oxygen bubble formation with overcharging in unpurified electrolyte, subsequent Raman acquisitions "after overcharging" were not completed.

The ratio of these Raman peak intensities was also calculated after the overcharging cycle to 0.85 V for the aged sample. The 480/560 cm^{-1} ratio increased from 1.42 for the aged sample to 1.48 after the overcharging sweep to 0.85 V, suggesting that a more γ-like NiOOH structure is formed after overcharging (though this increased ratio is still less than the 1.55 ratio observed on day 0). This intermediate peak-height ratio of 1.48 indicates that after overcharging, a mixture of γ- and β-NiOOH is present under OER conditions, i.e. that the film does not return *completely* to its original, as-deposited α/γ state with the peak ratio of 1.55. The appearance of two main oxidation waves in the voltammograms after overcharging (Fig. 3.9) also supports that both α- and β-$Ni(OH)_2$ phases are present and oxidize to their respective γ- and β-NiOOH phases, while in the cycles before overcharging, the β-$Ni(OH)_2$ phase is predominantly present and oxidizes to β-NiOOH. The QCM frequency change at the primary oxidation wave after overcharging (Fig. 3.10a) is between that of the day 0 and day 6 oxidation waves (Fig. 3.8a), further confirming that a mixture of the γ-NiOOH and β-NiOOH phases exists after overcharging.

After overcharging, some amount of α-$Ni(OH)_2$/γ-NiOOH reconverts (i.e. ages) to β-$Ni(OH)_2$/β-NiOOH on the timescale of minutes if maintained below 0.7 V. This conversion is clearly observable within slow, 1 mV s^{-1} voltammograms completed with concurrent Raman acquisitions (~20 min/cycle, Fig. S3.11.1 SI) but not during the faster, 10 mV s^{-1} CVs (~2 min/cycle) shown in Figure 3.9. The occurrence of the small oxidation wave at 0.7 V in the RDE voltammograms after aging (Fig. 3.2a) is further evidence that a small amount of β-NiOOH is reconverted to γ-NiOOH with each anodic potential scan.

In summation, despite previous reports examining $Ni(OH)_2$/NiOOH phase changes using electrolytes containing Fe impurities, structural changes observed after aging and overcharging in Fe-free electrolyte closely align with the commonly accepted structural transformation scheme previously detailed by Bode.[28] The work here represents the first time that detailed structural information in the Ni-(oxy)hydroxides has been examined under rigorously Fe-free conditions and definitively shows that structural transformations between the α/γ and β/β couples are inherent to the Ni-(oxy)hydroxides themselves and not simply a byproduct of Fe-impurity incorporation.

3.4.2 $Ni(OH)_2$/NiOOH structural changes with aging and overcharging in unpurified KOH

Aging of $Ni(OH)_2$ in unpurified (Fe-containing) KOH produces electrochemical and structural changes distinct from those observed after aging in Fe-free KOH, though the overall film is found to maintain a $Ni(OH)_2$/NiOOH-type structure. This conclusion is consistent with the work of Friebel et al., which showed that codeposited Ni-Fe films containing <25% Fe content were also structurally characteristic of $Ni(OH)_2$/NiOOH.[29] For $Ni(OH)_2$ films aged in unpurified electrolyte, the development of a second main oxidation feature is not as clearly defined, but an even greater shift (70 mV vs. 40 mV in Fe-free KOH) in the primary oxidation/reduction waves is

observed (Fig. 3.2b). This shift is primarily due to the incorporation of Fe-impurities; Fe addition is well-known to shift the main oxidation/reduction waves to more anodic potentials.[10-12,18,24]

After extended exposure to Fe impurities, additional changes are observed in the $Ni(OH)_2$/NiOOH structure. While some amount of β-NiOOH is formed after aging in unpurified electrolyte, it is clearly less than the amount formed in Fe-free electrolyte. This difference can be seen in both the 50 ng cm^{-2} QCM mass decrease with oxidation (Fig. 3.8) (which is less than the ~110 ng cm^{-2} decrease observed in films aged in Fe-free electrolyte), as well as a less intense 3580 cm^{-1} Raman feature (Fig. 3.7) after aging in unpurified KOH.

Additional Raman spectra differences indicate further NiOOH structural changes unique to the incorporation of Fe impurities. The ratio of 480/560 cm^{-1} Raman peak intensities in unpurified electrolyte is initially (day 0) comparable to that observed without Fe impurities (initially 1.3 at 0.45 V, stabilizing at 1.55 above 0.52 V), but after six days of aging, a distinct difference is observed. The ratio, 1.33 with initial NiOOH formation at ~0.5 V, further decreases with the Ni(II)/Ni(III) oxidation wave, reaching 1.28 at 0.6 V.

A greater reduction in the 480/560 cm^{-1} Raman peak height ratio, as well as a broadening of these features, is observed for $Ni(OH)_2$ films aged in unpurified electrolyte compared to those aged in Fe-free KOH (Table 3.1 and SI Fig. S3.9.1). These differences cannot be solely due to greater β-NiOOH formation in the unpurified electrolyte, since as previously noted, QCM results show that less β-NiOOH is formed in the presence of Fe impurities. Additionally, various iron phases, including α-FeOOH and Fe_3O_4, are expected to have other Raman-active modes below 800 cm^{-1}, [48] which are not observed in our current study. Therefore, this change in Raman peak height ratio with aging in the presence of Fe impurities must be the result of Fe incorporation. X-ray diffraction studies have shown that $Ni(OH)_2$ co-deposited with 25% Fe can generate a Ni-Fe layered-double-hydroxide (NiFe-LDH) structure.[30] Previous Raman studies also evidenced broader 480 cm^{-1} and 560 cm^{-1} intensities, as well as a lower 480/560 ratio, for an oxidized NiFe-LDH compared to pure NiOOH.[49] Therefore, we attribute the further decrease of the 480/560 cm^{-1} ratio after aging in unpurified KOH to the formation of NiFe-LDH, which is produced by substitution of Fe-impurities into the $Ni(OH)_2$/NiOOH lattice.

In unpurified KOH, the formation of the NiFe-LDH phase is also in line with the overcharging differences observed between Fe-free vs. unpurified KOH samples. The minimal mass change observed before and after overcharge in unpurified KOH (Fig. 3.10b) is a result of less β-$Ni(OH)_2$ formation due to the presence of the NiFe-LDH, indicating that the NiFe-LDH phase inhibits the conversion of α/γ to β/β. This inhibition of conversion to the β-$Ni(OH)_2$/β-NiOOH phase with aging was also recently observed for co-deposited NiFe-LDH.[30]

Fig. 3.11 illustrates how the current density and normalized intensity of the Raman band at 560 cm^{-1} (an indicator of NiOOH formation) change with applied potential. The oxidation wave is comparable for both Fe-free and unpurified electrolyte on day 0, but the transformation of $Ni(OH)_2$ to NiOOH, as observed by the formation of the 560 cm^{-1} band, exhibits a sharper onset when oxidation occurs in Fe-free electrolyte.

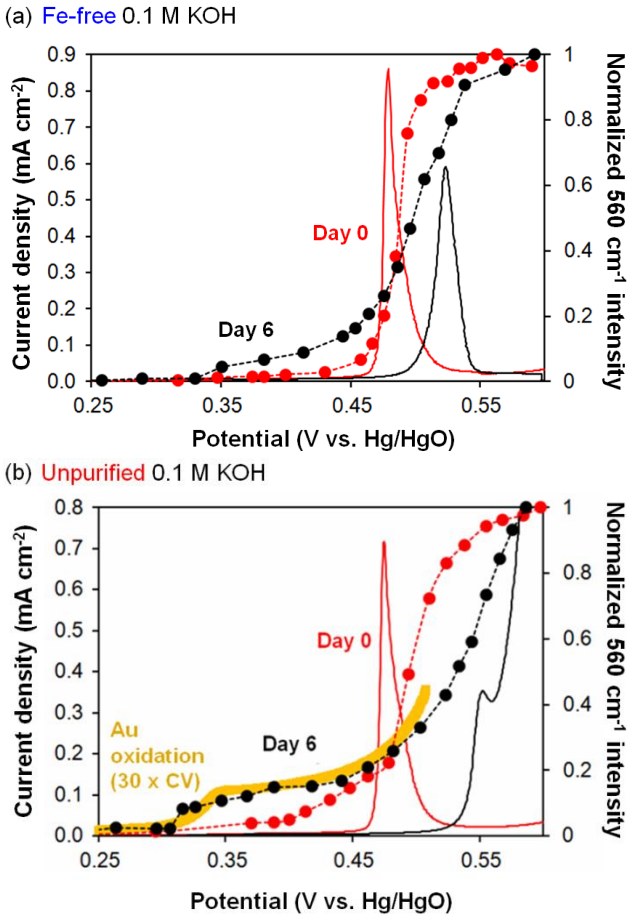

Figure 3.11. Normalized 560 cm^{-1} Raman intensity (an indicator of NiOOH formation) and concurrent 1 mV s^{-1} linear potential scans for $Ni(OH)_2$ films deposited on roughened Au in (a) Fe-free and (b) unpurified 0.1 M KOH before (red) and after (black) aging in 1 M KOH. The Au oxidation voltammogram wave is shown 30× for reference in (b). Oxygen evolution equilibrium potential is 0.365 V vs. Hg/HgO in 0.1 M KOH.

After aging for six days in unpurified KOH, the $Ni(OH)_2$/NiOOH oxidation wave shifts to significantly higher potentials compared to what is observed in Fe-free electrolyte. However, for both purified and unpurified electrolyte, NiOOH begins to form at potentials 0.1-0.2 V below the onset of the electrochemical Ni(II)/Ni(III) oxidation wave (~0.35 V). This initial NiOOH formation tracks with the onset of Au oxidation (shown for the sample in unpurified KOH in Fig. 3.11b). Although Au oxide has a broad feature at 570 cm^{-1},[33] the parallel emergence of the feature at 480 cm^{-1} confirms assignment of this mode to NiOOH. It has been shown that both the Au substrate and co-deposited Fe can exert charge-transfer effects to partially oxidize $Ni(OH)_2$.[25,30] After aging, stronger charge-transfer effects could result from the formation of a Au-Ni surface alloy. Such an alloy has been shown to form at room temperatures, and evidence for a mixed Au/Ni oxide or hydroxide has also been observed for thin Ni films (<5 monolayers) electrodeposited over Au.[25,50,51] Therefore, we propose a small amount of a NiOOH-type structure is formed with the onset of bulk Au oxidation after aging due to intermixing of Ni and Au at the substrate interface. We note, however, that this interfacial NiOOH likely produces disproportionately strong Raman intensities at 480/560 cm^{-1} due to strong surface-enhancement effects for the few monolayers of $Ni(OH)_2$/NiOOH closest to the Au substrate.

In summary, aging $Ni(OH)_2$ films in the presence of Fe impurities produces structural changes distinct from those changes which occur in Fe-free electrolyte. In contrast to films aged in Fe-free KOH, the primary structural change after aging in the presence of Fe impurities is the incorporation of Fe within the Ni-(oxy)hydroxide structure to produce a NiFe-LDH. This phase is found to inhibit the aging formation of β-$Ni(OH)_2$/β-NiOOH, as well as the overcharging conversion of β-NiOOH to γ-NiOOH, both of which are significant deviations from the Bode scheme.

3.4.3 Effect of NiOOH structure and Fe incorporation on OER activity

We next relate the OER activities of Ni-(oxy)hydroxide films to the corresponding structural changes observed before and after aging in the absence and presence of iron impurities in KOH electrolyte. The as-deposited γ-NiOOH free of Fe contamination is not very active for the OER, exhibiting an overpotential of 525 mV at 10 mA cm^{-2} (1 M KOH). As more β-NiOOH is formed, the overpotential rises to 620 mV. Furthermore, the Tafel slope for the OER is lower for the as-prepared samples (105 mV dec^{-1}) than for the aged samples (135 mV dec^{-1}). For all samples cycled in Fe-free electrolyte, both the γ-NiOOH and β-NiOOH phases exhibit extremely poor oxygen evolution activity, and the aged films (with more β-NiOOH) appear to be worse OER catalysts. However, it must be noted that this potential (0.926 V vs Hg/HgO) is well above the 0.7 V vs. Hg/HgO overcharging potential, so some amount of γ-NiOOH will be present (in addition to β-NiOOH) under OER conditions in Fe-free electrolyte. Therefore we cannot say definitively that *pure* β-NiOOH displays lower OER activity than pure γ-NiOOH.

Consistent with previous findings, Fe impurities present at < 1 ppm in the KOH electrolyte spontaneously incorporate into $Ni(OH)_2$/NiOOH films and significantly enhance the OER activity.[30] Maximum oxygen evolution activity occurs at approximately 12-17% Fe content (Fig. 3.5), attained after five days of aging. It is notable that the maximum activity achieved as a result of aging is comparable to that reported after intentional Fe addition to Ni-(oxy)hydroxide (j = 20 mA cm^{-2} at η = 300 mV and η = 280 mV at j = 10 mA cm^{-2} at 40 at % Fe).[24]

While the overpotential at j = 10 mA cm^{-2} does not exhibit improvement above Fe contents of 17%, Fe incorporates in excess of 25% after extended aging in unpurified 1 M KOH, as determined from elemental analysis (Fig. 3.3). Additionally, comparable Fe film contents calculated from both XPS (surface) and ICP (bulk) techniques show that Fe incorporates throughout the entire $Ni(OH)_2$ film, in agreement with previous work by Corrigan,[10] as well as Trotochaud et al. [30]

X-ray absorption spectroscopy (XAS) studies by Friebel et al. have shown that for mixed Ni-Fe oxyhydroxides, it is Fe^{3+} incorporated into a γ-NiOOH-like structure that displays enhanced OER activity.[29] The authors suggest that this high activity arises due to the bond contraction of Fe-O, measured to be 7% shorter than in γ-FeOOH, which occurs after the host $Ni(OH)_2$ oxidizes to NiOOH. Density-functional theory calculations confirm that Fe sites present within the NiOOH structure exhibit more optimal adsorption energies of proposed OER intermediates (OH, O, OOH), thereby reducing the required overpotential for this reaction.

Figure 3.12 plots turnover frequency (TOF, at η = 300 mV) on a per-Fe-site basis vs. Fe content. Iron sites were calculated as the total number of Fe atoms detected from ICP. The TOF is lower (~3 s^{-1}) for low Fe content, maximizes at 3-4 days of aging (~11% Fe content, close to the 12% Fe estimated from XPS for maximum activity), and then decreases with continued aging. The lower TOF after initial cycling and aging could be due to the Fe atoms 1) not initially incorporating within the NiOOH structure, 2) first incorporating within the NiOOH structure at locations that

are less OER-active, 3) existing at too low of a concentration within the NiOOH lattice to be optimally active (e.g. a minimum density of neighboring Fe sites could produce higher activity), and/or 4) incorporating into differing Ni structures with aging due to the concurrent partial transformation of α-$Ni(OH)_2$/γ-NiOOH to β-$Ni(OH)_2$/β-NiOOH.

The TOF decrease after exceeding 11% Fe content could be due to the NiOOH phase reaching critical saturation and the formation of a separate, inactive Fe-rich phase. The dashed line in Fig. 3.12 estimates the TOF assuming the formation of such an inactive phase, where any additional Fe sites added (past 11% Fe) are not OER-active (for calculation, see Supporting Information). These anticipated values closely track calculated TOFs at Fe = 11-28% and support that Fe present within the NiOOH structure are the active sites for the OER, and at higher Fe content, Fe incorporates into less OER-active Fe-rich phases.

Consistent with this hypothesis, Friebel et al.[29] observe direct XAS evidence that a separate, Fe-rich phase forms within Ni-Fe catalyst films at higher Fe contents (>25%), and OER activity decreases as this less active phase predominates. We note that differences between this "Fe saturation limit" estimated in the current work (11% Fe) vs. that of Friebel et al. (25% Fe) could be due to differences in sample preparation or aging. In contrast to our current study of Fe-impurity uptake within $Ni(OH)_2$/NiOOH films, Friebel et al. investigated co-deposited Ni-Fe films. It is also possible that in the previous study, a Fe-rich phase formed at Fe contents below 25% but remained below detection limits of XAS. In the present study, we do not observe direct structural evidence for a separate, Fe-rich phase after six days of aging, which is not incongruous with a disordered Fe phase exhibiting limited long-range order.

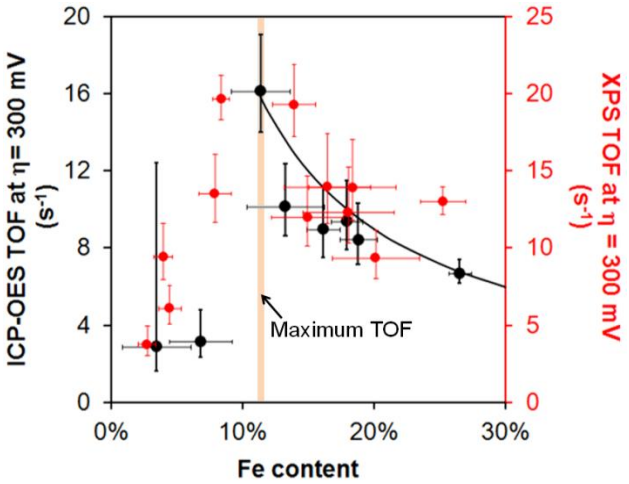

Figure 3.12. Turnover frequency (calculated on a per-Fe site basis) from total Fe content (ICP-OES: black, XPS: red) for $Ni(OH)_2$ films deposited on polished Au-RDEs as a function of Fe content. Solid line represents anticipated TOF assuming Fe content exceeding 11% is not OER-active. Error bars indicate the inherent uncertainty in the Fe content as determined by ICP-OES and XPS for each sample. See S13 for a complete discussion of error calculation.

3.5. Conclusions

Electrochemical characterization, in situ Raman spectroscopy, and quartz crystal microbalance measurements were used to differentiate the effects of structural changes vs Fe incorporation after aging $Ni(OH)_2$/NiOOH films in KOH. Ni hydroxide films aged in unpurified electrolyte incorporate > 20% Fe after 5 weeks of aging in 1 M unpurified, reagent-grade KOH. In addition, samples aged in unpurified electrolyte exhibit a much higher activity and lower overpotential, as well as a significantly lower Tafel slope, compared with samples aged in Fe-free KOH. Optimum catalyst activity, observed after 5 days of aging in unpurified 1 M KOH, is comparable to optimized activities reported for NiOOH catalysts with intentional Fe addition. Conversely, Fe-free films exhibit very poor activity, which further decreases with aging. $Ni(OH)_2$ aged in Fe-free electrolyte is mostly characteristic of disordered β-$Ni(OH)_2$. In line with the Bode scheme, overcharging occurs above 0.7 V in 1 M Fe-free KOH (0.76 V in 0.1 M KOH), coinciding with a large, secondary oxidation wave. After cycling to 0.85 V, β-NiOOH reconverts to γ-NiOOH in Fe-free electrolyte. In contrast, films aged in unpurified KOH evidence less phase transformation after aging and overcharging but do incorporate Fe impurities to form a NiFe-layered double (oxy)hydroxide structure. Turnover frequency comparisons, calculated on a per-Fe site basis, support that Fe within the NiOOH structure is the OER active site, and for Fe contents exceeding ∼11%, a separate, Fe-rich phase begins to form. These findings further elucidate the effects of Fe impurity incorporation on the Ni-(oxy)hydroxide catalyst structure and OER activity, which is critical for high OER activity over these materials.

References

1. Cook, T. R.; Dogutan, D. K.; Reece, S. Y.; Surendranath, Y.; Teets, T. S.; Nocera, D. G. Solar Energy Supply and Storage for the Legacy and Non Legacy Worlds. *Chem. Rev.* **2010**, *110*, 6474-6502.
2. Walter, M. G.; Warren, E. L.; McKone, J. R.; Boettcher, S. W.; Mi, Q.; Santori, E. A.; Lewis, N. S. Solar Water Splitting Cells. *Chem. Rev.* **2010**, *110*, 6446-6473.
3. Suntivich, J.; May, K. J.; Gasteiger, H. A.; Goodenough, J. B.; Shao-Horn, Y. A Perovskite Oxide Optimized for Oxygen Evolution Catalysis from Molecular Orbital Principles. *Science* **2011**, *334*, 1383-1385.
4. Hall, D. E. Ni(OH)2-Impregnated Anodes for Alkaline Water Electrolysis. *J. Electrochem. Soc*. **1983**, *130*, 317-321.
5. Lyons, M. E. G.; Brandon, M. P. The Oxygen Evolution Reaction on Passive Oxide Covered Transition Metal Electrodes in Aqueous Alkaline Solution. Part 1-Nickel. *Int. J. Electrochem. Soc*. **2008**, *3*, 1386-1424.
6. Cornilsen, B. C.; Karjala, P. J.; Loyselle, P. L. Structural Models for Nickel Electrode Active Mass. *J. Power Sources* **1988**, *22*, 351-357.
7. Desilvestro, J.; Corrigan, D. A.; Weaver, M. J. Characterization of Redox States of Nickel-Hydroxide Film Electrodes by In Situ Surface Raman-Spectroscopy. *J. Electrochem. Soc.* **1988**, *135*, 885-892.
8. Kostecki, R.; McLarnon, F. Electrochemical and In Situ Raman Spectroscopic Characterization of Nickel Hydroxide Electrodes. *J. Electrochem. Soc.* **1997**, *144*, 485-493.
9. Bediako, D. K.; Lassalle-Kaiser, B.; Surendranath, Y.; Yano, J.; Yachandra, V. K.; Nocera, D. G. Structure-Activity Correlations in a Nickel-Borate Oxygen Evolution Catalyst. *J. Am. Chem. Soc.* **2012**, *134*, 6801-6809.

10. Corrigan, D. A. The Catalysis of the Oxygen Evolution Reaction by Iron Impurities in Thin-Film Nickel-Oxide Electrodes. *J. Electrochem. Soc*. **1987**, *134*, 377-384.
11. Li, X. H.; Walsh, F. C.; Pletcher, D. Nickel Based Electrocatalysts for Oxygen Evolution in High Current Density, Alkaline Water Electrolysers. *Phys. Chem. Chem. Phys*. **2011**, *13*, 1162-1167.
12. Singh, R. N.; Pandey, J. P.; Anitha, K. L. Preparation of Electrodeposited Thin-Films of Nickel Iron-Alloys on Mild-Steel for Alkaline Water Electrolysis. 1. Studies on Oxygen Evolution. *Int. J. Hydrogen Energy* **1993**, *18*, 467-473.
13. Trotochaud, L.; Ranney, J. K.; Williams, K. N.; Boettcher, S. W. Solution-Cast Metal Oxide Thin Film Electrocatalysts for Oxygen Evolution. *J. Am. Chem. Soc.* **2012**, *134*, 17253-17261.
14. Gong, M.; Li, Y.; Wang, H.; Liang, Y.; Wu, J. Z.; Zhou, J.; Wang, J.; Regier, T.; Wei, F.; Dai, H. An Advanced Ni-Fe Layered Double Hydroxide Electrocatalyst for Water Oxidation. *J. Am. Chem. Soc.* **2013**, *135*, 8452-8455.
15. McCrory, C. C. L.; Jung, S. H.; Peters, J. C.; Jaramillo, T. F. Benchmarking Heterogeneous Electrocatalysts for the Oxygen Evolution Reaction. *J. Am. Chem. Soc.* **2013**, 135, 16977-16987.
16. Landon, J.; Demeter, E.; Inoglu, N.; Keturakis, C.; Wachs, I. E.; Vasic, R.; Frenkel, A. I.; Kitchin, J. R. Spectroscopic Characterization of Mixed Fe-Ni Oxide Electrocatalysts for the Oxygen Evolution Reaction in Alkaline Electrolytes. *ACS Catal.* **2012**, *2*, 1793-1801.
17. Miller, E. L.; Rocheleau, R. E. Electrochemical Behavior of Reactively Sputtered Iron-Doped Nickel Oxide. *J. Electrochem. Soc.* **1997**, *144*, 3072-3077.
18. Hu, C. C.; Wu, Y. R. Bipolar Performance of the Electroplated Iron-Nickel Deposits for Water Electrolysis. *Mater. Chem. Phys.* **2003**, *82*, 588-596.
19. Smith, R. D. L.; Prevot, M. S.; Fagan, R. D.; Zhang, Z. P.; Sedach, P. A.; Siu, M. K. J.; Trudel, S.; Berlinguette, C. P. Photochemical Route for Accessing Amorphous Metal Oxide Materials for Water Oxidation Catalysis. *Science* **2013**, *340*, 60-63.
20. Smith, R. D. L.; Prévot, M. S.; Fagan, R. D.; Trudel, S.; Berlinguette, C. P. Water Oxidation Catalysis: Electrocatalytic Response to Metal Stoichiometry in Amorphous Metal Oxide Films Containing Iron, Cobalt, and Nickel. *J. Am. Chem. Soc.* **2013**, *135*, 11580-11586.
21. Merrill, M. D.; Dougherty, R. C. Metal Oxide Catalysts for the Evolution of O2 from H2O. *J. Phys. Chem. C* **2008**, *112*, 3655-3666.
22. Cappadonia, M.; Divisek, J.; Vonderheyden, T.; Stimming, U. Oxygen Evolution at Nickel Anodes in Concentrated Alkaline-Solution. *Electrochim. Acta* **1994**, *39*, 1559-1564
23. Lu, P. W. T.; Srinivasan, S. Electrochemical-Ellipsometric Studies of Oxide Film Formed on Nickel during Oxygen Evolution. *J. Electrochem. Soc*. **1978**, *125*, 1416-1422.
24. Louie, M. W.; Bell, A. T. An Investigation of Thin-Film Ni-Fe Oxide Catalysts for the Electrochemical Evolution of Oxygen. *J. Am. Chem. Soc.* **2013**, *135*, 12329-12337.
25. Yeo, B. S.; Bell, A. T. In Situ Raman Study of Nickel Oxide and Gold-Supported Nickel Oxide Catalysts for the Electrochemical Evolution of Oxygen. *J. Phys. Chem. C* **2012**, *116*, 8394-8400.
26. Godwin, I. J.; Lyons, M. E. G. Enhanced Oxygen Evolution at Hydrous Nickel Oxide Electrodes via Electrochemical Ageing in Alkaline Solution. *Electrochem. Commun.* **2013**, *32*, 39-42.

27. Wehrens-Dijksma, M.; Notten, P. H. L. Electrochemical Quartz Microbalance Characterization of Ni(OH)(2)-Based Thin Film Electrodes. *Electrochim. Acta* **2006**, *51*, 3609-3621.
28. Bode, H.; Dehmelt, K.; Witte, J. Zur Kenntnis der Nickelhydroxidelektrode—I.Über Das Nickel (II)-Hydroxidhydrat. *Electrochim. Acta* **1966**, *11*, 1079-1087.
29. Friebel, D.; Louie, M.W.; Bajdich, M.; Sanwald, K.E.; Cai, Y.; Wise, A.M; Cheng, M.J.; Sokaras, D.; Weng, T.C.; Alonso-Mori, R.; Davis, R.C.; Bargar, J.R.; Norskov, J.K.; Nilsson, A.; Bell, A.T. Identification of Highly Active Fe Sites in (Ni,Fe)OOH for Electrocatalytic Water Splitting. *J. Am. Chem. Soc.* **2015**,*137*, 1305-1313.
30. Trotochaud, L.; Young, S. L.; Ranney, J. K.; Boettcher, S.W. Nickel-Iron Oxyhydroxide Oxygen-Evolution Electrocatalysts: The Role of Intentional and Incidental Iron Incorporation. *J. Am. Chem. Soc.* **2014**, *136*, 6744-6753.
31. Gao, P.; Gosztola, D.; Leung, L. W. H.; Weaver, M. J. J. Surface-Enhanced Raman-Scattering at Gold Electrodes - Dependence on Electrochemical Pretreatment Conditions and Comparisons with Silver. *Electroanal. Chem.* **1987**, *233*, 211-222.
32. Sauerbrey, G. Z. Verwendung Von Schwingquarzen Zur Wagung Dunner Schichten Und Zur Mikrowagung. *Zeitschrift Fur Physik* **1959**, *155*, 206-222.
33. Yeo, B. S.; Klaus, S. L.; Ross, P. N.; Mathies, R. A.; Bell, A. T. Identification of Hydroperoxy Species as Reaction Intermediates in the Electrochemical Evolution of Oxygen on Gold. *ChemPhysChem* **2010**, *11*, 1854-1857.
34. Oliva, P.; Leonardi, J.; Laurent, J. F.; Delmas, C.; Braconnier, J. J.; Figlarz, M.; Fievet, F.; Deguibert, A. Review of the Structure and the Electrochemistry of Nickel Hydroxides and Oxy-Hydroxides. *J. Power Sources* **1982**, *8*, 229-255.
35. Plyasunova, N. V.; Zhang, Y.; Muhammed, M., Critical Evaluation of Thermodynamics of Complex Formation of Metal Ions in Aqueous Solutions. IV. Hydrolysis and hydroxo-complexes of Ni2+ at 298.15 K. *Hydrometallurgy* 1998, *41*, 43-63.
36. Lyons, M. E. G.; Brandon, M. P. A Comparative Study of the Oxygen Evolution Reaction on Oxidised Nickel, Cobalt and Iron Electrodes in Base. *J. Electroanal. Chem.* **2010**, *641*, 119-130.
37. Dechialvo, M. R. G.; Chialvo, A. C. Oxygen Evolution Reaction on Thick Hydrous Nickel-Oxide Electrodes. *Electrochim. Acta* **1988**, *33*, 825-830
38. Lee, J.W.; Han, J.H.; Seo, M.; Pyun, S. Transport of alkaline cation and neutral species through the alpha-Ni(OH)(2)/gamma-NiOOH film electrode. *J. Solid State Electrochem.* **2001**, *5*, 459-465.
39. Johnston, C.; Graves, P. R. In Situ Raman-Spectroscopy Study of the Nickel Oxyhydroxide Electrode (NOE) System. *Appl. Spectrosc.* **1990**, *44*, 105-115.
40. Bantignies, J. L.; Deabate, S.; Righi, A.; Rols, S.; Hermet, P.; Sauvajol, J. L.; Henn, F. New Insight into the Vibrational Behavior of Nickel Hydroxide and Oxyhydroxide Using Inelastic Neutron Scattering, Far/Mid-Infrared, and Raman Spectroscopies. *J. Phys. Chem. C* **2008**, *112*, 2193-2201.
41. de Torresi, S. I. C.; Provazi, K.; Malta, M.; Torresi, R. M. Effect of Additives in the Stabilization of the Alpha Phase of Ni(OH)2 Electrodes. *J. Electrochem. Soc.* **2001**, *148*, A1179-A1184.
42. Vidotti, M.; Salvador, R. P.; de Torresi, S. I. C. Synthesis and Characterization of Stable Co and Cd Doped Nickel Hydroxide Nanoparticles for Electrochemical Applications. *Ultrason. Sonochem.* **2009**, *16*, 35-40.

43. Hall, D. S.; Lockwood, D. J.; Poirier, S.; Bock, C.; MacDougall, B. R., Raman and Infrared Spectroscopy of a and Beta Phases of Thin Nickel Hydroxide Films Electrochemically Formed on Nickel. *J Phys Chem A* **2012**, *116*, 6771-6784.
44. Hall, D.S.; Lockwood, D.J.; Poirier, S.; Bock, C.; MacDougall, B.R. Applications of In Situ Raman Spectroscopy for Identifying Nickel Hydroxide Materials and Surface Layers during Chemical Aging. *ACS Appl. Mater. -Interfaces*, **2014**, *6*, 3141-3149.
45. Kim, M. S.; Hwang, T. S.; Kim, K. B. A Study of the Electrochemical Redox Behavior of Electrochemically Precipitated Nickel Hydroxides Using Electrochemical Quartz Crystal Microbalance. *J Electrochem Soc* **1997**, *144*, 1537-1543.
46. MacArthur, D. M., The Hydrated Nickel Hydroxide Electrode Potential Sweep Experiments. *J Electrochem Soc* **1970**, *117*, 422-426.
47. Barnard, R.; Randell, C. F.; Tye, F. L., Studies Concerning Charged Nickel-Hydroxide Electrodes .1. Measurement of Reversible Potentials. *J Appl Electrochem* **1980**, *10*, 109-125.
48. de Faria, D. L. A.; Venâncio Silva, S.; de Oliveira, M. T., Raman Microspectroscopy of Some Iron Oxides and Oxyhydroxides. *Journal of Raman Spectroscopy* **1997**, *28*, 873-878.
49. Lu, Z.; Wenwen, X.; Zhu, W.; Yang, Q.; Lei, X.; Liu, J.; Li, Y.; Sun, X.; Duan, X. Three-Dimensional NiFe Layered Double Hydroxide Film for High-Efficiency Oxygen Evolution Reaction. *Chem. Commun.* **2014**, *50*, 6479-6482.
50. Santra, A. K.; Rao, C. N. R., Surface Alloy Formation in Pd/Ag, Cu/Au and Ni/Au Bimetallic Overlayers. *Applied Surface Science* **1995**, *84*, 347-350.
51. Zafeiratos, S.; Kennou, S., Photoelectron Spectroscopy Study of Surface Alloying in the Au/Ni (S) 5(0 0 1) × (1 1 1) System. *Applied Surface Science* **2001**, *173*, 69-75.

3.6. Supporting Information

S3.1. Electrolyte purification procedure.

The procedure used is adapted from the one outlined by Trotochaud et al.[1] In a 50 mL polypropylene centrifuge tube (VWR), 2 g of nickel nitrate hexahydrate (99.999% Sigma Aldrich) was dissolved in 4 mL water (18 MΩ resistance, Milli Q Millipore), to which 20 mL of 1 M KOH (prepared from 45% Baker Analyzed Electronic Grade KOH solution, VWR JT3144-3) was added to precipitate $Ni(OH)_2$. After shaking, the mixture was centrifuged and the supernatant decanted. The $Ni(OH)_2$ precipitate was then washed three times using 20 mL of 18.2 MΩ cm water and 2 mL of 1 M KOH. For each washing step, the nickel hydroxide was redispersed in solution and then re-centrifuged for 2 min at 4000 rpm.

After the third nickel hydroxide washing step, the $Ni(OH)_2$ was used to purify up to three 45-mL aliquots of 1 M KOH. For each purification, ~45 mL of 1 M KOH (from VWR JT3144-3) was added to the centrifuge tube, and the tube was shaken until the nickel hydroxide was fully dispersed (5-10 minutes). After at least three hours of resting, the tube was centrifuged at 4000 rpm for 5 minutes and the purified KOH was directly used for aging and RDE studies or diluted to 0.1 M for Raman and QCM experiments.

S3.2. Roughening procedure of the Au electrode for Surface-enhanced Raman Spectroscopy (SERS)

The gold electrodes for SERS experiments were electrochemically roughened in 0.1 M KCl by cycling the potential between -0.28 and 1.22 V vs. Ag/AgCl (4 M KCl filling solution, Pine Instruments) with the sweep rate of 1000 and 500 mV s^{-1}, and with a 5 and 10 s dwell at -0.3 and 1.2 V, respectively. After this potential cycle was repeated 25 times, the potential was held at -0.3 V for 500 s.[2]

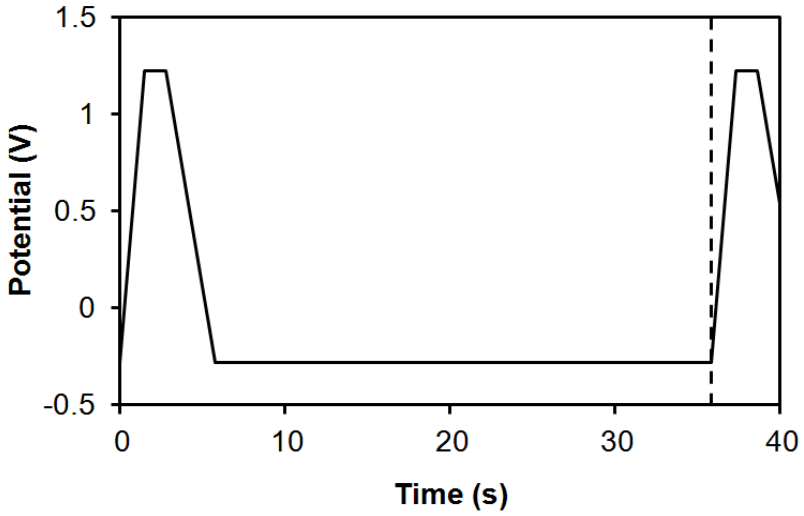

Figure S3.2.1. Applied waveform (vs. Ag/AgCl reference electrode) over polished Au electrode in 0.1 M KCl electrolyte for surface roughening.

S3.3. QCM calibration and electrodeposition thickness estimate

Quartz crystal microbalance experiments were used to estimate the deposited Ni film thickness. The Au/Ti quartz crystal was cleaned in 1 M H_2SO_4, then stabilized by electrochemical cycling in 1 M KOH prior to $Ni(OH)_2$ electrodeposition.

The resonant frequency FWHM determined by impedance analysis was unchanged before and after deposition of the $Ni(OH)_2$ film (FWHM = 49 Hz), indicating visco-elastic losses are not present. Therefore, resonant frequency changes can be directly related to film mass changes.[3]

The quartz crystal sensitivity factor C_f was measured by Faradaic deposition of silver using 0.05 M $AgNO_3$ in 0.5 M nitric acid. Resonant frequency was recorded in solution before and after a -0.2 mA current was applied for 100s over three quartz crystals; an Ag wire served as both the counter and reference electrodes. The resultant sensitivity factor, 54.5 ± 0.5 Hz μg^{-1} cm^2, is close to the 56.6 Hz μg^{-1} cm^2 value reported for 5 MHz AT-cut quartz crystals.

Film mass changes were estimated from changes in the resonant frequency using the Sauerbrey equation, $\Delta f = -C_f \times \Delta m$, where Δf is the observed frequency change (Hz), C_f is the sensitivity factor of the quartz crystal (discussed above), and Δm is the change in mass per unit area ($\mu g\ cm^{-2}$).[4]

The resulting deposition potential and frequency change over the Au quartz crystal are shown in Fig. S3.3.1. Assuming 4.1 g cm^{-3} $Ni(OH)_2$ density, as well as that the Sauerbrey equation holds (see discussion of visco-elastic losses above), the overall -722 Hz frequency change corresponds to a film thickness of 31 nm.

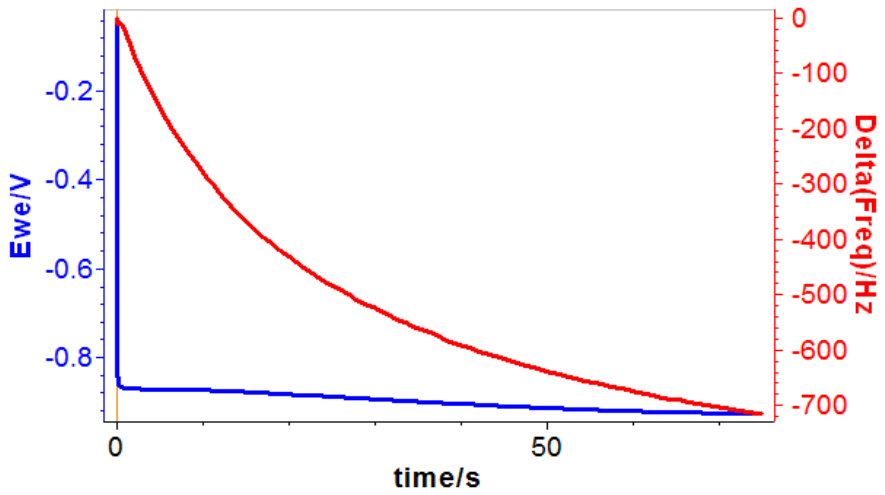

Figure S3.3.1. Potential (vs. Ag/AgCl) and frequency change profile vs. time during 1 mA cm^{-2} cathodic Ni deposition over Au/TiO_2 quartz crystal.

S3.4. XPS calculations and results

S3.4.1 Example XPS background subtraction for Ni/Fe ratio determination

To calculate surface ratios of Ni and Fe, the Fe2p and Ni2p3/2 regions were fit with various background corrections. The reported areas for these regions were then adjusted by sensitivity factors within CasaXPS (16 and 14 for Fe 2p and Ni 2p3/2 regions, respectively); the resulting Fe content is reported as a percentage of (Fe + Ni).

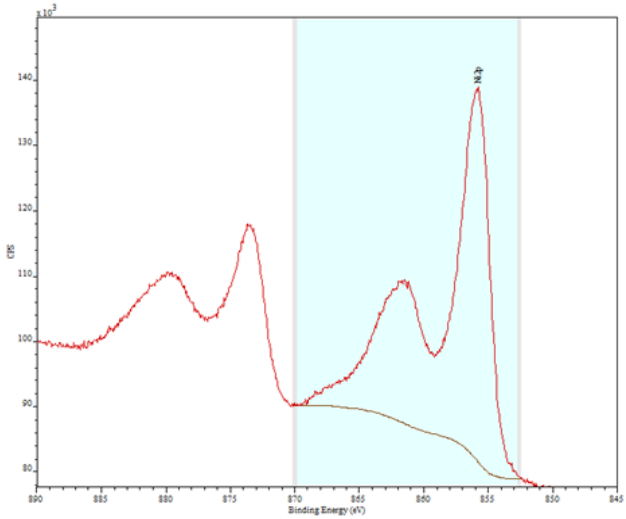

Figure S3.4.1a. Representative XPS Ni 2p3/2 region Shirley background fitting for $Ni(OH)_2$ film aged 1 day in unpurified 1 M KOH.

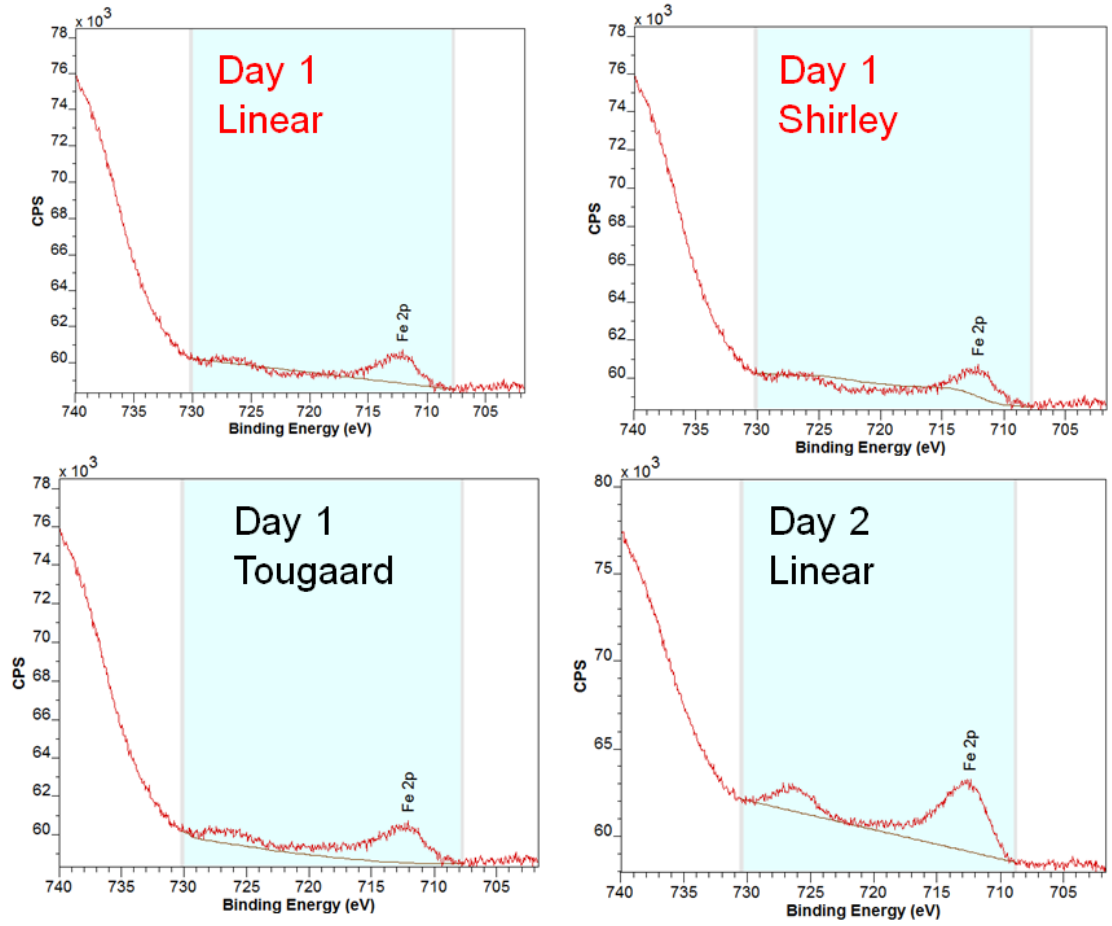

Figure S3.4.1b. Sample XPS background fittings of Fe2p region. Tougaard background subtraction was used for low Fe content (day 0 and day 1 of aging), since linear and Shirley background fittings over-subtract the baseline. Linear background subtraction was used for higher Fe contents (day 2 and longer of aging), since the Tougaard background fitting under-subtracted and Shirley background fitting over-subtracted the baseline due to the large O Auger contribution at binding energies above 730 eV.

S3.4.2. Iron incorporation observed from Fe2p XPS spectra

(a)

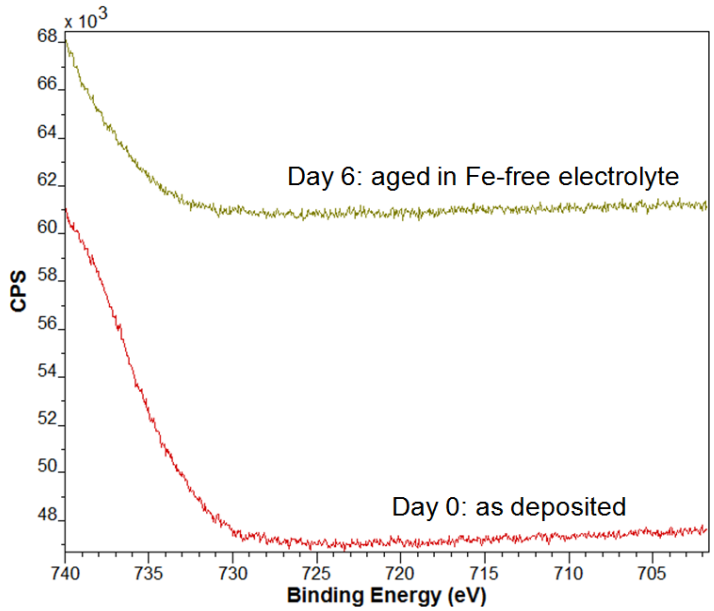

(b)

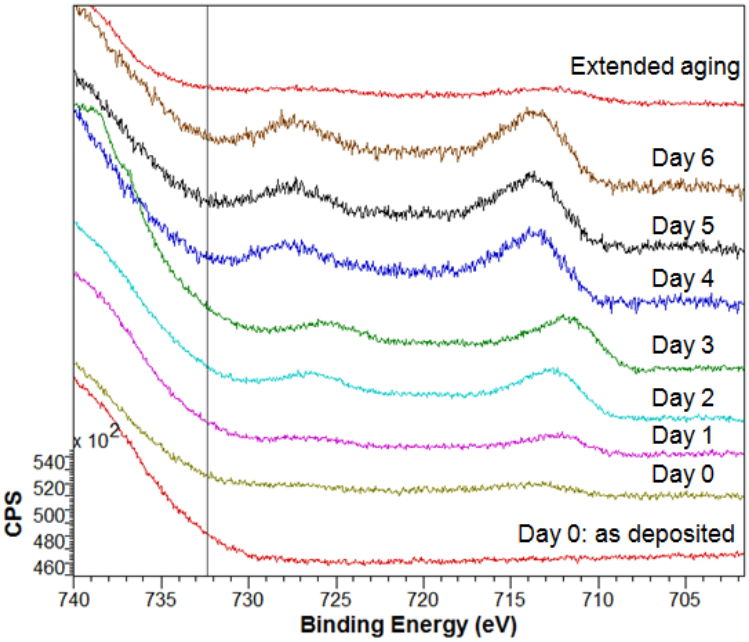

Figure S3.4.2. Fe2p XPS spectra for Ni films as deposited and aged in (a) Fe-free and (b) Fe-containing 1 M KOH. Samples have not been charge corrected on the eV axis, and spectra are offset on the y-axis (arbitrary units) for clarity. The overall XPS intensity was lower for the extended aging sample.

S3.4.3. XPS binding energy calculation

XPS binding energies were determined from XPS peaks after Shirley background subtraction within CASA XPS software. All binding energies were charge corrected to adventitious carbon at 284.8 eV.

Table S3.4.3: Sample binding energies (in eV)

	Ni2p3/2	Ni2p1/2	Fe2p3/2	Fe2p1/2	O1s
Day 0 as prepared	855.5	861.2			530.9
Day 6 Fe free KOH	855.6	861.0			530.8
Day 0 unpurified KOH	855.3	860.9	711.7	724.6	530.7
Day 1 unpurified KOH	855.6	861.4	711.6	725.2	530.9
Day 2 unpurified KOH	855.5	861.2	711.7	724.8	530.9
Day 3 unpurified KOH	855.3	861.0	711.1	724.9	530.6
Day 4 unpurified KOH	855.3	861.1	711.7	725.2	530.7
Day 5 unpurified KOH	855.4	861.0	711.7	725.2	530.7
Day 6 unpurified KOH	855.4	861.0	711.7	725.3	530.7
Day 6 unpurified KOH	855.6	861.7	712.1	724.7	530.9

S3.5. Extended aging peak position shift with continued aging

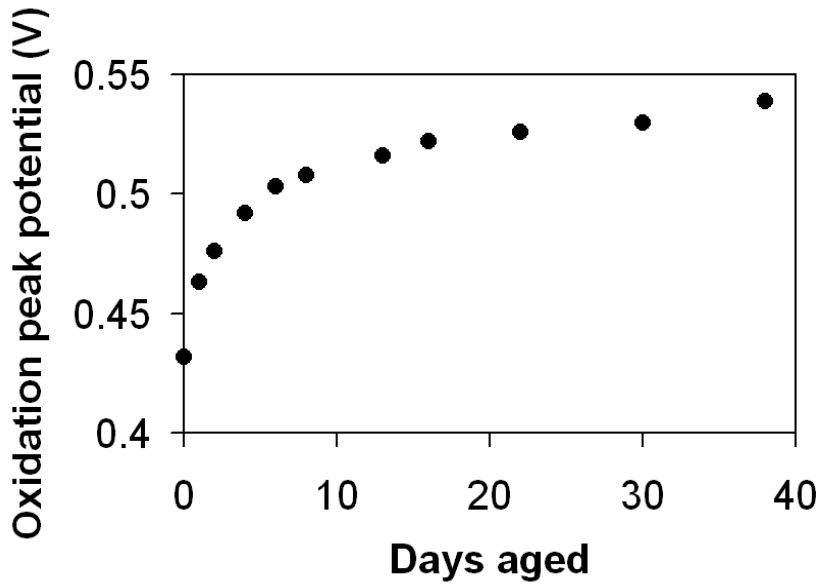

Figure S3.5.1. Potential of the main oxidation wave peak-potential vs. days aged for a $Ni(OH)_2$ thin-film over an Au RDE aged in unpurified 1 M KOH.

S3.6. Recorded ICP calibration plot and catalyst composition with aging

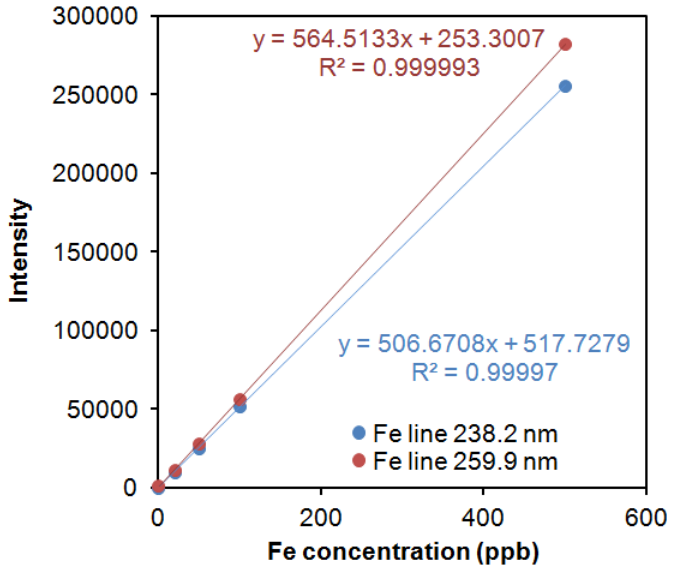

Figure S3.6.1. Example ICP-OES calibration plot.

Discussion of Fe content as determined by ICP-OES and XPS:
ICP-OES was calibrated using standard solutions with concentrations of Fe as low as 20 ppb. The 20 ppb Fe calibration standard was re-measured after calibration; using the calibration curve, the Fe content of this sample was calculated to be ~17 ppb. Thus, we take an estimate of the absolute error to be ± 3 ppb.

Table S3.6: Concentrations of Fe and Ni for $Ni(OH)_2$ films aged in unpurified 1 M KOH.

	Fe µg/L	Ni µg/L
as deposited	0.298	161.3
day 0	4.9	188.8
day 1	9.9	161.4
day 2	19.4	140.8
day 3	23.2	197.4
day 4	35.9	195.0
day 5	39.4	188.0
day 6	38.2	171.0
day 38	37.2	108.4

The solubility equilibrium constant of the following reaction

$Ni(OH)_2$ (s) + 2 H^+ (aq) ↔ Ni^{2+} (aq) + $2H_2O$ (l)

is reported to be $10^{-10.5\pm1.3}$.[5,6] At pH 14, this corresponds to an equilibrium concentration of [Ni^{2+}] = 3.2×10^{-18} M. For the sample aged for 38 days, total maximum electrolyte exposure would be ~ 2L, corresponding to a total maximum possible dissolution of 6×10^{-18} mol Ni. Films contain ~ 1.6×10^{-8} mol Ni, indicating that film loss due to dissolution during aging should be negligible.

The most likely cause for any loss in film mass is handling and rinsing of the sample. The gold RDEs were periodically (1) transferred from the 1 M KOH electrochemical cell to the 1 M KOH aging solutions, and (2) transferred back to the electrochemical cell. At points (1) and (2), the RDE holders were briefly rinsed (~ 1 s) with 18.2 MΩ cm H_2O (< 2 mL). Dissolution from exposure to pH 7 water would be significant at the solubility equilibrium (calculated as ~10^{-6} mol for equilibration with 10 mL of pH 7 water). However, it is clear that only the day 38 sample has significant mass loss; films aged for longer time periods will have more cycles of rinses (1) and (2), and thus greater total loss in film mass.

The sample containing the lowest measurable Fe detected by ICP-OES was determined to be 4 ppb Fe (~3% Fe in the film), which is comparable to the ~3% Fe quantification limit for XPS. We note that an as-deposited Fe-free film gave a similar iron ICP-OES concentration as the Fe-free calibration standard, and as-deposited Ni films and Ni films aged six days in Fe-free KOH had no observable Fe within the XPS Fe 2p region.

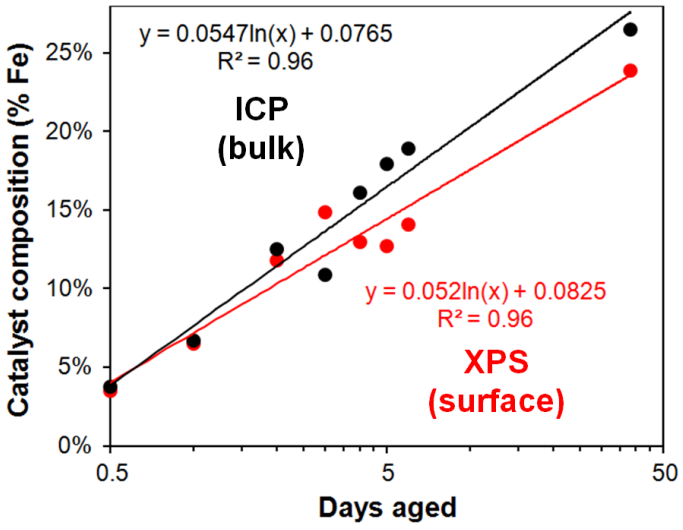

Figure S3.6.2. Iron content of $Ni(OH)_2$ films deposited on polished Au-RDEs measured from X-ray photoelectron spectroscopy (XPS) and inductively coupled plasma optical emission spectroscopy (ICP-OES) vs. days aged in unpurified 1 M KOH. Lines show a logarithmic best-fit ($y = aln(x) + b$) to each data set.

S3.7. Comparison of unpurified 1 M and 0.1 M KOH activities

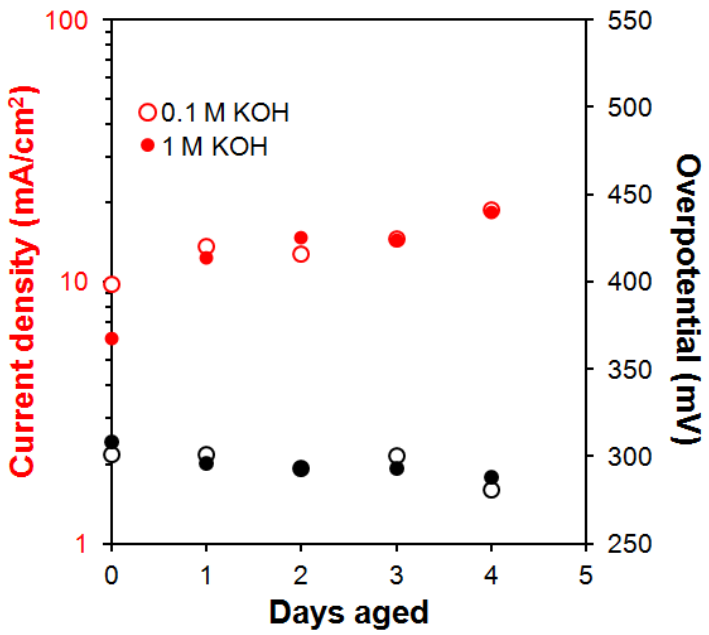

Figure S3.7.1. Oxygen evolution activity of electrodeposited $Ni(OH)_2$ films deposited on Au RDEs at 300 mV overpotential and 10 mA cm^{-2} geometric current density in 1 M KOH (filled circles) and 0.1 M KOH (outlined circles) with 1600 rpm rotation as a function of days aged.

S3.8. Tafel slope measurement

Tafel slopes were obtained from CV data collected at 1600 rpm to reduce mass transport effects. In selecting the region for the Tafel fit, we avoided high potentials at which oxygen bubble evolution causes mass transport limitations, and low potentials at which the redox transition for Ni(II)/Ni(III) occurs.

a)

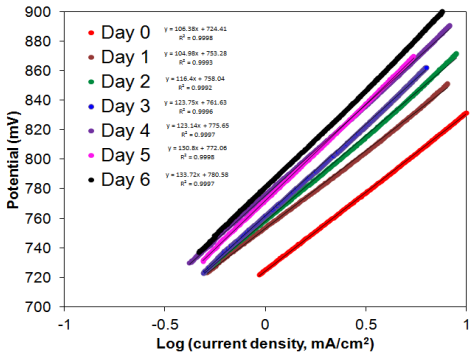

b)

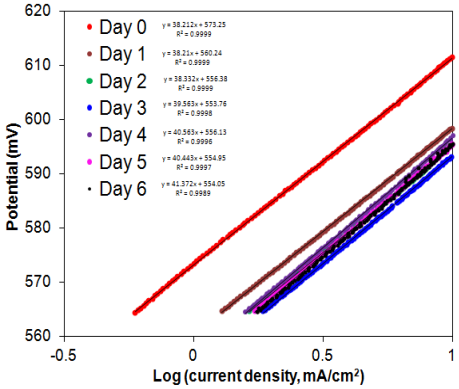

c)

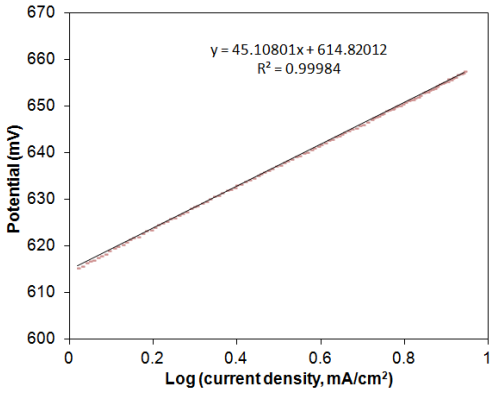

Figure S3.8.1. iR-corrected polarization curve in the OER region in 1 M KOH solution collected on a $Ni(OH)_2$ after aging in a) Day 0-6 (12^{th} cycle) in Fe-free 1 M KOH b) Day 0-6 (12^{th} cycle) in unpurified 1 M KOH and c) Day 0 (1^{st} cycle) in unpurified 1 M KOH.

S3.9. Additional Raman spectra, 560 cm^{-1} normalization, and laser-induction of 3581 cm^{-1}
S3.9.1. Raman spectra of NiOOH with aging

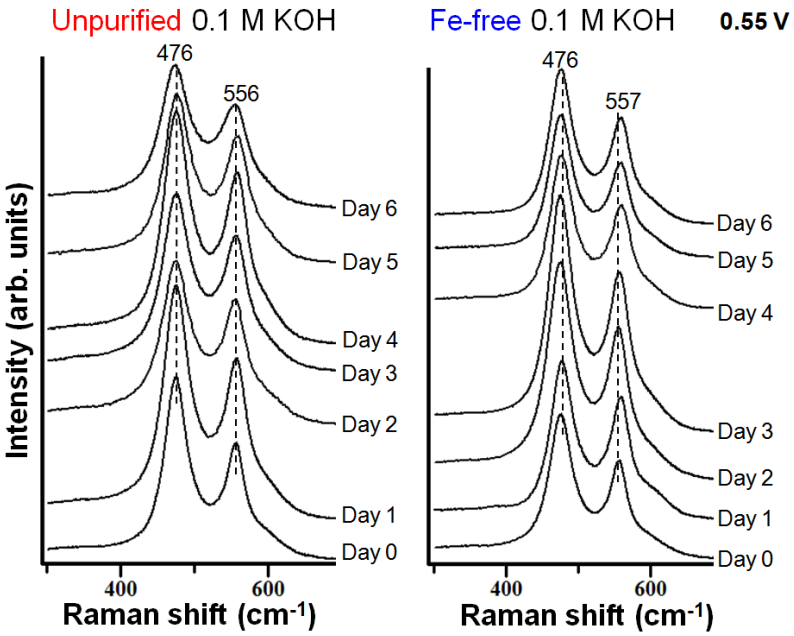

Figure S3.9.1. In situ Raman spectra collected over NiOOH on roughened Au at 0.55 V vs. Hg/HgO for Fe-free and unpurified 0.1 M KOH (both aged in 1 M KOH).

S3.9.2. Raman spectra in high-wavenumber region (3000-3800 cm^{-1})

Raman spectra for Day 0 and Day 6 in Fe-free and unpurified 0.1 M KOH are presented in Figs. S3.7.1a and S3.7.1b, respectively.

(a)

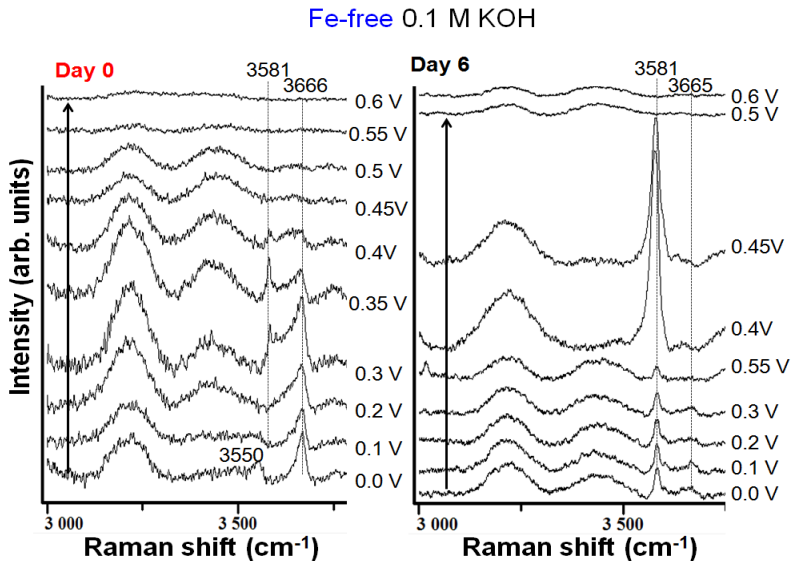

(b)

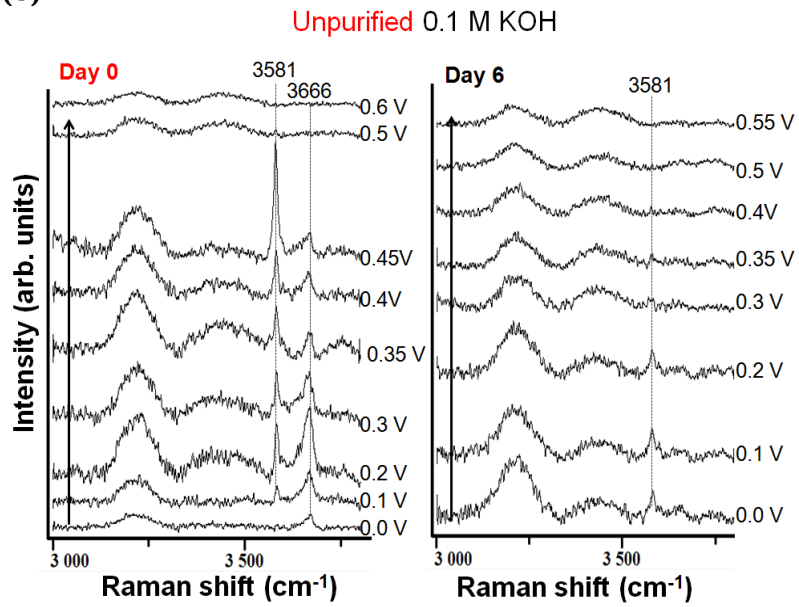

Figure S3.9.2. In situ Raman spectra collected over $Ni(OH)_2$ films deposited on roughened Au in (a) Fe-free and (b) unpurified 0.1 M KOH (both aged in 1 M KOH) on Day 0 and Day 6 of aging during 1 mV/s oxidation waves (potentials reported vs. Hg/HgO). Oxygen evolution equilibrium is 0.365 V vs. Hg/HgO. *Laser induced intensification of 3580 cm^{-1} feature at higher potentials.

S3.9.3. Background subtraction and normalization for 560 cm^{-1} Raman intensity comparison

To plot the normalized intensity of the 560 cm^{-1} Raman mode, spectra were proportionally adjusted to a value of 1500 arb. units at 700 cm^{-1}, an example of which is shown in Fig. S3.7.4. After this adjustment, the peak intensity was recorded and subtracted from 1500. Spectra were then normalized to the spectrum with the maximum intensity at 560 cm^{-1} for each sample run.

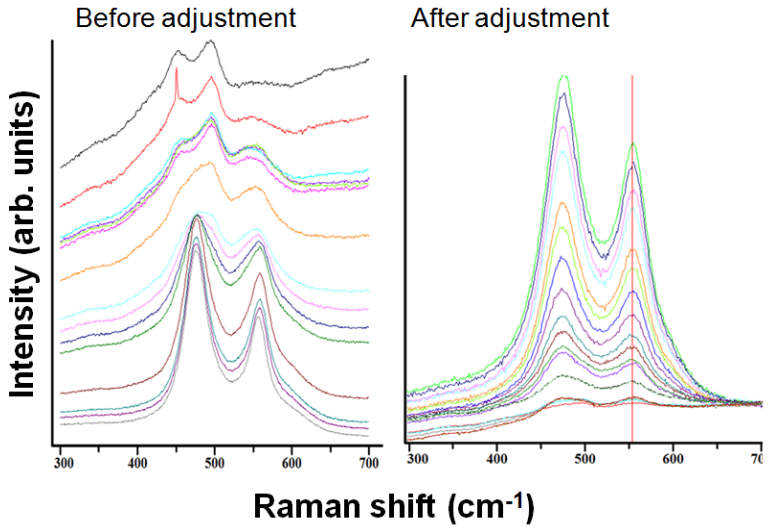

Figure S3.9.3. Spectra before and after background adjustment for 560 cm^{-1} peak height comparison.

S3.9.4. Raman 480/560 cm^{-1} peak height ratio with aging and overcharging

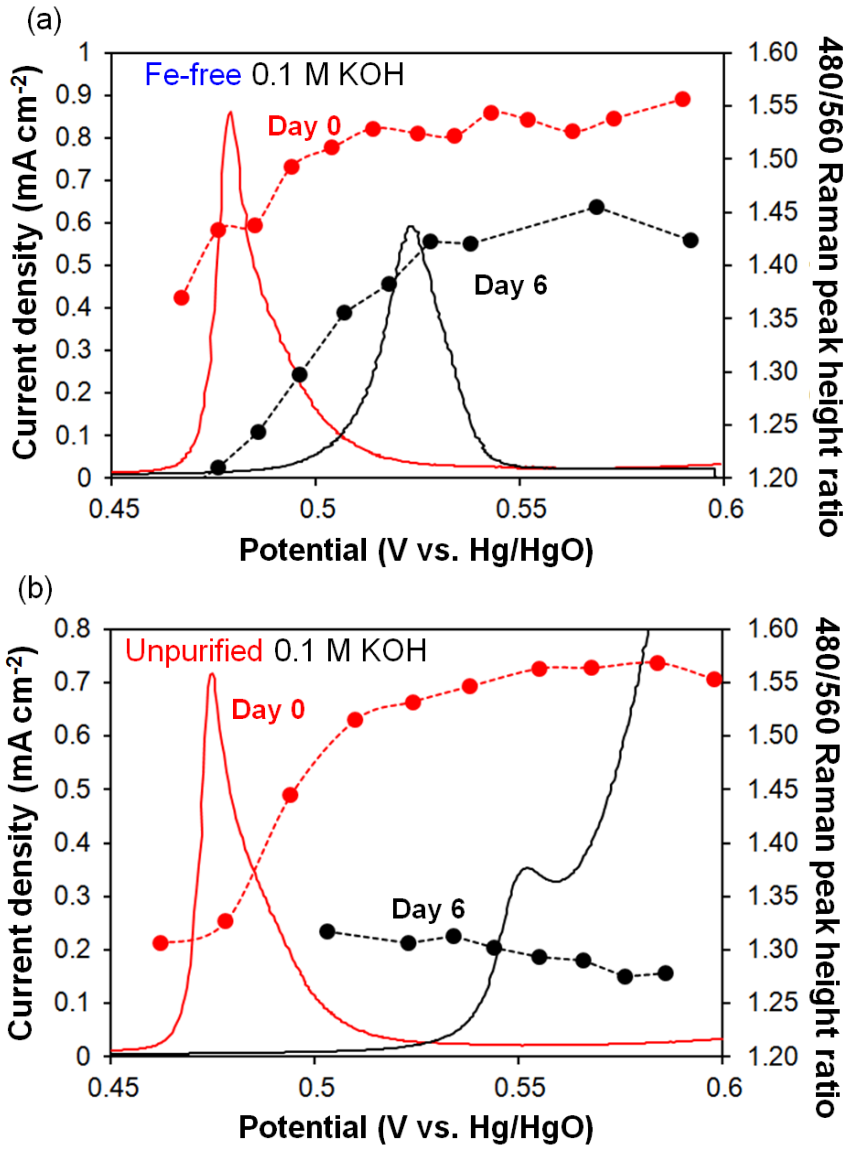

Figure S3.9.4. 480 cm^{-1}/560 cm^{-1} Raman peak height ratio and concurrent 1 mV s^{-1} potential scans for $Ni(OH)_2$ films deposited on roughened Au in (a) Fe-free and (b) unpurified 0.1 M KOH before and after aging in 1 M KOH. Oxygen evolution equilibrium potential is 0.365 V vs. Hg/HgO.

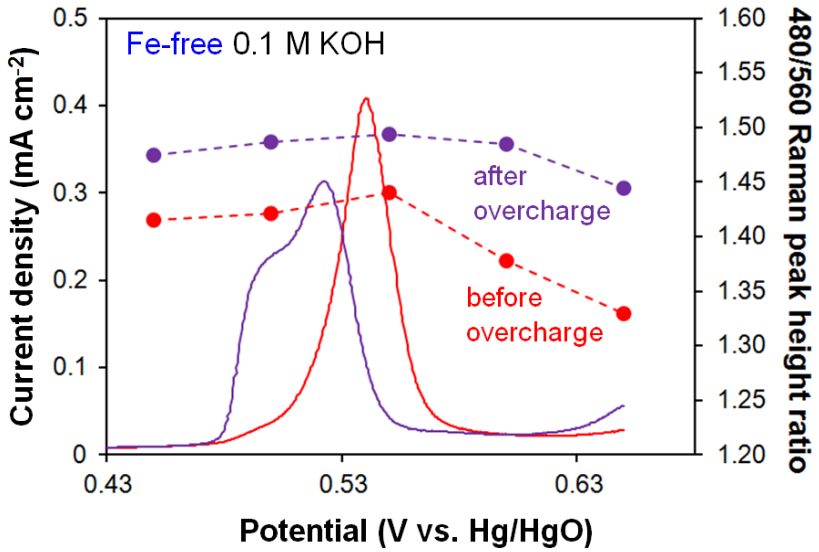

Figure S3.9.5. 480 cm^{-1}/560 cm^{-1} Raman peak height ratio and concurrent 1 mV s^{-1} potential scans for an aged $Ni(OH)_2$ film deposited on roughened Au in Fe-free 0.1 M KOH (after six days of aging in Fe-free 1 M KOH). Cycles are shown before and after the 10 mV s^{-1} overcharge scan to 0.85 V. The equilibrium potential of oxygen evolution is 0.365 V vs. Hg/HgO.

S3.9.5. Raman spectra at low potential (0.2 V vs. Hg/HgO) aquired after aging and overcharging

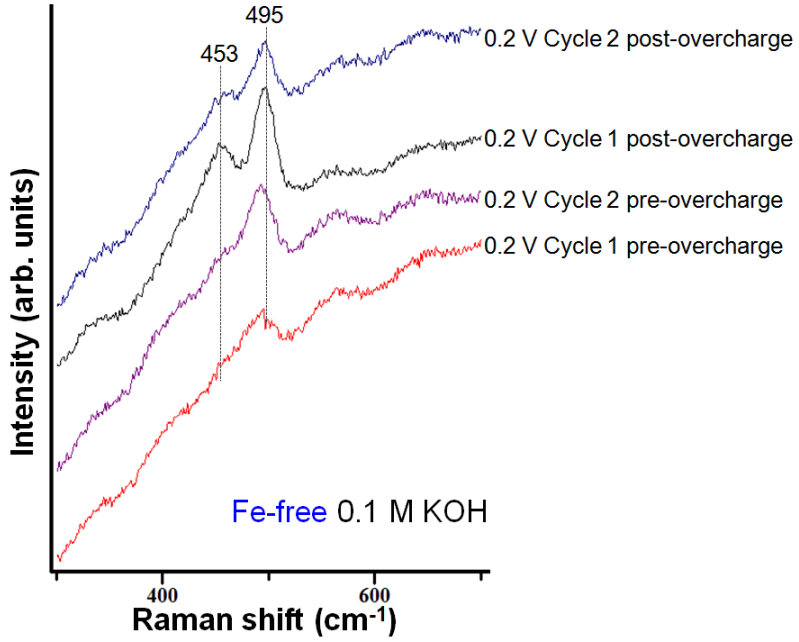

Figure S3.9.6. In situ Raman spectra collected over $Ni(OH)_2$ films deposited on roughened Au at 0.2 V vs. Hg/HgO in Fe-free 0.1 M KOH (aged in 1 M KOH) before and after overcharge.

S3.10. QCM frequency and current density change after aging and overcharging

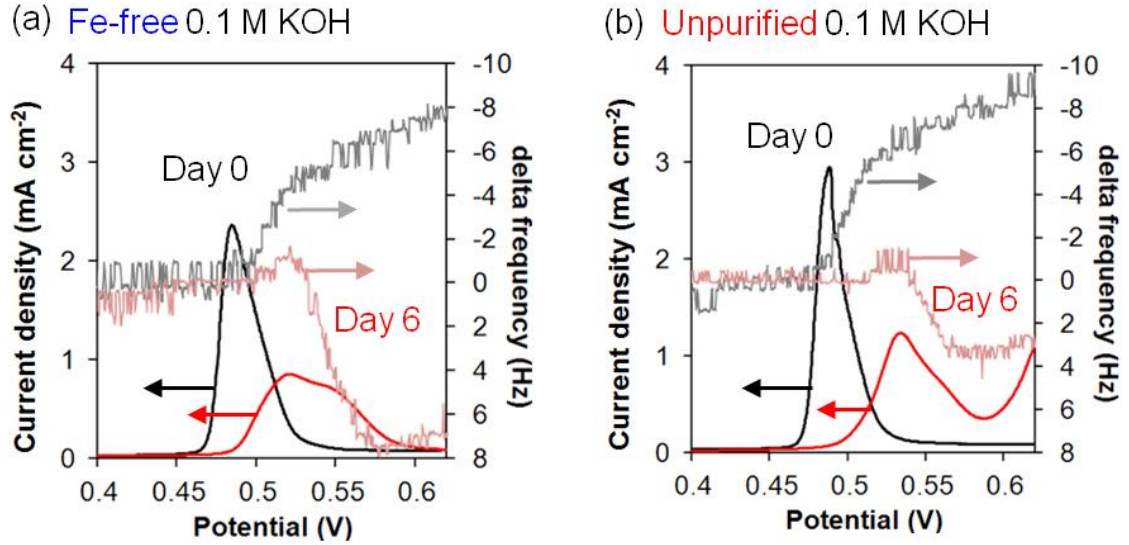

Figure S3.10.1. QCM frequency change with concurrent 10 mV s^{-1} potential scans for $Ni(OH)_2$ films deposited on Au/Ti quartz crystals in (a) Fe-free and (b) unpurified 0.1 M KOH before and after six days of aging in 1 M KOH. The oxygen evolution equilibrium potential is 0.365 V vs. Hg/HgO.

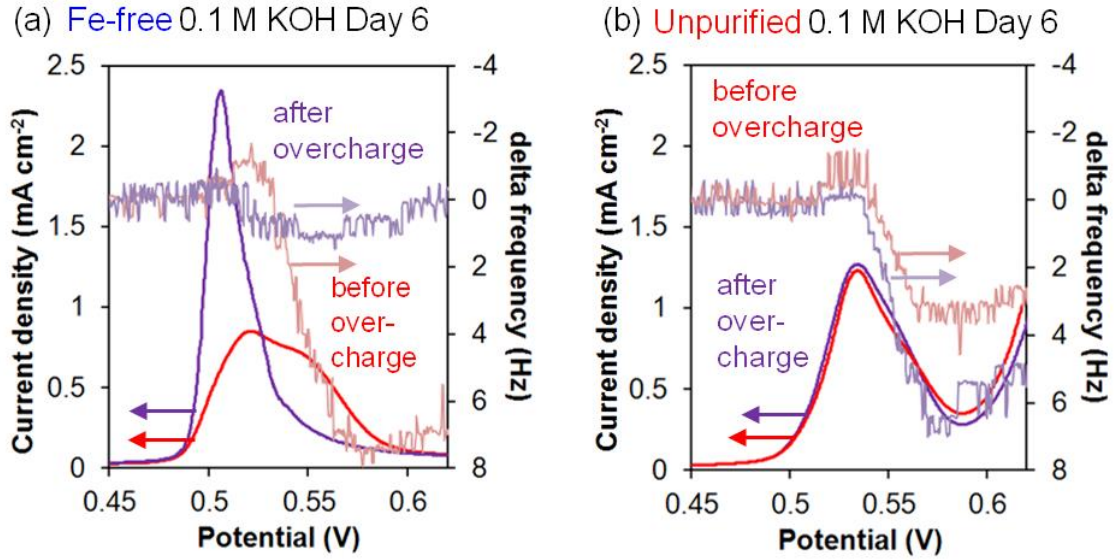

Figure S3.10.2. QCM frequency change with concurrent 10 mV s^{-1} potential scans for $Ni(OH)_2$ films deposited on Au/Ti quartz crystals in (a) Fe-free and (b) unpurified 0.1 M KOH (both after six days of aging in 1 M KOH). Cycles are shown before and after the 10 mV s^{-1} overcharge scan to 0.85 V. The oxygen evolution equilibrium potential is 0.365 V vs. Hg/HgO.

S3.11. Cycling before and after overcharge in Fe-free KOH

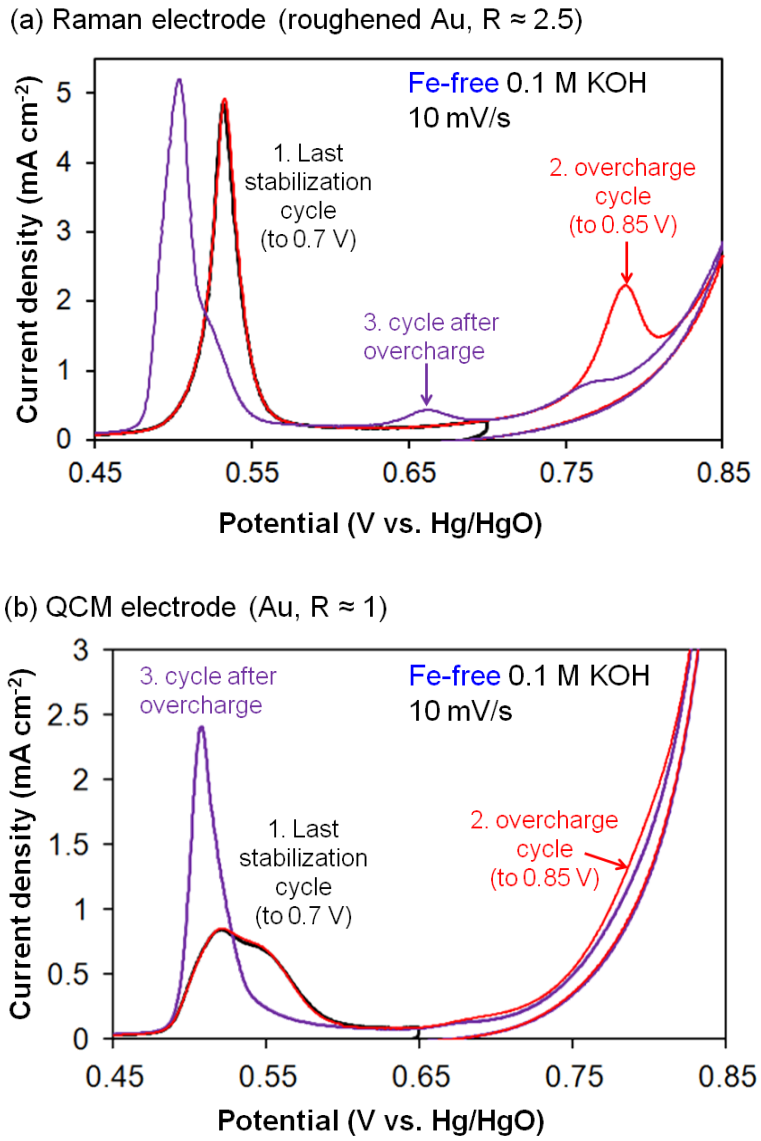

Figure S3.11.1. Cyclic voltammograms of an aged $Ni(OH)_2$ film over (a) a roughened Au and (b) an Au quartz crystal in 0.1 M Fe-free KOH (after six days of aging in 1 M Fe-free KOH) with a 10 mV s^{-1} scan rate. The electrodes were stabilized to 0.7 V before a 10 mV s^{-1} overcharge scan to 0.85 V. The oxygen evolution equilibrium potential is 0.365 V vs. Hg/HgO in 0.1 M KOH.

We integrated the primary and small (0.6/0.66 V) oxidation peaks in Figs. 3.2a and 3.9. The small oxidation feature (0.6/0.66 V, attributed to the presence of γ-NiOOH) area is 3.7 % and 1.4% of the main oxidation peak area for the Raman (Fig. 3.9) and RDE (Fig. 3.2a) electrodes, respectively. This indicates less β/β exists for the Raman sample (Fig. 3.9) vs. RDE (Fig. 3.2a) after overcharge cycling. We attribute this difference to differences in sample film thickness and electrolyte concentration.

The area of the small 0.6 V oxidation feature for the RDE sample is ~37% of the day 0 value after six days of aging, which indicates a mixture of α/γ and β/β are present within the film. The α/γ and β/β oxidation features appear to merge in the Fig. 3.2a voltammograms after aging due to the anodic shift of the α/γ transition overlapping with the β/β transition. Though not directly distinguishable in the main oxidation feature of Fig. 3.2a, α/γ is also present in addition to β/β after six days of aging.

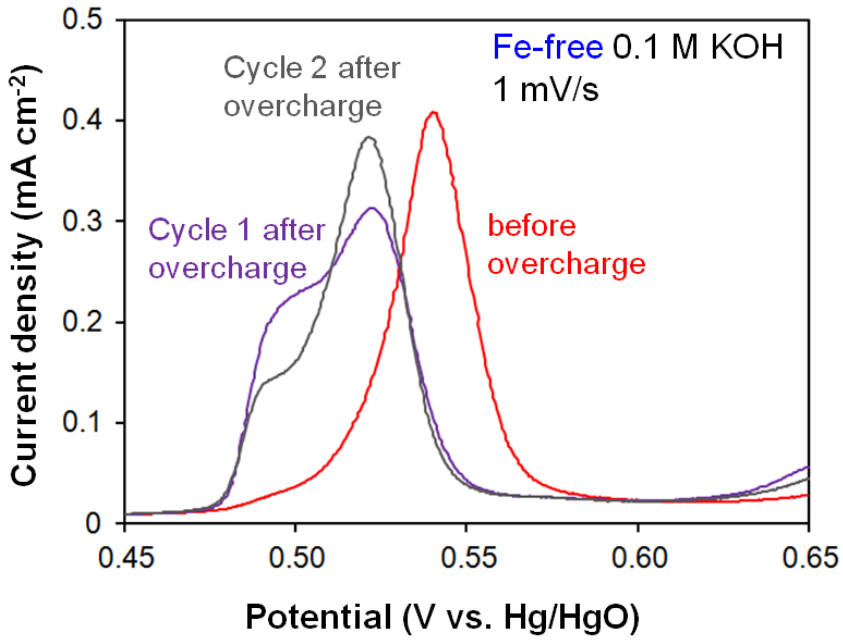

Figure S3.11.2. Cyclic voltammogram of an aged $Ni(OH)_2$ film in 0.1 M Fe-free KOH (after six days of aging in 1 M Fe-free KOH) with 1 mV s^{-1} with concurrent Raman. The electrode was stabilized to 0.7 V before a 10 mV s^{-1} overcharge scan to 0.85 V. A dramatic shift in the main peak oxidation potential is observed. The oxygen evolution equilibrium potential is 0.365 V vs. Hg/HgO.

S3.12. QCM mass change and current vs. applied potential during overcharging

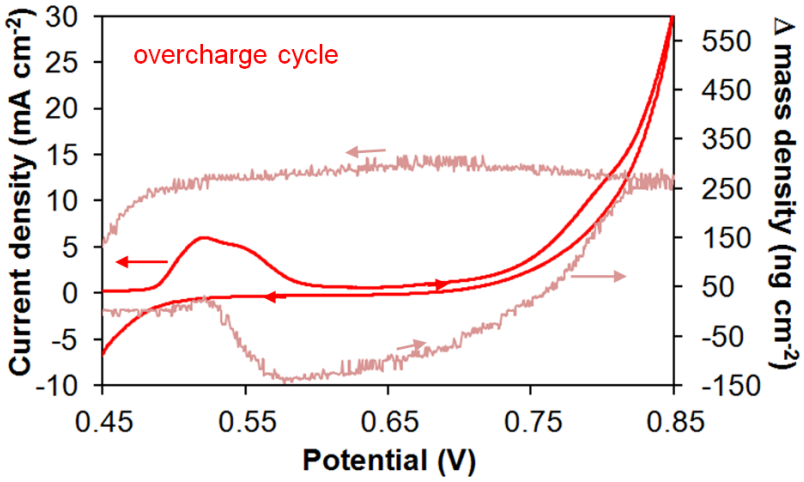

Figure S3.12.1. QCM mass density change with concurrent 10 mV s^{-1} potential scan for $Ni(OH)_2$ film deposited on Au/Ti quartz crystals in Fe-free and (after six days of aging in 1 M KOH). Cycle shown is the 10 mV s^{-1} overcharge scan to 0.85 V. The oxygen evolution equilibrium potential is 0.365 V vs. Hg/HgO in 0.1 M KOH.

S3.13. Calculation of estimated turnover frequency (TOF)

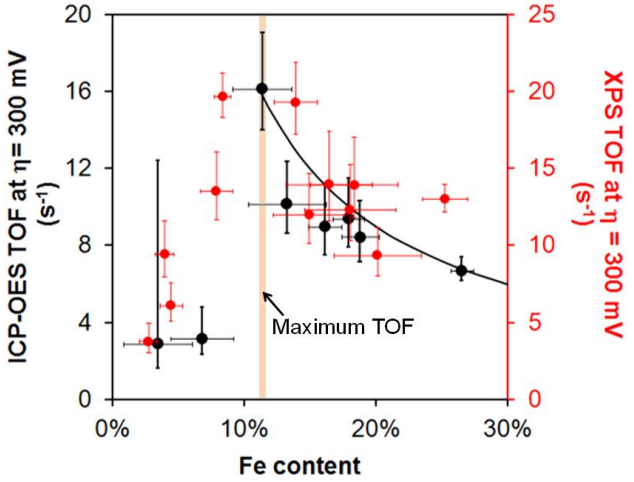

Figure S3.13.1. Turnover frequency (calculated on a per-Fe site basis) from total Fe content (ICP-OES: black, XPS: red) for $Ni(OH)_2$ films deposited on polished Au-RDEs as a function of percent Fe. Error bars indicate the inherent uncertainty in the Fe content as determined by ICP-OES and XPS for each sample.

TOF was calculated on a per-Fe site basis. For ICP data (black), the number of Fe sites was directly obtained from the resulting ICP-OES concentration of Fe and total sample volume (5 mL) for each dissolved film.

For XPS data (red), the number of Fe sites was estimated using the % Fe determined via XPS and an estimation of total Ni content within each film. To obtain total Ni content, the $NiOOH \rightarrow Ni(OH)_2$ reduction peak of the final voltammogram cycle for each sample was integrated, and it was assumed that one electron is transferred per Ni site.

The solid line represents the estimated TOF assuming Fe content exceeding 11% is not OER-active and is calculated as

$$TOF = TOF_{max} \frac{\%Fe_{TOFmax}}{\%Fe}$$

where *TOF* is the turnover frequency assuming Fe in excess of 11% catalyst composition is not OER-active, TOF_{max} is the maximum turnover frequency, 15.84 s^{-1}, $\%Fe_{TOFmax}$ is the catalyst Fe content, 11.4%, at the maximum turnover frequency, and *% Fe* is the percent Fe composition of the catalyst.

The greatest source of error is expected to be in the estimation of Fe content for each sample. Error bars were calculated as follows:

ICP-OES: Since the 20 ppb calibration standard measured after calibration was calculated to be ~17 ppb, we estimate the error for each sample to be ±3 ppb. This error was added to the maximum and minimum Fe contents, respectively, calculated from the two Fe lines measured (see S6 for

ICP-OES calibration plot). The resulting error bars show the calculated minimum and maximum values of resulting percent Fe (x-axis) and TOF using number of Fe sites (y-axis).

XPS: The Fe content of each film was measured with varying background subtractions (e.g. Shirley, Linear, and Tougaard), and a standard deviation of three fits was obtained to estimate error in the Fe content of each film. This error was then applied to the percent Fe (x-axis) and TOF with the total number of Fe sites (y-axis).
The anisotropic error bars for the y-axis occur due to the lower limit (negative error) of Fe content resulting in a considerably higher maximum (positive error) in the TOF. This is especially apparent in the ICP-OES TOF error at 3% Fe due to the iron content of this sample (4 ppb concentration vs ICP-OES) approaching the estimated ICP-OES error of 3 ppb.

References

S1. Trotochaud, L.; Young, S. L.; Ranney, J. K.; Boettcher, S.W. Nickel-Iron Oxyhydroxide Oxygen-Evolution Electrocatalysts: The Role of Intentional and Incidental Iron Incorporation. *J. Am. Chem. Soc.* **2014**, *136*, 6744-6753.
S2. Gao, P.; Gosztola, D.; Leung, L. W. H.; Weaver, M. J. J. Surface-Enhanced Raman-Scattering at Gold Electrodes - Dependence on Electrochemical Pretreatment Conditions and Comparisons with Silver. *Electroanal. Chem.* **1987**, *233*, 211-222.
S3. Buttry, D. A.; Ward, M. D., Measurement of Interfacial Processes at Electrode Surfaces with the Electrochemical Quartz Crystal Microbalance. *Chem Rev* **1992**, *92*, 1355-1379.
S4. Sauerbrey, G., Verwendung Von Schwingquarzen Zur Wagung Dunner Schichten Und Zur Mikrowagung. *Z. Phys.* **1959**, *155*, 206-222.
S5. Gamsjager, H.; Wallner, H.; Preis, W., Solid-Solute Phase Equilibria in Aqueous Solutions - Xvii. Solubility and Thermodynamic Data of Nickel(II) Hydroxide. *Monatsh Chem* **2002**, *133*, 225-229.
S6. Plyasunova, N. V.; Zhang, Y.; Muhammed, M., Critical Evaluation of Thermodynamics of Complex Formation of Metal Ions in Aqueous Solutions. IV. Hydrolysis and hydroxo-complexes of Ni2+ at 298.15 K. *Hydrometallurgy* 1998, *41*, 43-63.

Chapter 4

Experimental and Computational Evidence for Highly-Active Fe Sites Present on the Surface of Oxidized Gold for the Electrocatalytic Oxidation of Water in Basic Media

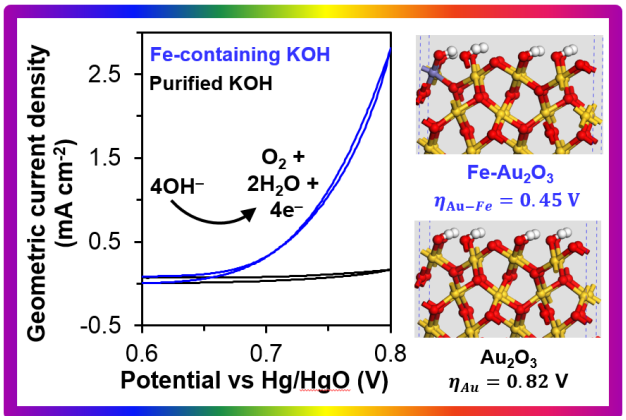

Abstract

The addition of Fe to Ni- and Co-based (oxy)hydroxides, either intentionally or as a result of exposure to ppm or lower levels of aqueous Fe impurities, has been shown to significantly enhance the activity of these materials as catalysts for electrochemical water oxidation, and recent studies point towards Fe as the active catalytic sites. However, better insight into the mechanism of the oxygen evolution reaction (OER) at Fe sites is necessary for development of new catalyst materials, and the study of individual Fe sites in the highly disordered layered (oxy)hydroxides is challenging. Here, we investigate the electrocatalytic oxygen evolution activity of Fe impurities bound to the surface of Au electrodes. A correlation between the concentration of Fe impurities in the electrolyte, the surface Fe content (determined via XPS and ICP-MS), and the OER activity was observed. However, in contrast to CoOOH and NiOOH, binding of Fe impurities at the Au surface was found to be reversible, and the loss of surface Fe coincided with an oxidation wave (attributed to both the formation of aqueous ferrate(VI) species and oxygen evolution) at an overpotential η = 0.4 – 0.9 V. A density functional theory analysis of the energetics of the OER reveals that oxygen evolution over Fe cations bound to an oxidized Au surface (Fe-Au_2O_3) occurs at an overpotential of 0.43 V, significantly lower than that at which the OER occurs on hydroxylated Au_2O_3 (0.86 V) and consistent with experimental results. Additionally, these findings suggest that enhanced OER activity over Au arises due to the presence of Fe impurities at the surface which are the active sites for the OER, in contrast to recent work implicating “superactive” Au(III) surfaquo species.

4.1 Introduction

The development of highly active, earth-abundant catalysts for the oxygen evolution reaction (OER, in basic media: $4HO^- \rightarrow 2H_2O + O_2 + 4e^-$) is critical for achieving the efficient photoelectrochemical conversion of solar energy to chemical fuels.[1-10] A number of studies have shown that the incorporation of Fe into various (oxy)hydroxides can improve their OER activity dramatically.[10-21] Investigations of Ni-(oxy)hydroxides have shown that ppb-level Fe impurities in basic electrolytes enhance the activity of Ni-based catalysts by as much as 200 fold.[12-13, 21] Experimental and theoretical analysis of the OER on such $Ni_{1-x}Fe_xOOH$ materials indicate that the Fe cations substituted into the Ni-(oxy)hydroxide lattice are the active sites responsible for high catalytic activity.[14] Similarly, recent work by Burke et al. has proposed that Fe substituted into Co-(oxy)hydroxides may be the catalytically active sites.[11] This work has also noted that the low activity of Fe^{3+} cations in FeOOH could be due to the low conductivity of this material and that the enhanced activity upon Fe addition into CoOOH (or NiOOH) is the result of the active Fe^{3+} sites being contained in an appropriately conductive and chemically stable host structure.

Despite these experimental efforts, the precise role that Fe plays in improving the energetics of the reaction is still unclear, and a better understanding of the OER mechanism at these highly active Fe-containing materials could enable the development of new catalysts with improved activity and/or stability (e.g., for use in acidic media). Density-functional theory (DFT) can provide mechanistic insight, but such efforts are often challenging. In the case of Ni-(oxy)hydroxides, recent work by Friebel et al. has found that Fe^{3+} cations within $Ni_{1-x}Fe_xOOH$ exhibit a significantly lower OER overpotential compared to Ni cations in either $Ni_{1-x}Fe_xOOH$ or pure NiOOH.[14] It should be noted, though, that the theoretical simulation of Ni- and Co-(oxy)hydroxides is complex because these materials have highly disordered layered structures and are known to intercalate alkali cations, water, and hydroxide anions, making it difficult to define unambiguously the composition and structure of the host catalyst.

The work presented here is motivated by the recent observation by Trotochaud et al. that removal of Fe impurities from alkaline electrolyte results in a decrease in OER activity over Au.[13] Subsequent work by Doyle and Lyons has stated that "superactive" sites are formed on the surface of an Au electrode during low-potential cycling in unpurified NaOH.[22] The authors ascribed the increased activity to the formation of highly active hydrous monomeric Au(III) surfaquo species. It should be noted, though, that studies reporting such activity improvement for Au were likely carried out using electrolytes containing Fe impurities.[22-23] It is also quite likely that Fe impurities in the electrolyte may have influenced other investigations of the oxygen evolution over Au in alkaline electrolytes.[24-28] It is well established that Au is oxidized at potentials relevant to the OER to Au(III) (either as $Au(OH)_3$ or Au_2O_3), and the structure of the surface oxide(s) formed is well-defined.[29-31] Therefore, the influence of Fe cations bound to the surface of Au_2O_3 is expected to be a simpler system for DFT analysis compared to Ni- and Co-(oxy)hydroxides.

Here, we report experimental and theoretical efforts aimed at identifying the role of Fe cations deposited onto the surface of Au oxide on the rate of oxygen evolution at low overpotentials (<0.4 V vs Hg/HgO). We confirm experimentally that in the presence of Fe electrolyte impurities, oxidized Au electrodes exhibit an enhancement in OER activity, which increases with increasing content of surface Fe. In contrast to Ni-(oxy)hydroxides, where Fe is incorporated throughout the (oxy)hydroxide structure,[12-13, 15] we show that Fe binds reversibly to the Au surface. Density functional theory analysis of the relative energies of OER reaction intermediates reveals that the overpotential for the OER onset on Fe^{3+}sites bound to the surface of Au_2O_3 is 0.4 V lower that for

Au^{3+} sites present on the surface of the host oxide, in very good agreement with the experimentally observed difference in overpotentials for Fe-containing and Fe-free Au_2O_3.

4.2. Experimental and Theoretical Methods

4.2.1. Electrode Preparation and Electrochemical Characterization

All electrochemical measurements were carried out in a Teflon PFA beaker (VWR 13917-582) to eliminate contamination due to glass etching from the alkaline electrolyte. A coiled Pt wire served as the counter electrode (99.95%, DOE Business Center for Precious Metals Sales and Recovery – BCPMSR) and was housed in a porous polypropylene compartment inside the electrochemical cell. Pt counter electrode wires were periodically cleaned by overnight soaking in 6 M nitric acid. Potentials are reported vs the Hg/HgO reference electrode (CH Instruments) filled with 1 M KOH, for which the equilibrium potential for OER is 0.306 V (in 1 M KOH). The uncompensated series resistance R_u was determined by potentiostatic electrochemical impedance spectroscopy prior to each voltammogram, and the measured R_u value was internally compensated at 95%.

Depending on the experiment, three types of KOH were utilized: "Fe-free", "reagent-grade", and "electronic-grade". "Fe-free" 1 M KOH electrolyte was obtained by following the procedure of Trotochaud et al.[13] (a full description is provided in the Supporting Information S1). "Reagent-grade" 1 M KOH was prepared using ACS reagent-grade KOH pellets (≥85%, ≤0.001% Fe, Sigma-Aldrich 221473), and "electronic-grade" 1 M KOH was prepared from Baker Analyzed Electronic Grade KOH solution (45%, < 1.000 ppm Fe, VWR JT3144-3). Investigations of activity changes due to the presence of Fe impurities were completed using all three electrolytes.

Au rotating disc electrodes (RDEs, 5 mm diameter) were used for all electrochemical measurements and were fabricated using 99.95% purity Au (DOE BCPMSR). Prior to electrochemical measurements on bare Au, Au RDEs were mechanically polished with 1 and 0.05 mm alumina slurries, with 10 min of sonication in ultrapure water (18.2 MΩ cm, EMD Millipore) after each polishing step. The Au surface was then stabilized through 25 electrochemical cycles from -1.0 to 0.7 V vs Hg/HgO at 10 mV s^{-1} in 0.1 M "Fe-free" KOH. The electrodes were then briefly rinsed with ultrapure water and dried under a N_2 gas stream prior to electrochemical measurements.

4.2.2. Inductively Coupled Plasma Mass Spectrometry

The measurement of Fe, Ni, and Co content of catalyst films and KOH electrolyte solutions was carried out using an Elan DRC (Perkin Elmer) inductively coupled plasma mass spectrometer (ICP-MS) with a glass nebulizer (Micromist) and spray chamber at 1300W RF power. Ammonia was used as a reaction gas to remove plasma-based interferences for Fe analysis. Films were dissolved in 5 M high purity nitric acid (Sigma-Aldrich 84385) overnight and sonicated for 20 min prior to dilution. Final solutions for analysis contained ~2 wt% nitric acid. Prior to ICP-MS measurement, the KOH electrolytes were diluted ~10 × with 2 wt% ultra-high purity nitric acid. Concentrations were calculated using 0–50 ppb calibration standards of Ni, Fe, and Co, and calibrations were confirmed by comparison to standard solutions of these elements. The most abundant isotopes of analytes were chosen for analysis (56, 60, and 59 for Fe, Ni and Co, respectively).

4.2.3. X-ray Photoelectron Spectroscopy

X-ray photoelectron spectra were collected with a Kratos Axis Ultra spectrometer using a non-monochromatic Mg Kα source (10 mA, 15 kV) to avoid any LMM Auger features from trace Ni overlapping with the Fe $2p_{3/2}$ region. The base pressure in the analytical chamber was ~7 × 10^{-}

^{9} Torr. Spectra were collected with 20 eV pass energy and 50 meV step size. The Fe 2p regions were collected using dwell times of 300-500 ms and averaged 20 scans to obtain sufficient spectral signal-to-noise. The Au 4f spectrum (Au $4f_{7/2}$ at 84.0 eV)[32] was used for spectral charge-shift calibration. All spectra were analyzed using CasaXPS (Casa Software, Ltd).

4.2.4. Computational Details

Density functional theory (DFT) calculations were performed using Vienna ab initio Simulation Package (VASP) with the projector augmented wave pseudopotentials and the PBE functional. The plane wave energy cutoff was set to 400 eV and the density cutoff was set to 700 eV, and electron smearing was employed using the Gaussian-smearing technique with a width of k_BT = 0.1 eV for the surfaces and 0.01 eV for molecules. All calculated values of energy were extrapolated to k_BT = 0.

For the surface calculations, at least 10 Å vacuum space between adjacent images was used to prevent the interaction between the replicas along the z-direction, while for all molecules, a 20 Å × 20 Å × 20 Å box was used for simulations. Spin-polarized wavefunctions were used for all calculations except H_2 and H_2O, in which non-spin-polarized wavefunctions were used. To convert electronic energies into Gibbs free energies, zero-point energy (ZPE), enthalpic, and entropic corrections, and solvation energies are needed. We used the numbers reported by Rossmeisl et al. for ZPE and thermodynamic corrections,[33] and the solvation corrections were calculated using the Poisson-Boltzmann implicit solvation model with a dielectric constant ε = 80 for water. The computational standard hydrogen electrode model proposed by Nørskov and co-workers[34] was used to calculate potential- and pH-dependent free energy surfaces. We emphasize that this is a purely thermodynamic study, which means no kinetic barriers are calculated or included in the Gibbs free energy surfaces. This simple thermodynamic analysis has been shown to satisfactorily predict experimental overpotentials for other electrocatalytic reactions,[33, 35] and the thermodynamic overpotentials provided here represent the lower bounds to the kinetic ones. Moreover, recent computational studies have shown that the kinetic barriers are small and thus surmountable at room temperature.[36-38]

4.3. Results and Discussion

4.3.1. Electrochemical characterization of Au in KOH electrolytes with varying Fe impurity contents

The concentrations of Fe, Ni, and Co impurities in each 1 M solution of KOH were determined using ICP-MS (Table 4.1). The "Fe-free" solution was prepared by following the method for removing Fe-impurities from KOH reported recently by Torotochaud et al.[13] and contains only ~ 3pbb of Fe. By contrast, the reagent-grade 1 M solution of KOH contains ~9 ppb Fe and the-grade KOH solution contains ~100 ppb. We note that the Fe-free electrolyte is the purified version of the electronic-grade KOH.

The amount of Ni in each solution follows the reverse trend (electronic-grade < reagent-grade < "Fe-free"). The amount of Ni is particularly high in the "Fe-free" 1 M KOH because $Ni(OH)_2$ is used in the purification step. Although "Fe-free" solutions are centrifuged to remove $Ni(OH)_2$, some Ni remains in the purified KOH solution. The Ni concentration in this electrolyte was highly variable, and appeared to depend upon how quickly the electrolyte was used after purification; the concentration of Ni decreased with time after purification, due most likely to the slow settling of $Ni(OH)_2$ to the bottom of the bottle in which the solution was contained. Minimal amounts of Co (0.3 ppb or less) were detected in each electrolyte.

Table 4.1: Metal contents of prepared 1 M KOH electrolyte solutions

	Fe concentration (ppb)	**Ni concentration** (ppb)	**Co concentration** (ppb)
Fe-free 1 M KOH	2.9 ± 0.4	41.4 ± 41.4	0.23 ± 0.01
Reagent-grade 1 M KOH	9.3 ± 1.5	17.6 ± 25.7	0.30 ± 0.03
Electronic-grade 1 M KOH	103 ± 14	0.34 ± 0.26	0.16 ± 0.11

Table 4.1 demonstrates that the purification procedure used to remove Fe impurities is effective. However, the concentrations of Ni impurities are greater than the concentrations of Fe impurities in both the Fe-free and reagent-grade electrolytes. This raises the question of whether Ni impurities together with the Fe impurities affect the catalytic properties of the Au electrode. We show below that that the Ni impurities have a negligible effect.

The influence of the electrolyte Fe concentration on the oxygen evolution current observed over Au is shown in Figure 1. A > 200 mV decrease in the OER onset potential is observed when Fe impurities are present. These findings are consistent with those reported by Trotochaud et al., who noted that the removal of Fe from the electrolyte dramatically increased the overpotential required for OER on bare Au substrates.[13] Figure 1 also shows that the increase in current above 0.6 V correlates with the amount of Fe present in each electrolyte (additional CVs with varying electrolyte Fe concentration are shown in Supporting Information, S3), and for all electrolytes, rotation of the Au electrode further decreases the OER onset potential. Since these current densities are below those at which mass-transfer effects are observed, the effect of rotation is presumably due to exposure of the electrode to a larger total volume of electrolyte (i.e., a larger quantity of Fe impurities).

When the electrode is rotated at 1600 rpm in 1 M Fe-free KOH, small oxidation/reduction features associated with the conversion of $Ni(OH)_2$/NiOOH are observed. (As noted above,

$Ni(OH)_2$ is present the electrolyte as a consequence of the cleaning procedure used, see Supporting Information S2). Apart from this sample, only the surface oxidation/reduction of Au is observed at 0.35/0.20 V and the position and intensity of this feature is unaffected by the level Fe present in the electrolyte, indicating that the surface of the Au electrode remains electrochemically accessible and the energetics of the Au redox processes are not affected by Fe (or Ni) impurities.

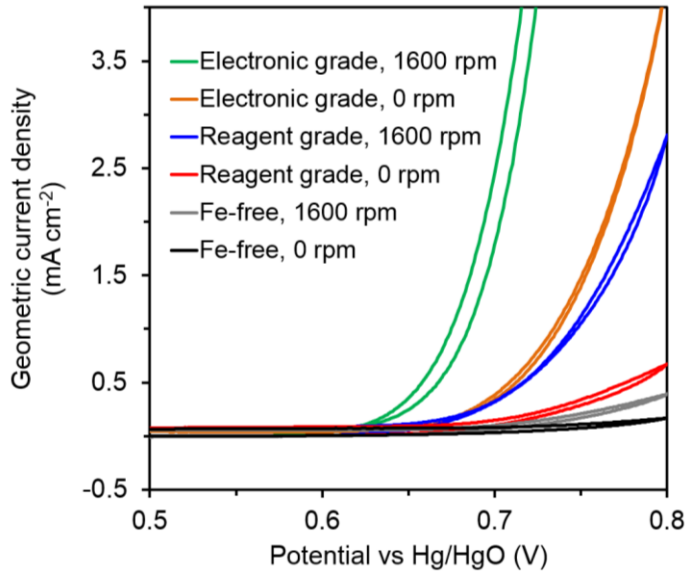

Figure 4.1. Cyclic voltammograms of Au cycled in 1 M KOH diluted from as-received stock solution or pellets (for electronic-grade and reagent-grade, respectively), or purified according to ref. 13 (Fe-free). The potential scan rate was 10 mV s^{-1} between 0.0 and 0.8 V vs Hg/HgO, for which E^0 for the OER is 0.306 V.

As shown in Figure 4.1, the OER current increases with increasing concentration of Fe impurities in the electrolyte. Since Ni impurities are also present, it is important to assess whether the observed increase in OER activity could be affected by Ni (or the combination of Fe and Ni, which is known to be highly-active for the OER). X-ray photoelectron spectra (XPS) were taken of Au electrodes at the end of a series of CV scans (Figure 4.2) in order to determine the uptake of Ni and Fe on the Au surface. A Fe XPS signal was not observed for the electrode cycled in purified ("Fe-free") 1 M KOH. However, low intensity features in the Fe 2p region can be seen for the Au electrodes cycled at both 0 rpm and 1600 rpm in reagent-grade KOH. The Au electrodes cycled with and without 1600 rpm rotation in electronic-grade KOH exhibits the greatest Fe 2p contributions, consistent with the higher Fe concentration in this electrolyte (see Table 1). For both reagent-grade and electronic-grade KOH, rotation during the CV acquisition resulted in greater uptake of Fe on the Au surface and a coincident increase in the OER current. Trace amounts of Ni were detected for all samples via XPS, except for Au cycled in Fe-free 1 M KOH at 1600 rpm, which has a significant Ni 2p contribution.

The XPS data combined with other experimental findings indicate that a the formation of a Fe-Ni (oxy)hydroxide is not the cause for the increased OER activity over Au seen in Figure 1 due to the following reasons:

1) $Ni(OH)_2$/NiOOH reduction/oxidation features were not observed for the majority of samples.
2) The surface coverage by Ni of each sample is small (less than 3% of the Au surface contribution via XPS – see Table S1) and is nearly constant (apart from the Fe-free sample rotated at 1600 rpm, see Table S1). By contrast, a clear trend in OER activity with the Fe impurity concentration is observed (see Figure 1).
3) The increase in OER activity correlates with the surface concentration of Fe observed by XPS and ICP-MS (as well as the Fe content present in each electrolyte).

Therefore, we conclude that while a small amount of Ni is present on the Au surface after CV cycling, this Ni does not appear to contribute to the observed changes in oxygen evolution activity over Au with increasing concentration of Fe in the electrolyte and on the surface of the electrode. For these reasons, the observed increase in activity is attributed to the presence of Fe on the electrode surface.

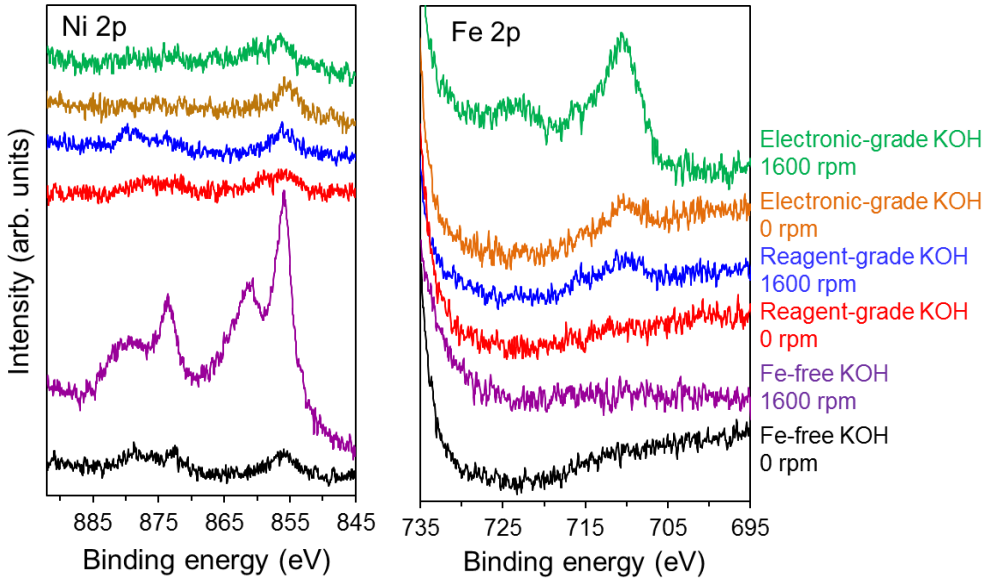

Figure 4.2. Ni 2p and Fe 2p photoelectron spectra of Au electrodes after 10 CV cycles (final cycle of which is shown in Figure 1) in Fe-free 1 M KOH at 0 and 1600 rpm (black and purple), reagent-grade 1 M KOH at 0 and 1600 rpm (red and blue), and electronic-grade 1 M KOH at 0 and 1600 rpm (orange and green). Raw data were smoothed using 3-point adjacent averaging.

4.3.2. Reversibility of Fe adsorption over Au

Additional CV and XPS experiments were carried out with the aim of identifying whether the Fe impurities bind reversibly or irreversibly onto the Au surface. Au electrodes cycled in electronic-grade KOH show dramatic increases in OER activity, but when these same electrodes are subsequently transferred to "Fe-free" KOH and additional CV cycles are carried out, the OER current decreases with each subsequent CV cycle until the voltamogram returns to that characteristic for Au cycled in Fe-free electrolyte (Figure 4.3). XPS of the electrodes after cycling in the "Fe-free" electrolyte show no signals corresponding to Fe.

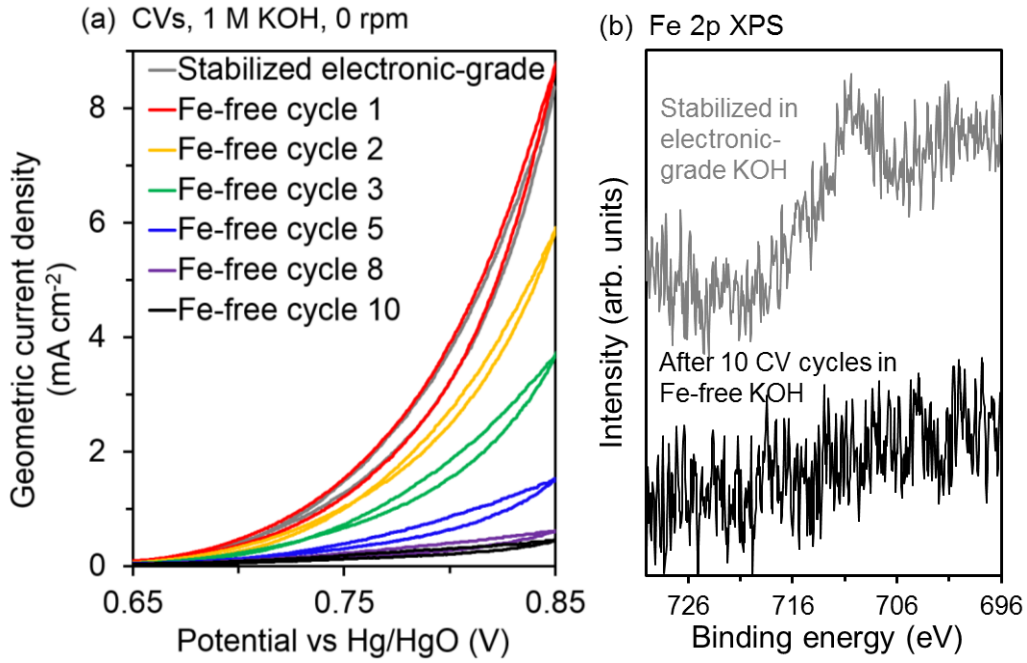

Figure 4.3. Cyclic voltammetry (a) and photoelectron spectra (b) of Au electrodes after initial cycling from 0.0 to 0.85 V in electronic-grade 1 M KOH (gray) and after subsequent transfer and cycling in "Fe-free" 1 M KOH (black). E^0 for OER is 0.306 V vs. Hg/HgO, and the scan rate is 10 mV s^{-1}. Raw XPS data were smoothed using 3-point adjacent averaging.

To investigate the stability of Fe over Au at OER current densities of practical interest (~10 mA cm^{-2}), voltammograms were acquired with higher anodic scan limits (0.9-1.1 V). An oxidation feature is clearly observed above 0.8 V vs Hg/HgO in reagent-grade KOH (Figure 4.4b) for CV scans carried out to higher anodic potentials, but this feature is very weak in purified ("Fe-free") KOH electrolyte (Figure 4.6a). After immersing a Au electrode overnight in 1 M reagent-grade KOH with no applied potential, a similar anodic peak is observed during the first CV cycle (Figure 4c). Based upon the difference between the CVs of Figures 4.4a and 4.4b, we hypothesize that the observed oxidation wave is related to the presence (and oxidation) of Fe surface species, and from the result shown in Figure 4c, that these surface species can accumulate spontaneously in the absence of applied potential.

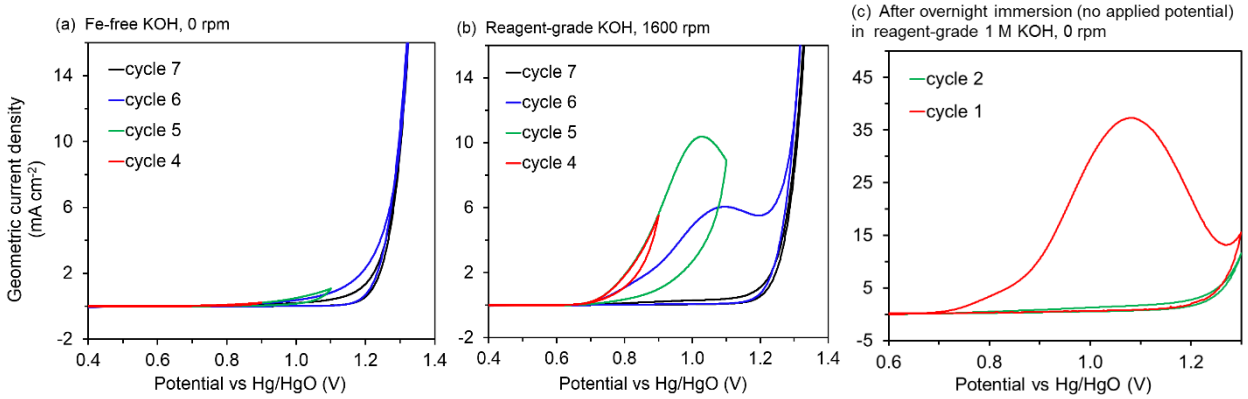

Figure 4.4. Cyclic voltammograms of Au cycled in (a) "Fe-free" 1 M KOH and (b) reagent-grade 1 M KOH, both after three cycles of stabilization cycling to 0.8 V, and (c) after overnight immersion (with no applied potential) in reagent-grade 1 M KOH. The potential was scanned at a rate of 10 mV s^{-1} between 0 and 0.9-1.3 V vs Hg/HgO, for which E^0 for the OER is 0.306 V.

The results presented above clearly demonstrate that the interaction of Fe^{3+}cations with the surface of the Au electrode is reversible. This then raises the question of how such cations react with the surface and are removed from it. We begin the discussion of these issues by noting that the surface of Au immersed in 1 M KOH contains a mixture of hydroxide and oxide species, depending on the applied potential: spectroscopic evidence shows that hydroxide anions will specifically adsorb on Au at potentials below 0.3 V vs Hg/HgO in 0.1 M KOH, and that a mixture of Au oxide/hydroxide is formed at potentials above about 0.3 V.[24, 39-40] In alkaline pH, soluble Fe^{3+} species are expected to be present as FeO_2^- anions.[41] Since the accumulation of surface Fe occurs in the absence of an applied potential, we hypothesize that the following reaction may occur:

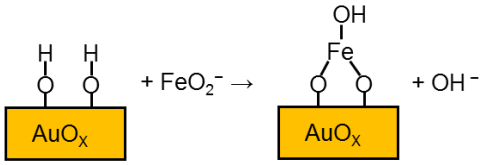

(4.1)

In this simplified representation (for a more detailed structure, see the next section), x = 0.0-1.5 in AuO_x, depending on the extent of oxidation of the Au surface.

We hypothesize that the oxidation wave observed in Figures 4.6b-c is attributable to oxygen evolution coupled with the electrochemical oxidation of surface Fe^{3+} to ferrate(VI) anions via the following reaction:

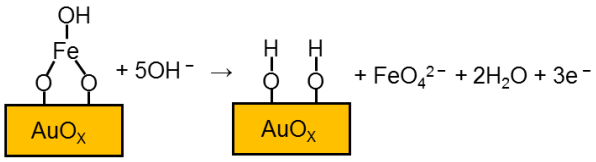

(4.2)

Reaction 4.2 is identical to that proposed to occur for Fe electrodes[42-43] and for a Pt electrode immersed in a solution containing 0.007M FeO_2^- [44] (all in highly concentrated, 10-15 M alkaline electrolytes). The oxidation peaks observed in these studies were attributed to the formation of ferrate(VI) ions (FeO_4^{2-}) and occurred at potentials overlapping the onset of oxygen evolution.[44-45] Thus, we suggest that the adsorption of Fe^{3+} cations via Reaction 4.1 occurs at low anodic potentials and that the removal of these cations from the surface occurs as the potential is raised, concurrent with the onset of OER. Since only a fraction of the Fe initially on the surface is removed in any CV cycle, repeated cycling leads to further removal of the Fe^{3+}cations and the loss in OER activity seen in Figures 4b and 4c.

Reactions 4.1 and 4.2 can also be used to explain the experimental observations of Doyle and Lyons for Au in 1 M NaOH. These authors (and others) observe an oxidation peak at η = 0.4-0.9 V after CV cycling from -0.8 to 0.8 V vs RHE (or -1.7 to -0.1 V vs Hg/HgO at pH 14),[22-23] which they attribute to oxygen evolution over a transient, catalytically active Au(III) surfaquo species. Using a rotating-ring disc setup, they detected an oxygen reduction current on the ring electrode for η = 0.4-0.9 V, confirming that the current generated at the working electrode disc

during the oxidation wave is due (at least in part) to oxygen evolution.[22] Since the surface Fe^{3+} species we propose are also expected to be the catalytically-active sites for oxygen evolution at these potentials, it is not possible to separate the current contributions due to the oxygen evolution reaction from those due to the formation of ferrate(VI) species, but it is clear that both processes occur in the same potential range. A plateau or decrease in current is observed with subsequent anodic potential scans because ferrate(VI) species are soluble and hence their formation results in the removal Fe from the electrode surface via Reaction 4.2, thereby lowering the number of active sites for OER and the OER contribution to the measured current.

Doyle and Lyons have also noted the occurrence of two reduction waves (termed C2' and C2") on "activated" Au,[22] which they suggest are due to the reduction of different forms of hydrous oxides. In the presence of Fe impurities, we observe similar reduction features in the same potential window, from 0.0 to -0.5 V vs Hg/HgO (Figure 4.). We note that the potentials at which these features appear coincide closely with the potentials at which ferrate(VI) reduction (Reaction 4.3) has been reported to occur.[41-44, 46]

$$FeO_4^{2-} + 2H_2O + 3e^- \rightarrow FeO_2^- + 4OH^- \quad (4.3)$$

Oxygen reduction is also expected to occur below ~0.0 V. An increase in the magnitude of these reduction features with additional activation cycling (as observed by Doyle and Lyons) would be consistent with the accumulation of Fe impurities on the Au surface via Reaction 4.1. With the subsequent anodic scan, a larger number of ferrate(VI) species would be formed, and during the return cathodic sweep, a greater reduction current due to Reaction 4.3 would be expected. We note that the ferrate reduction features are smaller than the oxidation wave above 0.7 V due to the removal of surface Fe via Reaction 4.2. This is likely due to 1) diffusion of the ferrate FeO_4^{2-} anions away from the electrode surface and 2) slow chemical decomposition of ferrate(VI) anions via the reaction $FeO_4^{2-} + 1/2H_2O \rightarrow FeO_2^- + O_2 + OH^-$. This decomposition has been observed after ~30 min in 5 M KOH.[41, 47] Therefore, we expect the electrochemical conversion of FeO_4^{2-} to FeO_2^- to predominate on the timescale of the CV experiments conducted in the present study.

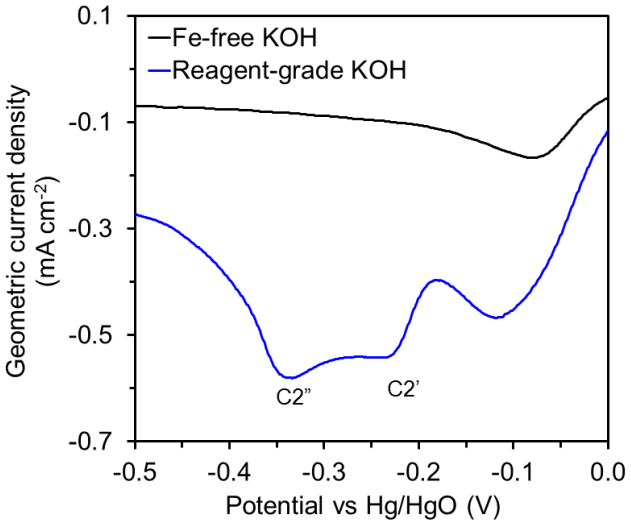

Figure 4.5. Cathodic scans of Au cycled in "Fe-free" and reagent-grade 1 M KOH. The potential was scanned at a rate of 10 mV s^{-1} after 10 cycles between 0 and 0.8 V vs Hg/HgO, for which E^0 for the OER is 0.306 V.

In summary, we attribute the oxidation and reduction waves ascribed previously[22] to the formation of a highly-active Au(III) surfaquo species and hydrous oxide reduction, respectively, to the formation and reduction of ferrate(VI) species in unpurified alkaline electrolytes. The Fe^{3+} electrolyte impurities (present as FeO_2^- in solution) can chemically bind to the Au oxide/hydroxide surface, even in the absence of an applied potential. These species appear to be significantly more catalytically active than pure Au_2O_3, but at overpotentials of 0.4-0.9 V, the surface-bound Fe^{3+} species are oxidized to ferrate(VI) and removed from the hydroxyl-terminated Au_2O_3 surface.

3.3 Theoretical analysis of oxygen evolution activity of Fe-Au_2O_3

DFT calculations (for complete computational details, see SI, S5) were carried out in order to obtain further insights into the cause for the decrease in the OER overpotental observed when Fe is chemically bound to the surface of Au_2O_3. Previous investigations have shown that under conditions relevant to oxygen evolution, Au is oxidized to Au_2O_3.[31] To establish the most appropriate surface structure to use in the model of oxygen evolution, several Au_2O_3 surface indices were investigated. Surface energy profiles as a function of the applied potential of the most stable surfaces are shown in Figure 4.6. At relevant experimental potentials (> 1.23 V vs SHE), the [010] OH-terminated, non-stoichiometric surface (i.e., the surface with the largest O/Au ratio relative to that for the bulk O/Au = 1.5) is found to be the most thermodynamically stable, and was therefore chosen for investigation of the energetics of the OER process.

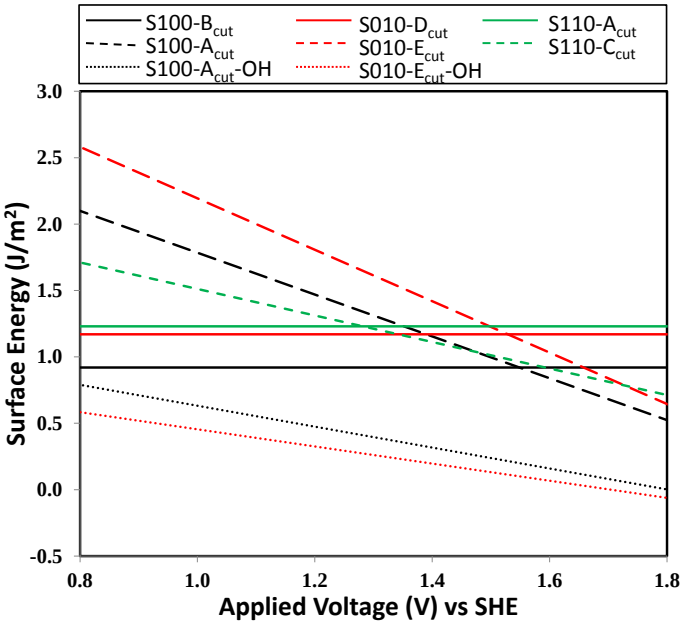

Figure 4.6. Effect of applied potential on the calculated surface free energies for the [100], [010], and [110] index surfaces of Au_2O_3. All possible terminations were considered. The most stable surface at OER-relevant potentials (> 1.23 V) is S010-E_{cut}-OH, which will be used to predict η^{OER}.

The theoretical overpotential calculated from the Gibbs free energy differences between each reaction step is independent of pH, and for greater convenience, can be modeled as if the reaction occurs in an acidic electrolyte:[14, 33-35, 48]

$$H_2O^* \rightarrow OH^* + e^- + H^+ \qquad (4.4)$$

$$OH^* \rightarrow O^* + e^- + H^+ \quad (4.5)$$
$$O^* + H_2O \rightarrow OOH^* + e^- + H^+ \quad (4.6)$$
$$OOH^* \rightarrow O_2 + e^- + H^+ \quad (4.7)$$

Here * represents a surface vacancy site. The calculated standard hydrogen electrode[34] was used to express the chemical potential of protons and electrons at pH 14 and applied potential *U*.

A schematic of the OER surface intermediates involved in Reactions 4.4-4.7 is shown in Figure 4.7 for both pure Au_2O_3 (top) and Fe-Au_2O_3 (bottom). Table 4.2 compares the theoretical OER overpotentials to those measured experimentally at a current density of 0.1 mA cm^{-2} (chosen to avoid potentials where Fe removal from the Au surface is observed in reagent-grade 1 M KOH). (Corresponding chronopotentiometry data is shown in SI, S6). Consistent with experiments, we find that the substitution of an Au site by Fe reduces η^{OER} by 0.29 V (from 0.82 to 0.53 V). For pure Au_2O_3, the *O intermediate is high in energy, and the potential determining step is therefore Reaction 4.5 (*OH oxidation to *O), while for Fe-Au_2O_3, the *O intermediate is relatively more stable and the potential determining step is Reaction 4.6 (*O oxidation to *OOH). These changes can be explained as follows: because the *d*-orbitals of Au are nearly filled and are unable to form π-bonds with oxygen, Au sites bind oxo species very weakly, whereas Fe has fewer *d*-electrons and can form π-bonds with oxygen, leading to a more stable Fe=O motif.[49] Consequently, the binding energetics of OER reaction intermediates attached to Fe cations bound to the surface of Au_2O_3 are more optimal than those of intermediates attached to Au cations.

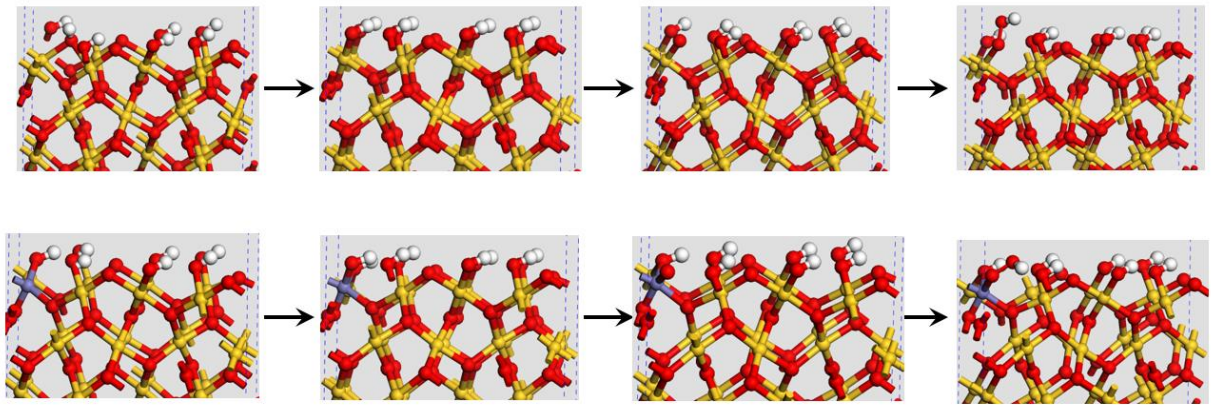

Figure 4.7. Structures of the intermediates (Reactions 4.1-4.4) of the OER over pure Au_2O_3 (top) and Fe chemically bound to Au_2O_3 (bottom).

Table 4.2: Comparison of experimental and computational OER overpotentials

	Experimental η ($j = 0.1$ mA cm^{-2}) (V)	Computational η (V)
Au_2O_3	0.84	0.82
Fe-Au_2O_3	0.49	0.53

4.4. Conclusions

Fe cations present as impurities in 1 M KOH react with the surface of Au electrodes and create active centers for the OER. An increase in the current density above the onset potential for the OER correlates with the Fe concentration in the electrolyte. The OER overpotential over Au decreases from ~0.85 to ~0.4 V with the presence of surface Fe sites at low current densities ($j = 0.1$ mA cm^{-2}), in close agreement with the decrease in the OER overpotential determined from DFT calculations for pure Au_2O_3 vs Fe chemically bound to Au_2O_3. This decrease in the OER overpotential is attributed to the more optimal adsorption energy of intermediates involved in the oxygen evolution reaction. The nearly-filled d-orbitals of Au cause the adsorbed oxo species present on the surface of Au_2O_3 to be weakly bound, while the less occupied d-orbitals of Fe can bind these oxo species more strongly. In contrast to what has been observed for CoOOH and NiOOH, the addition of Fe to Au oxide is reversible at the potentials of interest, and the removal of surface Fe coincides with an oxidation wave at 0.7-1.2 V vs Hg/HgO (η = 0.4-0.9 V). With increased current densities, the applied overpotential reaches a level where Fe removal occurs via the formation of aqueous ferrate(VI) species.

References

1. Katsounaros, I.; Cherevko, S.; Zeradjanin, A. R.; Mayrhofer, K. J. J., Oxygen Electrochemistry as a Cornerstone for Sustainable Energy Conversion. *Angewandte Chemie-International Edition* **2014**, *53*, 102-121.
2. Lewis, N. S.; Nocera, D. G., Powering the Planet: Chemical Challenges in Solar Energy Utilization. *Proceedings of the National Academy of Sciences of the United States of America* **2006**, *103*, 15729-15735.
3. Gust, D.; Moore, T. A.; Moore, A. L., Solar Fuels Via Artificial Photosynthesis. *Accounts of Chemical Research* **2009**, *42*, 1890-1898.
4. Yang, Z. G.; Zhang, J. L.; Kintner-Meyer, M. C. W.; Lu, X. C.; Choi, D. W.; Lemmon, J. P.; Liu, J., Electrochemical Energy Storage for Green Grid. *Chemical Reviews* **2011**, *111*, 3577-3613.
5. Walter, M. G.; Warren, E. L.; McKone, J. R.; Boettcher, S. W.; Mi, Q.; Santori, E. A.; Lewis, N. S., Solar Water Splitting Cells. *Chemical Reviews* **2010**, *110*, 6446-6473.
6. Cook, T. R.; Dogutan, D. K.; Reece, S. Y.; Surendranath, Y.; Teets, T. S.; Nocera, D. G., Solar Energy Supply and Storage for the Legacy and Nonlegacy Worlds. *Chemical Reviews* **2010**, *110*, 6474-6502.
7. McKone, J. R.; Lewis, N. S.; Gray, H. B., Will Solar-Driven Water-Splitting Devices See the Light of Day? *Chemistry of Materials* **2014**, *26*, 407-414.
8. Pletcher, D.; Li, X., Prospects for Alkaline Zero Gap Water Electrolysers for Hydrogen Production. *International Journal of Hydrogen Energy* **2011**, *36*, 15089-15104.
9. Singh, A.; Spiccia, L., Water Oxidation Catalysts Based on Abundant 1st Row Transition Metals. *Coordination Chemistry Reviews* **2013**, *257*, 2607-2622.
10. Suntivich, J.; May, K. J.; Gasteiger, H. A.; Goodenough, J. B.; Shao-Horn, Y., A Perovskite Oxide Optimized for Oxygen Evolution Catalysis from Molecular Orbital Principles. *Science* **2011**, *334*, 1383-1385.
11. Burke, M. S.; Kast, M. G.; Trotochaud, L.; Smith, A. M.; Boettcher, S. W., Cobalt–Iron (Oxy)Hydroxide Oxygen Evolution Electrocatalysts: The Role of Structure and Composition on Activity, Stability, and Mechanism. *Journal of the American Chemical Society* **2015**, *137*, 3638-3648.
12. Klaus, S.; Cai, Y.; Louie, M. W.; Trotochaud, L.; Bell, A. T., Effects of Fe Electrolyte Impurities on Ni(Oh)2/Niooh Structure and Oxygen Evolution Activity. *The Journal of Physical Chemistry C* **2015**, *119*, 7243-7254.
13. Trotochaud, L.; Young, S. L.; Ranney, J. K.; Boettcher, S. W., Nickel-Iron Oxyhydroxide Oxygen-Evolution Electrocatalysts: The Role of Intentional and Incidental Iron Incorporation. *Journal of the American Chemical Society* **2014**, *136*, 6744-6753.
14. Friebel, D., et al., Identification of Highly Active Fe Sites in (Ni,Fe)Ooh for Electrocatalytic Water Splitting. *Journal of the American Chemical Society* **2015**, *137*, 1305-1313.
15. Louie, M. W.; Bell, A. T., An Investigation of Thin-Film Ni–Fe Oxide Catalysts for the Electrochemical Evolution of Oxygen. *Journal of the American Chemical Society* **2013**, *135*, 12329-12337.
16. Iwakura, C.; Honji, A.; Tamura, H., The Anodic Evolution of Oxygen on Co3o4 Film Electrodes in Alkaline Solutions. *Electrochimica Acta* **1981**, *26*, 1319-1326.

17. Laouini, E.; Hamdani, M.; Pereira, M. I. S.; Douch, J.; Mendonça, M. H.; Berghoute, Y.; Singh, R. N., Preparation and Electrochemical Characterization of Spinel Type Fe–Co3o4 Thin Film Electrodes in Alkaline Medium. *International Journal of Hydrogen Energy* **2008**, *33*, 4936-4944.
18. Grewe, T.; Deng, X.; Tüysüz, H., Influence of Fe Doping on Structure and Water Oxidation Activity of Nanocast Co3o4. *Chemistry of Materials* **2014**, *26*, 3162-3168.
19. McCrory, C. C. L.; Jung, S.; Peters, J. C.; Jaramillo, T. F., Benchmarking Heterogeneous Electrocatalysts for the Oxygen Evolution Reaction. *Journal of the American Chemical Society* **2013**, *135*, 16977-16987.
20. May, K. J.; Carlton, C. E.; Stoerzinger, K. A.; Risch, M.; Suntivich, J.; Lee, Y.-L.; Grimaud, A.; Shao-Horn, Y., Influence of Oxygen Evolution During Water Oxidation on the Surface of Perovskite Oxide Catalysts. *The Journal of Physical Chemistry Letters* **2012**, *3*, 3264-3270.
21. Corrigan, D. A., The Catalysis of the Oxygen Evolution Reaction by Iron Impurities in Thin Film Nickel Oxide Electrodes. *Journal of The Electrochemical Society* **1987**, *134*, 377-384.
22. Doyle, R.; Lyons, M. G., The Mechanism of Oxygen Evolution at Superactivated Gold Electrodes in Aqueous Alkaline Solution. *J Solid State Electrochem* **2014**, *18*, 3271-3286.
23. Burke, L. D.; Cunnane, V. J.; Lee, B. H., Unusual Postmonolayer Oxide Behavior of Gold Electrodes in Base. *Journal of the Electrochemical Society* **1992**, *139*, 399-406.
24. Yeo, B. S.; Klaus, S. L.; Ross, P. N.; Mathies, R. A.; Bell, A. T., Identification of Hydroperoxy Species as Reaction Intermediates in the Electrochemical Evolution of Oxygen on Gold. *ChemPhysChem* **2010**, *11*, 1854-1857.
25. Karthik, P. E.; Jeyabharathi, C.; Phani, K. L., Oxygen Evolution Reaction Electrocatalyzed on a Fenton-Treated Gold Surface. *Chemical Communications* **2014**, *50*, 2787-2790.
26. Cherevko, S.; Zeradjanin, A. R.; Keeley, G. P.; Mayrhofer, K. J. J., A Comparative Study on Gold and Platinum Dissolution in Acidic and Alkaline Media. *Journal of the Electrochemical Society* **2014**, *161*, H822-H830.
27. Hoang, T. T. H.; Cohen, Y.; Gewirth, A. A., In Situ Electrochemical Stress Measurements Examining the Oxygen Evolution Reaction in Basic Electrolytes. *Analytical Chemistry* **2014**, *86*, 11290-11297.
28. Othman, S. H.; El-Deab, M. S.; Ohsaka, T., Superior Electrocatalytic Activity of Au (110)-Like Gold Nanoparticles Towards the Oxygen Evolution Reaction. *International Journal of Electrochemical Science* **2011**, *6*, 6209-6219.
29. Peuckert, M.; Coenen, F. P.; Bonzel, H. P., On the Surface Oxidation of a Gold Electrode in in H2so4 Electrolyte. *Surf. Sci.* **1984**, *141*, 515-532.
30. Juodkazis, K.; Juodkazyte, J.; Jasulaitiene, V.; Lukinskas, A.; Sebeka, B., Xps Studies on the Gold Oxide Surface Layer Formation. *Electrochem. Commun.* **2000**, *2*, 503-507.
31. Diaz-Morales, O.; Calle-Vallejo, F.; de Munck, C.; Koper, M. T. M., Electrochemical Water Splitting by Gold: Evidence for an Oxide Decomposition Mechanism. *Chemical Science* **2013**, *4*, 2334-2343.
32. Yeo, B. S.; Bell, A. T., In Situ Raman Study of Nickel Oxide and Gold-Supported Nickel Oxide Catalysts for the Electrochemical Evolution of Oxygen. *Journal of Physical Chemistry C* **2012**, *116*, 8394-8400.
33. Nist X-Ray Photoelectron Spectroscopy Database, Version 4.1. NIST X-ray Photoelectron Spectroscopy Database, Version 4.1: 2012.

34. Rossmeisl, J.; Qu, Z. W.; Zhu, H.; Kroes, G. J.; Nørskov, J. K., Electrolysis of Water on Oxide Surfaces. *Journal of Electroanalytical Chemistry* **2007**, *607*, 83-89.
35. Nørskov, J. K.; Rossmeisl, J.; Logadottir, A.; Lindqvist, L.; Kitchin, J. R.; Bligaard, T.; Jónsson, H., Origin of the Overpotential for Oxygen Reduction at a Fuel-Cell Cathode. *The Journal of Physical Chemistry B* **2004**, *108*, 17886-17892.
36. Rossmeisl, J.; Logadottir, A.; Nørskov, J. K., Electrolysis of Water on (Oxidized) Metal Surfaces. *Chemical Physics* **2005**, *319*, 178-184.
37. Tripković, V.; Skúlason, E.; Siahrostami, S.; Nørskov, J. K.; Rossmeisl, J., The Oxygen Reduction Reaction Mechanism on Pt(1 1 1) from Density Functional Theory Calculations. *Electrochimica Acta* **2010**, *55*, 7975-7981.
38. Janik, M. J.; Taylor, C. D.; Neurock, M., First-Principles Analysis of the Initial Electroreduction Steps of Oxygen over Pt(111). *Journal of The Electrochemical Society* **2009**, *156*, B126-B135.
39. Sun, J.; Fang, Y.-H.; Liu, Z.-P., Electrocatalytic Oxygen Reduction Kinetics on Fe-Center of Nitrogen-Doped Graphene. *Physical Chemistry Chemical Physics* **2014**, *16*, 13733-13740.
40. Desilvestro, J.; Weaver, M. J., Surface Structural Changes During Oxidation of Gold Electrodes in Aqueous Media as Detected Using Surface-Enhanced Raman Spectroscopy. *Journal of Electroanalytical Chemistry and Interfacial Electrochemistry* **1986**, *209*, 377-386.
41. Zhang, Y.; Gao, X.; Weaver, M. J., Nature of Surface Bonding on Voltammetrically Oxidized Noble Metals in Aqueous Media as Probed by Real-Time Surface-Enhanced Raman Spectroscopy. *The Journal of Physical Chemistry* **1993**, *97*, 8656-8663.
42. Beck, F.; Kaus, R.; Oberst, M., Transpassive Dissolution of Iron to Ferrate(Vi) in Concentrated Alkali Hydroxide Solutions. *Electrochimica Acta* **1985**, *30*, 173-183.
43. De Koninck, M.; Bélanger, D., The Electrochemical Generation of Ferrate at Pressed Iron Powder Electrode: Comparison with a Foil Electrode. *Electrochimica Acta* **2003**, *48*, 1435-1442.
44. Mácová, Z.; Bouzek, K.; Sharma, V., The Influence of Electrolyte Composition on Electrochemical Ferrate(Vi) Synthesis. Part I: Anodic Dissolution Kinetics of Pure Iron. *J Appl Electrochem* **2010**, *40*, 1019-1028.
45. Bouzek, K.; Roušar, I.; Bergmann, H.; Hertwig, K., The Cyclic Voltammetric Study of Ferrate(Vi) Production. *Journal of Electroanalytical Chemistry* **1997**, *425*, 125-137.
46. Híveš, J.; Mácová, Z.; Benová, M.; Bouzek, K., Comparison of Ferrate(Vi) Synthesis in Eutectic Naoh–Koh Melts and in Aqueous Solutions. *Journal of The Electrochemical Society* **2008**, *155*, E113-E119.
47. Beverskog, B.; Puigdomenech, I., Revised Pourbaix Diagrams for Iron at 25–300 °C. *Corrosion Science* **1996**, *38*, 2121-2135.
48. Wagner, W. F.; Gump, J. R.; Hart, E. N., Factors Affecting Stability of Aqueous Potassium Ferrate(Vi) Solutions. *Analytical Chemistry* **1952**, *24*, 1497-1498.
49. Venkatadri, A. S.; Wagner, W. F.; Bauer, H. H., Ferrate(Vi) Analysis by Cyclic Voltammetry. *Analytical Chemistry* **1971**, *43*, 1115-1119.
50. Shi, H. Q.; Asahi, R.; Stampfl, C., Properties of the Gold Oxides Au2o3 and Au2o: First-Principles Investigation. *Phys Rev B* **2007**, *75*.
51. Jones, P. G.; Rumpel, H.; Schwarzmann, E.; Sheldrick, G. M.; Paulus, H., Gold(Iii) Oxide. *Acta Crystallographica Section B* **1979**, *35*, 1435-1437.

4.5. Supporting Information

S4.1. Procedure for removal of Fe from 1 M KOH

To remove Fe from 1 M KOH, we used the procedure established by Trotochaud et al.[S1]

1. Within a 50 mL polypropylene centrifuge tube (VWR), ~2 g of nickel nitrate hexahydrate (99.999% Sigma Aldrich) was dissolved in 4 mL high-purity water (18 MΩ resistance, Milli Q Millipore),

2. 20 mL of 1 M KOH (prepared from 45% Baker Analyzed Electronic Grade KOH solution, VWR JT3144-3) was added to the tube to precipitate $Ni(OH)_2$. After shaking, the mixture was centrifuged and the supernatant decanted.

3. The $Ni(OH)_2$ precipitate was washed three times using 20 mL Millipore water and 2 mL of 1 M KOH. For each washing step, the nickel hydroxide was redispersed in solution and then re-centrifuged for 2 min at 4000 rpm.

4. After the third nickel hydroxide washing step, the $Ni(OH)_2$ was used to purify up to three 45-mL aliquots of 1 M KOH. For each purification, ~45 mL of 1 M KOH (from VWR JT3144-3) was added to the centrifuge tube, and the tube was shaken until the nickel hydroxide was fully dispersed (5-10 minutes).

5. After at least 30 minutes of resting, the tube was centrifuged at 4000 rpm for 4 minutes and the purified KOH decanted for direct use as “Fe-free” KOH electrolyte.

S4.2. Electrochemical and Spectroscopic Evidence of Ni over Au after 1 M KOH exposure

Additional CV features over Au due to the presence $Ni(OH)_2$/NiOOH are observed at 0.43 and 0.36 V and correspond to $Ni(OH)_2$ oxidation and NiOOH reduction, respectively, with 1600 rpm in Fe-free electrolyte (Figure S4.2). The increased Ni content of this electrolyte is due to the purification procedure outlined in Section S4.1. To minimize the accumulated Ni content over Au, most CV scans for Fe-free 1 M KOH were completed at 0 rpm.

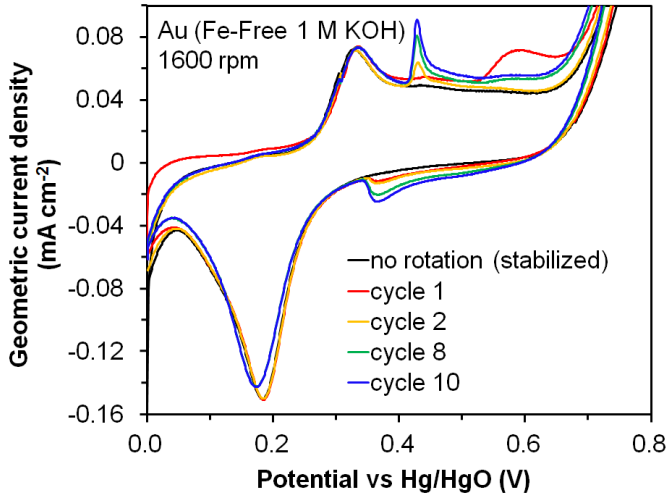

Figure S4.2. Cyclic voltammograms of Au cycled in 1 M Fe-free KOH with a rotation rate of 1600 rpm. E^0 for OER is 0.306 V vs. Hg/HgO, and the scan rate is 10 mV s^{-1}.

S4.3. Au with increasing Fe impurity concentration

The current above 0.65 V increases with increasing electrolyte Fe concentration, as shown in Figure S4.3.

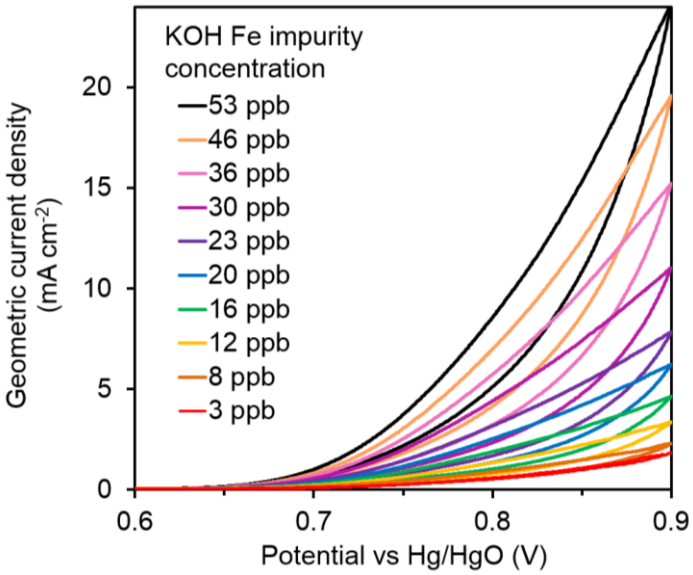

Figure S4.3. Cyclic voltammograms of Au cycled in 1 M KOH with varying Fe impurity concentration (increased by adding successive amounts of 1 M electronic-grade KOH to 1 M Fe-free KOH). A rotation rate of 1600 rpm was used. E^0 for OER is 0.306 V vs. Hg/HgO, and the scan rate is 10 mV s^{-1}.

S4.4. Surface Fe and Ni concentrations determined from XPS and ICP-MS

Table S4.4: XPS and ICP-MS quantification of Fe and Ni on Au electrodes after electrochemical experiments

	XPS			ICP-MS		
	(Fe/Fe+Au) %	(Ni/Ni+Au) %	(Fe/Fe+Ni) %	Ni ppb	Fe ppb	(Fe/Fe+Ni) %
Fe-free, 0 rpm	0.3%	2.4%	12%	6.4	3.0	32%
Fe-free, 1600 rpm	0.1%	3.3%	3%	21.5	4.9	19%
Reagent-grade, 0 rpm	0.8%	1.6%	32%	8.5	7.7	48%
Reagent-grade, 1600 rpm	1.5%	2.9%	33%	6.0	11.3	65%
Electronic-grade, 0 rpm	1.1%	1.8%	39%	--	--	--
Electronic-grade, 1600 rpm	2.1%	1.8%	54%	--	--	--

S4.5. Computational details

DFT calculations were performed using the Vienna ab initio Simulation Package (VASP)[S2-S5] with the projector augmented wave pseudopotentials[S6,S7] and the PBE functional.[S8] The plane wave energy cutoff was set to 400 eV, and electron smearing was employed using the Gaussian-smearing technique with a width of k_BT = 0.1 eV. All calculated values of energy were extrapolated to k_BT = 0. Monkhorst-Pack *k*-point grids of 2×2×6, 2×6×1, 6×2×1, 6×2×1 were chosen to sample the reciprocal spaces of the bulk Au_2O_3, and Au_2O_3 [100], [010], and [110] index surfaces, respectively. The optimized cell parameters are a = 12.90 Å, b = 10.57 Å, and c = 3.85 Å, which are close to the experimental values (a = 12.83 Å, b = 10.52 Å, c = 3.84 Å).[S9] For surface calculations, at least 10 Å vacuum spacing between adjacent images was used to prevent the interaction between the replicas along the *z*-direction. Spin-polarized wavefunctions were used for all calculations. It should be noted that calculating surface energy requires the top and bottom layers to be identical, as a result, due to having a low symmetry in Au_2O_3, among seven low index surfaces ([100], [010], [001], [110], [101], [011], and [111]) we only can consider three ([100], [010], and [110], all shown in Figure S5a). For those three index surfaces, we considered all possible terminations. Procedures for calculating applied-potential-dependent surface energy and η^{OER} were similar to those used in (1) Bajdich et al *J. Am. Chem. Soc.* **2013**, *135*, 13521 and (2) Cheng et al. *J. Phys. Chem. C*, **2014**, *118*, 29482, except that the solvation energies were calculated using the Poisson-Boltzmann implicit solvation model[S10,S11] with a dielectric constant ε = 80 for water.

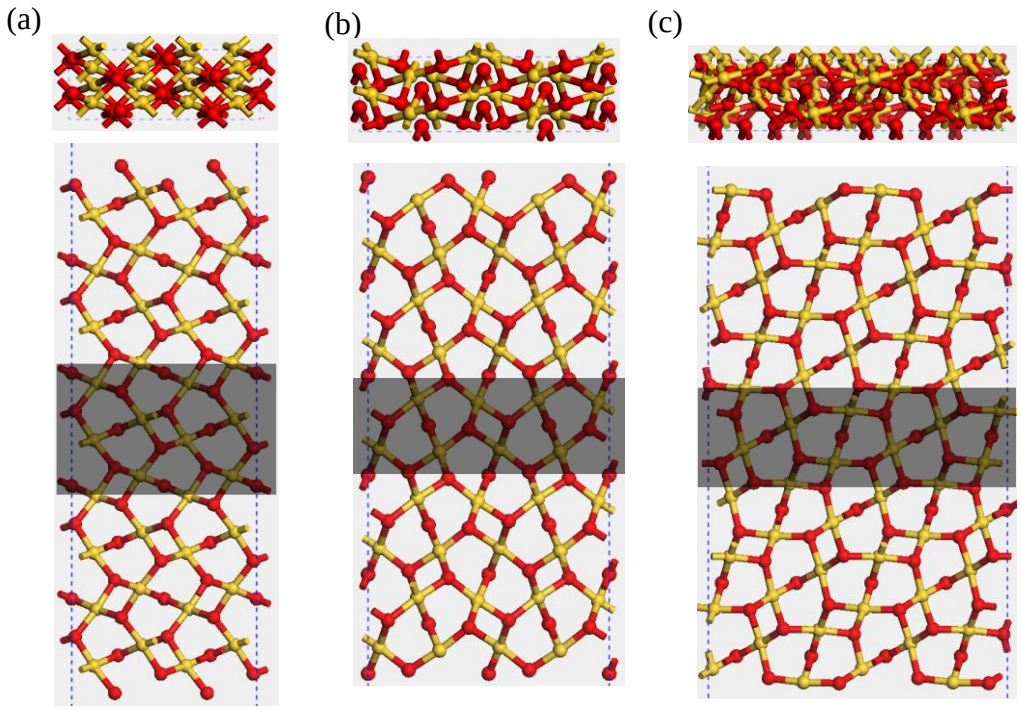

Figure S4.5a. The top and side views of the [100], [010], and [110] surfaces. The positions of the atoms in the shaded areas are fixed during geometry optimization.

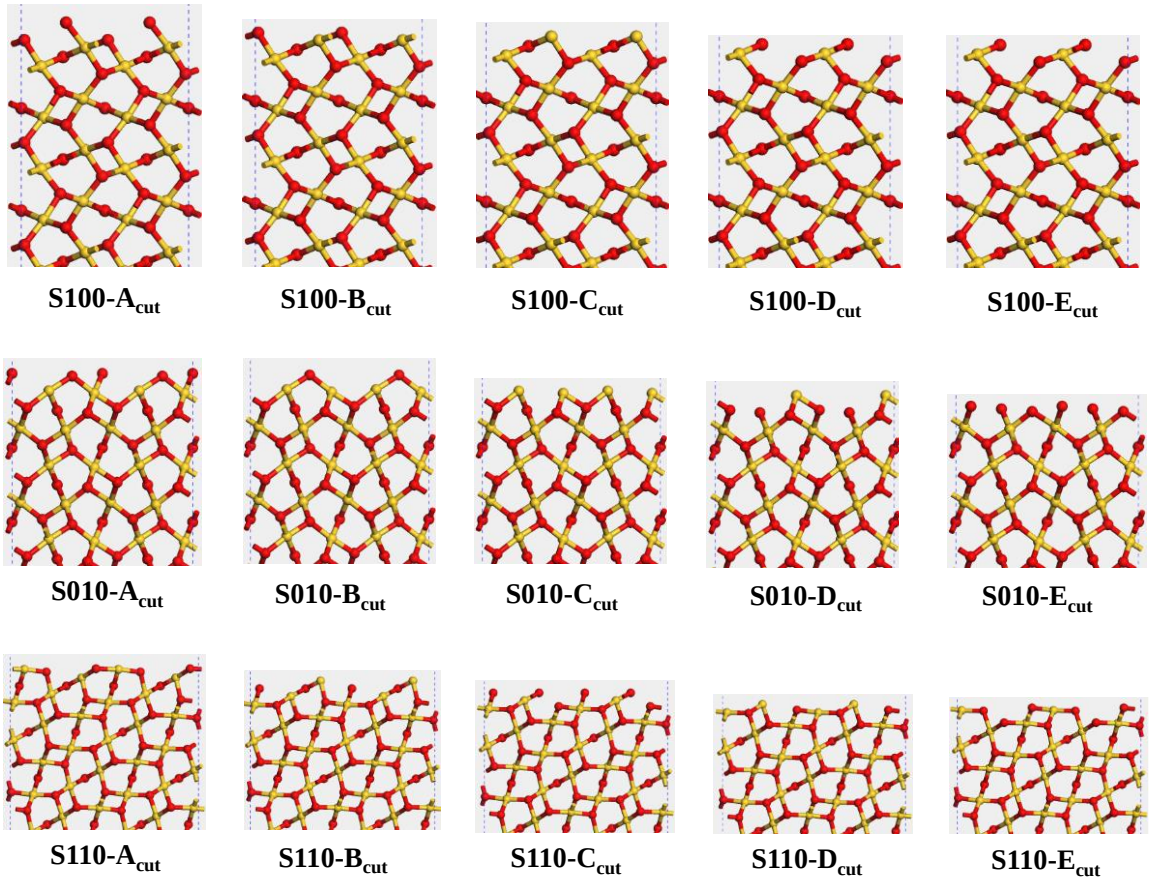

Figure S4.5b. Images of the top layers for [100], [010], and [110] surfaces with different terminations.

S4.6. Chronopotentiometry measurements in "Fe-free" and reagent-grade 1 M KOH

For more direct comparison of experimental to DFT-calculated OER overpotentials, chronopotentiometry experiments were carried out (Figure S4.6). A 0.1 mA cm^{-2} current density was chosen to avoid the potential regime at which Fe removal occurs from the Au surface. First, a 0.1 mA cm^{-2} current was held until a stable potential was reached (10-15 minutes) in Fe-free and reagent-grade 1 M KOH (a comparable potential is observed in both electrolytes). Next, to accumulate electrolyte Fe on the surface (in reagent-grade KOH, but also completed in Fe-free KOH), a -0.1 mA cm^{-2} geometric current density was applied for 80 s.

After this hold, a significant reduction in the potential required to reach 0.1 mA cm^{-2} is observed in reagent-grade KOH (1.15 V before the cathodic hold vs 0.8 V after the hold), while a similar potential is observed before and after this cathodic hold in Fe-free 1 M KOH (1.16 and 1.15 V, respectively), supporting that surface Fe is responsible for the overpotential decrease observed in reagent-grade 1 M KOH.

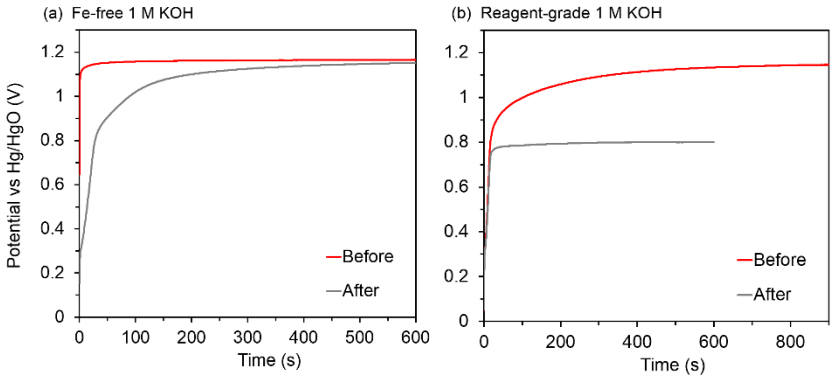

Figure S4.6. Representative chronopotentiometry measurements used for activity determination, for Au in (a) Fe-free 1 M KOH and (b) reagent-grade 1 M KOH before and after an 80 s hold at -0.1 mA cm^{-2}. Measurements were collected at a geometric current density of 0.1 mA cm^{-2}, and the OER equilibrium potential is 0.306 V.

References

S1. Trotochaud, L.; Young, S. L.; Ranney, J. K.; Boettcher, S. W., Nickel-Iron Oxyhydroxide Oxygen-Evolution Electrocatalysts: The Role of Intentional and Incidental Iron Incorporation. *J Am Chem Soc* **2014**, *136*, 6744-6753.

S2. Kresse, G.; Hafner, J. ab-Initio Molecular-Dynamics Simulation of the Liquid-Metal Amorphous-Semiconductor Transition in Germanium. *Phys. Rev. B* **1994**, 49, 14251-14269.

S3. Kresse, G.; Hafner, J. ab-initio Molecular-Dynamics for Liquid-Metals. Phys. Rev. B **1993**, 47, 558-561.

S4. Kresse, G.; Furthmuller, J. Efficient Iterative Schemes for ab Initio Total-Energy Calculations Using a Plane-Wave Basis Set. Phys. Rev. B **1996**, 54, 11169-11186.

S5. Kresse, G.; Furthmuller, J. Efficiency of Ab-Initio Total Energy Calculations for Metals and Semiconductors Using a Plane-Wave Basis Set. Comp. Mater. Sci. **1996**, 6, 15-50.

S6. Kresse, G.; Joubert, D. From Ultrasoft Pseudopotentials to the Projector Augmented-Wave Method. Phys. Rev. B **1999**, 59, 1758-1775.

S7. Blochl, P. E. Projector Augmented-Wave Method. Phys. Rev. B **1994**, 50, 17953-17979.

S8. Perdew, J. P.; Burke, K.; Ernzerhof, M. Generalized Gradient Approximation Made Simple. Phys. Rev. Lett. **1996**, 77, 3865-3868.

S9. Jones, P. G.; Rumpel, H.; Schwarzmann, E.; Sheldrick, G. M.; Paulus, H. Gold(Iii) Oxide. Acta. Crystallogr. B **1979**, 35, 1435-1437.

S10. Fishman, M.; Zhuang, H. L. L.; Mathew, K.; Dirschka, W.; Hennig, R. G. Accuracy of Exchange-Correlation Functionals and Effect of Solvation on the Surface Energy of Copper. Phys. Rev. B **2013**, 87.

S11. Mathew, K.; Sundararaman, R.; Letchworth-Weaver, K.; Arias, T. A.; Hennig, R. G. Implicit Solvation Model for Density-Functional Study of Nanocrystal Surfaces and Reaction Pathways. J. Chem. Phys. **2014**, 140.

Chapter 5

Role of Catalyst Preparation on the Electrocatalytic Activity of $Ni_{1-x}Fe_xOOH$ for the Oxygen Evolution Reaction

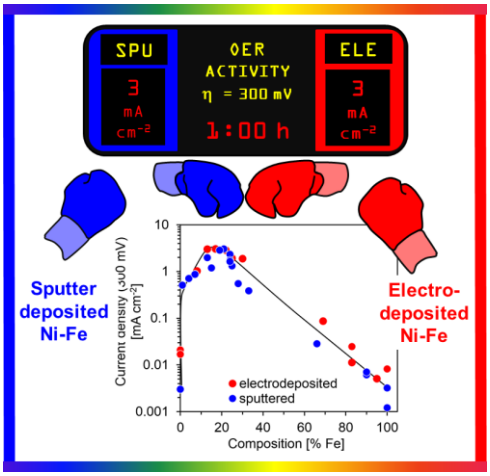

Abstract

$Ni_{1-x}Fe_xOOH$ thin films prepared via cathodic electrodeposition have been demonstrated to be highly active catalysts for the oxygen evolution reaction (OER) in basic media. Integration of these catalysts with light-absorbing semiconductors is required for photoelectrochemical fuel generation. However, the application of cathodic potentials required for typical electrochemical catalyst deposition limits the library of compatible photoanode materials. Sputter deposition of catalysts circumvents this limitation by enabling facile catalyst layering without cathodic potentials. In this work, we compare the structure and OER activity of sputter-deposited and electrodeposited $Ni_{1-x}Fe_xOOH$ thin films. Electrochemical cycling converts sputtered $Ni_{1-x}Fe_x$ metallic films to the desired oxides/(oxy)hydroxides. Both film preparation methods give catalysts with similar electrochemical behavior across all compositions. Additionally, OER activity is comparable between the deposition methods, with maximum activity for films with ~20% Fe content (320 mV overpotential at j = 10 mA cm^{-2} geometric). Electrochemical cycling to convert sputtered metallic $Ni_{1-x}Fe_x$ films to metal oxides/(oxy)hydroxides is found to lower the Fe:Ni ratio, while the electrodeposited films exhibit comparable Fe:Ni ratios before and after electrochemical cycling and characterization. Structurally, Fe is found to incorporate within the $Ni(OH)_2$/NiOOH lattice for films formed through both sputter-deposition and electrodeposition. Layered films were also compared to codeposited 1:1 Fe:Ni films. It is found that for layered films, an Fe top layer inhibits the electrochemical conversion of metallic Ni to $Ni(OH)_2$/NiOOH, thus reducing the amount of $Ni_{1-x}Fe_xOOH$ OER-active phase formed. In contrast, migration of metals within Ni-on-top films occurs readily during electrochemical cycling, resulting in films that are structurally and electrochemically indistinguishable from codeposited $Ni_{1-x}Fe_xOOH$. These findings enable direct application of $Ni_{1-x}Fe_xOOH$ sputtered films to a wider library of photoanodes for light-driven water-splitting applications.

5.1 Introduction

Nickel-iron (oxy)hydroxides ($Ni_{1-x}Fe_xOOH$) have been demonstrated as some of the best electrocatalysts for the oxygen evolution reaction (OER) in alkaline electrolytes,[1-5] with catalytic activities that surpass those of precious-metal iridium oxide catalysts.[2] $Ni_{1-x}Fe_xOOH$ and other OER catalysts have recently received renewed interest for application in photoelectrochemical devices for solar energy conversion and storage.[6-12] One of the most commonly reported preparation methods for $Ni_{1-x}Fe_xOOH$ is cathodic electrodeposition from a solution of nickel and iron sulfate and/or nitrate salts,[13-17] but such deposition conditions may not be amenable to integration with many semiconductor photoanode materials. The composition and uniformity of electrodeposited catalyst films can be greatly influenced by the lower electrical conductivity of semiconductors relative to the metallic substrates often used for study of the intrinsic catalyst properties.[8-9, 18] Furthermore, the surfaces of oxide photoanodes, such as hematite or bismuth vanadate, can be reduced under the cathodic deposition conditions, greatly affecting the properties of the photoanode and photoanode-catalyst interface.[8, 19]

High-efficiency photoelectrochemical devices can only be realized by enabling successful integration of electrocatalyst and photoanode materials in a way that minimally alters the optimized properties of the individual components. Physical vapor deposition methods may therefore be preferable to electrodeposition for coupling of electrocatalysts with certain photoanode substrates. Sputter deposition provides greater flexibility when choosing a substrate material (as electrochemical stability and electrical conductivity of the substrate are not important deposition parameters), ease of catalyst composition control, and high catalyst uniformity across the substrate. Considering the complexity and number of the different processes that occur at photoelectrode-catalyst interfaces,[8, 19-21] it is essential to understand whether changing the method of catalyst preparation alone influences catalyst activity and stability. To our knowledge, there is only one previous study of $Ni_{1-x}Fe_xOOH$ OER catalysts prepared by sputter deposition.[22] Miller and Rocheleau found that sputtered iron-doped NiO_x produced a more uniform catalyst layer with greater adhesion to the Ni substrate compared to electrodeposited Fe-doped NiO_x, enabling over 7000 hours of film stability under OER conditions. However, their work only investigated Fe contents below 6% (percent of total metals – maximum activity was found at 5.2% Fe, the highest codeposited Fe amount in the study). Furthermore, activities of sputtered films were compared to electrodeposited film activities presented in a previous study by Corrigan,[15] and differences could arise due to variations between the two studies in substrate roughness, film active surface area, and other film properties and characterization methods.[15, 22]

In this work, we present a detailed study of $Ni_{1-x}Fe_xOOH$ OER electrocatalysts across the entire composition range for both electrodeposited and sputtered films. We demonstrate that $Ni_{1-x}Fe_xOOH$ catalysts prepared by either method have essentially indistinguishable electrochemical behavior and OER activity, and the Fe:Ni ratio yielding optimal OER activity for sputtered films is well within the range of that measured here (and previously) for electrodeposited $Ni_{1-x}Fe_xOOH$. In addition, we show that the extended electrochemical cycling required to fully convert sputtered $Ni_{1-x}Fe_x$ metallic films to the OER active (oxy)hydroxides results in a significant decrease in the film Fe content. Once electrochemical conversion of sputtered $Ni_{1-x}Fe_x$ metal to $Ni_{1-x}Fe_xOOH$ is complete, however, the Fe:Ni ratio remains stable during ~2 h of oxygen evolution activity measurements. We also investigate differences in catalyst structure and activity due to cosputtering vs. layered-sputtering of Ni and Fe. This study provides a direct comparison of these different film preparation methods, demonstrating that highly active OER catalysts can be generated through either sputter deposition or electrodeposition. The availability of sputter-deposited $Ni_{1-x}Fe_xOOH$

with high catalytic activity and stability indistinguishable from electrodeposited $Ni_{1-x}Fe_xOOH$ may be advantageous for integration of these catalysts with certain semiconductor photoanode materials.

5.2 Experimental

5.2.1. Preparation of Catalyst Films

Electrocatalyst films were either electrodeposited or sputter-deposited onto gold rotating disc electrodes (Pine Research Instrumentation). The gold electrodes (5 mm diameter) were fabricated from 99.95% purity (DOE Business Center for Precious Metals Sales and Recovery – BCPMSR). Prior to electrodeposition or sputter deposition, Au discs were polished mechanically with 1 and 0.05 mm alumina slurries, with 10 min of sonication in ultrapure water (18.2 MΩ cm, EMD Millipore) after each polishing step. The Au surface was then stabilized through electrochemical cycling in 0.1 M "Fe-free" KOH from -1.0 to 0.7 V vs Hg/HgO (CH Instruments, filled with 1 M KOH) at 10 mV s^{-1} for ~30 cycles. Fe-free KOH electrolyte was obtained by following a procedure similar to that of Trotochaud et al.,[23] in which powders of $Ni(OH)_2$ are used to purify KOH solutions. The exact procedure used in this work is provided in the Supporting Information (SI S5.1). The electrodes were then briefly rinsed with ultrapure water and dried under a N_2 gas stream prior to film deposition.

Films produced by electrodeposition and sputter deposition were targeted to contain ~3-4 × 10^{15} metal atoms (~2 nm thick sputtered $Ni_{1-x}Fe_x$ metal; ~7 nm thick electrodeposited $Ni_{1-x}Fe_x(OH)_2$ assuming a total film density that is a weighted average of the constituents $Ni(OH)_2$ and $Fe(OH)_2$ – 4.1 and 3.4 g cm^{-3}, respectively). Film thicknesses of ~2 nm were targeted to ensure the sputtered metallic films fully converted to the (oxy)hydroxide phase, confirmed via XPS after electrochemical characterization and by integrating the Ni redox peak areas. (For example, 3.1-3.7 × 10^{15} electrons are transferred during the reduction of NiOOH to $Ni(OH)_2$ for a sputtered Ni film, which is comparable to the target value of Ni atoms sputtered.)

Films were electrodeposited with a cathodic current density of -50 μA cm^{-2} for 113 s using solutions of nickel sulfate hexahydrate (≥99.99% trace metals basis, Sigma-Aldrich 467901) and iron sulfate heptahydrate (ACS Reagent ≥99.0%, Sigma-Aldrich 215422). Preparation of nickel and iron sulfate deposition solutions are detailed in our previous work (concentrations of deposition solutions with resulting Fe compositions are detailed in Supporting Information S5.2), along with estimations of the film thicknesses as determined by inductively coupled plasma optical emission spectroscopy (ICP-OES).[24] We note that different nomenclature is used to distinguish target and measured compositions. For example, a 50% Fe target composition is noted as x = 0.5, while a 50% Fe composition determined via XPS is notated as $Ni_{0.5}Fe_{0.5}$.

Sputter depositions were carried out using an AJA International ATC Orion 5 sputtering instrument. $Ni_{1-x}Fe_x$ films were obtained by cosputtering two separate metallic Ni and Fe targets (Kurt Lesker, 99.9% Ni and 99.95% Fe, 2 in. diameter). DC and RF power supplies were used for Ni and Fe, respectively. Typical powers ranged from 15 to 107 W for Ni and 29 to 200 W for Fe. This enabled preparation of mixed $Ni_{1-x}Fe_x$ films with Fe contents of $0.05 \leq x \leq 0.95$. Total deposition rates ranged between 0.04 and 0.08 nm s^{-1}, depending on the targeted film composition (see SI for deposition parameters). The base pressure in the deposition chamber was below 1 × 10^{-7} Torr prior to deposition, and depositions were carried out at room temperature under an atmosphere of 15 mTorr Ar. An aluminum shadow mask was used to confine the deposition area to the 5 mm diameter gold electrode. The rates and compositions were estimated via individual rate calibrations with an internal quartz crystal microbalance and verified by ICP-OES (Supporting

Information). In the case of layered films, the deposition parameters were identical to those for mixed films of the same overall composition, except that the shutters were controlled to enable sequentially deposited elemental layers.

Since $Ni_{1-x}Fe_x$ films prepared by sputter deposition are metallic, they require electrochemical conversion to the $Ni_{1-x}Fe_xOOH$ catalytic phase in KOH. Although only the sputtered films require electrochemical conversion to the (oxy)hydroxide, for consistency, *both* sputtered *and* electrodeposited films were cycled between 0.0 and 0.7 V vs. Hg/HgO at 10 mV s^{-1} in 0.1 M KOH for the same duration (14-16 hours) prior to electrochemical characterization. Representative voltammograms collected throughout this cycling "stabilization" process for sputtered and electrodeposited films can be found in the Supporting Information.

5.2.2. Electrochemical Characterization

$Ni_{1-x}Fe_x$ films with $x \leq 0.90$ were characterized in "Fe-free" KOH. For films with $x > 0.90$, commercial KOH (prepared from Baker Analyzed Electronic Grade KOH solution, VWR JT3144-3) was used as the electrolyte, since the purified Fe-free electrolyte is expected to contain low-levels of $Ni(OH)_2$ impurities after the electrolyte cleaning process that may alter the film composition during electrochemical characterization. The uncompensated series resistance iR_u was determined by potentiostatic electrochemical impedance spectroscopy, and the measured ohmic resistance value was internally compensated at 95%. Cyclic voltammograms were collected at 10 mV s^{-1}. For chronopotentiometric experiments, the full iR_u value was corrected manually during data analysis. For rotating-disk electrode (RDE) experiments, a rotation rate of 1600 RPM was used. All electrochemical measurements were carried out in a glass-free environment to prevent etching of glass components by the caustic electrolyte, which can introduce Fe and other impurities into the solution. All potentials are reported vs a Hg/HgO reference electrode (CH Instruments) filled with 1 M KOH. The equilibrium potential for the oxygen evolution reaction 0.1 M KOH (pH 13) is 0.365 V vs. the Hg/HgO reference. A coiled Pt wire served as the counter electrode (99.95%, DOE BCPMSR) and was placed within a porous polypropylene compartment inside the electrochemical cell. The Pt counter electrodes were periodically cleaned by overnight soaking in 1 M H_2SO_4.

5.2.3. In Situ Raman Spectroscopy

Raman spectra were collected using a confocal Raman microscope (LabRAM HR, Horiba Yvon Jobin) with an excitation wavelength of 633 nm. The power was ~1.5 mW at the sample surface and the spot size of the laser beam is estimated to be between 1 and 2 μm. Acquisition times were typically 3 s and the spectral resolution is ~1 cm^{-1} with a 600 mm^{-1} grating. Spectral shifts were calibrated using the silicon phonon mode (520.7 cm^{-1}) of a silicon wafer. High wavenumber spectra were background subtracted in the instrument software (Labspec) to more clearly show features in this region.

In situ Raman spectra were collected for catalyst films of select compositions under controlled electrochemical potentials using a home-made cell fabricated from Teflon. The cell contained a Teflon-sheathed gold working electrode (5 mm diameter) oriented at the bottom of the cell. We employed a water-immersion objective (70 × mag., N. A. = 1.23, LOMO) which was protected from the corrosive KOH electrolyte by a 0.0005" thick Teflon film (American Durafilm). A droplet of water was placed between the objective lens and the film to retain high illumination/collection efficiencies.

Electrodeposited films were prepared on working electrodes in a Teflon cell, while sputter-deposited films were prepared using aluminum shadow masks which confined the deposition of the film to the exposed gold working electrode. All films were cycled for 15 h prior to

characterization by Raman spectroscopy. Raman spectra were collected as the potential of the working electrode was scanned at a rate of 1 mV s^{-1}. A Hg/HgO (filled with 1M KOH) reference electrode and a Pt wire counter electrode were used for electrochemical Raman experiments, and all experiments were performed in 0.1 M KOH electrolyte at room temperature.

5.2.4. X-ray Photoelectron Spectroscopy

X-ray photoelectron spectra were collected with a Kratos Axis Ultra spectrometer using a non-monochromatic Mg Kα source (10 mA, 15 kV). The Al Kα source was not used due to the presence of Ni LMM Auger features overlapping with the Fe $2p_{3/2}$ peak. The base pressure in the analytical chamber was ~7 x 10^{-9} Torr. Spectra shown in this work (Ni 2p, Fe 2p, O 1s, Au 4f, C 1s) were collected with a pass energy of 20 eV and a step energy of 50 meV. The Fe 2p and Ni 2p regions were collected using dwell times of 300-500 ms and were averages of 5-10 scans to obtain high spectral signal-to-noise. The composition (by metal content) was estimated using relative sensitivity factors of 21.1, 16.0, and 17.4 for Ni 2p, Fe 2p, and Au 4f, respectively. A Shirley background was used for the Ni 2p region, and a Shirley or linear background was used for the Fe 2p region to accommodate the rising background from an oxygen Auger feature (O KLL) with an onset near 732 eV binding energy. (See Supporting Information for representative spectra with background fits.) The Au 4f spectrum for the underlying gold substrate (Au $4f_{7/2}$ at 84.0 eV)[25] was used for spectral charge-shift calibration. Angle-resolved X-ray photoelectron spectroscopy (XPS) measurements were carried out by varying the electron takeoff angle between 0° and 70° with respect to the sample normal. All spectra were analyzed using CasaXPS (Casa Software, Ltd).

5.3. Results and Discussion

5.3.1 Comparison of Codeposited $Ni_{1-x}Fe_xOOH$ Films Prepared by Sputter Deposition and Electrodeposition

5.3.1.1. Effects of Stabilization Cycling and Electrochemical Characterization on Film Composition

To check compositional stability of both sputter-deposited and electrodeposited samples, Fe content was determined for x = 0.25 and x = 0.50 films prepared by each deposition method as-deposited and after completion of all electrochemical treatments (stabilization CV cycling followed by characterization). As shown in Table 1, the x = 0.25 electrodeposited sample displayed no clear loss of Fe after electrochemical stabilization and characterization, while the x = 0.50 electrodeposited sample exhibits a small reduction in Fe content (56% Fe as-deposited vs 44% Fe, with % Fe given as the percent of total metals [Ni + Fe] as determined via XPS).

In contrast, significant Fe loss is observed for both sputter-deposited samples after electrochemical stabilization and characterization. The sample with x = 0.25 was determined to contain 14% Fe, while the x = 0.50 sample contained 29% Fe. To determine if the Fe:Ni ratio is changing during the 15 h stabilization cycling or during electrochemical characterization, the Fe contents of sputtered films were also determined after 15 h of stabilization cycling but before electrochemical characterization. For both x = 0.25 and x = 0.50 sputtered films, the Fe contents (~15% and ~30% Fe, respectively) were similar after stabilization cycling vs after electrochemical characterization.

From these results (as well as the angle-resolved XPS measurements discussed in Section 3.2), it is clear that a significant amount of Fe is lost from the sputtered films when the films convert from as-deposited metal to metal oxide/hydroxide during stabilization cycling. However, once this transformation is complete, the relative Fe contents remain stable during electrochemical characterization (i.e. under oxygen evolution conditions). We observed Fe loss during stabilization for sputtered films with target compositions of $0.25 \leq x \leq 0.75$ (Table S2.1). Therefore, all further

comparisons are made using % Fe contents determined by XPS after electrochemical characterization.

Table 5.1: Comparison of Fe contents as determined by XPS before (as-deposited) and after electrochemical stabilization and characterization for select $Ni_{1-x}Fe_x$ films.

Sample type	As-deposited [mol % Fe]	After electrochemical stabilization [mol % Fe]	After electrochemical characterization [mol % Fe]
x = 0.25 electrodeposited	28%	--	30%
x = 0.50 electrodeposited	56%	--	44%
x = 0.25 sputter-deposited	25%	15%	14%
x = 0.50 sputter-deposited	52%	30%	29%

5.3.1.2. Effects of Electrochemical Stabilization on Voltammetry

Figure 5.1 shows voltammograms of electrodeposited and sputtered films with 0%, 8%, and 20% Fe, shown at the beginning of stabilization (gray, second stabilization cycle) and after electrochemical characterization (red and blue). The only samples for which there is a significant change in electrochemical behavior after 15 h stabilization cycling are sputtered and electrodeposited 100% Ni. For pure Ni films, a significant amount of Ni is found to further convert from metal to (oxy)hydroxide during the OER activity measurements, as evidenced by an increase in the area under the Ni redox waves[26-27] (Figure S3.2). However, despite the change in redox peak, only minimal improvement in OER activity is observed, consistent with recent observation that Fe-free NiOOH is a very poor OER catalyst.[23]

Films prepared by both deposition methods show qualitatively similar electrochemical behavior exhibit features characteristic of $Ni_{1-x}Fe_xOOH$,[13-17, 22-24, 28] specifically a redox couple in the range of 0.40–0.63 V corresponding to the oxidation/reduction of Ni in $Ni(OH)_2$/NiOOH and an increase in current density at higher potentials due to the electrocatalytic oxidation of water. As reported in our previous work,[24] the positions and intensities of both features depend on the composition of the films. Specifically, the $Ni(OH)_2$/NiOOH redox peaks shift to higher potentials with increasing Fe content, and the OER current densities are the lowest for pure Ni and pure Fe films and highest for intermediate Fe contents. (In addition, features associated with reversible oxidation and reduction of the underlying Au substrate can be observed for some samples at ~0.36 and ~0.24 V vs. Hg/HgO, respectively.)

Despite these general similarities, notable differences exist between the electrochemical characteristics of sputtered and electrodeposited films. Sputtered films containing Ni initially show smaller Ni redox peaks, with the Ni oxidation wave almost not visible for samples with sufficiently high Fe contents (e.g. 20% Fe). With repeated cycling, there is a significant growth in the total area under the redox features (the integrated area of the oxidation wave for the 20% Fe sample increases more than three-fold, from 0.39 to 1.4 mC cm^{-2}), stabilizing after ~300 cycles. On the other hand, electrodeposited films are predominantly deposited as oxides/hydroxides (further discussion detailed in Section 3.1.6) and do not exhibit the same behavior. $Ni_{1-x}Fe_x(OH)_2$ electrodeposited films exhibit minimal changes in the reduction peak areas after extended cycling (e.g., the reduction wave for the 20% Fe sample is comparable after deposition vs after stabilization – 1.47 vs 1.42 mC cm^{-2}). Additionally, the voltammograms for sputtered films display sharper redox peaks than those for electrodeposited films, indicating

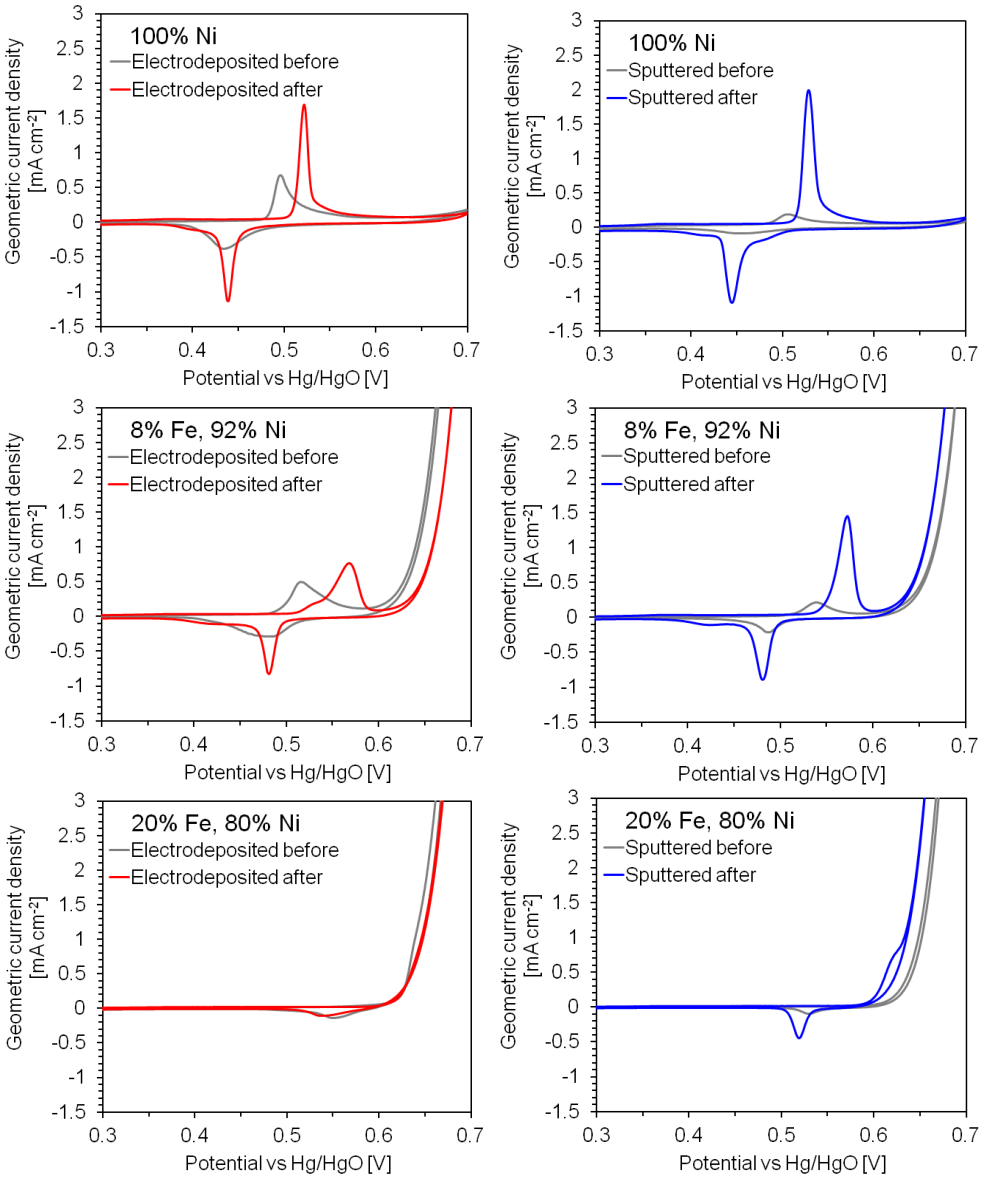

Figure 5.1. Cyclic voltammograms of $Ni_{1-x}Fe_x(OH)_2/Ni_{1-x}Fe_xOOH$ films for both electrodeposited (left) and sputtered (right) films, showing the change in activity as-deposited (before, gray) and after stabilization and electrochemical characterization (red, blue). CVs were collected in 0.1 M KOH at 10 mV s^{-1}.

greater uniformity in sputtered films compared to electrodeposited films. With the exception of pure Ni (for which no significant OER current is observed up to 0.7 V vs. Hg/HgO), sputtered films tended to show an increase in OER activity after cycling, while electrodeposited films displayed a slight decrease or negligible change in activity.

Figure 5.2 shows a comparison of the Ni reduction/oxidation peak positions and areas for electrodeposited and sputtered films with ~30% Fe or less after electrochemical characterization. (For film compositions exceeding 30% Fe, oxidation waves become increasingly difficult to fit

and analyze due to overlap with oxygen evolution currents. Representative peak fits are shown in Supporting Information S 5.3.1.) Within sample-to-sample variation (across different samples of the same composition), the redox areas and peak positions are comparable, apart from the oxidation peak area of 100% Ni, for which sputtered Ni shows a larger oxidation peak area compared to electrodeposited Ni. Despite the qualitative differences in the peak shape discussed above, this analysis shows that the amount of redox-accessible material is comparable for any given $Ni_{1-x}Fe_x(OH)_2/Ni_{1-x}Fe_xOOH$ film composition, regardless of the film deposition method.

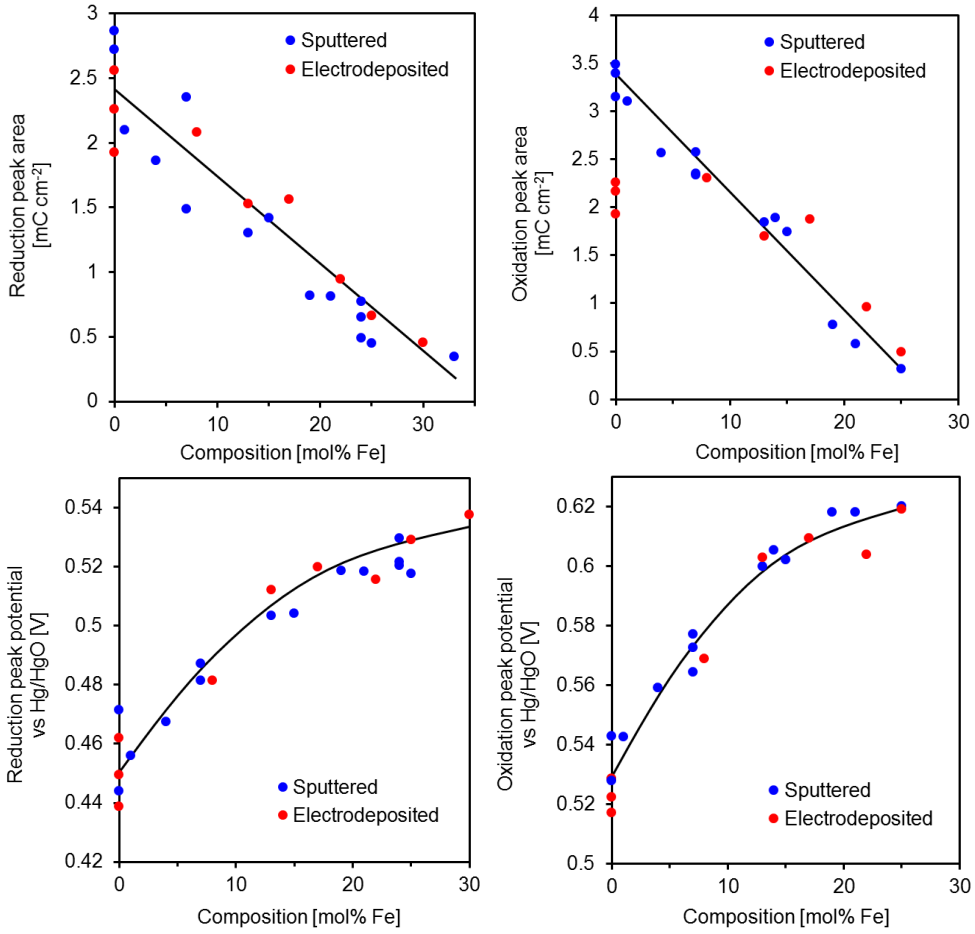

Figure 5.2. Comparison of redox characteristics for sputtered (blue) and electrodeposited (red) $Ni_{1-x}Fe_x(OH)_2/Ni_{1-x}Fe_xOOH$ films. Oxidation and reduction peak areas (top) and potentials (bottom) are plotted as a function of Fe content. Values were obtained from fitting the redox peaks in cyclic voltammograms measured in 0.1 M KOH after electrochemical activity measurements, with a scan rate of 10 mV s^{-1} and a rotation speed of 1600 RPM. Curves are included to guide the eye.

5.3.1.3 Comparison of OER Activity and Turnover Frequency for Stabilized Films

The activity for the OER was quantified using (1) the geometric current density, j, at a constant overpotential of 300 mV and (2) the overpotential, η, at j = 10 mA cm^{-2}, each after holding for 1 h at the specified condition. These two metrics are plotted for both sputtered and electrodeposited films in Figure 5.3. Within sample-to-sample variation, the activities of electrodeposited and sputtered films of any given composition are comparable. The current density

varies by approximately three orders of magnitude across the entire composition range, reaching a maximum of ~3 mA cm^{-2} for ~15-20% Fe, and with minima on the order of $j = 1 \times 10^{-3}$ mA cm^{-2} for NiOOH or FeOOH. Likewise, the overpotential reaches a minimum of ~ 320 mV at 15-20% Fe, compared to overpotentials as high as 750 mV for Ni and 500 mV for Fe. The composition with the maximum OER activity observed here is well within the range measured in previous studies, between 10 and 50 % Fe.[15-16, 24, 28] We note the electrodeposited films reported here exhibit 10× lower current density at 300 mV overpotential than those reported in previous work from our group,[24] coinciding with a 10× decrease in catalyst loading (~3.5×10^{15} atoms deposited in the current study vs ~3.5×10^{16} atoms deposited previously). This difference could be due to differences in the real vs geometric surface area or a greater number of active sites due to the electrolyte/ion permeability of Ni-based (oxy)hydroxides.[23, 29-31]

Tafel slope values are shown in Fig. 5.3c (with slope fits shown in the Supporting Information S5.3.5). Both sputtered and electrodeposited NiOOH exhibit comparable Tafel slopes to those previously reported for Fe-free NiOOH (115-120 mV dec^{-1}).[29] With even a 1% addition of Fe, a substantial decrease in the Tafel slope (and increase in activity) is observed, consistent with the enhancement in OER activity observed over NiOOH after incorporation of ppb-level Fe impurities.[23, 29] Tafel slopes for $Ni_{1-x}Fe_xOOH$ are ~45-50 mV dec^{-1}, in agreement with Tafel slopes measured for other Ni-Fe(oxy)hydroxide electrocatalysts (40-50 mV dec^{-1}).[24, 32-34] As Fe content increases above 75%, an increase in Tafel slopes to ~64 and ~60 mV dec^{-1} is observed for electrodeposited and sputtered 100% Fe films, respectively. Previous work has shown a higher Tafel slope for pure Fe (~55 mV dec^{-1}) vs those for $Ni_{1-x}Fe_xOOH$ films.[24]

Note that in the case of sputtered films, the increase in OER current does not appear to be proportional to the change in Ni redox peak areas. For example, for the sputtered film with 20% Fe, the reduction peak area increases by more than three-fold, while the OER current (at 665 mV vs. Hg/HgO, or 300 mV overpotential) increases by less than two-fold (2.8 to 5.2 mA cm^{-2}). Similarly, for sputtered films with 8% Fe, the reduction peak area increases by almost four-fold (0.6 to 2.1 mC cm^{-2}) while the OER current density increases by less than two-fold (0.78 to 1.4 mA cm^{-2}). This suggests that not all (if any) of the electrochemically accessible (i.e. redox-active) Ni population is participating in OER catalysis. This is consistent with recent work for Ni- and Co-(oxy)hydroxide thin films indicating the Fe atoms as the actual OER active sites.[35-36]

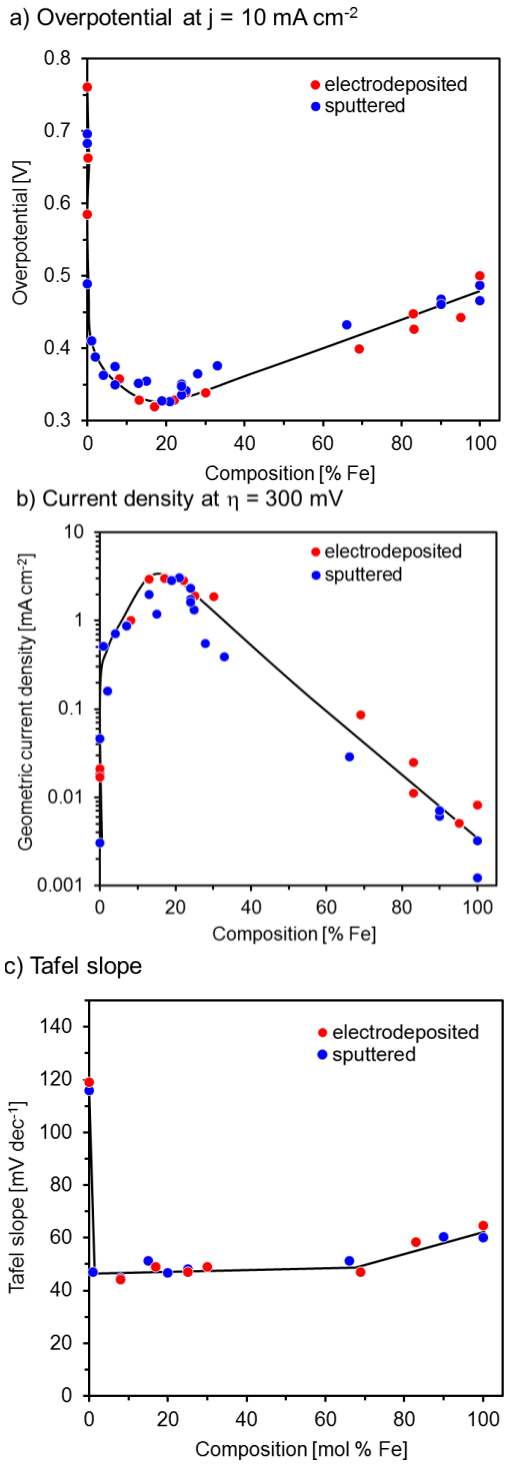

Figure 5.3. Activity plots for sputtered and electrodeposited $Ni_{1-x}Fe_xOOH$ films. Activity values were obtained after holding for 1 h at either constant (a) overpotential (300 mV) or (b) geometric current density (10 mA cm^{-2}), with (c) Tafel slopes obtained from 10 mV s^{-1} CV scans. Measurements were obtained in 0.1 M KOH with a RDE rotation rate of 1600 RPM. Curves are included to guide the eye.

5.3.1.4 Long-Term Stability Comparison of Sputtered and Electrodeposited 20% Fe Films

Previous work investigating sputter-deposited Fe-doped NiO_X films found a greater long-term stability(i.e. catalyst did not separate from the substrate) of sputtered films relative to electrodeposited films during oxygen evolution.[22] This stability increase was attributed to better adhesion of the sputtered Fe:NiO_x film to the underlying Ni substrate. To further investigate effects of deposition method on catalyst stability, we measured oxygen evolution activity on both a short-term (1 h) and long-term (38 h) basis. After 1 h at 10 mA cm^{-2} (anodic), electrodeposited films with ~20% Fe exhibited a ~9 mV increase in overpotential (670 to 679 mV) compared to a 3-4 mV increase in overpotential for 20% Fe (stabilized) sputter-deposited films. To test the long-term stability of electrodeposited vs sputtered films, 20% Fe films produced by both depositions were held at a 10 mA cm^{-2} current density for 38 h. Cyclic voltammograms for each film before and after 38 h of oxygen evolution are shown in Figure 5.4. The sputtered film initially exhibits higher OER current compared to the electrodeposited film at potentials above 0.7 V. However, after 38 h of sustained oxygen evolution, the CV of the electrodeposited film is largely unchanged, while a loss in activity is apparent for the sputtered film.

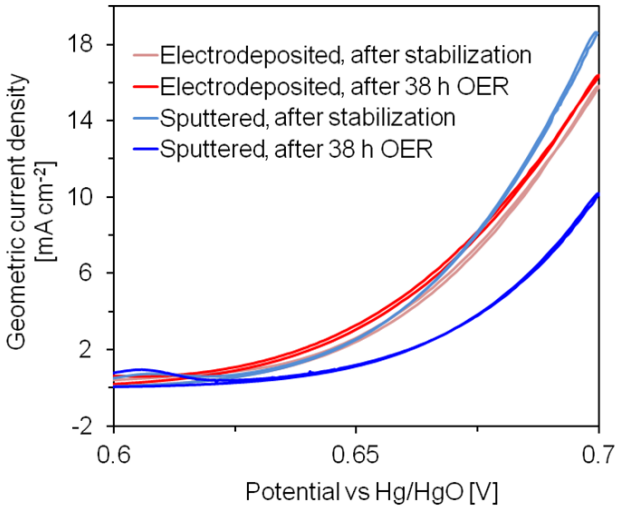

Figure 5.4. Cyclic voltammograms of films with 20% Fe deposited by sputtering (blue) and electrodeposition (red) after electrochemical stabilization cycling and after 38 h at a geometric current density of 10 mA cm^{-2}. CVs were collected on RDEs with a rotation rate of 1600 rpm and scan rate 10 mV s^{-1} in 0.1 M KOH.

Additional activity and composition comparisons are shown in Table 5.2. Even after 6 h at j = 10 mA cm^{-2}, comparable overpotentials are observed for the electrodeposited (327 mV) and sputter-deposited (325 mV) films with 20% Fe. After 38 h of oxygen evolution, however, the electrodeposited film exhibited a lower overpotential (317 mV), while the sputtered film showed a slight increase in overpotential (334 mV). The Fe content of each film was also determined after 38 h of sustained oxygen evolution using XPS; the electrodeposited film contained 18% Fe (close to the 20% Fe targeted), while the sputter-deposited sample exhibited significant Fe loss, with only 13% Fe remaining in the film after sustained oxygen evolution. The loss of Fe and activity of the sputtered $Ni_{1-x}Fe_xOOH$ film cannot be due to complete degradation of the film, since the Ni reduction peak area of the sputtered sample significantly increases (rather than decreasing as would

be expected with film dissolution) during the 38 h of sustained oxygen evolution. (We use this metric to evaluate film stability since the 2 nm $Ni_{1-x}Fe_xOOH$ film is too thin for accurate quantification of total metal content by ICP-OES.) In summary, both sputter-deposited and electrodeposited films demonstrate high activity and stability for the OER, though the sputtered films exhibit some loss of Fe and a slight decrease in activity after 38 h of oxygen evolution.

Table 5.2: Comparison of overpotential at 10 mA cm^{-2}, composition, and reduction peak area change for stabilized 20% Fe sputter-deposited and electrodeposited films.

	Overpotential after 1 h **[mV]**	Overpotential after 6 h **[mV]**	Overpotential after 38 h **[mV]**	Surface composition after 38 h **[at% Fe]**	Reduction peak area change **[% increase]**
Electrodeposited	314	327	317	18%	7%
Sputter-deposited	317	325	334	13%	28%

5.3.1.5 In Situ Raman Spectroscopy of $Ni_{1-x}Fe_xOOH$ After Electrochemical Stabilization

To further investigate structural differences between electrodeposited and sputter-deposited films, in situ Raman spectra were obtained for $Ni_{1-x}Fe_xOOH$ films of select compositions (100% Ni, 25% Fe and 100% Fe). Spectra were collected during a 1 mv s^{-1} oxidation sweep (from 0.00 to 0.65 V vs. Hg/HgO) in 0.1 M KOH after electrochemical stabilization (corresponding voltammograms are presented in SI, S5). For all three compositions, Raman spectra for the electrodeposited and sputter-deposited samples are similar, indicating comparable structures exist between the corresponding compositions of sputtered and electrodeposited films.

Figure 5.5 shows the Raman spectra acquired in the high-wavenumber (3000-3800 cm^{-1}) O-H stretching regime for sputter-deposited and electrodeposited 100% Ni films. Both sputter-deposited and electrodeposited 100% Ni films exhibit three Raman modes at 3581, 3600 and 3665 cm^{-1} between 0.0 to 0.2 V. The Raman feature present at 3665 cm^{-1} feature is characteristic of α-$Ni(OH)_2$, while the feature at 3581 cm^{-1} is attributed to β-$Ni(OH)_2$.[26, 37-40] Additionally, the 3600 cm^{-1} peak corresponds to a stacking fault disorder within the β-$Ni(OH)_2$ phase.[40] With oxidation to 0.3 V, however, only a weak feature at 3581 cm^{-1} is observed due to the phase conversion of $Ni(OH)_2$ to NiOOH with the anodic potential scan. These results suggest that the $Ni(OH)_2$ phase is best described as a mixture of α-$Ni(OH)_2$ and disordered β-$Ni(OH)_2$, consistent with our previous observations over similar films.[24] In contrast, none of the O-H stretching modes of either the α- or β-$Ni(OH)_2$ phases were observed for the 25% and 100% Fe films (SI, S5), consistent with previous studies showing these features are not observable for electrodeposited films with > 19% Fe co-deposition or after Fe electrolyte impurity incorporation into the $Ni(OH)_2$ structure.[24, 29] Apart from the Raman features ascribed to $Ni(OH)_2$, only contributions due to bulk water modes from 3100-3600 cm^{-1} are observed,[26, 40-41] which are present in the spectra of all samples.

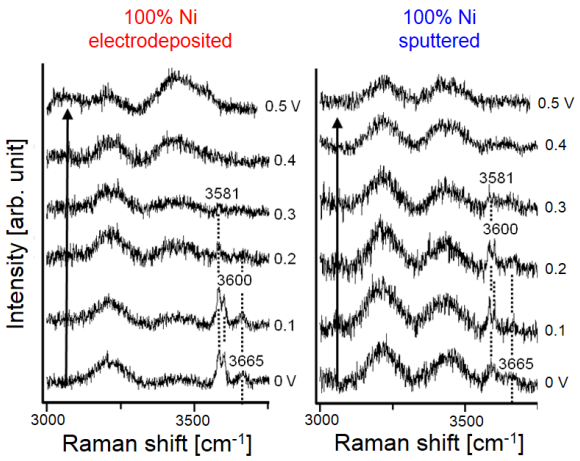

Figure 5.5. High-wavenumber in situ Raman spectra for 100% Ni electrodeposited and sputter-deposited on roughened Au substrates as a function of potential vs. Hg/HgO in 0.1 M Fe-free KOH, for which the OER equilibrium potential is 0.365 V.

Raman spectra acquired at low wavenumbers (200-800 cm^{-1}) for 100% Fe, 25% Fe, and 100% Ni are presented in Figure 5.6. The Raman spectra of 100% Fe films for both sputter-deposited and electrodeposited contain no discernible features apart from a weak ~580 cm^{-1} contribution above 0.4 V due to electrochemical oxidation of the underlying Au substrate.[42] The absence other of spectral features for the Fe samples, an incongruity with our previous investigation, is attributed to the ten-fold film thickness decrease in the present study (previous 25 nm vs. current 2.5 nm estimated thickness over roughened Au electrodes).[24]

For electrodeposited and sputter-deposited 100% Ni films, a weak Raman feature at 493 cm^{-1} is initially observed at 0.1 V vs. Hg/HgO. This feature is attributed to a defective or disordered $Ni(OH)_2$ structure.[24, 26, 43] Features at ~480 and 560 cm^{-1}, characteristic of NiOOH,[24, 38, 44] appear at 0.4 V and intensify most greatly from 0.45 to 0.5 V, coinciding with the $Ni(OH)_2$/NiOOH oxidation wave within the voltammograms (Figure S5.1) for both samples. The sputter-deposited 100% Ni film exhibits sharper, more defined NiOOH features, indicating greater structural order within this film. Note that this is consistent with the observation of sharper Ni redox features in cyclic voltammograms of sputtered films in comparison to electrodeposited films.

For the 25% Fe films, several differences compared to 100% Ni films indicate the presence of Fe within the $Ni(OH)_2$/NiOOH structure. While the 480 and 560 cm^{-1} features are also present for these samples at 0.4 V and above, these peaks exhibit weaker intensities and a lower 480 cm^{-1} to 560 cm^{-1} peak height ratio. Such differences are consistent with reports of an oxidized Ni-Fe layered double hydroxide structure.[29, 45] Additionally, the 480 and 560 cm^{-1} Raman features intensify most strongly when the potential increases from 0.50 to 0.55 V, a 0.05 V anodic shift in comparison to the 100% Ni films (0.45 to 0.50 V). This delayed onset of

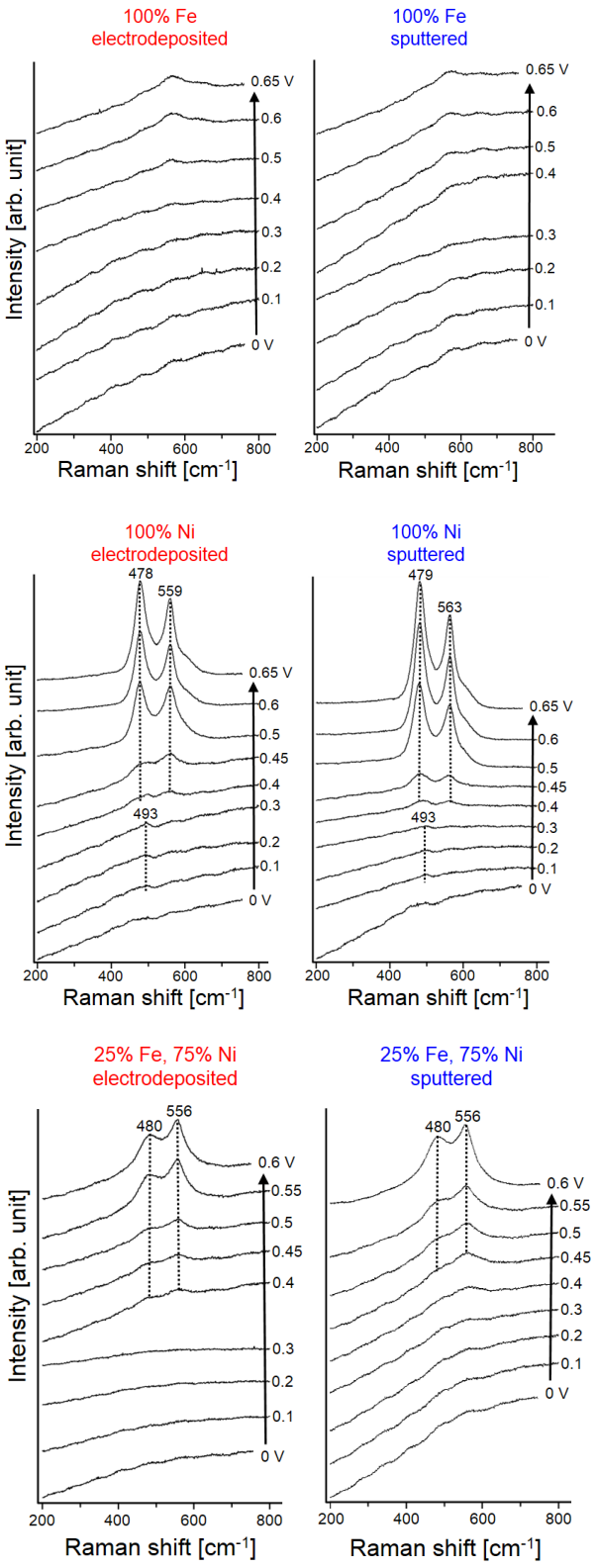

Figure 5.6. Low-wavenumber in situ Raman spectra for 100% Fe, 100% Ni and 25% Fe films electrodeposited and sputter-deposited on roughened Au substrates as a function of potential vs. Hg/HgO in 0.1 M Fe-free KOH, for which the OER equilibrium potential is 0.365 V.

oxyhydroxide formation coincides with the anodic shift of the Ni oxidation wave observed in the corresponding voltammograms, indicating Fe incorporation into the Ni structure. [24, 29]
In summary, in situ Raman spectra show clearly that minimal structural differences exist between $Ni_{1-x}Fe_xOOH$ films prepared by sputtering and electrodeposition. It should be noted that films deposited via both methods exhibit structural disorder, as indicated by the presence of the 490 and 3600 cm^{-1} features for the 100% Ni films, as well as the absence of Raman features for the pure Fe films. This finding is consistent with previous in-situ Raman and X-ray diffraction studies of electrodeposited nickel-iron hydroxides, which also observed disordered structures for $Ni_{1-x}Fe_xOOH$. [22-23, 39]

5.3.1.6 X-ray Photoelectron Spectroscopy of Films As-Deposited and After Electrochemical Characterization

Conversion of the sputtered $Ni_{1-x}Fe_x$ metallic films to the (oxy)hydroxides after extended cycling was also confirmed via XPS. The Ni 2p, Fe 2p and O 1s spectra for sputtered and electrodeposited x = 0.25 (as-deposited composition) films are shown in Figure 5.7. Ni is initially present as metal (870.0 and 852.6 eV) and NiO (856.0/861.4 eV Ni $2p_{3/2}$, 873.5/879.3 eV Ni $2p_{1/2}$) in the as-sputtered film,[25, 46] but only peaks consistent with a nickel (oxy)hydroxide phase are observed after electrochemical characterization (856.3/862.0 eV Ni $2p_{3/2}$, 874.0/880.0 eV Ni $2p_{1/2}$).[25, 46] The Fe 2p spectrum for the as-sputtered $Ni_{0.75}Fe_{0.25}$ film exhibits peaks at 707.0 and 719.8 eV, attributed to metallic Fe,[25, 47] while the remaining peaks (724.0 and 710.9 eV) are attributed to iron oxide or hydroxide phases.[47] The specific phase of iron oxide/hydroxide cannot

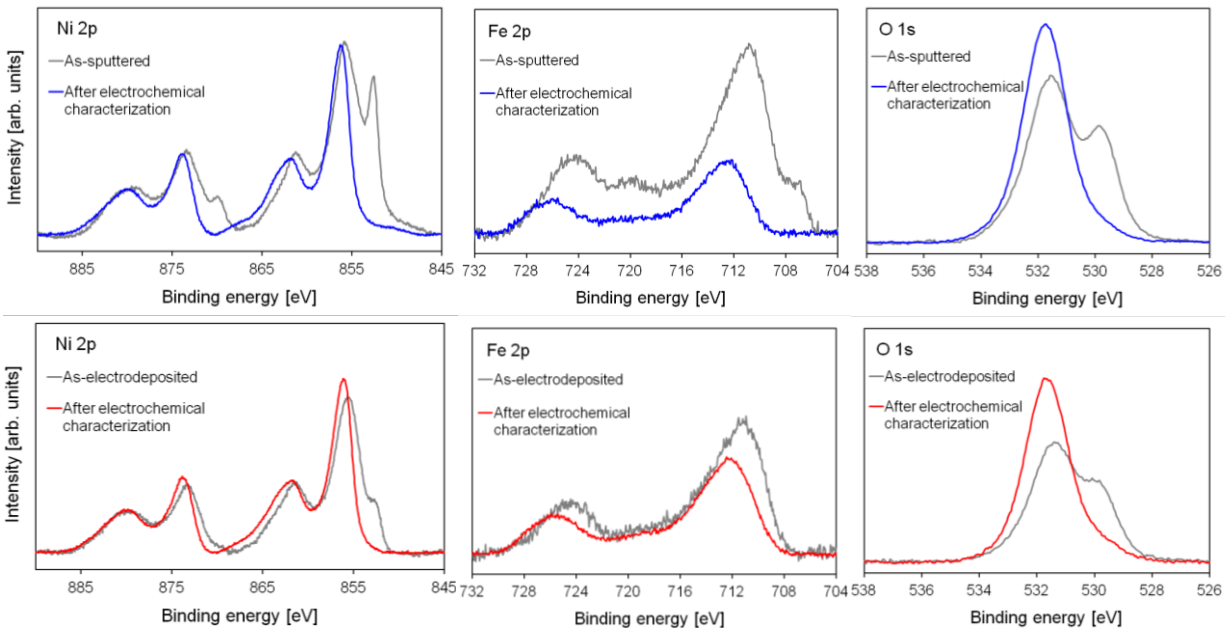

Figure 5.7. Comparison of Ni 2p, Fe 2p and O 1s XPS spectra (background-subtracted) for sputtered and electrodeposited films with target compositions x = 0.25, as-deposited (grey) and after electrochemical stabilization and characterization (blue, red).

be uniquely identified due to similarities in the Fe 2p binding energies and spectral shapes of the higher oxides of iron and limitations in the spectral line resolution with the non-monochromated Mg Kα source. The O 1s spectrum for the as-sputtered film displays two peaks due to unprotonated oxygen (~530 eV) and protonated oxygen (~531.5 eV), while after characterization, only one peak at 531.5 eV is observed.

The Ni 2p spectra for the as-electrodeposited $Ni_{0.75}Fe_{0.25}(OH)_2$ film exhibits peaks consistent with nickel hydroxide (855.6/861.4 eV Ni $2p_{3/2}$, 873.3/880 eV Ni $2p_{1/2}$).[25, 46] Additionally, a peak observed at 852.8 eV is consistent with metallic Ni. After electrochemical stabilization and characterization, peaks again consistent with a nickel (oxy)hydroxide are observed (856.1/861.9 eV Ni $2p_{3/2}$, 873.9/880 eV Ni $2p_{1/2}$ region). The as-electrodeposited $Ni_{0.75}Fe_{0.25}(OH)_2$ film exhibits a Fe 2p spectrum with peaks at 711.1 and 724.3 eV, again consistent with Fe oxide/hydroxide phases. (No contribution from metallic Fe is observed.) The as-electrodeposited sample also exhibits O 1s spectral features consistent with both protonated and unprotonated oxygen (at 530.1 and 531.5 eV) in the O 1s region, while after characterization, only a protonated oxygen contribution (~531.6 eV) is present.

Figure 5.8 compares the XPS spectra of electrodeposited (Figure 5.8a) and sputtered (Figure 5.8b) films after electrochemical characterization. The Ni 2p peaks shift to slightly lower binding energies for films with Fe contents of 66% and above but remain otherwise unchanged. For sputtered and electrodeposited films with Fe contents of 25-30% and below, the Fe 2p binding energy increases between ~1.0-2.0 eV. While no previous XPS studies have detailed the differences in binding energy for Fe present as $Ni_{1-x}Fe_xOOH$, Fe present in an oxyhydroxide has been reported to exhibit similar Fe 2p and O 1s spectra to the low Fe content films reported here.[48] Additionally, the ~530 eV O 1s peak observed in the spectra of 100% Fe films is not observed for films with Fe contents below ~25 % (electrodeposited) and ~31% (sputter-deposited). Instead, the O1s spectra of films with low Fe-contents (~15-17% Fe and below) exhibit only one primary O 1s peak at ~531.6 eV, consistent with a protonated oxygen,[25, 48] which may be bound to Ni and/or Fe.

The presence of one primary O 1s peak below ~20% Fe indicates that a single phase predominates after electrochemical stabilization/characterization of sputtered and electrodeposited $Ni_{1-x}Fe_xOOH$, which appears characteristic of a Ni(oxy)hydroxide-type structure. This finding is consistent with the in situ Raman spectra in Figure 5.6, as well as previous reports from our group, which found that Fe can incorporate into the $Ni(OH)_2$/NiOOH structure for Fe contents below 25%.[29, 35] In our current study, we find that a separate, Fe-rich phase (characteristic of pure Fe oxide/hydroxide) is first observable (evidenced most clearly by the observation of an additional O 1s peak) between 17% and 25% Fe contents for sputtered films and between 15 and 21% Fe contents for electrodeposited films.

In summary, spectroscopic evidence suggests a single $Ni_{1-x}Fe_xOOH$ phase predominates below 20 mol% Fe after electrochemical characterization for both sputtered and electrodeposited films. As Fe content increases above 20%, the formation of a Fe-rich phase and a decrease in OER activity is observed. This further supports our previous hypothesis that Fe is the active site for oxygen evolution and that the decrease in activity for catalyst films with Fe contents in excess of 20% is due to the formation of a separate, Fe-rich phase.[29, 35] It is possible that such a phase is less OER-active due to low electrical conductivity, which has been previously reported for FeOOH under oxygen-evolving potentials in alkaline electrolyte,[36] and/or due to less optimal binding energetics of OER-intermediates relative to Fe within a Ni (oxy)hydroxide structure.[35]

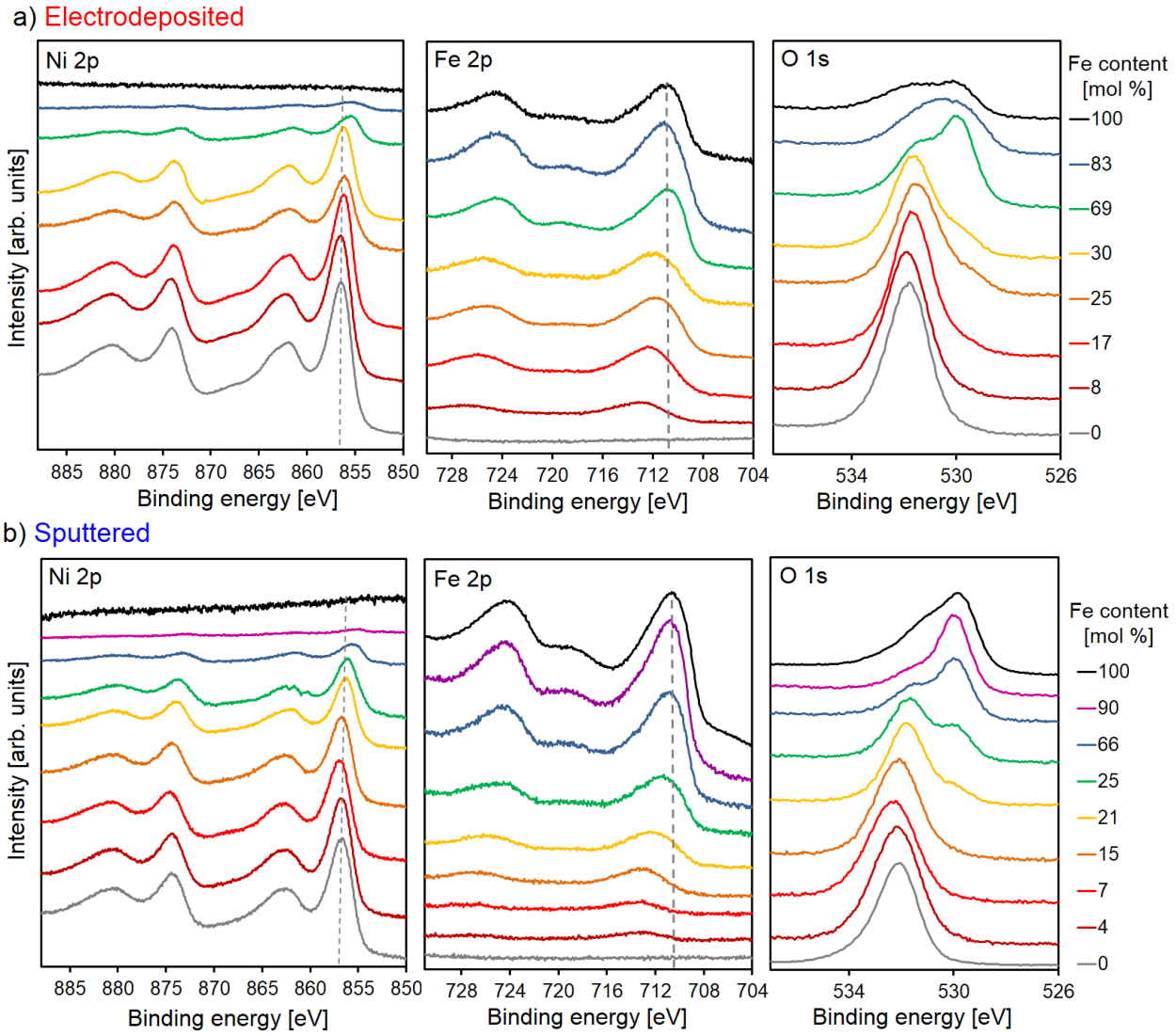

Figure 5.8. Comparison of Ni 2p, Fe 2p and O 1s XPS spectra (charge-corrected) for a) electrodeposited and b) sputtered films after electrochemical characterization. Gray dashed lines (at 710.7 and 856.6 eV for Fe and Ni, respectively) are shown for pure Fe and Ni peak positions for reference. Fe contents are those determined by XPS after electrochemical stabilization and characterization.

5.3.2 Comparison of Codeposited and Layered $Ni_{1-x}Fe_x$ Films

In the previous section, we demonstrated that $Ni_{1-x}Fe_xOOH$ catalysts prepared by sputter deposition and electrodeposition are essentially identical with respect to activity, stability, and structure. Sputtering may be a preferable catalyst deposition method for integration with certain photoanodes, but optimizing conditions for codeposition of Ni and Fe at a desired composition in any individual sputtering system can be tedious, and some sputtering systems may be limited by the number of power sources or targets that can be used simultaneously, making codeposition unfeasible. Therefore, it may be more practical in certain circumstances to sequentially deposit Ni and Fe to form a layered structure. There may also be advantages to having either Ni(OOH) or Fe(OOH) as the layer in direct contact with the substrate, either to improve charge transfer between the catalyst and photoanode or adhesion of the catalyst to the substrate material. In fact, one recent study used NiOOH deposited on top of FeOOH as a way to engineer a more favorable interface between a $BiVO_4$ semiconductor and the OER catalysts by reducing interface recombination.[7]

It would thus be useful to understand how such layered catalyst systems differ from codeposited catalysts, as this may have great implications on the design of optimized photoelectrode-catalyst interfaces. In this section, we compare the activity of catalysts prepared by sputtering where the elements were either deposited at the same time (codeposition) or with sequentially deposited layers of Ni and Fe. Previous work has shown that the presence of ppm and ppb levels of Fe impurities can greatly influence the OER activity of NiOOH catalysts,[23,38] indicating that Fe can migrate and incorporate into Ni with relative ease under appropriate conditions. We found that the order of the catalyst layers greatly affects the degree of mixing of the metal centers in sputtered catalyst films.

We sputter-deposited three types of films, each 2 nm thick with an overall as-deposited target composition of 50% Fe. One of these films was cosputtered 50:50 Fe:Ni (identical to the films discussed in the previous section, hereafter denoted as "mixed Ni-Fe"). The remaining two catalyst films were made by sputtering sequential layers of the Ni and Fe elements to form layered structures, one with Ni immediately adjacent to the underlying gold substrate and Fe on top of the Ni (Au/Ni/Fe, denoted from this point forward as "Fe-on-top"), and the second with Fe immediately adjacent to gold and Ni on top (Au/Fe/Ni, or "Ni-on-top").

Angle-resolved XPS profile analysis of each film type as-deposited and after electrochemical characterization is presented in Figure 5.9. The photoelectron inelastic mean free path (IMFP) is estimated to be ~2 nm for both Ni and Fe using the 1254.6 eV Mg Kα excitation source, and the probability that inelastic scattering of emitted electrons will occur increases exponentially with increasing sample depth.[49] Therefore, the greatest contribution of signal in the photoelectron spectra originates from material closest to the sample surface; as higher take-off angles are probed, further surface sensitivity is attained. The increased surface sensitivity is readily observed in the Au substrate contribution to the total signal from all metals, which for most samples decreases from 35-45% Au at a 0° take-off angle to less than 20% Au at a 70° take-off angle. (Note that in this section, percentages of individual metals are given as the percent of the total [Fe + Ni + Au], as determined by XPS).

In the as-deposited mixed Ni-Fe film, the amounts of Ni and Fe observed at each take-off angle are similar, e.g. 34% Fe and 31% Ni at 0°, and 41% Fe and 39% Ni at 70°, consistent with equal distribution of Ni and Fe throughout the film. For Ni-on-top, significantly more Ni is observed (~50%) than Fe (~16%) at 0°, and the relative amount of Ni further predominates (68%) at increased take-off angles, while the %Fe is essentially constant at all take-off angles. Similarly, the Fe-on-top sample exhibits greater Fe surface content (42%) compared to Ni (10%) at 0°; with

a take-off angle of 70°, an Fe content of 57% is observed, while the %Ni remains essentially constant. Since equal amounts of both Ni and Fe were deposited for each sample, the relative predominance of Ni for the Ni-on-top sample and Fe for the Fe-on-top confirms that a layered-type structure is formed as expected with sequential deposition of these films.

After electrochemical characterization, the Ni and Fe percentages are still highest for the Ni-on-top and Fe-on-top samples, respectively. The data for Fe-on-top show a lower Fe:Ni ratio across all take-off angles than in the as-deposited film, which could be consistent with loss of some of the Fe capping layer. The mixed Ni-Fe sample has significantly more Ni content (60%) than Fe content (20%) at all take-off angles, consistent with the loss of Fe during stabilization cycling discussed previously (a decrease of the as-deposited 50:50 Fe:Ni ratio to 25:75 Fe:Ni after electrochemical cycling and characterization).

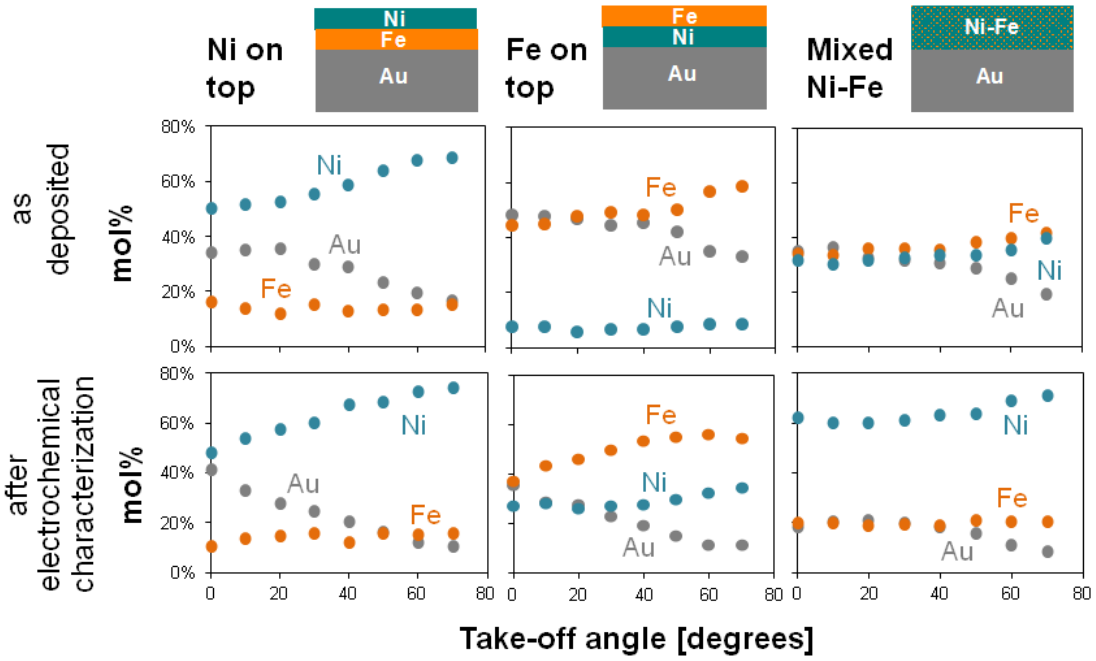

Figure 5.9. Depth profiles obtained from Ni 2p, Fe 2p and Au 4f XPS spectra for films as-deposited (sputtered) and after electrochemical characterization for Ni-on-top, Fe-on-top, and mixed Ni-Fe samples (50:50 Fe:Ni)

It is important to comment on the similarities between the three plots in Figure 5.9 for as-deposited Ni-on-top and both Ni-on-top and mixed Ni-Fe after characterization. It is clear from knowledge of the deposition methods that a layered structure is present in the Ni-on-top sample as-deposited, which is consistent with the data in Figure 5.9. However, the data for Ni-on-top and mixed Ni-Fe after characterization are nearly identical to the data for as-deposited Ni-on-top. Therefore, in the case of the Ni-on-top film after electrochemical characterization, the angle-resolved XPS data alone cannot distinguish conclusively between a layered film and a mixed Ni-Fe film with unequal Ni and Fe contents. To determine whether significant mixing of the Ni and Fe layers is occurring during stabilization, cycling, and operation under electrochemical conditions, we compared data taken by cyclic voltammetry and in situ Raman spectroscopy.

The voltammograms of the sequentially and co-deposited Ni-Fe films after electrochemical characterization are presented in Figure 5.10. The positions of the oxidation and reduction waves for Ni-on-top and mixed Ni-Fe nearly overlap. Furthermore, for all three samples, the positions of the Ni oxidation and reduction waves are shifted anodic relative to those of the 100% Ni samples (see Figure 5.1), indicating that the Ni and Fe are mixing in the layered-deposited films. A comparison of the OER region of the CVS shows a 1 mA cm^{-2} current density is observed at a similar potential for the Ni-on-top and mixed Ni-Fe films (~0.65 V) but at a higher potential for Fe-on-top (~0.67 V).

Table 5.3 provides further details comparing the electrochemical behavior of the co-deposited and layered samples. The geometric current density at η = 300 mV for Fe-on-top is significantly lower than those observed for Ni-on-top and mixed Ni-Fe films, while the Fe-on-top overpotential (at 10 mA cm^{-2} current density) is higher than that for the Ni-on-top and mixed Ni-Fe films by 59 and 45 mV, respectively. Additionally, we observe that the activity vs surface composition of the layered samples (18% Fe for Ni-on-top and 54% Fe for Fe-on-top, as determined by XPS at 0º take-off after electrochemical characterization) agrees with the activity trends observed for the $Ni_{1-x}Fe_xOOH$ films discussed in the previous section (for direct comparison, see Figure S6.4).

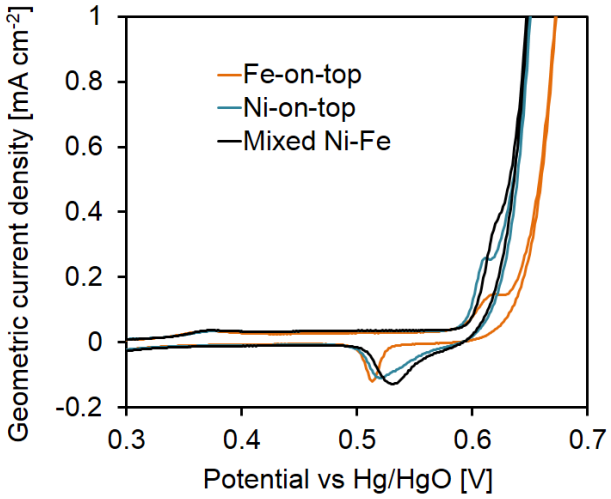

Figure 5.10. Cyclic voltammograms for sequentially- (i.e. layered) and co-deposited 50% Fe films over Au. CVs were collected in 0.1 M Fe-free KOH at a scan rate of 10 mV s^{-1} and RDE rotation rate of 1600 RPM.

Table 5.3. Activity, reduction peak area, and surface composition of sequentially- and co-deposited Ni-Fe films after electrochemical cycling

	η = 0.3 V current density **[mA cm^{-2}]**	j = 10 mA cm^{-2} overpotential **[mV]**	Reduction peak area **[mC cm^{-2}]**
Fe-on-top	0.3 ± 0.2	390 ± 4	97 ± 61
Ni-on-top	2.2 ± 0.3	331 ± 7	443 ± 234
Mixed Ni-Fe	1.9 ± 0.4	344 ± 8	560 ± 168

In situ Raman spectra were acquired for both mixed and layered Ni-Fe films (after electrochemical stabilization) during a 1 mV s^{-1} scan from 0.0 to 0.7 V in 0.1 M Fe-free KOH (corresponding voltammograms are shown in Figure S6.3). In contrast to the Raman spectra of the electrodeposited and sputtered samples for Figures 5.5 and 5.6, which were acquired over roughened Au electrodes, polished Au electrodes were used to preserve the relative thickness and layering of the Ni-on-top, Fe-on-top, and mixed Ni-Fe films. Figure 5.11 shows the spectra collected over each film. The Ni-on-top and mixed Ni-Fe samples exhibit similar spectral features, with the 480/560 cm^{-1} features of NiOOH appearing at 0.4 V and higher potentials. In contrast, the Raman modes of NiOOH at 480/560 cm^{-1} are much less intense (even at 0.6 V) for the Fe-on-top sample, indicating less NiOOH formation after 15 h of electrochemical stabilization cycling. (Note that Raman is a bulk measurement, so a capping layer of Fe would not be expected to significantly screen signal from an underlying NiOOH or $Ni_{1-x}Fe_xOOH$ layer.)

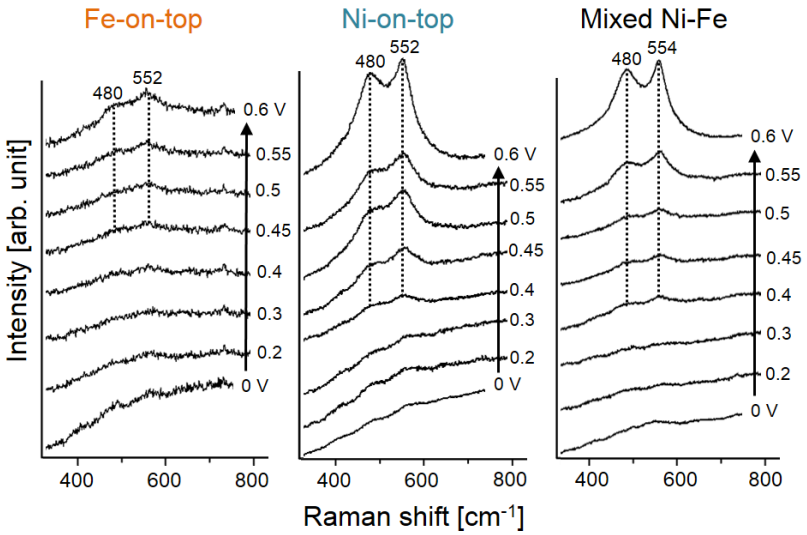

Figure 5.11. In situ Raman spectra for Fe-on-top, Ni-on-top, and mixed Ni-Fe films sputter-deposited on *polished* Au substrates as a function of potential vs. Hg/HgO in 0.1 M Fe-free KOH, for which the OER equilibrium potential is 0.365 V.

From the analysis of the data above, it is clear that after electrochemical stabilization, the Ni-on-top film converts during electrochemical stabilization/characterization to a material similar to the stabilized mixed Ni-Fe film. The relative Fe:Ni ratios determined via angle-resolved XPS (Figure 5.9, 18% Fe for Ni-on top vs 24% Fe for mixed Ni-Fe) are comparable after electrochemical characterization, and the samples are also structurally and electrochemically comparable, with essentially indistinguishable OER activities and reduction peak positions (Table 3).

In contrast, distinct differences are observed for Fe-on-top films. As detailed in Table 3, the Ni reduction peak area is 97 mC cm^{-2} for Fe-on-top, significantly less than the 560 mC cm^{-2} reduction peak area for mixed Ni-Fe. Less NiOOH formation is also observed via in situ Raman (Figure 5.11) after oxidation of the Fe-on-top sample compared to the Ni-on-top and mixed Ni-Fe samples, indicating a lower conversion of the sputtered, metallic Ni to $Ni(OH)_2$/NiOOH for the Fe-on-top sample. This could be due to the Fe-capping layer acting as a non-porous barrier over some Ni sites, preventing access to the electrolyte and slowing the conversion process. The

geometric current density at $\eta = 0.3$ V for Fe-on-top is 15% of that for mixed Ni-Fe, while the area of the CV reduction peak (indicative of the extent of NiOOH formation) for the Fe-on-top sample is 17% of that for the mixed Ni-Fe film. Previous investigations in our group support that it is Fe within a NiOOH structure which is critical for high oxygen evolution activity.[35] The close correlation between the reduction peak area ratio and observed oxygen evolution current are consistent with the finding that formation of the NiOOH parent structure is a critical requirement for high oxygen evolution activity over $Ni_{1-x}Fe_xOOH$ catalyst films.

In summary, Ni-on-top and mixed Ni-Fe sputtered films convert with electrochemical stabilization cycling to essentially indistinguishable materials with OER activity and structures comparable to electrodeposited $Ni_{1-x}Fe_xOOH$. In contrast, Fe-on-top layered films exhibit lower OER activity and a decreased formation of a NiOOH-type structure, indicating that the metallic Fe capping layer impedes electrochemical conversion of metallic Ni to NiOOH. This suggests that the formation of NiOOH precedes incorporation of Fe into highly active OER sites, and supports previous work showing that Fe sites within a NiOOH structure are the critical component for high OER activity.

5.4 Conclusions

We compared the activity and structure of electrodeposited vs. sputter-deposited $Ni_{1-x}Fe_xOOH$ films for water-splitting applications in alkaline electrolyte. Films produced by sputter deposition are initially metallic but convert to metal (oxy)hydroxide after 15 h of electrochemical stabilization cycling. During this conversion, a significant amount of Fe leaches from the sputtered films. In contrast, electrodeposited films are predominantly deposited as hydroxides and maintain the as-deposited Fe:Ni ratio. $Ni_{1-x}Fe_xOOH$ films exhibit significantly higher OER activities compared to pure Ni or Fe (oxy)hydroxide, with $Ni_{1-x}Fe_xOOH$ films containing ~20% Fe exhibiting the highest OER activity ($j = \sim 3$ mA cm^{-2} at 300 mV overpotential, and ~320 mV overpotential at $j = 10$ mA cm^{-2}). In situ Raman spectroscopy reveals that 25% Fe films deposited by both methods have similar structures after electrochemical stabilization, and the spectra are suggestive of a predominantly nickel-iron (oxy)hydroxide-type structure. Optimal OER activity coincides with the maximum Fe content which maintains a single Ni-Fe oxy(hydroxide)-type phase; above ~20% Fe, a separate Fe-rich phase is formed, which appears significantly less OER-active.

Sputter deposition was also used to compare co-deposited and layered films. Ni-on-top layered films are found to transform during electrochemical cycling to produce a film with indistinguishable structure and activity to that of co-deposited 50:50 Fe:Ni. In contrast, Fe-on-top films exhibit a greater Fe surface concentration, which appears to impede the transformation of sputter-deposited Ni metal to Ni (oxy)hydroxide, resulting in a significantly reduced OER activity. These findings demonstrate that $Ni_{1-x}Fe_xOOH$ catalyst films deposited by either sputter deposition or electrodeposition are similar in structure and OER activity, enabling the use of either technique for catalyst deposition over photoanode substrates.

References

1. Matsumoto, Y.; Sato, E., Electrocatalytic Properties of Transition-Metal Oxides for Oxygen Evolution Reaction. *Materials Chemistry and Physics* **1986**, *14*, 397-426.
2. Trotochaud, L.; Ranney, J. K.; Williams, K. N.; Boettcher, S. W., Solution-Cast Metal Oxide Thin Film Electrocatalysts for Oxygen Evolution. *J Am Chem Soc* **2012**, *134*, 17253-17261.
3. Corrigan, D. A.; Bendert, R. M., Effect of Coprecipitated Metal-Ions on the Electrochemistry of Nickel-Hydroxide Thin-Films - Cyclic Voltammetry in 1m Koh. *Journal of the Electrochemical Society* **1989**, *136*, 723-728.
4. Smith, R. D. L.; Prevot, M. S.; Fagan, R. D.; Zhang, Z. P.; Sedach, P. A.; Siu, M. K. J.; Trudel, S.; Berlinguette, C. P., Photochemical Route for Accessing Amorphous Metal Oxide Materials for Water Oxidation Catalysis. *Science* **2013**, *340*, 60-63.
5. McCrory, C. C. L.; Jung, S. H.; Peters, J. C.; Jaramillo, T. F., Benchmarking Heterogeneous Electrocatalysts for the Oxygen Evolution Reaction. *J Am Chem Soc* **2013**, *135*, 16977-16987.
6. Lin, F. D.; Boettcher, S. W., Adaptive Semiconductor/Electrocatalyst Junctions in Water-Splitting Photoanodes. *Nat Mater* **2014**, *13*, 81-86.
7. Kim, T. W.; Choi, K. S., Nanoporous Bivo4 Photoanodes with Dual-Layer Oxygen Evolution Catalysts for Solar Water Splitting. *Science* **2014**, *343*, 990-994.
8. Park, Y.; McDonald, K. J.; Choi, K. S., Progress in Bismuth Vanadate Photoanodes for Use in Solar Water Oxidation. *Chemical Society Reviews* **2013**, *42*, 2321-2337.
9. Seabold, J. A.; Choi, K. S., Efficient and Stable Photo-Oxidation of Water by a Bismuth Vanadate Photoanode Coupled with an Iron Oxyhydroxide Oxygen Evolution Catalyst. *Journal of the American Chemical Society* **2012**, *134*, 2186-2192.
10. Kenney, M. J.; Gong, M.; Li, Y. G.; Wu, J. Z.; Feng, J.; Lanza, M.; Dai, H. J., High-Performance Silicon Photoanodes Passivated with Ultrathin Nickel Films for Water Oxidation. *Science* **2013**, *342*, 836-840.
11. Yang, J. H., et al., Efficient and Sustained Photoelectrochemical Water Oxidation by Cobalt Oxide/Silicon Photoanodes with Nanotextured Interfaces. *Journal of the American Chemical Society* **2014**, *136*, 6191-6194.
12. Trotochaud, L.; Mills, T. J.; Boettcher, S. W., An Optocatalytic Model for Semiconductor-Catalyst Water-Splitting Photoelectrodes Based on in Situ Optical Measurements on Operational Catalysts. *J Phys Chem Lett* **2013**, *4*, 931-935.
13. Hu, C. C.; Wu, Y. R., Bipolar Performance of the Electroplated Iron-Nickel Deposits for Water Electrolysis. *Mater Chem Phys* **2003**, *82*, 588-596.
14. Potvin, E.; Brossard, L., Electrocatalytic Activity of Ni-Fe Anodes for Alkaline Water Electrolysis. *Materials Chemistry and Physics* **1992**, *31*, 311-318.
15. Corrigan, D. A., The Catalysis of the Oxygen Evolution Reaction by Iron Impurities in Thin-Film Nickel-Oxide Electrodes. *J Electrochem Soc* **1987**, *134*, 377-384.
16. Li, X. H.; Walsh, F. C.; Pletcher, D., Nickel Based Electrocatalysts for Oxygen Evolution in High Current Density, Alkaline Water Electrolysers. *Phys Chem Chem Phys* **2011**, *13*, 1162-1167.
17. Singh, R. N.; Pandey, J. P.; Anitha, K. L., Preparation of Electrodeposited Thin-Films of Nickel Iron-Alloys on Mild-Steel for Alkaline Water Electrolysis .1. Studies on Oxygen Evolution. *Int J Hydrogen Energ* **1993**, *18*, 467-473.

18. Seabold, J. A.; Choi, K.-S., Effect of a Cobalt-Based Oxygen Evolution Catalyst on the Stability and the Selectivity of Photo-Oxidation Reactions of a Wo3 Photoanode. *Chemistry of Materials* **2011**, *23*, 1105-1112.
19. Hamann, T. W., Splitting Water with Rust: Hematite Photoelectrochemistry. *Dalton T* **2012**, *41*, 7830-7834.
20. Walter, M. G.; Warren, E. L.; McKone, J. R.; Boettcher, S. W.; Mi, Q. X.; Santori, E. A.; Lewis, N. S., Solar Water Splitting Cells. *Chem Rev* **2010**, *110*, 6446-6473.
21. Gamelin, D. R., Water Splitting Catalyst or Spectator? *Nat Chem* **2012**, *4*, 965-967.
22. Miller, E. L.; Rocheleau, R. E., Electrochemical Behavior of Reactively Sputtered Iron-Doped Nickel Oxide. *J Electrochem Soc* **1997**, *144*, 3072-3077.
23. Trotochaud, L.; Young, S. L.; Ranney, J. K.; Boettcher, S. W., Nickel-Iron Oxyhydroxide Oxygen-Evolution Electrocatalysts: The Role of Intentional and Incidental Iron Incorporation. *Journal of the American Chemical Society* **2014**, *136*, 6744-6753.
24. Louie, M. W.; Bell, A. T., An Investigation of Thin-Film Ni-Fe Oxide Catalysts for the Electrochemical Evolution of Oxygen. *J Am Chem Soc* **2013**, *135*, 12329-12337.
25. Nist X-Ray Photoelectron Spectroscopy Database, Version 4.1. NIST X-ray Photoelectron Spectroscopy Database, Version 4.1: 2012.
26. Kostecki, R.; McLarnon, F., Electrochemical and in Situ Raman Spectroscopic Characterization of Nickel Hydroxide Electrodes. *Journal of the Electrochemical Society* **1997**, *144*, 485-493.
27. Lyons, M. E. G.; Brandon, M. P., The Oxygen Evolution Reaction on Passive Oxide Covered Transition Metal Electrodes in Aqueous Alkaline Solution. Part 1-Nickel. *International Journal of Electrochemical Science* **2008**, *3*, 1386-1424.
28. Landon, J.; Demeter, E.; Inoglu, N.; Keturakis, C.; Wachs, I. E.; Vasic, R.; Frenkel, A. I.; Kitchin, J. R., Spectroscopic Characterization of Mixed Fe-Ni Oxide Electrocatalysts for the Oxygen Evolution Reaction in Alkaline Electrolytes. *Acs Catalysis* **2012**, *2*, 1793-1801.
29. Klaus, S.; Cai, Y.; Louie, M. W.; Trotochaud, L.; Bell, A. T., Effects of Fe Electrolyte Impurities on Ni(Oh)2/Niooh Structure and Oxygen Evolution Activity. *The Journal of Physical Chemistry C* **2015**, *119*, 7243-7254.
30. Wehrens-Dijksma, M.; Notten, P. H. L., Electrochemical Quartz Microbalance Characterization of Ni(Oh)2-Based Thin Film Electrodes. *Electrochimica Acta* **2006**, *51*, 3609-3621.
31. Lee, J.-W.; Han, J.-N.; Seo, M.; Pyun, S.-I., Transport of Alkaline Cation and Neutral Species through the A-Ni(Oh)2/Γ-Niooh Film Electrode. *J Solid State Electrochem* **2001**, *5*, 459-465.
32. Singh, R. N.; Pandey, J. P.; Anitha, K. L., Preparation of Electrodeposited Thin Films of Nickel-Iron Alloys on Mild Steel for Alkaline Water Electrolysis. Part I: Studies on Oxygen Evolution. *International Journal of Hydrogen Energy* **1993**, *18*, 467-473.
33. Miller, E. L.; Rocheleau, R. E., Electrochemical Behavior of Reactively Sputtered Iron-Doped Nickel Oxide. *Journal of The Electrochemical Society* **1997**, *144*, 3072-3077.
34. Landon, J.; Demeter, E.; İnoğlu, N.; Keturakis, C.; Wachs, I. E.; Vasić, R.; Frenkel, A. I.; Kitchin, J. R., Spectroscopic Characterization of Mixed Fe–Ni Oxide Electrocatalysts for the Oxygen Evolution Reaction in Alkaline Electrolytes. *ACS Catalysis* **2012**, *2*, 1793-1801.
35. Friebel, D., et al., Identification of Highly Active Fe Sites in (Ni,Fe)Ooh for Electrocatalytic Water Splitting. *J Am Chem Soc* **2015**, *137*, 1305-1313.

36. Burke, M. S.; Kast, M. G.; Trotochaud, L.; Smith, A. M.; Boettcher, S. W., Cobalt–Iron (Oxy)Hydroxide Oxygen Evolution Electrocatalysts: The Role of Structure and Composition on Activity, Stability, and Mechanism. *Journal of the American Chemical Society* **2015**, *137*, 3638-3648.
37. Desilvestro, J.; Corrigan, D. A.; Weaver, M. J., Characterization of Redox States of Nickel-Hydroxide Film Electrodes by Insitu Surface Raman-Spectroscopy. *J Electrochem Soc* **1988**, *135*, 885-892.
38. Johnston, C.; Graves, P. R., Insitu Raman-Spectroscopy Study of the Nickel Oxyhydroxide Electrode (Noe) System. *Appl Spectrosc* **1990**, *44*, 105-115.
39. Bernard, M. C.; Bernard, P.; Keddam, M.; Senyarich, S.; Takenouti, H., Characterisation of New Nickel Hydroxides During the Transformation of Alpha Ni(Oh)(2) to Beta Ni(Oh)(2) by Ageing. *Electrochim Acta* **1996**, *41*, 91-93.
40. Hall, D. S.; Lockwood, D. J.; Poirier, S.; Bock, C.; MacDougall, B. R., Applications of in Situ Raman Spectroscopy for Identifying Nickel Hydroxide Materials and Surface Layers During Chemical Aging. *ACS Applied Materials & Interfaces* **2014**, *6*, 3141-3149.
41. Hibben, J. H., The Raman Spectra of Water, Aqueous Solutions and Ice. *J Chem Phys* **1937**, *5*, 166-172.
42. Yeo, B. S.; Klaus, S. L.; Ross, P. N.; Mathies, R. A.; Bell, A. T., Identification of Hydroperoxy Species as Reaction Intermediates in the Electrochemical Evolution of Oxygen on Gold. *Chemphyschem* **2010**, *11*, 1854-1857.
43. de Torresi, S. I. C.; Provazi, K.; Malta, M.; Torresi, R. M., Effect of Additives in the Stabilization of the Alpha Phase of Ni(Oh)(2) Electrodes. *J Electrochem Soc* **2001**, *148*, A1179-A1184.
44. Cornilsen, B. C.; Karjala, P. J.; Loyselle, P. L., Structural Models for Nickel Electrode Active Mass. *J Power Sources* **1988**, *22*, 351-357.
45. Lu, Z.; Xu, W.; Zhu, W.; Yang, Q.; Lei, X.; Liu, J.; Li, Y.; Sun, X.; Duan, X., Three-Dimensional Nife Layered Double Hydroxide Film for High-Efficiency Oxygen Evolution Reaction. *Chemical Communications* **2014**, *50*, 6479-6482.
46. Biesinger, M. C.; Payne, B. P.; Lau, L. W. M.; Gerson, A.; Smart, R. S. C., X-Ray Photoelectron Spectroscopic Chemical State Quantification of Mixed Nickel Metal, Oxide and Hydroxide Systems. *Surf Interface Anal* **2009**, *41*, 324-332.
47. Temesghen, W.; Sherwood, P. M. A., Analytical Utility of Valence Band X-Ray Photoelectron Spectroscopy of Iron and Its Oxides, with Spectral Interpretation by Cluster and Band Structure Calculations. *Anal Bioanal Chem* **2002**, *373*, 601-608.
48. McIntyre, N. S.; Zetaruk, D. G., X-Ray Photoelectron Spectroscopic Studies of Iron Oxides. *Analytical Chemistry* **1977**, *49*, 1521-1529.
49. Powell, C. J., The Quest for Universal Curves to Describe the Surface Sensitivity of Electron Spectroscopies. *Journal of Electron Spectroscopy and Related Phenomena* **1988**, *47*, 197-214.

5.5. Supporting Information

S5.1. Electrolyte Purification Procedure

1 M KOH electrolyte solutions were purified with high-purity $Ni(OH)_2$ powders following a procedure similar to that reported by Trotochaud et al.[3] All centrifuge tubes and storage bottles used were pre-cleaned by soaking with 1 M sulfuric acid for ~30 min. Fe-free 0.1 M KOH electrolyte solutions used in this work were diluted further from purified 1 M KOH. The procedure used was as follows:

Preparing $Ni(OH)_2$ powders

a. Dissolve 2 g of 99.999% $Ni(NO_3)_2{\cdot}6H_2O$ (Sigma Aldrich 203874) in 4 mL of 18.2 MΩ cm water.
b. Add 20 mL of 1 M KOH (prepared from 45% Baker Analyzed Electronic Grade KOH solution, VWR JT3144-3) to precipitate $Ni(OH)_2$.
c. Shake and then centrifuge (4000 RPM, 3 min) the mixture. Decant and discard the liquid.
d. Wash the $Ni(OH)_2$ precipitate three times, each time by redispersing the solid in ~20 mL of 0.1 M KOH. Once redispersed, centrifuge the mixture and decant and discard the liquid.

Electrolyte Purification

e. Fill the centrifuge tube containing washed $Ni(OH)_2$ powder to 50 mL total volume with 1 M KOH and redisperse the solid.
f. Shake for approximately 10 min and let sit for 3 h.
g. Centrifuge the mixture, and decant the now "purified" KOH into a pre-cleaned polypropylene or high-density polyethylene bottle for storage. $Ni(OH)_2$ precipitate can reused for purification of additional 1 M KOH by repeating steps e-g an additional two times.

S5.2. Film Thickness and Composition for Sputtered $Ni_{1-x}Fe_x$ Films

The thicknesses and compositions of sputtered $Ni_{1-x}Fe_x$ films targeted using a quartz crystal microbalance internal to the sputtering unit were verified by inductively-coupled plasma optical emission spectroscopy, ICP-OES (ICP Optima 7000 DV, Perkin-Elmer) and X-ray photoelectron spectroscopy (XPS). Films 5-20 nm thick were sputter deposited onto glass slides of known lateral dimensions, estimated via Image J[1]. (Note that 2 nm thick films were deposited for XPS and electrochemical measurements as presented in the main text, but thicker films were used here to generate solutions with sufficiently high concentrations for ICP-OES calibration.) Films were analyzed by XPS and then dissolved by sonication in high-purity 5 M HNO_3 (Sigma-Aldrich 84385 or EMD Millipore NX0407). The resulting solutions were diluted with 18.2 MΩ cm H_2O to give 5% w/w HNO_3 and 1000 ppb of yttrium as an internal standard (Sigma Aldrich 01357). Calibration solutions contained 5% w/w HNO_3, 1000 ppb Y, and both Ni and Fe, each with concentrations between 0 and 2000 ppb (Sigma-Aldrich 28944 and 43149 for Ni and Fe solutions, respectively).

The thicknesses of the sputtered films were calculated using a weighted average of the densities of Ni and Fe metal (8.91 and 7.87 gm cm^{-3}, respectively). Figure S5.2.1a shows a plot of as-deposited composition (determined from ICP-OES) and percent of target thickness vs. target composition, with each film thickness (calculated from ICP-OES results) normalized by the target thickness (5-20 nm). The thickness ranged from 70–100% of the target thickness as the Fe content was increased. A comparison of ICP-OES film compositions to compositions extracted from X-ray photoelectron spectroscopy (XPS) is also shown in Figure S5.2.1b. While ICP-OES yielded compositions which closely matched target compositions, XPS analysis reveals higher than anticipated Fe content for 50-80% targeted Fe, which could be in part due to difficulties in background subtracting the XPS Fe 2p region. However, such a deviation in Fe composition from the target composition (determined via XPS) was not observed for 2 nm films deposited over Au RDEs, and in general, the composition of films determined by both methods are relatively comparable. Therefore, all main text compositions reported were determined via XPS, since the catalyst film thickness used is too thin for accurate ICP-OES quantification.

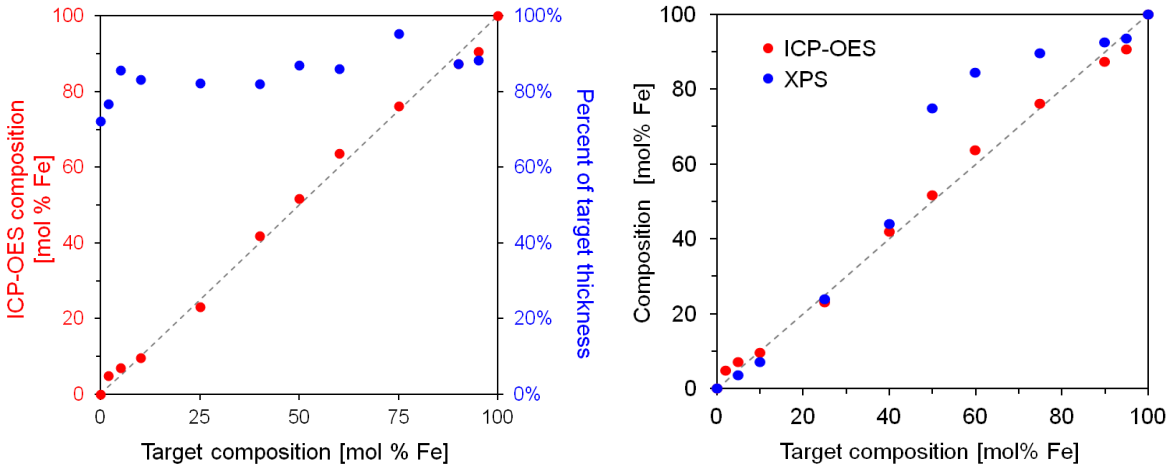

Figure S5.2.1. Calibration plots for sputtered $Ni_{1-x}Fe_x$ films. (A) Plot of Fe content and estimated film thickness as a function of target Fe content for co-sputtered $Ni_{1-x}Fe_x$ films, and (B) comparison of compositions obtained by XPS and ICP-OES.

Activity measurements are compared on an Fe-content basis determined via XPS after electrochemical characterization. As shown in Table S5.2.1a and discussed in the main text, significant Fe loss is observed for sputtered films with target Fe contents of 25-75%. In the case of electrodeposited films, the thicknesses were estimated from previous work[2] and compositions were determined from XPS after electrochemical characterization (Table S5.2.1b). No significant loss of Fe compared to the target Fe composition was observed after electrochemical characterization.

Table S5.2.1. Composition of $Ni_{1-x}Fe_x$ sputtered films as-depositied and after electrochemical stabilization with representative sputtering parameters at room temperature under 15 mTorr Ar.

Target Composition	As Deposited Composition	Stabilized Composition	Fe Power (RF)	Ni Power (DC)	Total Deposition Rate	Deposition Time for 2 nm
mol % Fe		*mol % Fe*	*W*	*W*	*nm s^{-1}*	*s*
0	0	0	0	101	0.040	51
5	4*	4	29	101	0.041	49
10	8	7	40	101	0.043	47
25	24	14	80	101	0.053	38
40	44*	20	140	101	0.068	29
50	50	29	200	101	0.083	24
75	78	66	200	41	0.056	36
95	93*	90	200	16	0.045	44
100	100	100	200	0	0.043	46

** Denotes $Ni_{1-x}Fe_x$ films deposited over glass slides*
Red values denote compositions for which significant Fe loss is observed after electrochemical stabilization and characterization

Table S5.2.1b. Representative compositions of Ni-Fe electrodeposited films after electrochemical characterization with representative deposition parameters at room temperature.

Film Composition	Solution Composition	Ni Concentration	Fe Concentration
mol % Fe	*mol % Fe*	*mol L^{-1}*	*mol L^{-1}*
0	0	0.0100	0.00000
8	1	0.0100	0.00010
17	8	0.0100	0.00087
30	50	0.0100	0.01000
69	85	0.0018	0.01000
83	95	0.0005	0.01000
100	100	0.0000	0.01000

S5.2.2. Electrochemical Conversion of Sputtered Ni to $Ni(OH)_2$/NiOOH

The reduction peak areas from cyclic voltammograms of films with various $Ni_{1-x}Fe_x$ compositions are presented in Table S5.2.2 and were used to estimate the amount of Ni metal converted to $Ni(OH)_2$/NiOOH. The reduction peak areas after electrochemical characterization were comparable to the first cycle of stabilization for electrodeposited films (Qf/Qi = 0.8-1.2), while the reduction peak areas of sputtered films were found to increase 3- to 6-fold. Note that for the 100% Ni film, a significant increase in the reduction peak areas occurs during electrochemical characterization (i.e. the metallic Ni films are not entirely converted to $Ni(OH)_2$/NiOOH after 15 h of electrochemical stabilization cycling).

Table S5.2.2. Comparison of reduction peak areas, reported as charge passed, Q. Subscripts refer to first cycle of stabilization (i, initial), the last cycle of stabilization (s, stabilized) and final cycle after electrochemical characterization (f, final) for select Fe compositions (determined after electrochemical characterization)

	Sputtered				Electrodeposited			
Composition [% Fe]	Q_i [mC cm^{-2}]	Q_s [mC cm^{-2}]	Q_f [mC cm^{-2}]	Q_f/Q_i	Q_i [mC cm^{-2}]	Q_s [mC cm^{-2}]	Q_f [mC cm^{-2}]	Q_f/Q_i
0	0.61	1.61	2.72	**4.5**	1.81	1.80	2.18	**1.2**
7	0.61	2.15	2.26	**3.7**	1.94	1.99	2.08	**1.1**
20	0.39	1.40	1.42	**3.6**	1.47	1.42	1.56	**1.1**
25	0.06	0.34	0.39	**6.5**	0.78	0.96	0.66	**0.8**

S5.3. Electrochemical Characterization

S5.3.1 Redox Peak Analysis: Baseline Fitting

Redox peak areas were obtained with linear or polynomial baseline subtraction, depending on whether the oxidation wave was partially overlapping with current from the OER, which makes peak fitting more challenging at higher Fe concentrations as the redox peaks shift to higher potentials and the OER current increases. Figure S5.3.1 shows representative cyclic voltammograms for $Ni_{1-x}Fe_x$ film compositions ranging from 0 to 25% Fe (after characterization), for which both oxidation and reduction waves are visible. Typically, polynomial baselines for the oxidation waves were suitable for compositions ranging from 20-30% Fe.

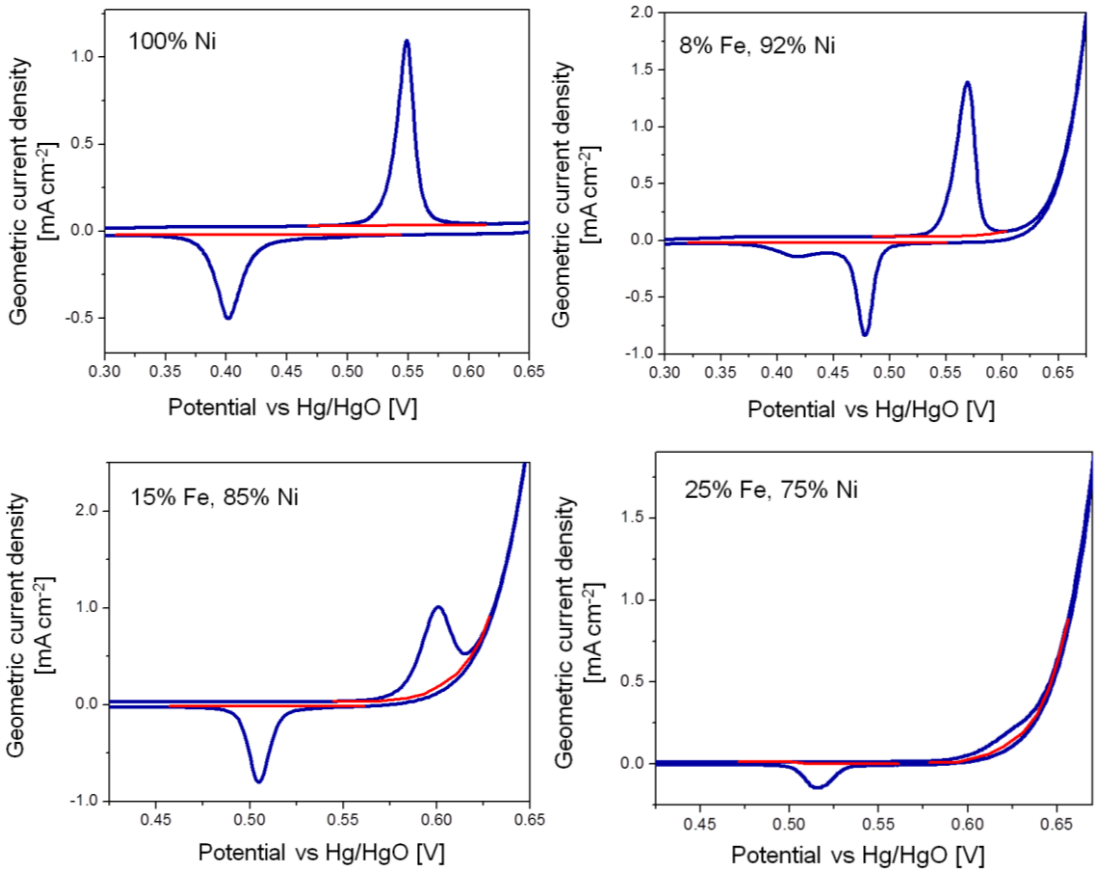

Figure S5.3.1. Representative cyclic voltammograms (blue; 10 mV s^{-1}, 0.1 M KOH, 1600 RPM) for sputtered $Ni_{1-x}Fe_x$ films after electrochemical stabilization/characterization showing baselines (red) used for integration of redox waves.

S5.3.2. Electrochemical Stabilization Voltammograms

Stabilization voltammograms are shown in Figure S5.3.2. Note that after electrochemical characterization (i.e. ~2 h of oxygen evolution), the redox features of Ni films are more pronounced. The only oxidation/reduction waves observed for 100% Fe films are those of the underlying Au substrate. (Note that Au redox waves are also observed for samples containing Ni, but are typically much smaller than Ni redox waves.)The increase in the Au redox features during stabilization cycling and higher Au:Fe XPS ratio for 100% Fe films after electrochemical characterization (vs as deposited) is consistent with increased exposure of Au due to some loss of Fe or formation of islands or cracks in the catalyst films. (We note that a slight increase in Au redox features are also slightly observed for all samples after electrochemical stabilization.)

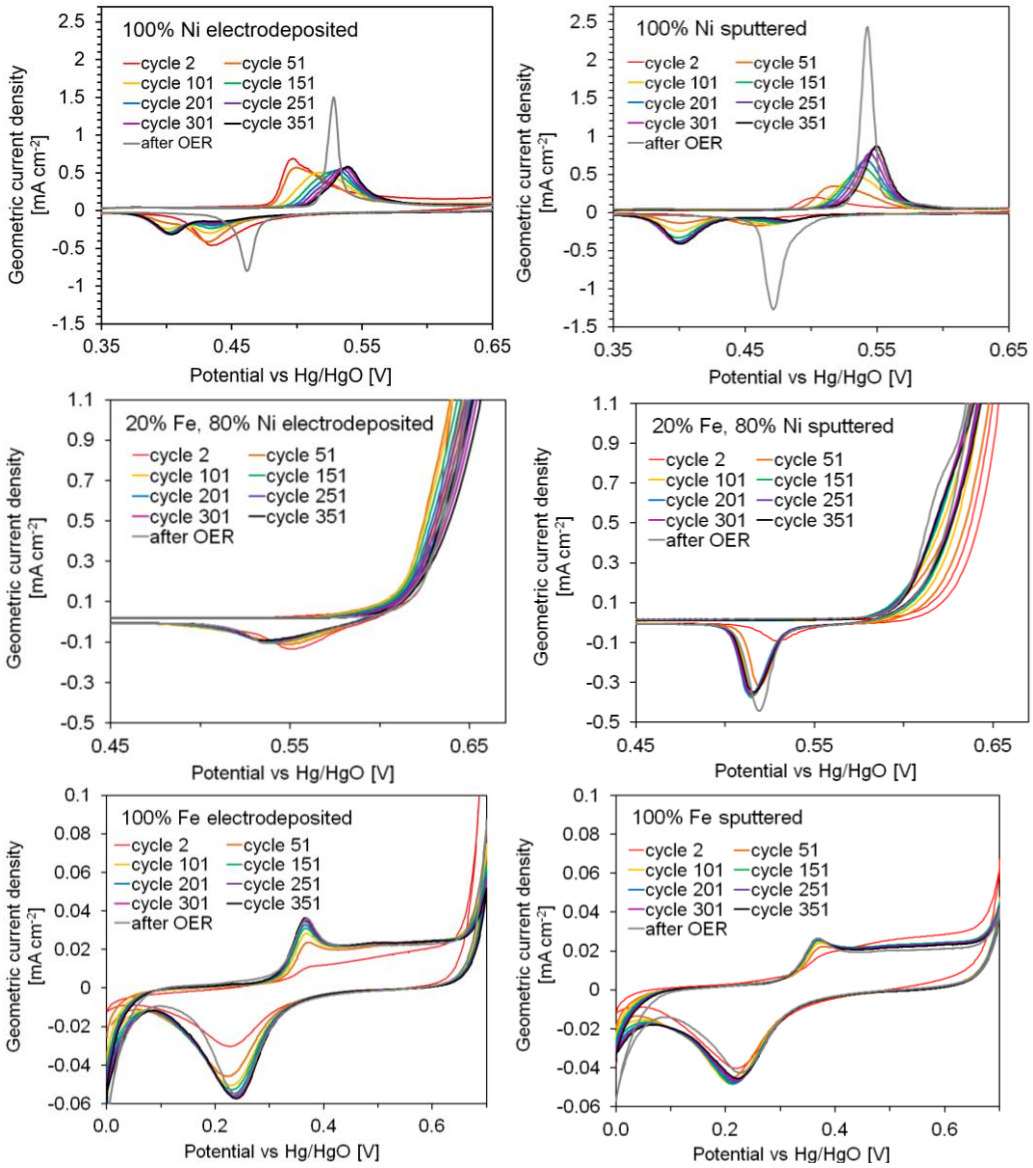

Figure S5.3.2. Cyclic voltammograms for sputtered and electrodeposited Ni, $Ni_{1-x}Fe_x$, and Fe films measured in 0.1 M KOH with a scan rate of 10 mV s^{-1} and no RDE rotation, except 1600 rpm for the "after OER" cycle. Electrochemical stabilization cycling lasted for a total of 14-16 hours and CVs shown here are at 50-cycle intervals (~2 h of continuous cycling between each CV shown).

S5.3.3. Comparison of Electrodeposited and Sputtered Voltammograms after Electrochemical Characterization

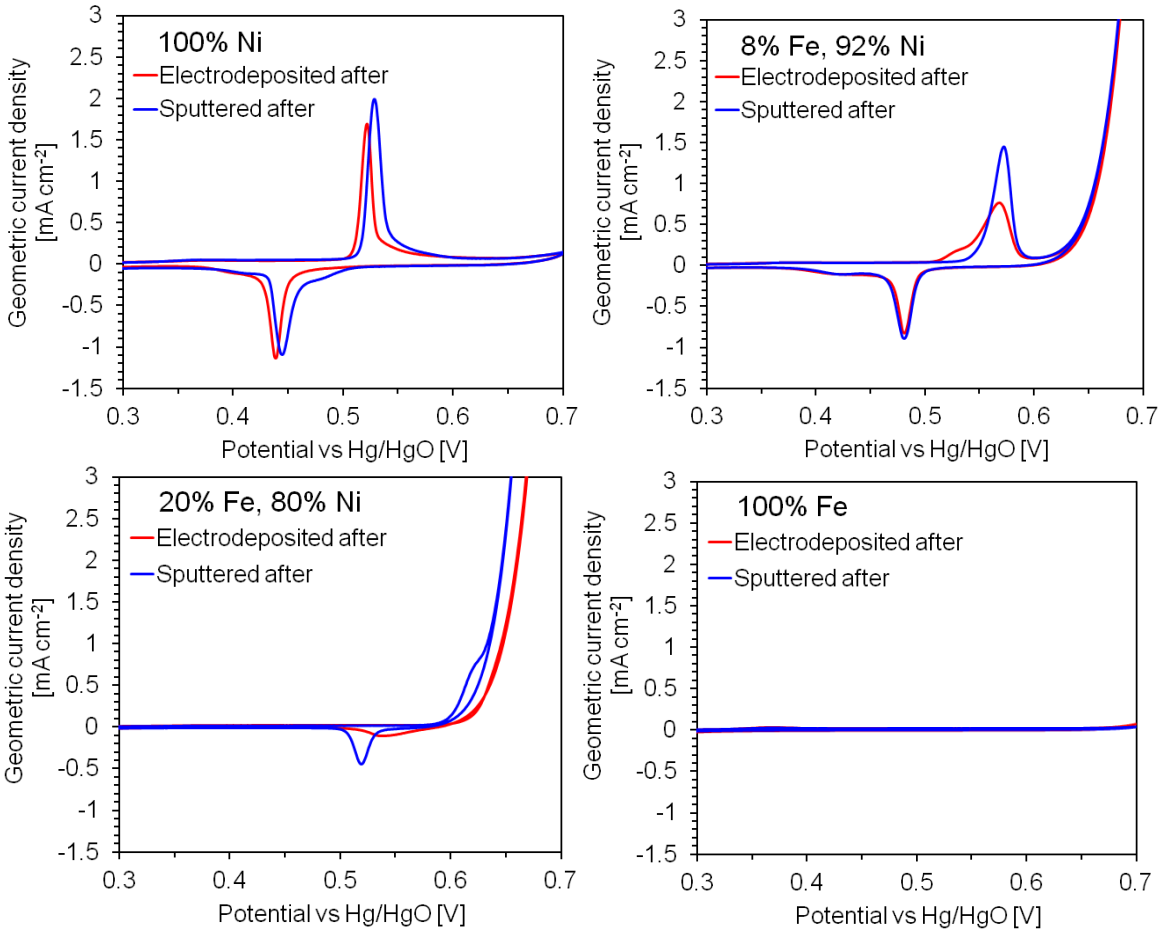

Figure S5.3.3. Comparison of cyclic voltammograms for electrodeposited and sputtered Ni-Fe films of select compositions (compositions determined after electrochemical characterization). CVs were collected at a scan rate of 10 mV s^{-1} in 0.1 M KOH with a RDE rotation rate of 1600 RPM.

S5.3.4. Determination of Oxygen Evolution Activity

Representative activity measurements are shown in Figure S5.3.4. The current and potential values used to calculate catalyst activity were recorded immediately after any bubbles which accumulated at the electrode were cleared by pausing the measurement and removing the electrode briefly from the electrolyte, since accumulated bubbles block surface sites and decrease the measured current (chronoamperometry) or increase the potential (chronopotentiometry). This effect was most apparent in chronopotentiometry measurements in which a high current density was applied, visible as the drop in the measured potential when accumulated bubbles were cleared.

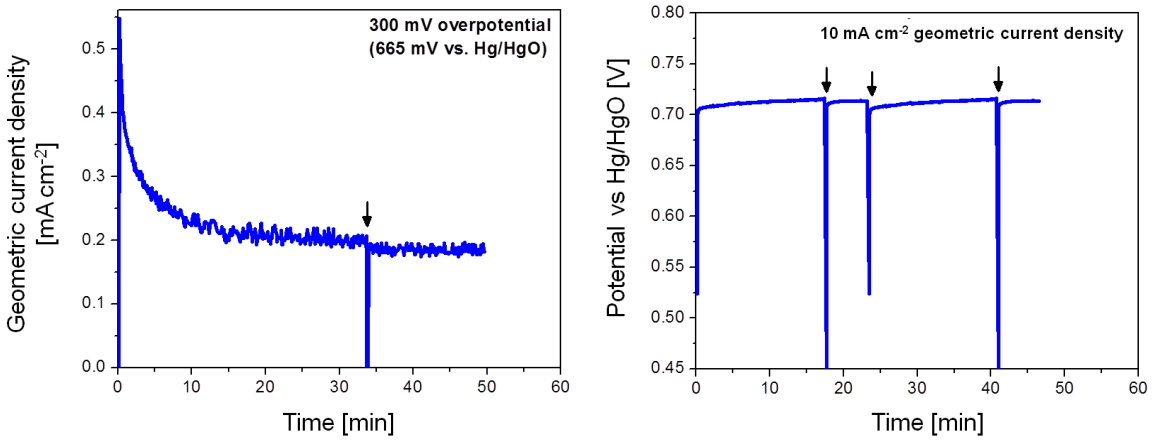

Figure S5.3.4. Representative chronoamperometry (left) and chronopotentiometry (right) measurements used for activity determination, shown here for a sputtered film with 14% Fe (stabilized) content. Arrows indicate where the measurement program was paused and the oxygen bubbles were cleared from the working electrode by retracting the RDE from the electrolyte. Measurements were collected in 0.1 M KOH with a RDE rotation rate of 1600 RPM.

S5.3.5 Tafel Slopes

Tafel slope fits are shown in Fig. S5.3.5. We note that non-linearity was observed at higher currents (this can be seen, for example in the 25% Fe and 30% Fe electrodeposited films), as well as for high Fe-content films.

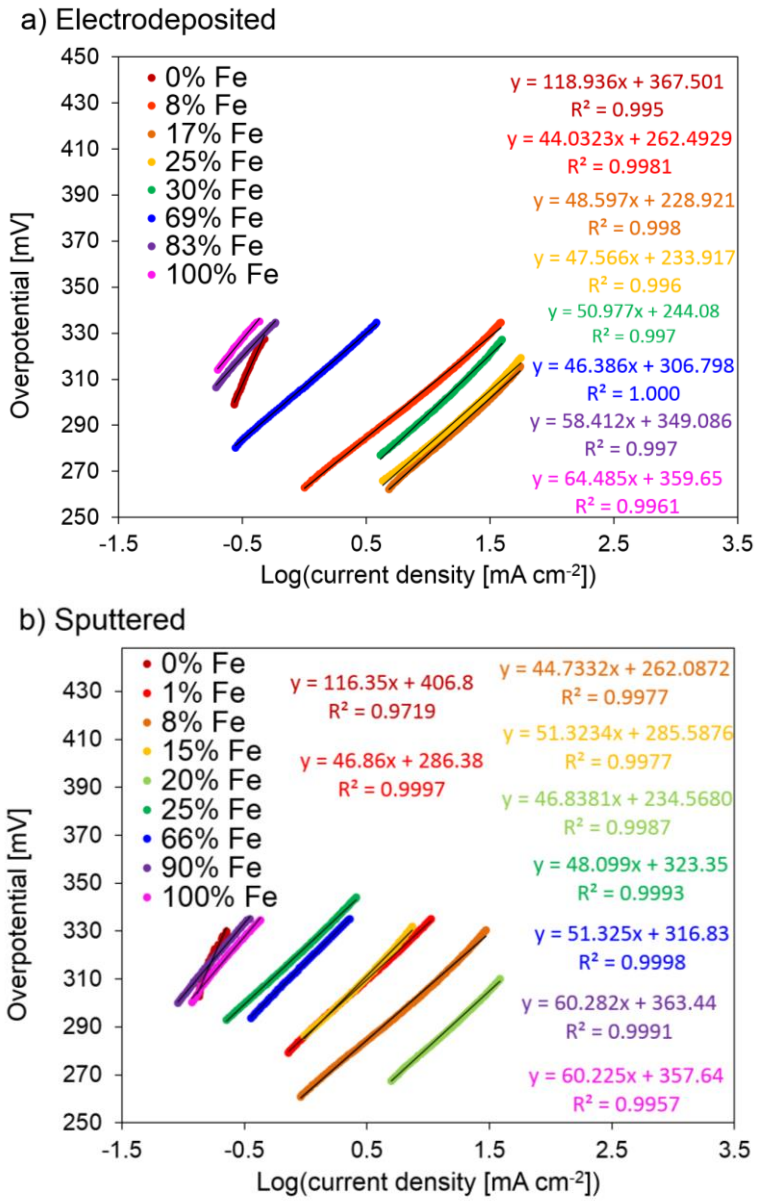

Figure S5.3.5. Representative Tafel slope fits for a) electrodeposited and b) sputtered $Ni_{1-x}Fe_xOOH$ films. Values were obtained from 10 mV s^{-1} CV scans in 0.1 M KOH with a RDE rotation rate of 1600 RPM.

S5.4. X-ray Photoelectron Spectroscopy

S5.4.1. Background Fitting

Figure S5.4.1 shows example X-ray photoelectron spectra of $Ni_{1-x}Fe_x$ films to illustrate the background fits used for composition analysis. Shirley background fits were used for the Ni 2p regions. Depending upon the appropriateness of the Shirley background fit, a linear (≤ 25% Fe) or Shirley (>25% Fe) background was selected for the Fe 2p region. Apart from satellite subtraction (due to use of a non-monochromatic Mg source), the data shown in Figure S5.4.1 are raw spectra.

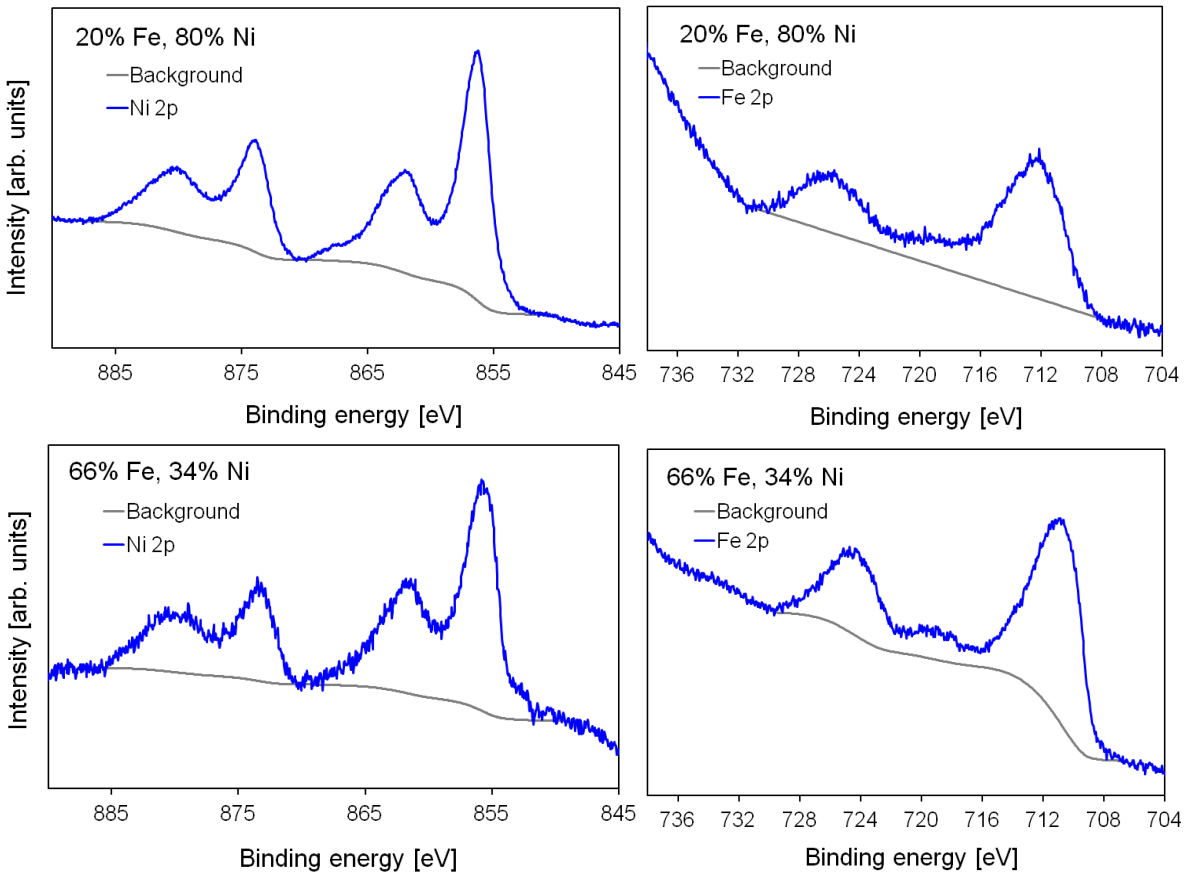

Figure S5.4.1. Representative background fits for X-ray photoelectron spectra of sputtered $Ni_{1-x}Fe_x$ films with 20 % and 66% Fe content after electrochemical characterization

S5.4.2. X-ray Photoelectron Spectra of 100% Ni and 100% Fe films

Figure S5.4.2 shows the XPS spectra for 100% Ni films as deposited and after electrochemical characterization. The Ni 2p spectrum for as-sputtered film shows six peaks total, 852.7, 855.7 and 861.2 eV for the Ni $2p_{3/2}$ region and 870.1, 873.4 and 880.0 eV for the Ni $2p_{1/2}$ region. After electrochemical stabilization and activity measurements, peaks at 856.4 and 861.9 eV for the Ni $2p_{3/2}$ region and at 874.1 and 880.1 eV for the Ni $2p_{1/2}$ region are observed. The spectral features of the as-sputtered film are consistent with a mixture of Ni and NiO phases,[4-5] which are expected based on the exposure of as-sputtered Ni metal to air. The spectral features of the film after electrochemical conditioning are attributed to $Ni(OH)_2$, consistent with cyclic voltammogram redox features observed after stabilization cycling. As-sputtered Ni displays an O 1s peak at 531.3 eV with a shoulder at 529.8 eV, consistent with NiO.[5] After electrochemical conditioning, the single peak at 532.1 eV can be attributed to a $Ni(OH)_2$ phase.[5-6] The transformation observed in the O 1s spectra supports the conclusions drawn from the Ni 2p region.

On the other hand, XPS spectra for electrodeposited films exhibit fewer changes with electrochemical stabilization and characterization. The XPS spectra for films before and after conditioning/characterization exhibit peaks at 856.4 and 861.8 eV for the Ni $2p_{3/2}$ region and at 874.1 and 879.9 eV for the Ni $2p_{1/2}$ region. These are in agreement with the presence of a $Ni(OH)_2$ phase in both before and after stabilization/characterization. The O 1s spectra for electrodeposited Ni before and after stabilization/characterization exhibit one oxygen peak, also consistent with a $Ni(OH)_2$ phase. These observations indicate that electrodeposition of Ni primarily produces hydroxide phases which exhibit less phase transformation during electrochemical stabilization/characterization.

It should be noted that the Ni 2p spectra for $Ni(OH)_2$ and NiOOH phases are very similar.[4-5] Therefore, the two phases are often distinguished by their differing O 1s characteristics, with NiOOH exhibiting an additional peak at lower binding energies due to the deprotonation of an oxygen. In contrast to our previous study in which Ni-Fe films were polarized to OER potentials prior to characterization by XPS,[2] films in the present study were cathodically scanned below the $Ni(OH)_2$/NiOOH redox couple prior to XPS measurement. Therefore, a major contribution from a NiOOH phase is not expected here, although the slight difference in peak position of the spectra for electrochemically prepared films may be in part due to contributions from NiOOH present within the film. Thus, after electrochemical characterization, both sputter deposited and electrodeposited Ni films are comprised primarily of $Ni(OH)_2$, with perhaps a small amount of NiOOH also present.

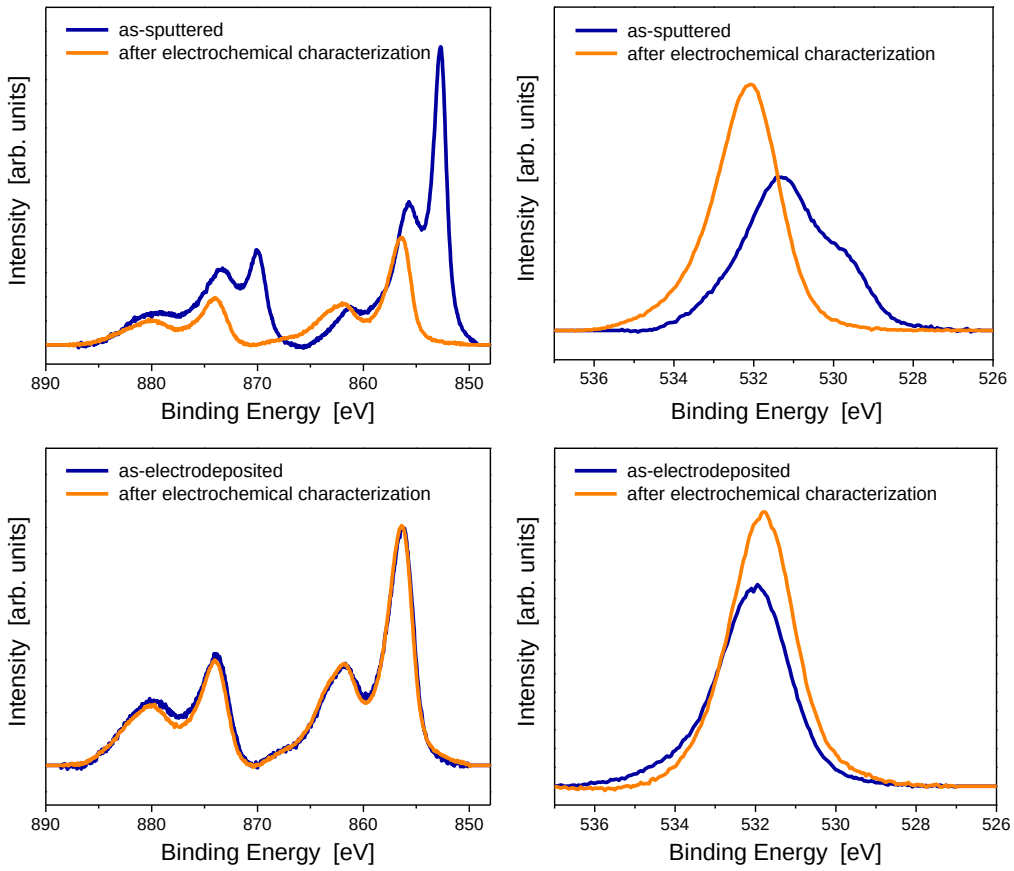

Figure S5.4.2a. Comparison of Ni 2p and O 1s XPS spectra (background-subtracted) for sputtered and electrodeposited Ni thin film before (blue) and after (orange) electrochemical characterization.

The XPS spectra for pure Fe films, both as-deposited and after electrochemical stabilization/characterization are shown in S4.2b. As-sputtered Fe exhibits XPS peaks at 711.1 and ~719 eV for the Fe $2p_{3/2}$ region and at 724.4 and ~733 eV for the Fe $2p_{1/2}$ region. After electrochemical characterization, the peaks appear slightly broader, but the observed binding energies are almost identical to those of the as-deposited sputtered film (specifically, 711.2 and ~719 eV for Fe $2p_{3/2}$ region and 724.6 and ~733 eV for the Fe $2p_{1/2}$ region). Qualitative comparison of the spectral shape to references in literature suggests that possible phases include Fe_3O_4, α/γ-Fe_2O_3 and/or α/γ-FeOOH.[7] However, oxide phase(s) present cannot be uniquely identified due to similarities in the Fe 2p binding energies and spectral shapes of the higher oxides of iron. For example, the Fe $2p_{3/2}$ binding energies for Fe_3O_4, α/γ-Fe_2O_3 and α/γ-FeOOH differ only by 0.6 eV.[7] We note that for sputtered Fe both as-deposited and after electrochemical characterization, no contribution from metallic Fe, expected at 707 eV, is observed.[4, 7]

The O 1s spectral characteristics may provide some information on changes in the film before and after stabilization. Both as-sputtered and stabilized/characterized Fe films exhibit an O 1s peak at 530.1 eV and shoulder at ~532 eV, with the peak at 530.1 eV growing in relative intensity after electrochemical characterization. These two contributions are attributed to two differing types of oxygen found in iron hydr(oxides): deprotonated (530.1 eV) and protonated (~532 eV) oxygen bound to iron.

The as-electrodeposited Ni film exhibits Fe peaks at 711.3 and ~719 eV for the $2p_{3/2}$ region and 724.6 and ~733 eV for the $2p_{1/2}$ region. After electrochemical cycling, Fe 2p peaks are observed at 710.9 and ~719 eV for the $2p_{3/2}$ region and 724.4 and ~733 eV for the $2p_{1/2}$ region. O 1s contributions are observed at 530.1 and 531.7 eV for electrodeposited Fe both before and after electrochemical characterization. However, electrochemical stabilization/characterization results in the growth of the peak at 530.1 eV relative to that at 531.7 eV.

As-prepared films are noticeably different in their O 1s spectra; as-sputtered films have a greater oxide contribution (consistent with metal exposure to air) while as-electrodeposited films have a greater hydroxide contribution. After electrochemical characterization, however, the O 1s spectra for both sputtered and electrodeposited films are qualitatively similar. The increase in relative intensity of the 530.1 eV peak for both Fe films with electrochemical treatment implies an increase in the oxide contributions (Fe-O at 530.1 eV) relative to hydroxide contributions (Fe-O-H at 531.7 eV).[7] (A 1:1 ratio in the O 1s peak areas implies a stoichiometric FeOOH phase). Therefore, after electrochemical characterization, both sputter deposited and electrodeposited Fe is primarily present as Fe_3O_4 and/or Fe_2O_3, with some amount of FeOOH additionally present.

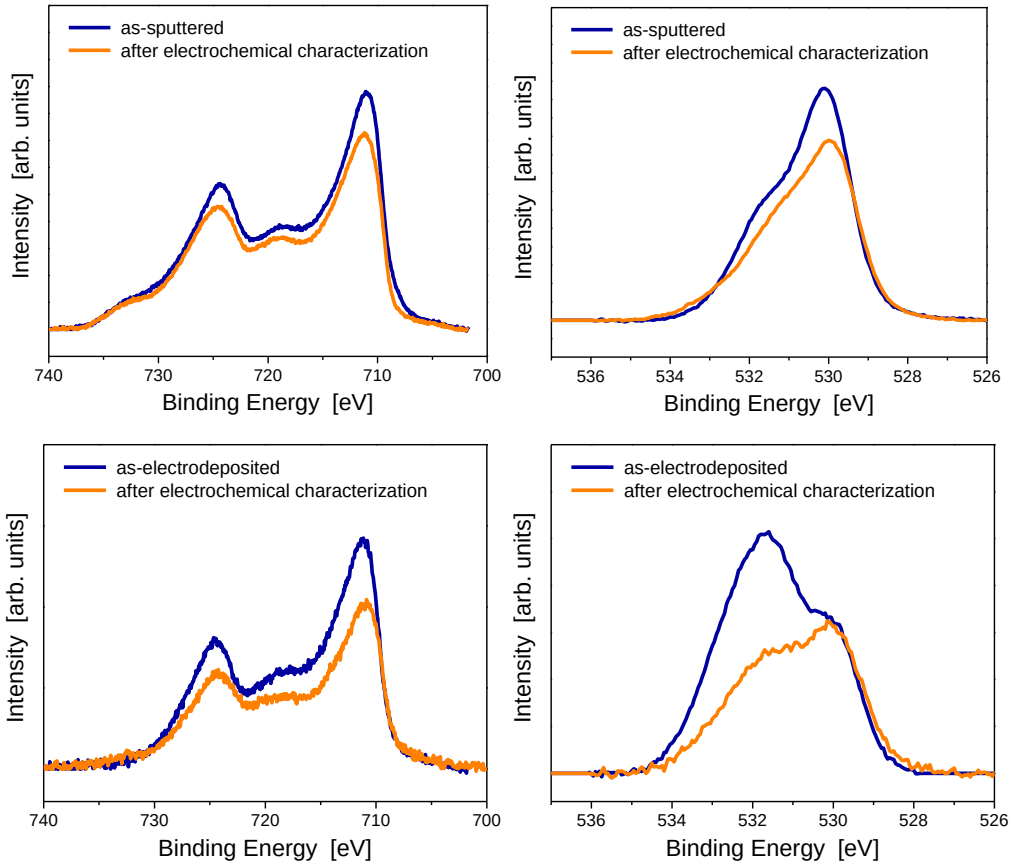

Figure S5.4.2b. Comparison of Fe 2p and O 1s XPS spectra (background-subtracted) for sputtered and electrodeposited Fe thin film before (blue) and after (orange) electrochemical characterization.

S5.5. Additional Raman Spectra and Concurrent Voltammograms

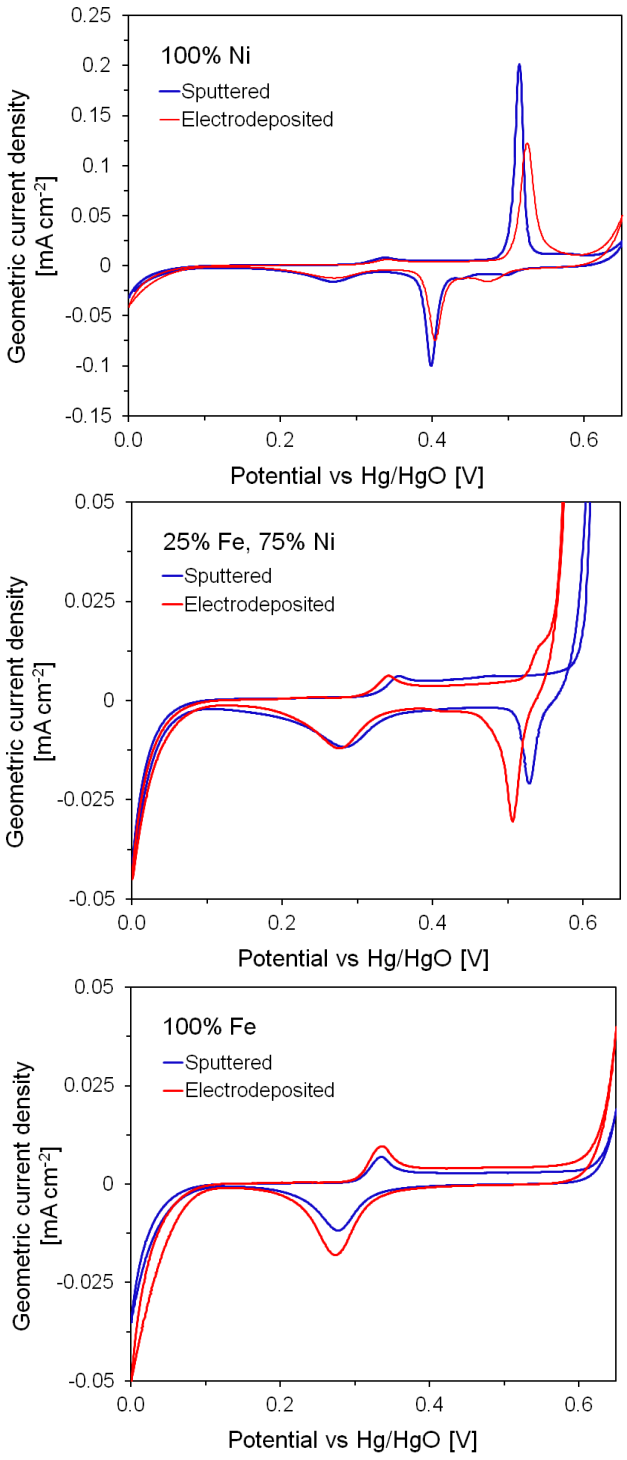

Figure S 5.5.1. Representative cyclic voltammograms acquired concurrently with Raman spectra for Ni, $Ni_{1-x}Fe_x$, and Fe films sputter deposited or electrodeposited over roughened Au. CVs were collected at a scan rate of 1 mV s^{-1} in 0.1 M KOH.

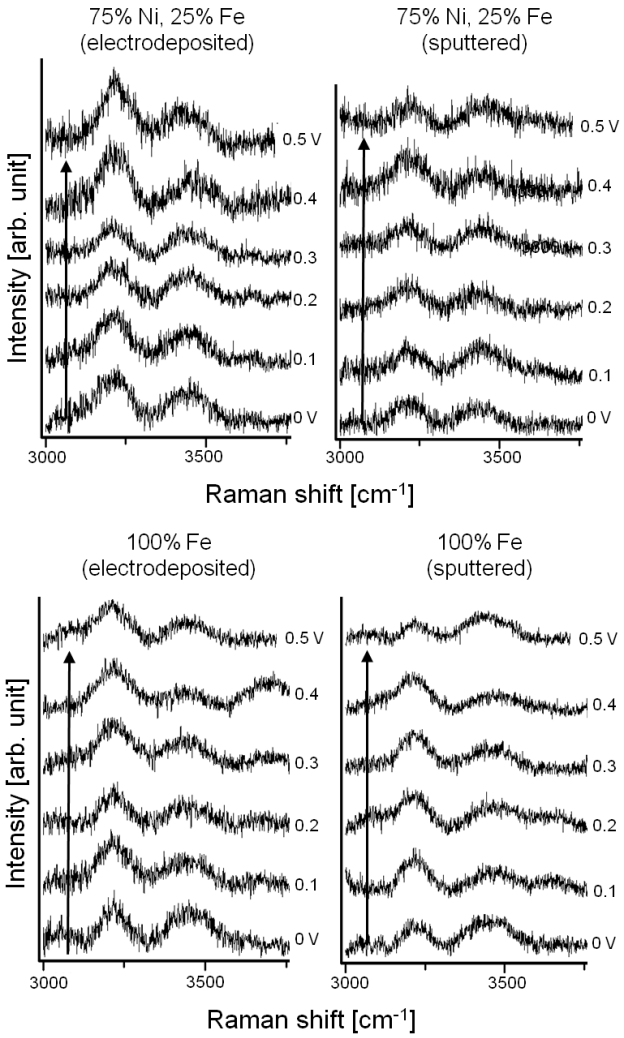

Figure S5.5.2. High-wavenumber in situ Raman spectra for 25% Fe, 75% Ni% and 100% Fe (stabilized) electrodeposited and sputter deposited on roughened Au substrates as a function of potential vs. Hg/HgO in 0.1 M Fe-free KOH, for which the equilibrium OER potential is 0.365 V.

S5.6. Additional Voltammetry and Activity Measurements of Layered and Mixed Ni-Fe Sputtered Films

Prior to activity measurements, sequential and co-sputtered Ni/Fe films were electrochemically stabilized (Figure S5.6.1). During stabilization cycling, the Ni-on-top film initially exhibits a very high OER current which continues to decay (likely due in part to massive bubble formation on the electrode surface), while the Fe-on-top sample initially has a lower current that increases with electrochemical stabilization cycling. The co-sputtered sample decreases in current with increased stabilization cycling, however the current decrease is not as dramatic as in the Ni-on-top sample.

After electrochemical stabilization and characterization, the NiOOH reduction peak area increased for the Fe-on-top and mixed Ni-Fe films (Figure S5.6.2). However, the OER current for the Fe-on-top sample decreases after characterization (Fe:Ni ratio decrease from 85% Fe as-deposited to 58% Fe after characterization), while the OER current increases after characterization for the mixed Ni-Fe film. In contrast, the Ni-on-top sample exhibits a similar reduction peak area and oxygen evolution activity before and after electrochemical characterization. However, these changes in activity and peak areas are transient, and it is difficult to definitively establish why these changes are occurring. We therefore focus on stabilized samples in the main text.

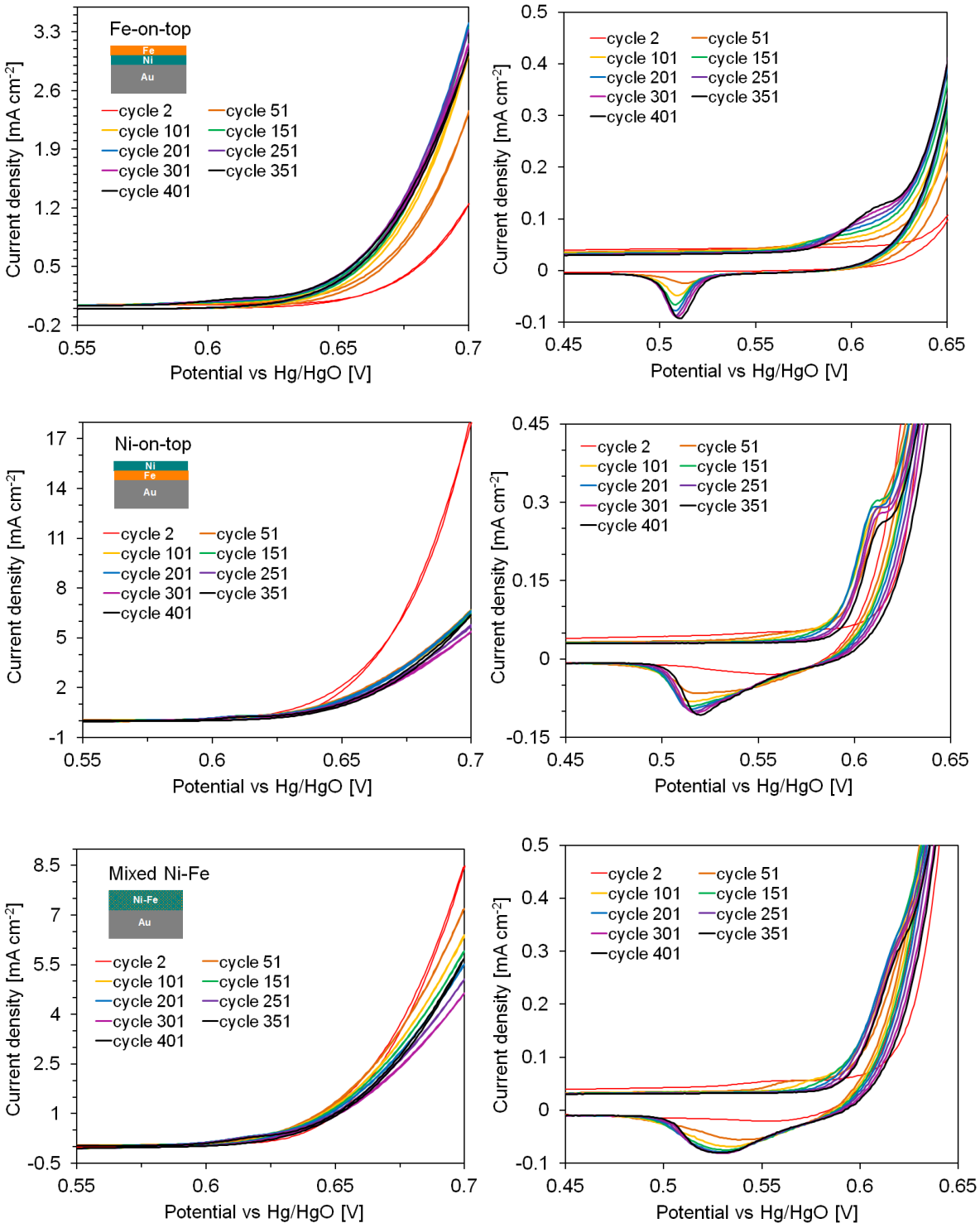

Figure S5.6.1. Stabilization cyclic voltammograms for sequentially and co-deposited 50:50: Fe:Ni films over Au. CVs were collected at a scan rate of 10 mV s^{-1} in 0.1 M KOH with no rotation. Cycling lasted for 15-16 hours and are shown here in 50-cycle intervals (~2 h of continuous cycling between each CV shown).

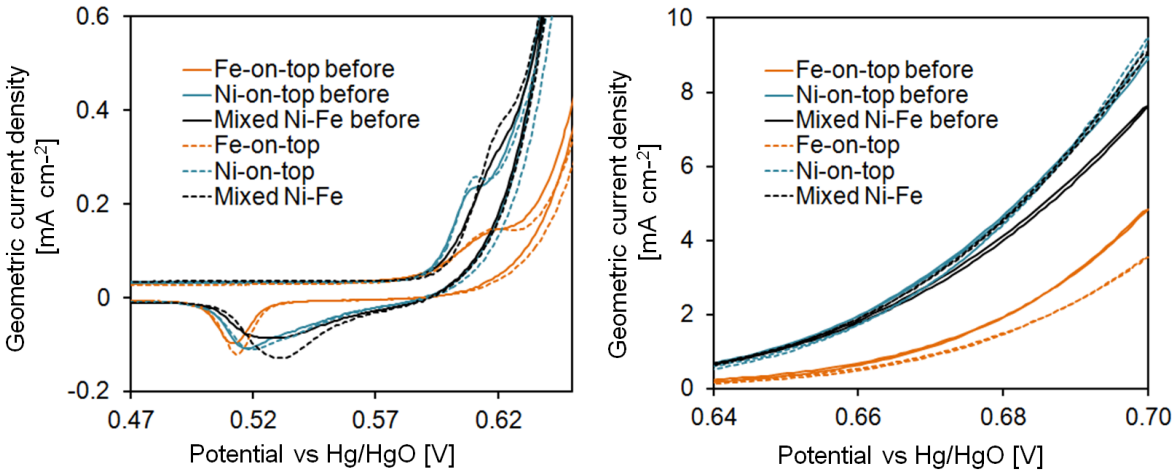

Figure S5.6.2. Cyclic voltammograms before electrochemical characterization, after stabilization cycling (before, solid lines) and after electrochemical characterization (after, dashed line for sequentially and co-deposited 50:50: Fe:Ni films over Au. CVs were collected at a scan rate of 10 mV s^{-1} in 0.1 M KOH with 1600 RPM.

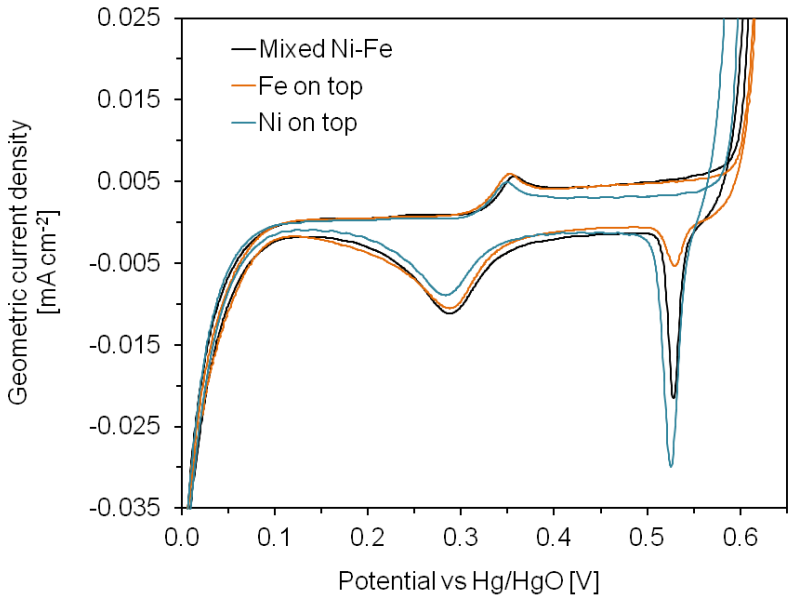

Figure S5.6.3. Cyclic voltammograms concurrent with Raman acquisitions for mixed and layered Ni-Fe films sputter deposited over polished Au. CVs were collected at a scan rate of 1 mV s^{-1} in 0.1 M KOH

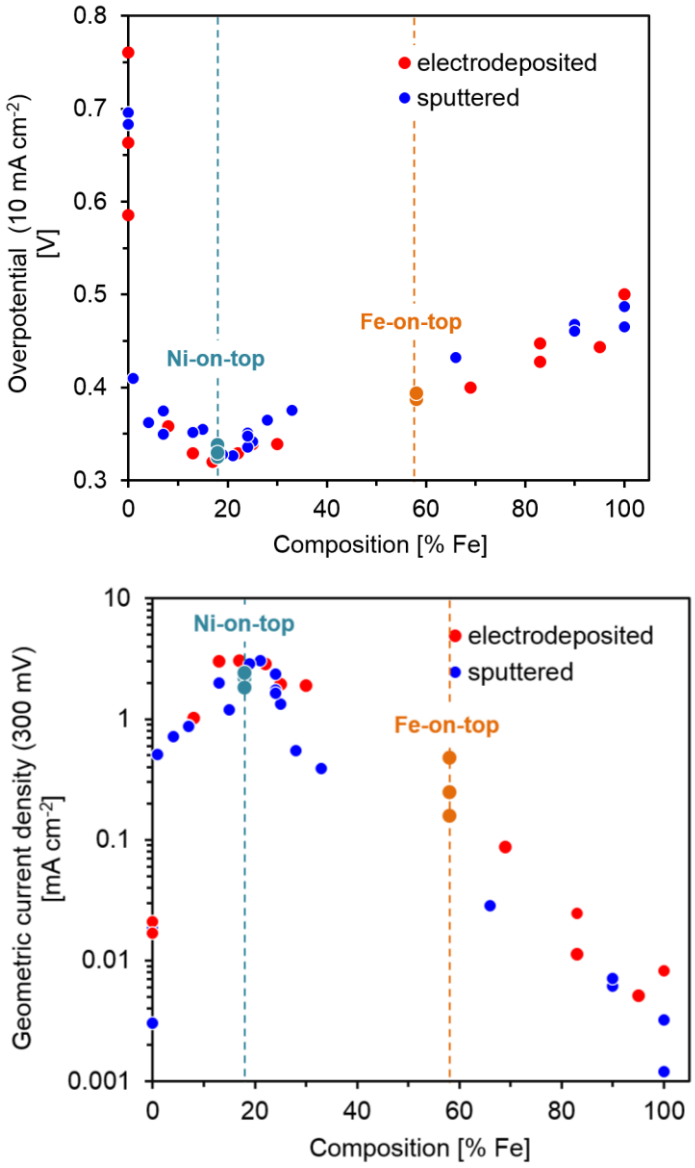

Figure S5.6.4. Activity plots of layered samples overlaid with data from codeposited Ni-Fe films as shown in Figure 5.3 of the main text. Activity measurements were obtained in 0.1 M KOH after 1 h at either constant applied overpotential (300 mV) or geometric current density (10 mA cm^{-2}).

References

S1. Schneider, C. A.; Rasband, W. S.; Eliceiri, K. W., Nih Image to Imagej: 25 Years of Image Analysis. *Nat Methods* **2012**, *9*, 671-675.

S2. Louie, M. W.; Bell, A. T., An Investigation of Thin-Film Ni-Fe Oxide Catalysts for the Electrochemical Evolution of Oxygen. *J Am Chem Soc* **2013**, *135*, 12329-12337.

S3. Trotochaud, L.; Young, S. L.; Ranney, J. K.; Boettcher, S. W., Nickel-Iron Oxyhydroxide Oxygen-Evolution Electrocatalysts: The Role of Intentional and Incidental Iron Incorporation. *J Am Chem Soc* **2014**, *136*, 6744-6753.

S4. Nist X-Ray Photoelectron Spectroscopy Database, Version 4.1. NIST X-ray Photoelectron Spectroscopy Database, Version 4.1: 2012.

S5. Biesinger, M. C.; Payne, B. P.; Lau, L. W. M.; Gerson, A.; Smart, R. S. C., X-Ray Photoelectron Spectroscopic Chemical State Quantification of Mixed Nickel Metal, Oxide and Hydroxide Systems. *Surf Interface Anal* **2009**, *41*, 324-332.

S6. Trotochaud, L.; Ranney, J. K.; Williams, K. N.; Boettcher, S. W., Solution-Cast Metal Oxide Thin Film Electrocatalysts for Oxygen Evolution. *J Am Chem Soc* **2012**, *134*, 17253-17261.

S7. Temesghen, W.; Sherwood, P. M. A., Analytical Utility of Valence Band X-Ray Photoelectron Spectroscopy of Iron and Its Oxides, with Spectral Interpretation by Cluster and Band Structure Calculations. *Anal Bioanal Chem* **2002**, *373*, 601-608.